JOURNAL HOMEPAGE: http://www.ofioliti.it ISSN 0391-2612

CONSIGLIO NAZIONALE DELLE RICERCHE

ofioliti

An International Journal
on Ophiolites and Modern Oceanic Lithosphere

VOLUME 45 • N. 1
JANUARY 2020
PP. 1-69

Edizioni ETS

Printed by Edizioni ETS, Palazzo Roncioni - Lungarno Mediceo 16, 56127 Pisa, Italy
e-mail: *ofioliti@edizioniets.com*
ISBN 978-884675779-1

This journal is covered by SCIENCE CITATION INDEX EXPANDED (Sci Search®), ISI ALERTING SERVICE, CURRENT CONTENTS®/PHY. CHEM. & EARTH SCIENCE, GEOBASE, GEOLOGICAL ABSTRACT, GEOREF, PASCAL THEMA, SCOPUS.

Impact Factor (IF) value for 2018: **0.857**
5-year Impact Factor: **1.41**

Ofioliti was established in 1976, and provides an international forum for original contributions and reviews in the field of the geodynamics, petrology, geochemistry, biostratigraphy, stratigraphy, tectonics and paleogeography applied to ophiolitic terrains and modern oceanic lithosphere, including their sedimentary cover. Studies of topics such as geodynamics of the mantle, the evolution of orogens including ophiolites and paleoceanography are also welcome.
Ofioliti is issued twice per year, with possible supernumerary special issues. The subscription price for the EU countries is EUR 150.00 for institutions and libraries; EUR 35.00 for individuals. The subscription price for the other countries is EUR 200.00 for institutions and libraries; EUR 50.00 for individuals Airmail service needs extra: EUR 20.00. The subscription price includes both the printed and the online journal versions.
Payment should be made by Bank draft or Eurocheque addressed to Edizioni ETS, or by Credit Card (VISA, EuroCard and Master Card are welcome) using the subscription order form or by postal cheque addressed to "Edizioni ETS, Abbonamento ofioliti" c.c.p. 14721567.

The manuscripts need to be submitted on-line using the following web address **http://www.ofioliti.it/index.php/ofioliti/author/submit/**

The corresponding author must indicate the manuscript title, authors, and corresponding author data. Moreover a pdf version of the manuscript must be uploaded (max 12Mb). Author guidelines for submission can be found at: https://www.ofioliti.it/index.php/ofioliti/about/submissions#authorGuidelines

Autorizzazione alla pubblicazione del Tribunale di Firenze, n. 4608 del 29 luglio 1996, Iscrizione nel Registro Nazionale della Stampa n. 02137, Spedizione in A.P., art. 2 comma 20/B L. 662/96, n. 1042 del 03/06/2002, Pisa. Direttore responsabile: Valerio Bortolotti.

In memory of Professor Pietro Passerini

AWARD FOR AN OUTSTANDING PHD THESIS ON OPHIOLITES

To commemorate Prof. Pietro Passerini's human and scientific contributions, the journal Ofioliti - published by the Working Group on Mediterranean Ophiolites (GLOM) @ Edizioni ETS S.r.l. offers an award for the best PhD Thesis on ophiolite topics, financed by the Passerini Family.

Pietro Passerini was an admired professor of Geology at the University of Florence. He led for several decades, together with the colleagues of the "ophiolitic team" of Florence, outstanding and original research on various geological aspects of the peri-Mediterranean orogenic belts, the eastern Africa and Iceland. His research was field-based and mainly focused on the Ligurian ophiolites. He achieved two important conclusions on these ophiolites: (i) the classically defined "Penrose" ophiolitic succession is different from that of the 'peculiar' Ligurian ophiolites, and (ii) mantle and gabbroic units experienced oceanic metamorphism and exposure in the Jurassic Ligurian Ocean before extrusions of basaltic lavas. Pietro Passerini and the "ophiolitic team" also discovered that some of the Ligurian ophiolites were translated and included as huge blocks and debris within Cretaceous flysch sequences. Another field in which Pietro Passerini became interested in his later research years was the study of brittle deformation recorded by minor fault systems. In particular, he discovered the unpredicted presence of important transcurrent movements parallel to the Red Sea, the Afar western margin and the central rift of Island. These findings were subsequently used to propose a new interpretation for the origin of the Afar Depression and adjacent regions.

The Passerini family, in collaboration with the Working Group on Mediterranean Ophiolites, of which Pietro was one of the founding and most active members, wishes to honour the memory of Pietro Passerini with an award to encourage research on ophiolites among young students.

The award is designed to bring to the attention of the scientific community young PhD students who contributed to the understanding of ophiolites with innovative and significant ideas and studies.

The gross amount of the prize is EUR 5,000.00.

The candidate must have concluded the PhD Thesis during the years 2016-2020 (before April 30th, 2020) discussing a topic on ophiolitic successions.

Candidates must submit the application following the instructions indicated in the attached pdf file or in the Ofioliti home page (www.ofioliti.it).

Art. 1. Purpose of the award

The award is designed to bring to the attention of the scientific community young PhD students who contributed to the understanding of ophiolites with innovative and significant ideas and studies. This was an important scientific interest of Pietro Passerini.

Art. 2. Amount of the award

The gross amount of the prize is EUR 5,000.00

Art. 3. Requirements for admission

The candidate must have concluded the PhD Thesis during the years 2016-2020 (before April 30th, 2020) discussing a topic on ophiolitic successions.

Art. 4. How to apply and deadline

Applicants must submit the attached application form to the Selection Committee (att. Marta Marcucci, address below), on plain paper and accompanied by the following documents:

- auto-certification showing the obtained degree, the University which awarded it, the final vote/grade obtained, the title of the thesis and the name(s) of the supervisor(s) of the thesis;
- photocopy of an identity document;
- certified paper copy of the thesis (mandatory), and a copy in electronic format (PDF).

All documents must be sent by registered mail by April 30th, 2020.

The date of the postmark will be considered as official in the case of a registered letter. Please write on the envelope "**Concorso Premio di Dottorato Pietro Passerini anno 2020**". All material must be delivered or mailed to the following address:

att. Marta Marcucci
"Concorso Premio di Dottorato Pietro Passerini anno 2020"
c/o Edizioni ETS
Piazza Carrara 16/19 - 56126 Pisa, ITALY
e-mail info@edizioniets.com

In the application, the candidate must indicate under her or his own responsibility (under penalty of exclusion):
- First name and surname
- Date and place of birth
- Tax code
- Complete personal address
- Phone number and e-mail

The candidate has to promptly notify to the committee any change of address, residence, phone number and e-mail. Applications not signed, missing any of the data mentioned above and those submitted beyond the deadline, will not be considered valid.

The **Committee** is not responsible for the loss of the parcels due to errors in address that the candidate provided, failure or late change of address indicated in the application, to any postal or to third parties causes, and major circumstances.

The copies of the thesis will be returned only at the request of the candidates.

Art. 5. Evaluation criteria

Applications will be preliminary evaluated using the requirements presented in this application. The Examiner Scientific Committee will subsequently examine a restricted number of applications that fulfill these requirements.

For the selection of the winner, the Commission will use the following criteria:
- originality of the approach;
- adequacy of the geological models of reference;
- use of appropriate references sources;
- use of fieldwork techniques and/or adequate analytical techniques;
- complexity of the approach and analysis of the problems;
- significance and novelty of the results.

The Commission may identify two joint winners. In this case, the gross premium of € 5,000.00 will be divided equally among them.

Art. 6. Examiner Scientific Committee

The Committee, appointed during a meeting of the Working Group on Mediterranean Ophiolites, is composed of three members. For the 2020 Award, the Scientific Committee is composed of:
Prof. Marta Marcucci President of the Commitee (representing the Passerini family);
Prof. Valerio Bortolotti (Senior editor of journal Ofioliti);
Prof. Riccardo Tribuzio, secretary (Coordinator of the Working Group on Mediterranean Ophiolites).

Art. 7. Notification of results

The award winner and the results of the evaluation will be published on the website of the Ofioliti journal (www.ofioliti.it).

Art. 8. Awards

The award may be subject to taxation under the country law of the winner and it will be remitted in accordance with it.
The Prize will be awarded through a bank transfer. At this purpose, the winner must promptly provide his bank coordinates to Prof. Marta Marcucci at the e-mail address: marta.marcucci39@gmail.com
The award ceremony will take place during the first meeting of the Working Group on Mediterranean Ophiolites after the conclusion of the evaluation process. During this meeting, the Prize winner is invited to give an oral presentation of her/his thesis.
The Prize winner is also invited to submit the results of her/his thesis as a paper to the journal Ofioliti.

PLAGIOCLASE-FACIES THERMOBAROMETRIC EVOLUTION OF THE EXTERNAL LIGURIDE PYROXENITE-BEARING MANTLE (SUVERO, ITALY)

Valentin Basch*,✉, Giulio Borghini, Patrizia Fumagalli**, Elisabetta Rampone*,✉, Andrea Gandolfo*** and **Carlotta Ferrando*****

* *Dipartimento di Scienze della Terra, dell'Ambiente e della Vita, University of Genova, Italy.*
** *Dipartimento di Scienze della Terra "Ardito Desio", University of Milano, Italy.*
*** *CRPG, University of Lorraine, Nancy, France.*
✉ *Corresponding authors: Rampone, email: elisabetta.rampone@unige.it; Basch, email: valentin.basch@gmail.com*

Keywords: *pyroxenites; plagioclase peridotite; veined mantle exhumation; geobarometer; extending lithosphere; Suvero; Northern Apennines; Italy.*

ABSTRACT

Plagioclase peridotites are an important marker of the shallow geodynamic evolution of the lithospheric mantle at extensional settings. Based on low-pressure experiments, a recent study by Fumagalli et al. (2017) defined and calibrated a geobarometer for peridotitic bulk compositions, based on the Forsterite-Anorthite-Ca-Tschermak-Enstatite (FACE) pressure-sensitive equilibrium. The Suvero plagioclase-bearing peridotites, on which the FACE geobarometer was calibrated, are primarily associated to plagioclase pyroxenites. Assuming that the pyroxenites record the same Pressure-Temperature evolution than the plagioclase peridotites, they represent ideal candidates to test the applicability of the FACE geobarometer on pyroxenitic compositions. As documented in the plagioclase peridotites, the pyroxenites are characterized by the development of fine-grained neoblastic assemblages, indicative of partial recrystallization under plagioclase-facies conditions. Chemical zonations in these neoblastic mineral aggregates suggest equilibration stages at variable pressure and temperature and allowed to document two re-equilibration stages corresponding to the onset of plagioclase-facies recrystallization (830-850°C, 6.9-8.1±0.5 kbar) and a shallower colder re-equilibration (770-790°C, 5.8-5.9±0.5 kbar), respectively. The decompressional evolution reported for pyroxenitic bulk compositions is consistent with the exhumation history documented in the associated Suvero peridotite, although at slightly higher equilibrium pressures (~ 1 kbar). Remarkably, the much lower X_{Cr} in pyroxenites reflects in lower Cr incorporation in pyroxenes and, consequently, in significantly higher Ca-Tschermak activity in clinopyroxene that might introduce the systematic pressure overestimation by FACE geobarometer.

INTRODUCTION

Plagioclase peridotites are extensively described in slow to ultraslow-spreading ridges and passive margins (e.g., Kelemen et al., 2007; Dick et al., 2010; Martin et al., 2014; Warren, 2016; Basch et al., 2018), where extension is dominated by tectonic denudation and mantle is exhumed by kilometre-scale detachment faults (e.g., Piccardo et al., 1993; 2002; Rampone and Piccardo, 2000; Manatschal and Müntener, 2009; MacLeod et al., 2009). The formation of plagioclase in these mantle rocks can be related either to magmatic crystallization during percolation of tholeiitic melts within the peridotites or metamorphic recrystallization at plagioclase-facies conditions. The two processes imply a different thermal structure of the lithosphere and can affect different mantle sections of an extending lithosphere, i.e. hot, infiltrated mantle domains affected by melt percolation and melt-rock interaction during exhumation, or cold mantle sectors which were exhumed at subsolidus conditions, thus recording low-pressure metamorphic recrystallization (Rampone et al., 2018). In both cases, plagioclase peridotites constitute an important marker of the shallow geodynamic evolution of the lithospheric mantle at extensional settings.

Experiments on fertile and depleted peridotites within the subsolidus plagioclase stability field (Borghini et al., 2010) demonstrated that the compositions of coexisting plagioclase and pyroxenes are not dependent on the peridotite bulk composition and vary significantly over a rather narrow pressure range. Borghini et al. (2011) proposed an empirical geobarometer based on the composition of plagioclase and applied it on chemically zoned plagioclase-bearing neoblastic aggregates in the Suvero plagioclase peridotites (External Liguride Unit, Northern Apennines, Italy), obtaining pressure estimates from 7 to 3 kbar (i.e. ~ 21 to 9 km; Borghini et al., 2011). More recently, Fumagalli et al. (2017) further investigated experimentally the variability of mineral chemistry in a Na-rich peridotite within the plagioclase-facies. Profiting of a consistent experimental database, covering a wide range of P-T conditions (3-9 kbar, 1000-1150°C) and variable bulk compositions, they calibrated a geobarometer for plagioclase peridotites based on the reaction $Forsterite^{Ol} + Anorthite^{Pl} = Ca\text{-}Tschermak^{Cpx} + Enstatite^{Opx}$ (FACE geobarometer, Fumagalli et al., 2017). The application of the FACE geobarometer, adequately supported by detailed microstructural and mineral chemistry investigations, provides a valuable tool to track the exhumation of the lithospheric mantle in extensional environments.

The Suvero ultramafic body is heterogeneous and characterized by the occurrence of parallel spinel pyroxenite layers within spinel lherzolites (Borghini et al., 2011; 2013; 2016; 2019). These pyroxenite layers were interpreted as the result of old (Ordovician; 433±51 Ma; Borghini et al., 2013) high-pressure segregation (P > 15 kbar) and reactive crystallization of low-MgO silica-saturated melts likely originated by melting of a heterogeneous mantle source (Borghini et al., 2016). Host peridotites and pyroxenite layers were already associated prior to the Jurassic exhumation of this subcontinental mantle sector and presumably experienced the same decompressional Pressure-Temperature evolution leading to partial recrystallization at plagioclase-

facies conditions. Pyroxenite layers are characterized by rather fertile bulk compositions and are, therefore, more sensible to plagioclase-facies recrystallization (Hidas et al., 2013; Fumagalli et al., 2017; Borghini and Fumagalli, 2018). Subsolidus phase relations have been experimentally defined for a pyroxenite sample (GV10) from the Suvero massif (Borghini and Fumagalli, 2018). Few experiments on pyroxenite GV10 at plagioclase-facies conditions have provided plagioclase composition comparable with those observed in the host peridotite, but more experimental data on plagioclase-bearing pyroxenites are needed to extend the applicability of the FACE geobarometer to pyroxenitic compositions. The more fertile character of pyroxenites with respect to peridotites enhances subsolidus recrystallization processes (Hidas et al., 2013; Borghini et al., 2016; Borghini and Fumagalli, 2018) and can therefore facilitate the geobarometric estimates for pyroxenite-bearing mantle sectors. Moreover, fertile pyroxenites are expected to encounter plagioclase appearance at significantly higher pressure than peridotite (Borghini and Fumagalli, 2018) and thus they are potentially good markers of low-pressure equilibration of the mantle rocks.

In this article, we present a detailed microstructural-based chemical work on the neoblastic plagioclase-facies mineral assemblage on selected pyroxenite samples. The main objectives of this paper are to: *i)* document the low-pressure evolution as recorded by pyroxenite layers that are directly associated to plagioclase peridotites previously investigated (Borghini et al., 2011); and *ii)* test the applicability of the FACE geobarometer on pyroxenitic compositions.

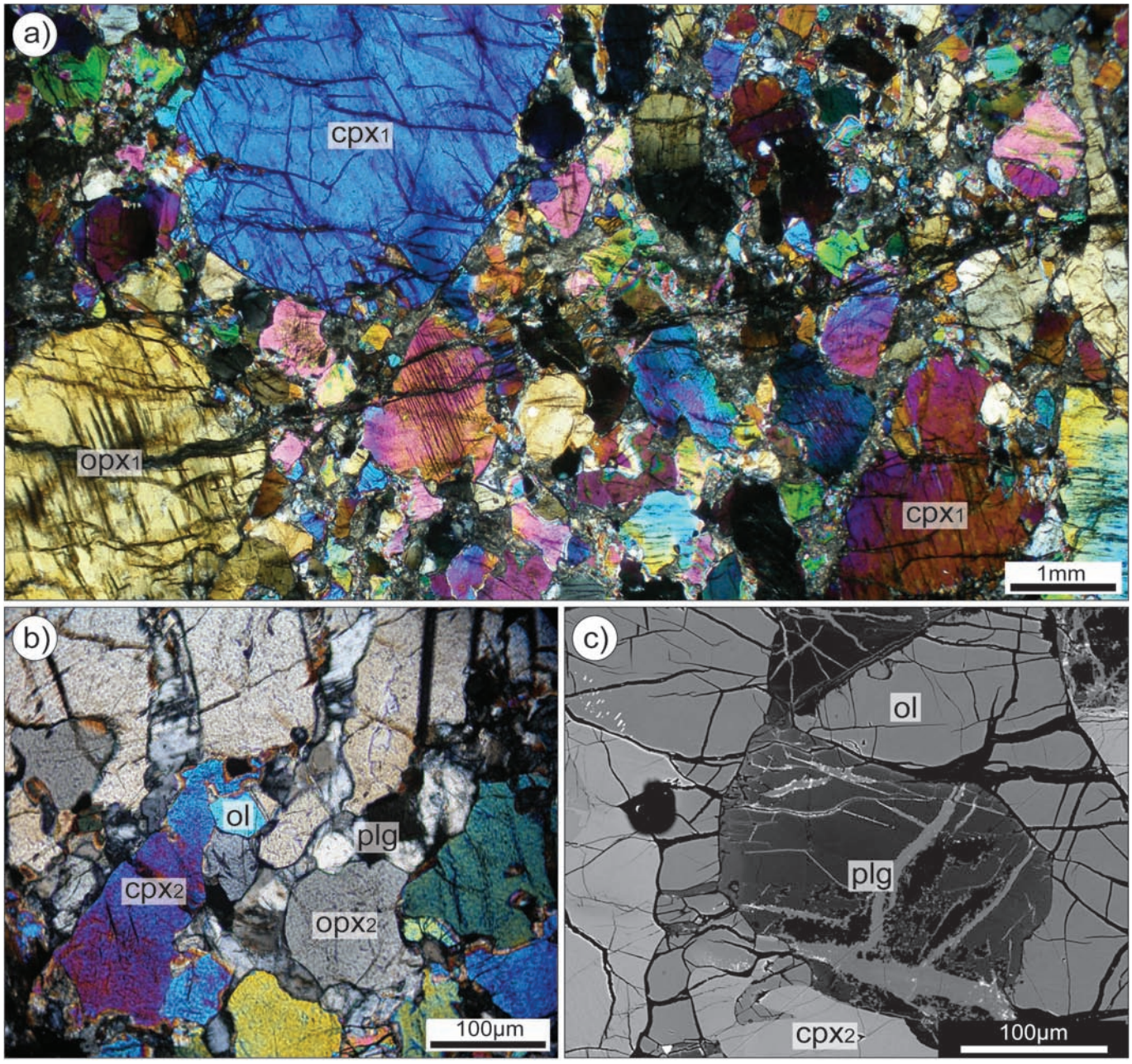

Fig. 1 - Photomicrographs and BSE image of representative textures observed in the Suvero plagioclase-bearing pyroxenites. a) Partially recrystallized spinel-facies porphyroclastic assemblage; b) Detail of the plagioclase-bearing neoblastic assemblage; c) BSE image of the plagioclase-bearing neoblastic assemblage. The colour variation within plagioclase is indicative of a core-rim chemical zoning. cpx- clinopyroxene; opx- orthopyroxene; plg- plagioclase; ol- olivine.

PETROLOGICAL BACKGROUND AND SAMPLES

The Alpine-Apennine ophiolites represent lithospheric remnants of the Ligurian Tethys Ocean (e.g., Rampone et al., 2018 and references therein). Jurassic opening of the oceanic basin led to a progressive uplift and exhumation of subcontinental lithospheric mantle (e.g., Manatschal and Müntener, 2009). Most of these mantle bodies have been affected by refertilization processes related to the asthenospheric upwelling during rifting and subsequent oceanization (e.g., Rampone et al., 1997; 2004; 2008; 2016; 2018, Müntener et al., 2004; Borghini et al., 2007; Piccardo et al., 2002; 2007; Basch et al., 2018; 2019a; 2019b). However, some mantle units from the Northern Apennines (including the External Liguride Unit) have escaped this melt-rock interaction history and preserve their pristine subcontinental lithospheric mantle composition (Beccaluva et al., 1984; Rampone et al., 1995; Montanini et al., 2006; Borghini et al., 2011; 2016).

The External Liguride (EL) ophiolites are composed of kilometre-scale bodies of ultramafic rocks and minor MORB-type gabbros and basalts, embedded in Cretaceous sedimentary mélanges that were obducted during closure of the Ligurian Tethys oceanic basin (Rampone et al., 1993; 1995; Tribuzio et al., 2004; Montanini et al. 2008). The External Liguride ophiolitic mantle sequences have therefore been inferred to represent remnants of a fossil ocean-continent transition, where exhumed subcontinental mantle was associated with embryonic oceanic crust and rocks of continental origin (Marroni et al., 1998; Rampone and Piccardo, 2000; Tribuzio et al., 2004; Montanini et al., 2008). The mantle sequences consist of fertile spinel and plagioclase lherzolites with disseminated Ti-rich amphibole and widespread spinel- or garnet-bearing pyroxenite layers (Beccaluva et al., 1984; Rampone et al., 1993; 1995; Montanini et al., 2006; 2012; Borghini et al., 2013; 2016; Montanini and Tribuzio, 2015).

In the Suvero peridotites, the development of fine-grained plagioclase-bearing neoblastic aggregates is indicative of partial metamorphic recrystallization of the spinel-facies porphyroclastic mineral assemblage (Rampone et al., 1993; 1995; Borghini et al., 2011). This recrystallization witnesses the decompressional evolution of the peridotites from spinel-facies (1.2-1.5 GPa, 950-1000°C) to plagioclase-facies conditions (< 1 GPa, 800-900°C; Borghini et al., 2011). Moreover, compositional zoning in neoblasts (e.g., anorthite content reverse zoning; An = Ca/(Ca + Na) mol%) resulted from subsolidus decompressional evolution of the peridotites within plagioclase-facies stability field. In the peridotites, detailed microstructural-geochemical analyses (Borghini et al., 2011) combined with the application of the FACE geobarometer (Fumagalli et al., 2017), allowed to estimate two stages of recrystallization, from 6.3-7.0 kbar at 840-900°C to 4.3-4.8 kbar at 800-850°C (Fumagalli et al. 2017).

At Suvero, peridotites are associated to spinel-bearing pyroxenite occurring as parallel layers within the lherzolites and ranging in thickness from millimetre- to decimetre-scale. Pyroxenite layers are parallel to the mantle tectonite foliation plane and show sharp contacts with the host peridotites characterized by occurrence of thin irregular orthopyroxene-rich borders along pyroxenite-peridotite contact (Borghini et al., 2019). Pyroxenite abundance is variable and can be as high as 50% in some outcrops (see Fig. 2 in Borghini et al., 2016). In some places, pyroxenite layers alternate with harzburgite and dunite, forming compositional layering parallel to the tectonite.

Pyroxenites consist of a primary spinel-bearing mineral association made by coarse-grained clinopyroxene, orthopyroxene and spinel (up to centimetre-size crystals; Fig. 1a), elongated along the mantle foliation observed in the peridotites. The porphyroclastic minerals are partially recrystallized, indicating low-pressure metamorphic reequilibration during decompression from spinel- to plagioclase-facies conditions (Borghini et al., 2016). This recrystallization is marked by the development of: *i)* sub-millimetre to millimetre-size coronas of plagioclase and olivine around coarse porphyroclasts of greenish spinel; *ii)* orthopyroxene and plagioclase exsolution in porphyroclastic clinopyroxenes; and *iii)* fine-grained neoblastic aggregates (~ 100-200 μm) of pyroxenes, plagioclase and olivine partially replacing the spinel-facies pyroxene porphyroclasts (Fig. 1b, c).

In order to study the plagioclase-facies geothermobarometric evolution recorded in the pyroxenite layers, we selected three pyroxenite samples previously investigated by Borghini et al. (2016). They are two websterites (GV8 and GV10) and a clinopyroxene-rich websterite (BG13) and preserve unaltered neoblastic aggregates of clinopyroxene$_2$ + orthopyroxene$_2$ + plagioclase + olivine. These samples exhibit more fertile bulk compositions than the host peridotites i.e. they are characterized by lower Mg-values (82.53-84.98 mol%), higher CaO (12.6-14.0 wt%), Al_2O_3 (9.9-13.8 wt%) and Na_2O (0.4-0.5 wt%) (Table 1, Fig. 2). The Na_2O/CaO and Cr/(Cr + Al) ratios of the pyroxenite samples (Na_2O/CaO = 0.032-0.041; Cr/(Cr + Al) = 0.007-0.011 mol%) also plot far from the compositional range defined by the host plagioclase peridotites (Fig. 3). Moreover, the pyroxenite GV10 has been selected as starting bulk composition for partial melting and subsolidus experiments at 7-15 kbar (Borghini et al., 2017; Borghini and Fumagalli, 2018).

ANALYTICAL METHODS

Major element (SiO_2, TiO_2, Al_2O_3, Cr_2O_3, FeO, MgO, MnO, CaO, NiO and Na_2O) compositions of olivine, clinopyroxene, orthopyroxene and plagioclase were analyzed by JEOL JXA 8200 Superprobe equipped with five

Table 1 - Bulk rock major element compositions of the plagioclase pyroxenite, after Borghini et al. (2016).

wt%	BG13	GV8	GV10
SiO_2	43.84	46.46	45.99
TiO_2	0.42	0.45	0.44
Cr_2O_3	0.14	0.17	0.16
Al_2O_3	13.83	11.5	9.94
FeOt	6.55	6.71	7.77
MnO	0.19	0.14	0.16
MgO	18.06	19.17	18.53
CaO	13.33	12.64	13.96
Na_2O	0.42	0.52	0.48
LOI	4.48	3.13	2.82
Total	101.26	100.89	100.25
Mg#	84.52	84.98	82.53
Na_2O/CaO	0.032	0.041	0.034
Cr/(Cr+Al)	0.007	0.010	0.011

Mg# = Mg/(Mg + Fe).

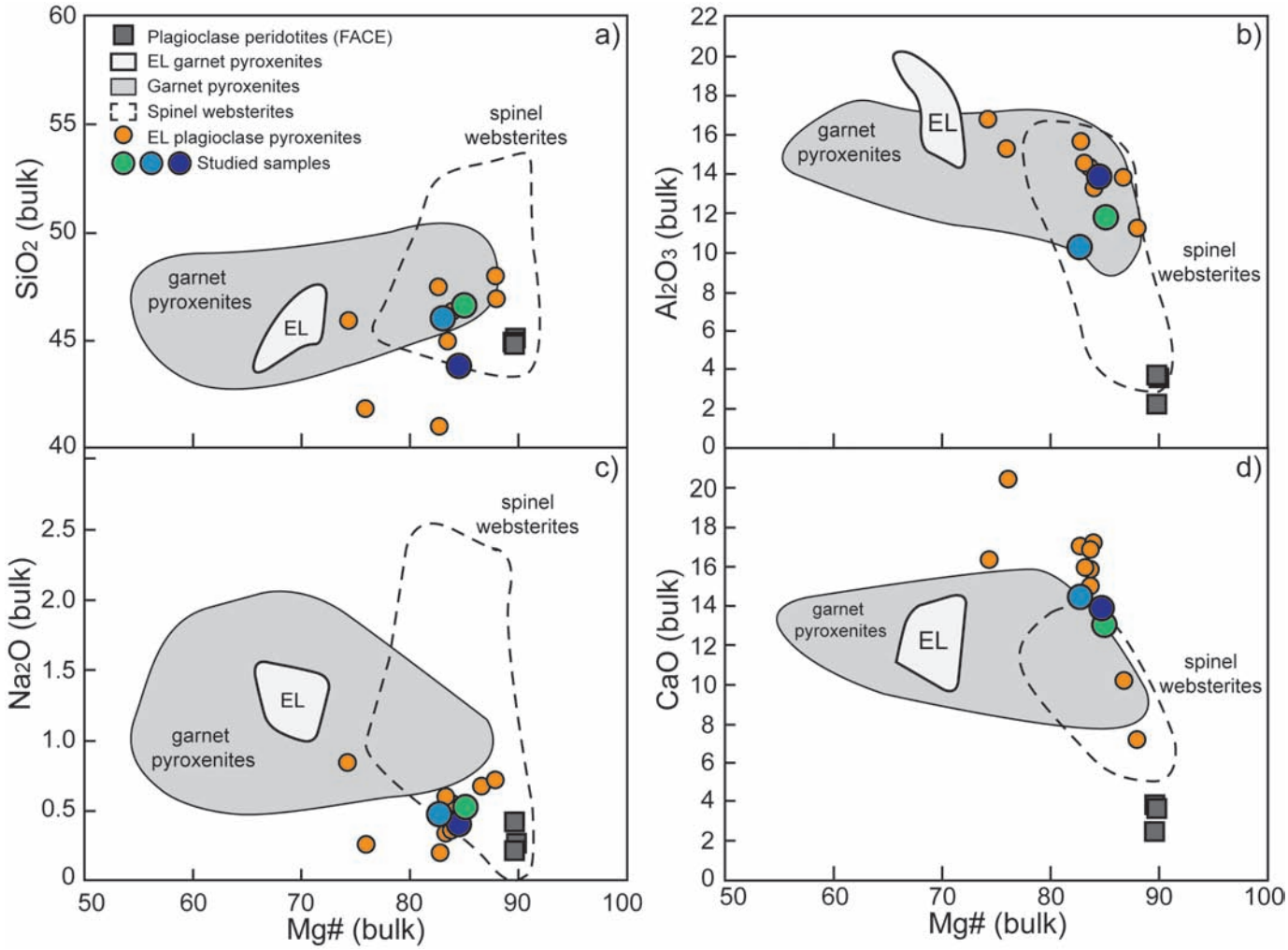

Fig. 2 - Variation diagrams of Mg# vs a) SiO_2, b) Al_2O_3, c) Na_2O, d) CaO (wt%) for the External Ligurides (EL) plagioclase pyroxenites (Borghini et al., 2016) and studied samples. Compositional fields are garnet pyroxenites and spinel websterites from ultramafic orogenic massifs: Beni Bousera, Morocco (Pearson et al., 1993; Kumar et al., 1996; Gysi et al., 2011); Ronda, Spain (Suen and Frey, 1987; Garrido and Bodinier, 1999; Bodinier et al., 2008); Horoman, Japan (Takazawa et al., 1999; Morishita and Arai, 2001); Pyrénées, France (Bodinier et al., 1987a; 1987b); Balmuccia, Italy (Sinigoi et al., 1983; Voshage et al., 1988; Mukasa and Shervais, 1999). The EL field refers to the bulk compositions of garnet pyroxenites of the External Liguride Units investigated by Montanini et al. (2006), and the grey squares represent the bulk composition of the Suvero plagioclase peridotites used by Fumagalli et al. (2017) to calibrate the FACE geobarometer. Mg# = Mg/(Mg+Fe) x 100.

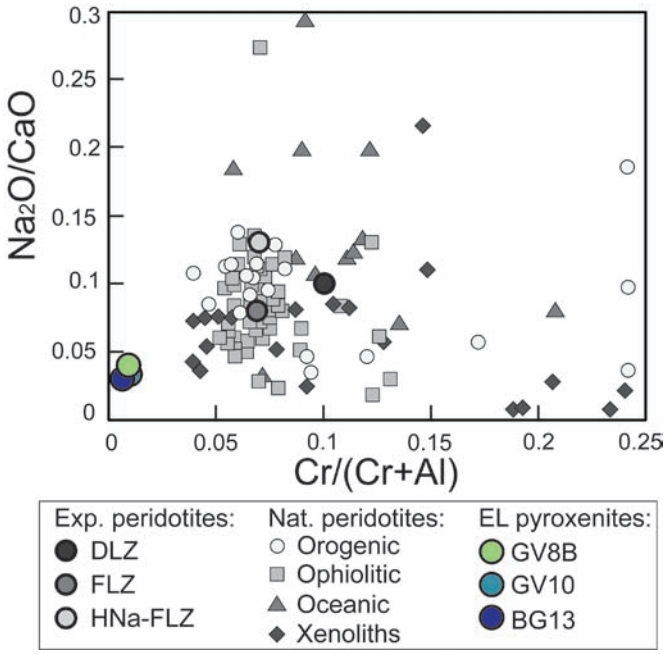

Fig. 3 - Cr/(Cr + Al) vs. Na_2O/CaO diagram comparing the External Ligurides pyroxenite bulk compositions (Table 1) to the composition of starting materials used in experimental studies. *FLZ* fertile lherzolite (Borghini et al., 2010; 2011; Fumagalli et al., 2017), *DLZ* depleted lherzolite (Borghini et al., 2010; Fumagalli et al., 2017) and *HNa-FLZ* high-Na fertile lherzolite (HNa-FLZ, Fumagalli et al., 2017) bulk compositions have been used to calibrate the FACE geobarometer (Fumagalli et al., 2017). Experimental starting materials are compared with the compositions of ophiolitic, orogenic and oceanic peridotites (Sinigoi et al., 1980; Bodinier et al., 1988; 2008; Voshage et al., 1988; Piccardo et al., 1988; Frey et al., 1991; Van der Wal and Vissers, 1996; Rampone et al., 1995; 1996; 2005; 2008; Takazawa et al., 2000; Niu 2004; Sano and Kimura, 2007; Le Roux et al., 2007; Kaczmarek and Müntener, 2010), and mantle xenoliths (Ionov et al., 1995; Bonadiman et al., 2005; Martin et al., 2014).

wavelength-dispersive spectrometers, an energy dispersive spectrometer, and a cathodoluminescence detector (accelerating potential 15 kV, beam current 15nA), operating at the Dipartimento di Scienze della Terra, University of Milano. Mineral chemistry of clinopyroxene, orthopyroxene, plagioclase and olivine from the studied pyroxenites are reported in Supplementary Tables 1S-4S. Our data are consistent with mineral compositions reported for these pyroxenite samples by Borghini et al. (2016).

MINERAL CHEMISTRY

Clinopyroxene, orthopyroxene and olivine show Mg-values consistent with their respective bulk-rock major element composition (Table 1). Within each sample, pyroxenes and olivine also show variations in Mg-value correlated to the mineral assemblage (porphyroclasts vs neoblasts) and microstructural site (core vs rim) they are found in.

Clinopyroxene (Table 1S) porphyroclasts show increasing Mg-values and decreasing Al_2O_3 contents from crystal cores (coloured circles; GV10: Mg# = 81.8-82.4 mol%, GV8 and BG13: Mg# = 83.7-84.0 mol%, Al_2O_3 = 7.8-8.4 wt%, Al a.p.f.u. = 0.32-0.37) to rims (open circles; BG13: Mg# = 85.2-87.5 mol%, Al_2O_3 = 3.7-5.7 wt%, Al a.p.f.u. = 0.16-0.25; Fig. 4a). They exhibit lower Cr_2O_3 contents (Cr_2O_3 = 0.10-0.35 wt%) than spinel-facies clinopyroxenes analyzed in the host peridotite (Borghini et al., 2011). Neoblastic clinopyroxenes (triangles in Fig. 4a) show higher Mg-values, lower Al_2O_3 and similar Cr_2O_3 contents relative to porphyroclasts, and increasing Mg-values at decreasing Al_2O_3 contents from crystal cores (GV10: Mg# = 81.2-82.0 mol%, GV8 and BG13: Mg# = 84.6-86.8 mol%, Al_2O_3 = 4.5-6.4 wt%, Al a.p.f.u. = 0.20-0.28, Cr_2O_3 = 0.09-0.39 wt%) to rims (GV10: Mg# = 81.3-82.0 mol%, GV8 and BG13: Mg# = 85.0-88.2 mol%, Al_2O_3 = 3.1-5.8 wt%, Al a.p.f.u. = 0.14-0.26, Cr_2O_3 = 0.13-0.39 wt%).

Orthopyroxene (Table 2S) porphyroclasts show increasing Mg-values at decreasing Al_2O_3 contents from crystal cores (GV10: Mg# = 81.5-82.3 mol%, GV8 and BG13: Mg# = 83.7-85.3 mol%, Al_2O_3 = 4.8-6.7 wt%, Al a.p.f.u. = 0.16-0.28) to rims (GV8: Mg# = 84.1-86.7 mol%, Al_2O_3 = 2.3-3.7 wt%, Al a.p.f.u. = 0.09-0.15; Fig. 4b). Porphyroclasts show similar CaO contents (CaO = 0.6-1.4 wt%) and lower Cr_2O_3 contents (Cr_2O_3 = 0.11-0.31 wt%) than spinel-facies orthopyroxenes analyzed in the host peridotite (Borghini et al., 2011). Granular orthopyroxenes (cores and rims) show similar Mg-values (GV10: Mg# = 81.1-81.5 mol%, GV8 and BG13 = 83.8-86.9 mol%), Al_2O_3 (Al_2O_3 = 2.0-3.9 wt%, Al a.p.f.u. = 0.09-0.15) and Cr_2O_3 contents (Cr_2O_3 = 0.04-0.21 wt%) to orthopyroxene porphyroclast rims (Fig. 4b).

Plagioclase (Table 3S) cores show rather homogeneous composition in all the analyzed samples. Anorthite content in plagioclase (An = Ca/(Ca + Na) × 100) varies from 56.2 to 62.4 mol%, and almost overlaps the anorthite variation observed in associated peridotite (An = 56-59 mol%, Borghini et al., 2011; Fig. 5). Rims of plagioclase crystals show variable compositions depending on which phase they are associated with. Rims at the contact with granular orthopyroxene and olivine show compositions similar to plagioclase cores (An = 55.5-59.2 mol%, Fig. 5). Some plagioclase rims at the contact with granular clinopyroxene show higher anorthite content (An = 74.3-76.6 mol%, Fig. 5), similar to the compositions of plagioclase rims in the host peridotites (An = 74-79 mol%, Borghini et al., 2011).

Olivine (Table 4S) cores in the different samples show rather homogeneous Forsterite contents that are positively correlated with their respective bulk-rock Mg-value (GV10: Fo = 80.5-81.7 mol%, GV8 and BG13: Fo = 86.1-86.9 mol%).

DISCUSSION

Thermobarometry of pyroxenites at plagioclase-facies conditions

The selected samples record the development of neoblastic aggregates (cpx_2 + opx_2 + plagioclase + olivine) at the expense of the primary spinel-facies porphyroclastic minerals, as a witness of partial plagioclase-facies recrystallization (Fig. 1). Core-to-rim chemical zonations in neoblastic mineral aggregates (Figs. 4, 5) suggest their re-equilibration at different stages of pressure and temperature (Borghini et al., 2011).

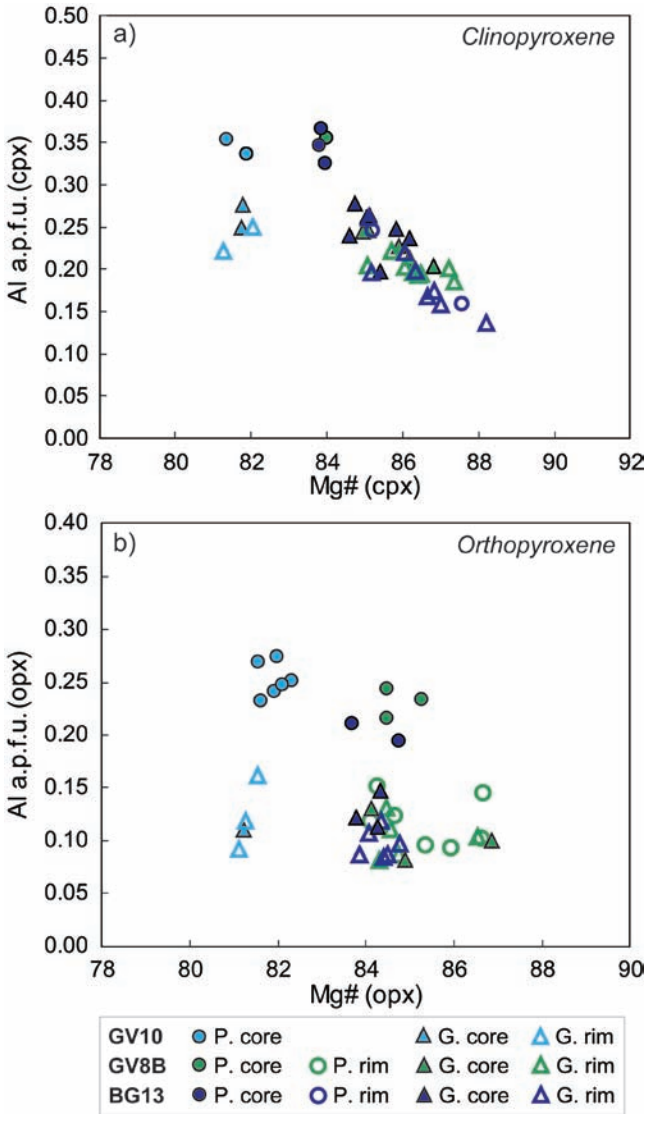

Fig. 4 - Variation of Mg# vs. Al content (a.p.f.u.) in clinopyroxenes (a) and orthopyroxenes (b) from the studied pyroxenites.

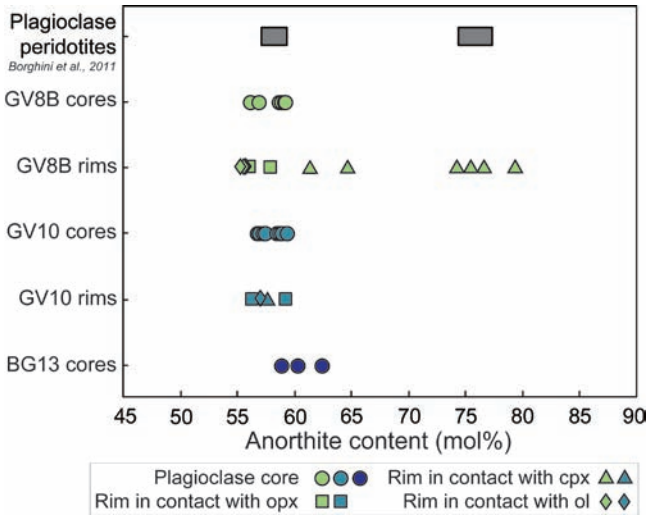

Fig. 5 - Variation in Anorthite content [An = Ca/(Ca+Na) x 100] between the different samples and the different microstructural sites. The grey squares report the compositions of plagioclase analyzed in the associated plagioclase peridotite (Borghini et al., 2011).

Following Borghini et al. (2011) approach on Suvero plagioclase peridotites, we focused on the most preserved plagioclase-bearing neoblastic assemblages in the studied pyroxenites. Careful microstructural observations combined with detailed mineral chemistry analysis allowed us to group the compositions of neoblasts cores, referring to an earlier recrystallization stage (Stage 1), and those of neoblastic rims, which record a shallower re-equilibration (Stage 2). The assumption that cores and rims of plagioclase and pyroxenes neoblasts are in chemical equilibrium is strongly supported by microstructural evidence indicating textural equilibrium (Fig. 3).

Element partitioning between texturally associated minerals has been used to test chemical equilibrium, mandatory for application of geothermobarometry. X_{Mg} in clinopyroxene, orthopyroxene and olivine cores and rims are coherent with Fe,Mg partitioning in ultramafic compositions (Table 1 and Table 1S, 2S, 4S). Plagioclase and clinopyroxene compositions further establish chemical equilibrium: anorthite in plagioclase vs. aluminium content in M1 of clinopyroxene (X_{Al}^{M1}; Fig. 6) follows the pressure-related trend observed in experiments (Fumagalli et al., 2017). Furthermore, Ca, Na partitioning between clinopyroxene and plagioclase (Fig. 6b) is strictly consistent with previous experimental and natural observations (Borghini et al., 2010; 2011; Fumagalli et al., 2017).

The geothermobarometric estimates obtained for the two equilibration conditions, Stage 1 and Stage 2, are reported in Table 2. Only the equilibrated mineral couples, i.e. respecting the documented Al_{M1}-An and Ca-Na element partitioning, were used for geothermobarometric calculations. We first estimated temperatures applying the two-pyroxene Fe-Mg geothermometer (Brey and Kohler, 1990; Taylor, 1998) and Ca-in-orthopyroxene geothermometer (Brey and Kohler, 1990). Overall, crystal cores yield equilibrium temperatures ($T_{Fe\text{-}Mg}$ ~ 830-850°C) higher than the crystal rims ($T_{Fe\text{-}Mg}$ ~ 770-790°C), consistently with the temperatures computed for the plagioclase-facies assemblages of the Suvero peridotites using the same geothermometers (Borghini et al., 2011; Fumagalli et al., 2017).

Pressure estimates were then obtained using the spreadsheet provided as supplementary material in Fumagalli et al. (2017) (Table 2). Cores record equilibrium pressures ranging from 6.9 to 8.1±0.5 kbar (Stage 1). According to the decompressional evolution recorded by plagioclase peridotites, the FACE estimates on the rims (Stage 2) give pressures of 5.8-5.9±0.5 kbar (Table 2). These two pressure intervals respectively represent the upper and lower pressure condition limits of the reequilibration stage in the plagioclase stability field. The core-rim zoning in neoblasts is likely the result of continuous chemical re-equilibration via solid-state element diffusion among plagioclase and pyroxenes during the decompressional evolution. In the peridotites, this has been well documented by progressive chemical variation along profiles on neoblasts (Borghini et al., 2011).

Plagioclase-facies evolution of the Suvero pyroxenite-peridotite association

FACE geobarometer applied to the Suvero plagioclase peridotites provided two stages of low-pressure re-crystallization at 6.3-7.0 and 4.3-4.8±0.5 kbar (Fumagalli et al., 2017). As the pyroxenites formation predates the exhumation of this mantle sector, we can assume that they experienced the same decompressional path. Indeed, thermobarometric estimates for pyroxenites (Table 2) indicate comparable pressure and temperature decrease (approx. 60°C, and 1.0-1.5 kbar) from the event recorded by neoblastic cores to the stage testified by rims. Nonetheless, pyroxenites yield slightly lower temperatures (ΔT ~ -30-40°C) and higher pressures (ΔP ~ 1 kbar) than neoblastic cores and rims in plagioclase peridotites.

Subsolidus experiments on mantle peridotites in complex chemical systems determined that the pressure of the plagioclase to spinel transition is strongly influenced by the

Table 2 - Geothermobarometric estimates based on major element compositions of the neoblastic minerals.

		Brey & Kohler (1990)		Taylor (1998)	Fumagalli et al. (2017)					
Sample	Assemblage	opx-cpx	Ca-in-opx	opx-cpx	aCaTs (cpx)	aEn	Xan (plg)	aFo	Kd (FACE)	P (kbar)
GV10	g. core	850	972	838	0.025	0.630	0.745	0.648	0.0327	7.5
GV10	g. core	809	972	789	0.031	0.630	0.723	0.648	0.0412	8.1
GV8B	g. core	806	922	768	0.025	0.725	0.738	0.756	0.0328	7.5
GV8B	g. core	938	887	926	0.017	0.687	0.942	0.756	0.0165	7.5
BG13	g. core	889	965	869	0.027	0.674	0.742	0.756	0.0327	6.9
BG13	g. core	828	962	814	0.017	0.685	1.003	0.756	0.0157	7.2
GV8B	rim-rim	772	883	747	0.022	0.677	0.781	0.744	0.0259	5.9
GV8B	rim-rim	801	907	786	0.025	0.668	0.770	0.744	0.0294	5.8

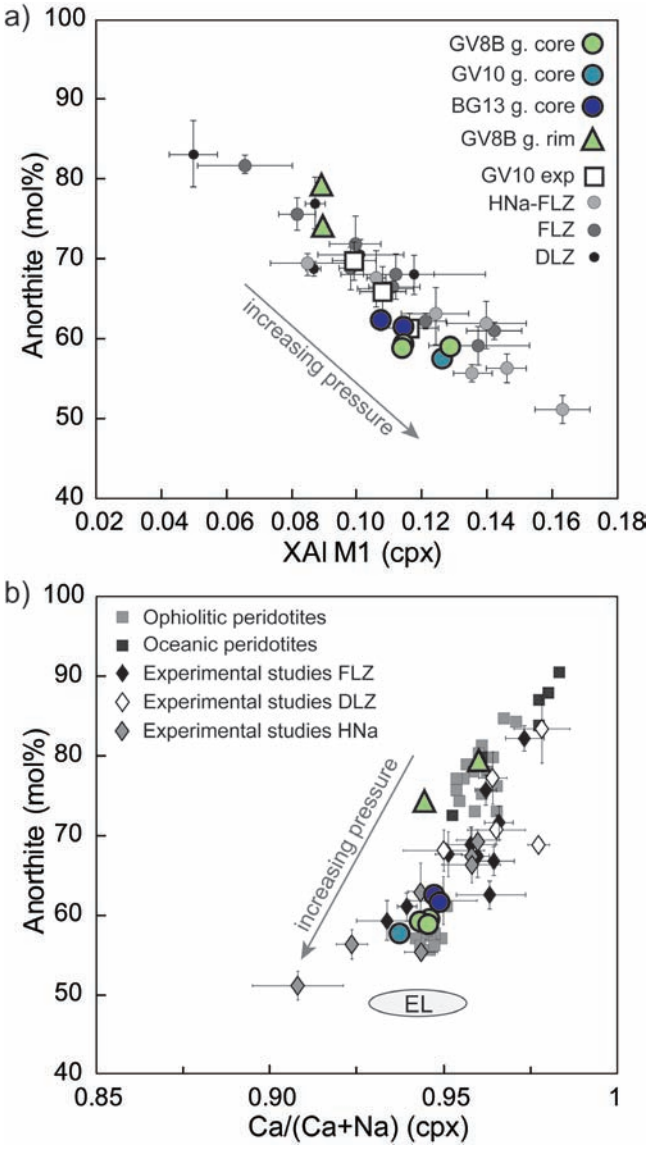

Fig. 6 - Diagrams showing the element partitioning between plagioclase and clinopyroxene from the selected mineral associations; a) pressure-dependent correlation between the XAl M1 in clinopyroxene and Anorthite content in plagioclase. Experimental data are from Fumagalli et al. (2017) and Borghini and Fumagalli et al. (2018); b) correlation between Ca/(C + Na) in clinopyroxene and Anorthite content in plagioclase. Data for comparison are from Borghini et al. (2010; 2011) and references therein.

combined effect of Na_2O/CaO (Ab/Di) and Cr/(Cr+Al) (X_{Cr}) ratios of the bulk composition (Green and Falloon, 1998; Borghini et al., 2010; Fumagalli et al., 2017). Increasing Ab/Di ratio favours the stability of plagioclase towards higher pressures, whereas an increase in X_{Cr} moves the plagioclase appearance to lower pressures (Borghini et al., 2010). Therefore, the plagioclase stability field is expected to progressively expand toward higher pressure from depleted peridotite to fertile peridotite and pyroxenite. Suvero pyroxenites have slightly lower Ab/Di (0.09-0.11) than the associated peridotites (Ab/Di = 0.15-0.16) and much lower bulk X_{Cr} (pyroxenites: X_{Cr} = 0.01; peridotites: X_{Cr} = 0.07). Accordingly, the transition from plagioclase to spinel facies for pyroxenite bulk compositions (GV10) has been experimentally located at 1 kbar higher than fertile peridotitic compositions, mostly due to its lower X_{Cr} (Fig. 2; Borghini and Fumagalli, 2018).

Fig. 7 displays the thermobarometric estimates obtained in the Suvero pyroxenites and peridotites at plagioclase-facies conditions (Fumagalli et al., 2017), compared to the experimentally determined plagioclase to spinel transition for their respective bulk composition (Fumagalli et al., 2017; Borghini and Fumagalli, 2018). The onset of plagioclase crystallization provided by the pressure estimate on the neoblastic cores (stage S1; Fig. 7) falls at the upper limit of the plagioclase-bearing field experimentally determined for the pyroxenite GV10 and the fertile lherzolite, respectively 8 kbar and 7 kbar at 850°C (Fig. 7). This result could indicate that pyroxenites record an initial stage of plagioclase-facies recrystallization at higher pressure than the associated peridotites in response to their more fertile bulk composition (i.e. much lower X_{Cr}). However, the shift towards higher pressure also obtained for Stage 2 (Fig. 7) suggests a slight systematic deviation when the FACE geobarometer is applied to pyroxenitic bulks. Indeed, FACE geobarometer was calibrated for mantle peridotites and a bulk composition effect on its pressure estimates on pyroxenites need to be further considered (Borghini and Fumagalli, 2018).

Bulk composition effect on FACE barometric estimates

As the Suvero peridotites and pyroxenites were exhumed together, they are expected to record the same, or rather similar, pressure and temperature conditions of the plagioclase-facies recrystallization stages (S1 and S2, Fig. 7). Although the onset of plagioclase-bearing crystallization may be anticipated to slightly higher depth in the pyroxenite as an effect of more fertile bulk composition, the pressure shift of Stage 2 is not easily explainable. FACE geobarometer was calibrated for peridotite bulks having a narrow range of Na_2O/CaO and X_{Cr} ratios (Fig. 2). Olivine-bearing websterites may have bulk composition significantly different from the peridotite range and this potentially introduces a deviation in the FACE

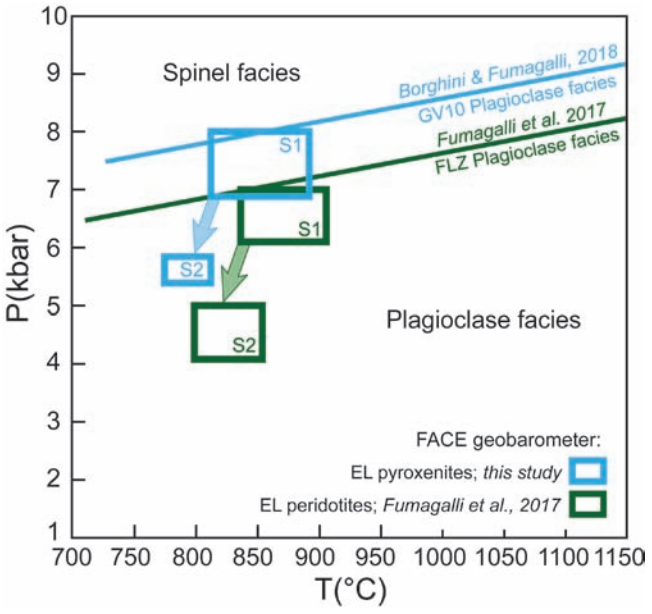

Fig. 7 - Geothermobarometric estimates for the peridotite and pyroxenite samples represented in a Pressure-Temperature diagram. Plagioclase-out boundaries for FLZ and GV10 bulk compositions were determined experimentally by Fumagalli et al. (2017) and Borghini and Fumagalli (2018). Stage S1 corresponds to the partial plagioclase-facies recrystallization provided by the cores of the neoblastic minerals (onset of recrystallization) and stage S2 corresponds to the subsequent shallower equilibration indicated by the compositions of the neoblastic rims

pressure estimates. Equilibrium temperatures yielded by pyroxenites are similar, or very close, to those estimated for peridotite; anyway, temperature has a minor effect on pressures computed by FACE geobarometer (Fumagalli et al., 2017).

This deviation might be considered looking at the activities used to calculate the Kd of the reaction Forsterite^{Ol} + Anorthite^{Pl} = Ca-Tschermak^{Cpx} + Enstatite^{Opx} (Table 2). In spite of different bulk Na_2O/CaO ratios, anorthite in plagioclase is not significantly different between the Suvero pyroxenites and peridotites (Fig. 5). This reflects the coherent Na-Ca partitioning between plagioclase and clinopyroxene in pyroxenites as well as in peridotites (Fig. 6b). The activity of enstatite in orthopyroxene (a_{en}) and of forsterite in olivine (a_{fo}) decreases concomitantly in agreement with the bulk X_{Mg} (Table 2). The discrepancy between the two compositional systems (pyroxenite vs. peridotite) is related to the variability of Ca-Tschermak activity in clinopyroxene ($a_{CaTs} = 4X_{Ca}X_{Al}{}^{M1}X_{Al}{}^{T}X_{Si}{}^{T}$). The latter is significantly higher in clinopyroxenes of pyroxenites resulting in higher pressure estimates provided by the FACE equation. Cr-Al partitioning between spinel and pyroxene is controlled by the spinel-pyroxene and clinopyroxene-orthopyroxene exchange reactions (Borghini et al., 2010):

$$\underset{\text{spinel}}{MgCr_2O_4} + 2\underset{\text{cpx}}{CaAl_2SiO_6} = \underset{\text{spinel}}{MgAl_2O_4} + 2\underset{\text{cpx}}{CaCrAlSiO_6} \quad (1)$$

$$\underset{\text{spinel}}{MgCr_2O_4} + 2\underset{\text{cpx}}{MgAl_2SiO_6} = \underset{\text{spinel}}{MgAl_2O_4} + 2\underset{\text{cpx}}{MgCrAlSiO_6} \quad (2)$$

$$\underset{\text{cpx}}{CaAl_2SiO_6} + \underset{\text{cpx}}{MgCrAlSiO_6} = \underset{\text{cpx}}{CaCrAlSiO_4} + \underset{\text{cpx}}{MgAl_2SiO_6} \quad (3)$$

At relatively low pressure, this partitioning is further complicated by the contribution of plagioclase according to the reaction:

$$\underset{\text{spinel}}{MgCr_2O_4} + \underset{\text{anorthite}}{CaAl_2Si_2O_8} = \underset{\text{opx}}{MgCrAlSiO_6} + \underset{\text{cpx}}{CaCrAlSiO_6} \quad (4)$$

As demonstrated by Borghini et al. (2010), X_{Cr} of spinel is positively correlated to the abundance of plagioclase, therefore, according to the continuous spinel-plagioclase reaction, at decreasing pressure the increase of X_{Cr} in spinel and pyroxenes is balanced by the modal plagioclase increase that is coupled to the decrease of spinel and pyroxene abundances. Hence, despite the role of spinel in incorporating Cr, pyroxenes represent important Chromium hosts even at low pressure (Borghini et al., 2010). For very low-X_{Cr} bulk compositions, as those of the pyroxenites studied here, the low Cr contents strongly limits these exchange reactions inhibiting the formation of Ca,Cr-Tschermak and Mg,Cr-Tschermak molecules in clinopyroxene and orthopyroxene, respectively. Therefore, at fixed P-T conditions and decreasing bulk X_{Cr}, the activity of Ca-Tschermak in equilibrium clinopyroxene is expected to increase. This is indeed shown by the negative correlation of the a_{CaTs} and X_{Cr} in clinopyroxene observed in Suvero peridotites and associated pyroxenites (Fig. 8). This could explain the deviation observed in pressure estimates computed for plagioclase-facies recrystallization stages by FACE geobarometer. However, experimental data on the mineral chemistry and element partitioning (e.g., Cr-Al partitioning between spinel and pyroxene) in low-pressure pyroxenite assemblages are so far very limited and more evidence of such deviation would need to be further investigated.

CONCLUDING REMARKS

Suvero pyroxenites show fine-grained neoblastic assemblages indicative of partial recrystallization at plagioclase-facies conditions. Core to rim chemical zonations in neoblastic mineral aggregates suggest equilibration stages at variable pressure and temperature. Combining microstructural observations and mineral chemistry, we identified two re-equilibration stages referring to the onset of plagioclase-facies re-crystallization ($T_{Fe\text{-}Mg}$ ~ 830-850°C, Stage 1) and a shallower colder re-equilibration ($T_{Fe\text{-}Mg}$ ~ 770-790°C, Stage 2). Application of FACE geobarometer provided equilibrium pressures ranging from 6.9 to 8.1±0.5 kbar for the Stage 1 and 5.8-5.9±0.5 kbar for the Stage 2. This decompressional evolution is consistent with exhumation history documented in the associated Suvero peridotite although at slightly higher equilibrium pressures. As the FACE geobarometer was calibrated for mantle peridotites, its application to pyroxenites, having significantly different bulk Na_2O/CaO and X_{Cr} compositions, may introduce a systematic deviation in pressure estimates. The variation of anorthite in plagioclase is rather similar in Suvero pyroxenites and peridotites. Remarkably, the much lower X_{Cr} in pyroxenites reflects in lower Cr incorporation in pyroxenes and, consequently, in significantly higher Ca-Tschermak activity in clinopyroxene. This might imply the systematic higher equilibrium pressure derived by FACE geobarometer.

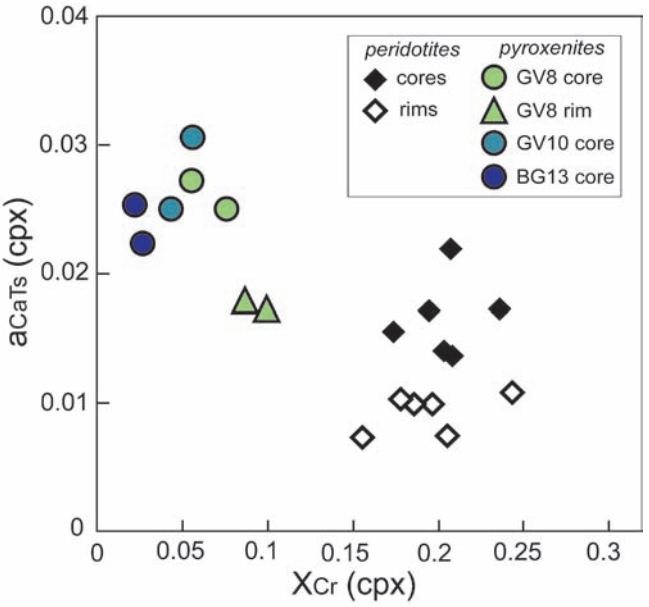

Fig. 8 - Activity of Ca-Tschermak vs. X_{Cr} (X_{Cr} = Cr/(Cr + Al_{VI}) in clinopyroxene from Suvero pyroxenites and peridotites. Data for peridotites are from Fumagalli et al. (2017). a_{CaTs} is calculated using the spread sheet provided by Fumagalli et al. (2017).

ACKNOWLEDGEMENTS

We thank R. Tilhac and C. Marchesi for constructive reviews of the manuscript, and A. Montanini for her work as editor. We also thank Paolo Campanella and Alessandra Gavoglio for realization of the thin section and Andrea Risplendente for assistance with the EPMA analyses. This research has been supported by the Italian Ministry of Education, University and Research (MIUR) through the grant [PRIN-2015C5LN35] "Melt-rock reaction and melt migration in the MORB mantle through combined natural and experimental studies".

Supplementary data to this article are available online at https://doi.org/10.4454/ofioliti.v45i1.529

REFERENCES

Basch V., Rampone E., Crispini L., Ferrando C., Ildefonse B. and Godard M., 2018. From mantle peridotites to hybrid troctolites: textural and chemical evolution during melt-rock interaction history (Mt. Maggiore, Corsica, France). Lithos, 323: 4-23, doi:10.1016/j.lithos.2018.02.025.

Basch V., Rampone E., Crispini L., Ferrando C., Ildefonse B. and Godard M., 2019a. Multi-stage reactive formation of troctolites in slow-spreading oceanic lithosphere (Erro-Tobbio, Italy): a combined field and petrochemical study. J. Petrol., 60: 873-906, doi: 10.1093/petrology/egz019.

Basch V., Rampone E., Borghini G., Ferrando C. and Zanetti A., 2019b. Origin of pyroxenites in the oceanic mantle and their implications on the reactive percolation of depleted melts. Contrib. Miner. Petrol., 174: 97, doi: 10.1007/s00410-019-1640-0.

Beccaluva L., Maciotta G., Piccardo G.B. and Zeda O., 1984. Petrology of lherzolitic rocks from the Northern Apennine ophiolites. Lithos, 17: 299-316, doi: 10.1016/0024-4937(84)90027-6.

Bodinier J.-L., Dupuy C. and Dostal J., 1988. Geochemistry and petrogenesis of Eastern Pyrenean peridotites. Geochim. Cosmochim. Acta, 52: 2893-2907, doi: 10.1016/0016-7037(88)90156-1.

Bodinier J.-L., Fabries J., Lorand J.-P., Dostal J. and Dupuy C., 1987a. Geochemistry of amphibole pyroxenite veins from the Lherz and Freychinede ultramafic bodies (Ariège, French Pyrénées). Bull. Minér., 110: 345-358.

Bodinier J.-L., Garrido C.J., Chanefo I., Bruguier O. and Gervilla F., 2008. Origin of pyroxenite-peridotite veined mantle by refertilization reactions: Evidence from the Ronda peridotite (Southern Spain). J. Petrol., 49: 999-1025, doi: 10.1093/petrology/egn014.

Bodinier J.-L., Guiraud M., Fabries J., Dostal J. and Dupuy C., 1987b. Petrogenesis of layered pyroxenites from the Lherz, Freychinède and Prades ultramafic bodies (Ariège, French Pyrénées). Geochim. Cosmochim. Acta, 51: 279-290, doi: 10.1016/0016-7037(87)90240-7.

Bonadiman C., Beccaluva L., Coltorti M. and Siena F., 2005. Kimberlite-like metasomatism and 'garnet signature' in spinel-peridotite xenoliths from Sal, Cape Verde archipelago: relics of a subcontinental mantle domain within the Atlantic oceanic lithosphere? J. Petrol., 46: 2465-2493, doi: 10.1093/petrology/egi061.

Borghini G. and Fumagalli P., 2018. Subsolidus phase relations in a mantle pyroxenite: an experimental study from 0.7 to 1.5 GPa. Eur. J. Mineral., 30 (2): 333-348, doi: 10.1127/ejm/2018/0030-2735.

Borghini G., Fumagalli P. and Rampone E., 2010. The stability of plagioclase in the upper mantle: subsolidus experiments on fertile and depleted lherzolite. J. Petrol., 51: 229-254, doi: 10.1093/petrology/egp079.

Borghini G., Fumagalli P. and Rampone E., 2011. The geobarometric significance of plagioclase in mantle peridotites: A link between nature and experiments. Lithos, 126: 42-53, doi: 10.1016/j.lithos.2011.05.012.

Borghini G., Fumagalli P. and Rampone E., 2017. Partial melting of secondary pyroxenite at 1 and 1.5 GPa, and its role in upwelling heterogeneous mantle. Contrib. Miner. Petrol., 172: 70, doi: 10.1007/s00410-017-1387-4.

Borghini G., Rampone E., Crispini L., De Ferrari R. and Godard M., 2007. Origin and emplacement of ultramafic-mafic intrusions in the Erro-Tobbio mantle peridotite (Ligurian Alps, Italy). Lithos, 94: 210-229, doi: 10.1016/j.lithos.2006.06.014.

Borghini G., Rampone E., Zanetti A., Class C., Cipriani A., Hofmann A.W. and Goldstein S.L., 2013. Meter-scale Nd isotopic heterogeneity in pyroxenite-bearing Ligurian peridotites encompasses global-scale upper mantle variability. Geology, 41: 1055-1058, doi: 10.1130/G34438.1.

Borghini G., Rampone E., Zanetti A., Class C., Cipriani A., Hofmann A.W. and Goldstein S.L., 2016. Pyroxenite layers in the Northern Apennines' upper mantle (Italy). Generation by pyroxenite melting and melt infiltration. J. Petrol., 57: 625-653, doi: 10.1093/petrology/egv074.

Borghini G., Rampone E., Zanetti A., Class C., Fumagalli P. and Godard M., 2019. Ligurian pyroxenite-peridotite sequences (Italy) and the role of melt-rock reaction in creating enriched-MORB mantle sources**.** Chem. Geol., in press, doi: 10.1016/j.chemgeo.2019.07.027, doi: 10.1016/j.chemgeo.2019.07.027.

Brey G.P. and Köhler T., 1990. Geothermobarometry in four phase lherzolites II. New thermobarometers, and practical assessment of existing thermobarometers. J. Petrol., 31: 1353-1378, doi: 10.1093/petrology/31.6.1353.

Dick H.J.B., Lissemberg C.J. and Warren J., 2010. Mantle melting, melt transport, and delivery beneath a slow-spreading ridge: the paleo-MAR from 23°15'N to 23°45'N. J. Petrol., 51: 425-467, doi: 10.1093/petrology/egp088.

Frey F.A., Shimizu N., Leinbach A., Obata M. and Takazawa E., 1991. Compositional variations within the Lower Layered Zone of the Horoman peridotite, Hokkaido, Japan: Constraints on models for melt-solid segregation. In: M.A. Menzies et al. (Eds.), Orogenic lherzolite and mantle processes. J. Petrol., 2: 211-227, doi: 10.1093/petrology/Special_Volume.2.211.

Fumagalli P., Borghini G., Rampone E. and Poli S., 2017. Experimental calibration of Forsterite-Anorthite-Ca**-**Tschermak-Enstatite (FACE) geobarometer for mantle peridotites. Contrib. Miner. Petrol., 172: 38, doi: 10.1007/s00410-017-1352-2.

Garrido C.J. and Bodinier J.-L., 1999. Diversity of mafic rocks in the Ronda peridotite: evidence for pervasive melt-rock reaction during heating of subcontinental lithosphere by upwelling asthenosphere. J. Petrol., 40: 729-754, doi: 10.1093/petroj/40.5.729.

Green D.H. and Falloon T.J., 1998. Pyrolite: a Ringwood concept and its current expression. In I. Jackson (Ed.), The Earth's mantle, Cambridge Univ. Press, Cambridge, p. 311-378, doi: 10.1017/CBO9780511573101.010.

Gysi A.P., Jagoutz O., Schmidt M.W. and Targuisti K., 2011. Petrogenesis of pyroxenites and melt infiltrations in the ultramafic complex of Beni Bousera, Northern Morocco. J. Petrol., 52: 1676-1735, doi: 10.1093/petrology/egr026.

Hidas K., Garrido C.J., Tommasi A., Padròn-Navarta J.A., Thielmann M., Konc Z., Frets E. and Marchesi C., 2013. Strain localization in pyroxenite by reaction-enhanced softening in the shallow subcontinental lithospheric mantle. J. Petrol., 54: 1997-2031, doi: 10.1093/petrology/egt039.

Ionov D.A., O'Reilly S.Y. and Ashchepkov V., 1995. Feldspar-bearing lherzolite xenoliths in alkali basalts from Hamar-Daban Baikal region, Russia. Contrib. Miner. Petrol., 122: 174-190, doi: 10.1007/s004100050120.

Kaczmarek M.A. and Müntener O., 2010. The variability of peridotite composition across a mantle shear zone (Lanzo massif, Italy): interplay of melt focusing and deformation. Contrib. Miner. Petrol., 160: 663-679, doi: 10.1007/s00410-010-0500-8.

Kelemen P.B., Kikawa E. and Miller D.J., 2007. Leg 209 summary: processes in a 20-km-thick conductive boundary layer beneath the Mid-Atlantic Ridge, 14°-16°N. In: P.B. Kelemen, E. Kikawa and D.J. Miller (Eds.), Proceed. ODP, Sci. Res., 209: 1-33, doi: 10.2973/odp.proc.sr.209.001.2007.

Kumar N., Reisberg L. and Zindler A., 1996. A major and trace element and strontium, neodymium, and osmium isotopic study of a thick pyroxenite layer from the Beni Bousera ultramafic complex of northern Morocco. Geochim. Cosmochim. Acta, 60: 1429-1444, doi: 10.1016/0016-7037(95)00443-2.

Le Roux V., Bodinier J.-L., Tommasi A., Alard O., Dautria J.M., Vauchez A. and Riches A.J.V., 2007. The Lherz spinel lherzolite: refertilized rather than pristine mantle. Earth Planet. Sci. Lett., 259: 599-612, doi: 10.1016/j.epsl.2007.05.026.

MacLeod C.J., Searle S.C., Murton B.J., Casey J.F., Mallows C., Unsworth S.C. and Achenbach K.L., 2009. Life cycle of oceanic core complexes. Earth Planet. Sci. Lett., 287: 333-344, doi: 10.1016/j.epsl.2009.08.016.

Manatschal G. and Müntener O., 2009. A type sequence across an ancient magma-poor ocean-continent transition: the example of the western Alpine Tethys ophiolites. Tectonophysics, 473: 4-19, doi: 10.1016/j.tecto.2008.07.021.

Marroni M., Molli G., Montanini A. and Tribuzio R., 1998. The association of continental crust rocks with ophiolites in the Northern Apennines (Italy): implications for the continent-ocean transition in the Western Tethys. Tectonophysics, 292: 43-66, doi: 10.1016/S0040-1951(98)00060-2.

Martin A.P., Cooper A.F. and Price R.C., 2014. Increased mantle heat flow with on-going rifting of the West Antarctic rift system inferred from characterisation of plagioclase peridotite in the shallow Antarctic mantle. Lithos, 190-191: 173-190, doi: 10.1016/j.lithos.2013.12.012.

Montanini A. and Tribuzio R., 2015. Evolution of recycled crust within the mantle: constraints from the garnet pyroxenites of the External Ligurian ophiolites (Northern Apennines, Italy). Geology, 43: 911-914, doi: 10.1130/G36877.1.

Montanini A., Tribuzio R. and Anczkiewicz R., 2006. Exhumation history of a garnet pyroxenite-bearing mantle section from a continent ocean transition (Northern Apennine ophiolites, Italy). J. Petrol., 47: 1943-1971, doi: 10.1093/petrology/egl032.

Montanini A., Tribuzio R. and Thirlwall M., 2012. Garnet clinopyroxenite layers from the mantle sequences of the Northern Apennine ophiolites (Italy): Evidence for recycling of crustal material. Earth Planet. Sci. Lett., 351-352: 171-181, doi: 10.1016/j.epsl.2012.07.033.

Montanini A., Tribuzio R. and Vernia L., 2008. Petrogenesis of basalts and gabbros from an ancient continent-ocean transition (External Liguride ophiolites, Northern Italy). Lithos, 101: 453-479, doi: 10.1016/j.lithos.2007.09.007.

Morishita T. and Arai S., 2001. Petrogenesis of corundum-bearing mafic rock in the Horoman Peridotite Complex, Japan. J. Petrol., 42: 1279-1299, doi: 10.1093/petrology/42.7.1279.

Mukasa S.B. and Shervais J.W., 1999. Growth of sub-continental lithosphere: Evidence from repeated injections in the Balmuccia lherzolite massif, Italian Alps. Lithos, 48: 287-316, doi: 10.1016/S0419-0254(99)80016-0.

Müntener O., Pettke T., Desmurs L., Meier M. and Schaltegger R., 2004. Refertilization of mantle peridotite in embryonic ocean basins: trace element and Nd isotopic evidence and implications for crust-mantle relationships. Earth Planet. Sci. Lett., 221: 293-308, doi: 10.1016/S0012-821X(04)00073-1.

Niu Y.L., 2004. Bulk-rock major and trace element compositions of abyssal peridotites: implications for mantle melting, melt extraction and post-melting processes beneath mid-ocean ridges. J. Petrol., 45: 2423-2458, doi: 10.1093/petrology/egh068.

Pearson D.G., Davies G.R. and Nixon P.H., 1993. Geochemical constraints on the petrogenesis of diamond facies pyroxenites from the Beni Bousera peridotite massif, North Morocco. J. Petrol., 34: 125-172, doi: 10.1093/petrology/34.1.125.

Piccardo G.B., Messiga B. and Vannucci R., 1988. The Zabargad peridotite-pyroxenite association: petrological constraints on its evolution. Tectonophysics, 150: 135-162, doi: 10.1016/0040-1951(88)90299-5.

Piccardo G.B., Rampone E. and Romairone A., 2002. Formation and composition of the oceanic lithosphere of the Ligurian Tethys: inferences from the Ligurian ophiolites. Ofioliti, 27: 145-161.

Piccardo G.B., Rampone E., Vannucci R., Shimizu N., Ottolini L. and Bottazzi P., 1993. Mantle processes in the sub-continental lithosphere: the case study of the rifted spinel-lherzolites from Zabargad (Red Sea). Eur. J. Miner., 5 (6): 1039-1056. https://doi.org/10.1127/ejm/5/6/1039.

Piccardo G.B., Zanetti A. and Müntener O., 2007. Melt-peridotite interaction in the southern Lanzo peridotite: field, textural and geochemical evidence. Lithos, 94: 181-209, doi: 10.1016/j.lithos.2006.07.002.

Rampone E. and Piccardo G.B., 2000. The ophiolite-oceanic lithosphere analogue: new insights from the Northern Apennine (Italy). In: J. Dilek, E. Moores, D. Elthon and A. Nicolas, (Eds.), Ophiolites and oceanic crust: New insights from field studies and Ocean Drilling Program, vol. 49. Geol. Soc. Am. Spec. Pap., p. 21-34, doi: 10.1130/0-8137-2349-3.21.

Rampone E., Borghini G. and Basch V., 2018. Melt migration and melt-rock reaction in the Alpine-Apennine peridotites: insights on mantle dynamics in extending lithosphere. Geosci. Front., in press, doi: 10.1016/j.gsf.2018.11.001.

Rampone E., Borghini G., Godard M., Ildefonse B., Crispini L. and Fumagalli P., 2016. Melt/rock reaction at oceanic peridotite/gabbro transition as revealed by trace element chemistry of olivine. Geochim. Cosmochim. Acta, 190: 308-331, doi: 10.1016/j.gca.2016.06.029.

Rampone E., Hofmann A.W., Piccardo G.B., Vannucci R., Bottazzi P. and Ottolini L., 1995. Petrology, mineral and isotope geochemistry of the External Liguride peridotites (Northern Apennines, Italy). J. Petrol., 123: 61-76, doi: 10.1093/petrology/36.1.81.

Rampone E., Hofmann A.W., Piccardo G.B., Vannucci R., Bottazzi P. and Ottolini L., 1996. Trace element and isotope geochemistry of depleted peridotites from an N-MORB type ophiolite (Internal Liguride, N. Italy). Contrib. Miner. Petrol., 123: 61-76, doi: 10.1007/s004100050143.

Rampone E., Piccardo G.B. and Hofmann A.W., 2008. Multistage melt-rock interaction in the Mt. Maggiore (Corsica, France) ophiolitic peridotites: microstructural and geochemical records. Contrib. Miner. Petrol., 156: 453-475, doi: 10.1007/s00410-008-0296-y.

Rampone E., Piccardo G.B., Vannucci R. and Bottazzi P., 1997. Chemistry and origin of trapped melts in ophiolitic peridotites. Geochim. Cosmochim. Acta, 61: 4557-4569, doi: 10.1016/S0016-7037(97)00260-3.

Rampone E., Piccardo G.B., Vannucci R., Bottazzi P. and Ottolini L., 1993. Subsolidus reactions monitored by trace element partitioning: the spinel- to plagioclase-facies transition in mantle peridotites. Contrib. Miner. Petrol., 115: 1-17, doi: 10.1007/BF00712974.

Rampone E., Romairone A., Abouchami W., Piccardo G.B. and Hofmann W., 2005. Chronology, petrology and isotope geochemistry of the Erro-Tobbio peridotites (Ligurian Alps, Italy): records of late Palaeozoic lithospheric extension. J. Petrol., 46: 799-827, doi: 10.1093/petrology/egi001.

Rampone E., Romairone A. and Hofmann A.W., 2004. Contrasting bulk and mineral chemistry in depleted peridotites: evidence for reactive porous flow. Earth Planet. Sci. Lett., 218: 491-506, doi: 10.1016/S0012-821X(03)00679-4.

Sano S. and Kimura J.I., 2007. Clinopyroxene REE geochemistry of the Red Hills peridotite, New Zealand: interpretation of magmatic processes in the upper mantle and in the Moho transition zone. J. Petrol., 48: 113-139, doi: 10.1093/petrology/egl056.

Sinigoi S., Comin-Chiaramonti P. and Alberti A.A., 1980. Phase relations in the partial melting of the Baldissero spinel-lherzolite (Ivrea-Verbano Zone, Western Alps, Italy). Contrib. Miner. Petrol., 75: 111-121, doi: 10.1007/BF00389772.

Sinigoi S., Comin-Chiaramonti P., Demarchi G. and Siena F., 1983. Differentiation of partial melts in the mantle: evidence from the Balmuccia peridotite, Italy. Contrib. Miner. Petrol., 82: 351-359, doi: 10.1007/BF00399712.

Suen C.J. and Frey F.A., 1987. Origin of the mafic and ultramafic rocks in the Ronda peridotite. Earth Planet. Sci. Lett., 85: 183-202, doi: 10.1016/0012-821X(87)90031-8.

Takazawa E., Frey F.A., Shimizu N., Saal N. and Obata M., 1999. Polybaric petrogenesis of mafic layers in the Horoman peridotite complex, Japan. J. Petrol., 40: 1827-1831, doi: 10.1093/petroj/40.12.1827.

Takazawa E., Frey F.A., Shimizu N. and Obata M., 2000. Bulk rock compositional variations in an upper mantle peridotite (Horoman, Hokkaido, Japan): are they consistent with a partial melting process? Geochim. Cosmochim. Acta, 64: 695-716, doi: 10.1016/S0016-7037(99)00346-4.

Taylor W.R., 1998. An experimental test of some geothermometer and geobarometer formulations for upper mantle peridotites with application to the thermobarometry of fertile lherzolite and garnet websterite. N. Jahrb. Miner., Abhandl., 172: 381-408.

Tribuzio R., Thirlwall M.F. and Vannucci R., 2004. Origin of the gabbro-peridotite association from the Northern Apennine ophiolites (Italy). J. Petrol., 45: 1109-1124, doi: 10.1093/petrology/egh006.

Van der Wal D. and Vissers R.L.M., 1996. Structural petrology of the Ronda peridotite, SW Spain: deformation history. J. Petrol., 37: 23-43, doi: 10.1093/petrology/37.1.23.

Voshage H., Sinigoi S., Mazzucchelli M., Demarchi G., Rivalenti G. and Hofmann A.W., 1988. Isotopic constraints on the origin of ultramafic and mafic dikes in the Balmuccia peridotite (Ivrea Zone). Contrib. Miner. Petrol., 100: 261-267, doi: 10.1007/BF00379737.

Warren J.M., 2016. Global variations in abyssal peridotite compositions. Lithos, 248-251: 193-219, doi: 10.1016/j.lithos.2015.12.023.

Received, October 15, 2019
Accepted, November 23, 2019
First published online, November 24, 2019

MELT-ROCK INTERACTION BETWEEN GRANITIC PEGMATITES AND HOSTING AMPHIBOLITES FROM THE CHIAVENNA OPHIOLITIC UNIT (TANNO PEGMATITIC FIELD, CENTRAL ALPS, NORTH ITALY)

Francesco Arrigoni*, Patrizia Fumagalli*,✉, Stefano Zanchetta** and **Alessandro Guastoni*****

* *Dipartimento di Scienze della Terra "Ardito Desio", Università degli Studi di Milano, Italy.*
** *Dipartimento di Scienze dell'Ambiente e della Terra, Università degli Studi di Milano Bicocca, Italy.*
*** *Dipartimento di Geoscienze, Università di Padova, Italy.*
✉ *Corresponding author, email: patrizia.fumagalli@unimi.it*

Keywords: *Melt-rock interaction; pegmatites; amphibolites; Chiavenna Ophiolitic Unit; Central Alps.*

ABSTRACT

The Tanno pegmatitic field, placed southward of Chiavenna (Central Alps, Sondrio, Italy), develops a large number of subplanar dykes that crosscut the Chiavenna Unit, an ophiolitic complex mainly composed, in the study area, of amphibolite rocks. This study focuses on the contact between a pegmatitic dyke and the amphibolitic country rock. We distinguished four zones across the contact: I) inner amphibolite, II) contact amphibolite, III) contact pegmatite, IV) inner pegmatite. The inner amphibolite, not affected by melt-rock interaction, is composed of amphibole, phlogopite, ilmenite, titanite and rutile. Two amphibole generations occur, both of them showing a patchy compositional zoning. Amphibole I are Mg-hornblende, whereas Amphibole II have a pargasitic composition. The contact amphibolite shows an enrichment of mica belonging to the phlogopite-biotite series, titanite and the presence of fluorapatite and plagioclase (Ab_{45-60}), that is absent in the inner amphibolite. Close to the contact, amphiboles display no zoning and gain an Mg-horneblenditic composition. The contact pegmatite has quartz, albitic plagioclase, garnet (almandine-spessartine series), muscovite, K-feldspar and fluorapatite. It shows a comb texture, with elongation of plagioclase crystals normal to the contact itself. Far from the contact, the inner pegmatite has an increasing grain-size and a less organized texture. In this zone several accessory phases occur, including gahnite, columbite-(Fe), monazite-(Ce), xenotime-(Y), uraninite and betafite. Whole rock analyses suggest that a chemical exchange, concerning both major elements and trace elements, occurred between the pegmatitic melt and the hosting amphibolite. A considerable increase of SiO_2, Na_2O and, to a lesser extent, of Al_2O_3 is observed from the amphibolite towards the pegmatite; K_2O and CaO show a decrease at the same extent. The REE pattern in the pegmatite highlights an enrichment in HREE at the contact. Mineral chemistry confirms this trend with variations observable in plagioclase, gradually more albitic from the amphibolite to the pegmatite. Mineralogical characters and geochemical features allow to classify the Tanno pegmatite in the LCT (Lithium, Cesium, Tantalium) family. Based on the metamorphic peak conditions reported from the Lepontine Dome the ambient conditions during pegmatite intrusion were ca. 550°C and 5 kbar. The reduced thermal difference between pegmatite and wall rock explains the diffuse contact observed by X-ray micro-computed tomography. The collected data suggest a chemical interaction between melt and wall rock, according to the following reaction taking place in the amphibolite

Amphibole I + Amphibole II + Ilmenite + Pegmatitic melt → Amphibole III + Plagioclase + Phlogopite + Titanite + Fluorapatite

INTRODUCTION

The development of a pegmatite field in the Valchiavenna area is related to the emplacement of the Novate Granite, which occurred about 24±1.2 Ma (zircon U-Pb ages; Liati et al., 2000). The northernmost field is located south of Chiavenna and close to the Tanno village (Fig. 1), where pegmatites intruded the Chiavenna Unit, an ophiolitic complex consisting mainly of serpentinites, amphibolites and minor metagabbros.

The intrusion of the Tanno pegmatite and aplitic dykes into the amphibolites of the Chiavenna Unit has led to metasomatic reactions and the development of geochemical gradients. Although several studies deal with the Tanno pegmatitic field, they mainly focus on minerals of gemmological and collecting interest, while poor attention has been given to the metasomatic reactions involving the country rocks.

The aim of this study is to investigate the relationships between dykes and the wall rocks, on the basis of main mineralogical changes and the temperature-pressure regime at the time of the pegmatitic melt emplacement.

GEOLOGICAL SETTING

The area of interest is located in Valchiavenna (Val Mera, Central Alps, N Italy), which extends N-S from the northern tip of Lake Como (Fig. 1). The central Alps section of the Alpine belt is characterized by Barrovian-type metamorphism of Cenozoic age with high-grade metamorphic rocks exposed in the so called "Lepontine Dome" (Trommsdorf, 1966) with roughly concentric metamorphic isograds. The Barrovian overprint is abruptly truncated to the south by the Insubric Fault, a major structure, active since the Oligocene (Schmid et al., 1989), that divides the north Alps belt from the south-vergent Southalpine domain. In the Valchiavenna area, North of the Insubric Fault, the Alpine nappe stack consists chiefly of: (i) Penninic units derived from distal European margin (Adula Nappe); (ii) the Chiavenna and Misox Zone ophiolites derived from the Valais Ocean (Steinmann and Stille, 1999; Stucki et al., 2003); (iii) the Tambò and Suretta units, derived from the Brianconnais microcontinent (Schmid et al., 1990); (iv) the Gruf Complex, a metamorphic complex with HT-LP metamorphism, of debated age (Galli et al., 2012; Nicollet et al., 2018); (v) thin slivers belonging to the Austroalpine domain along the Insubric Fault; (vi) the Bergell pluton, a composite magmatic unit that intruded the Alpine nappe stack between 33 and 30 Ma (Von Blanckenburg, 1992; Rosenberg et al., 1995).

The southern part of the Lepontine Dome is characterized by the widespread occurrence of migmatites, pegmatites and leucogranites (e.g. Guastoni et al., 2014). Such occurrences are due to crustal anatexis limited to the area close to the

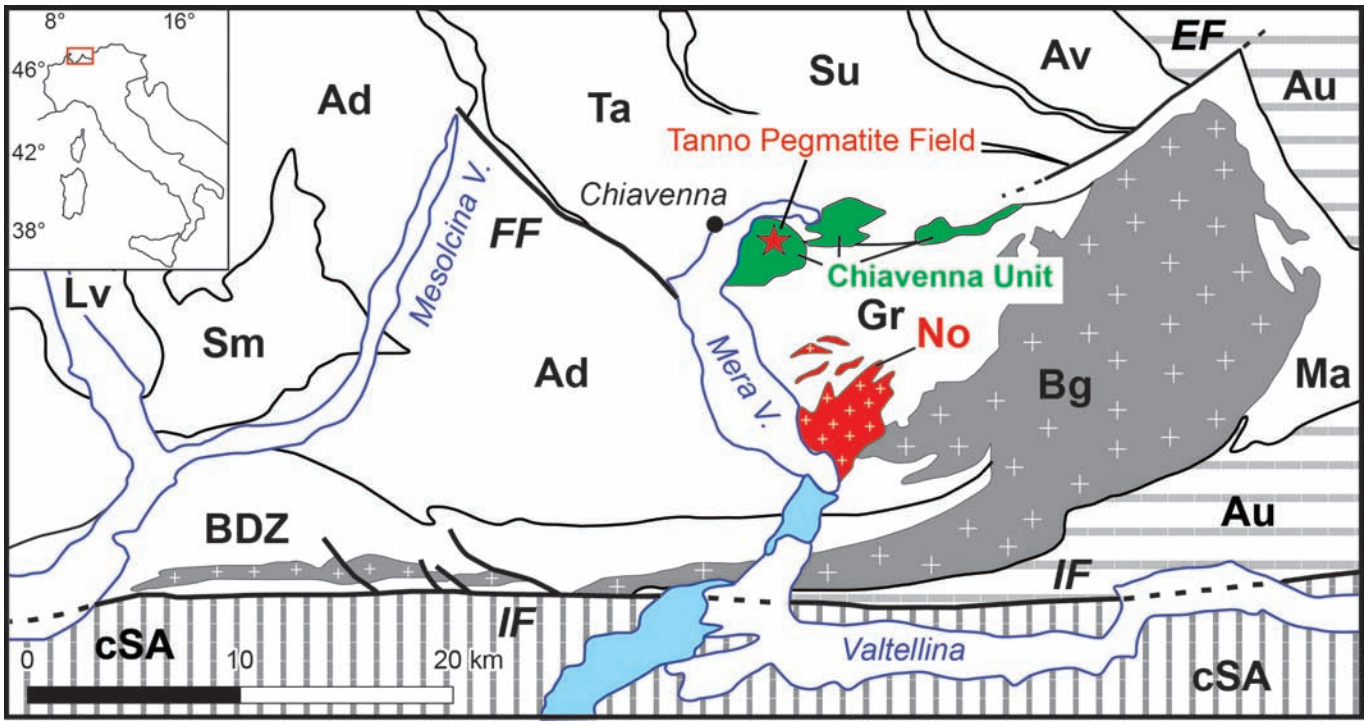

Fig. 1 - Simplified tectonic scheme of the Central Alps. The location of the Tanno pegmatite field is marked with a red star. Ad- Adula nappe; Av- Avers bundnerschiefers; Au- Austroalpine units; BDZ- Bellinzona-Dascio Zone; Bg- Bergell pluton; cSA- central Southern Alps; G-: Gruf complex; Ma- Malneco unit; Lv- Leventina nappe; No- Novate granite; Sm- Simano nappe; Su- Suretta nappe; Ta- Tambò nappe. EF- Engadine Fault; FF- Forcola Fault; IF- Insubric Fault.

Insubric Fault (Burri et al., 2005) and are related to protracted fluid-induced melting that took place in the 32 Ma to 22 Ma time lapse (Rubatto et al., 2009). The most prominent feature of this event in the Chiavenna area is the Novate granite body (Fig.1), a two-mica leucogranite which intrusion is constrained at 24±1.2 Ma (Liati et al., 2000). The northern boundaries of the southern migmatite belt (Burri et al., 2005) runs in the Valchiavenna area just N of Chiavenna along the Italian Bregaglia Valley (Fig. 1), with ophiolites of the Chiavenna Unit that are located within the area where migmatisation occurred.

The Chiavenna Unit represents an incomplete ophiolitic complex, in which subcontinental mantle rocks, instead of oceanic lithosphere, have been tectonically exposed on the ocean floor and covered by N-MORB basalts (Liati et al., 2003). The age of the ophiolites has been constrained to the Late Jurassic - 93±0.2 Ma (Liati et al., 2003) - representing the youngest remnants of the Valais ocean exposed in the Central Alps. The entire unit experienced an amphibolites facies syntectonic metamorphism (Ring, 1992).

The Chiavenna Unit crops out in three areas, alternated with metacarbonates, located on the left side of Chiavenna and Bregaglia valleys, between Aurosina Valley to the North and Prata Camportaccio village to the S.

The ultramafic rocks consist mainly of lherzolites deformed and serpentinized during the Alpine metamorphism (Huber and Marquer, 1998; Talerico, 2001). Beside ultramafic rocks, lenses of metagabbros occur, usually displaying well-preserved pre-deformation magmatic structure. Regarding the basalt-derived amphibolites, they form more than 50% of the Chiavenna Unit. In the present-day tectonic setting derived from the Alpine deformation, the amphibolites are situated structurally below the metaperidotites. The unit also comprises metacarbonate lenses and layers interleaved with the amphibolites.

The Tanno pegmatite-aplite field, as other similar fields in the Valchiavenna area, is likely genetically related to the Novate leucogranite (Fig. 1). The Novate granite is a S-type two-mica peraluminous leucogranite derived from partial melting of a metapelitic source (Oschidari and Zieger, 1992; von Blanckenburg et al., 1992) and genetically not related to the nearby calc-alkaline Bergell pluton (Fig. 1). The Tanno pegmatitic field exhibits a high degree of differentiation, as demonstrated by the occurrence of some accessory minerals as beryl, columbite, gahnite, uraninite and xenotime. Referring to the Černý and Ercit (2005) classification of granitic pegmatites, these pegmatites belongs to the *rare elements* class, which corresponds to the most differentiated one. Alongside, these pegmatites belong to the LCT (Lithium, Cesium, Tantalum) petrogenetic family of typical peraluminous composition (Černý and Ercit, 2005).

FIELD RELATIONSHIPS BETWEEN PEGMATITIC DYKES AND AMPHIBOLITIC WALL ROCK

The main outcrop of the Tanno pegmatitic field (46°18’52’’N, 9°24’19’’E) is visible looking southeastward from the town of Chiavenna (Fig. 1). It is a steep vertical cliff composed of mafic and ultramafic rocks crosscut by subplanar set of aplite-pegmatite dykes. These dykes intrude the wall rock on an exposed portion of the left side of Valchiavenna, near the small village of Tanno (Fig. 1). The main outcrop cliff, exposed northward, is made of anphibolites of the Chiavenna Unit, with a vertical extension of more than 100 meters (Fig. 2a). The thickness of dykes ranges from few centimeters to few meters. Pegmatites crosscut amphibolite schistosity and compositional layering.

The thicker dykes are subhorizontal to each other, while

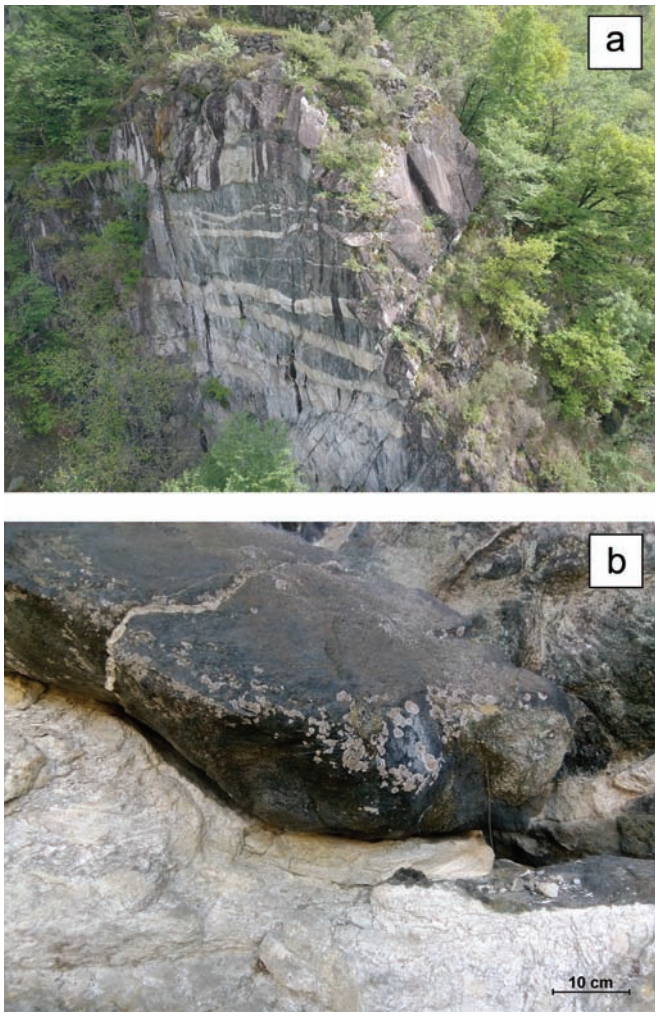

Fig. 2 - a) Aerial view of the Tanno pegmatitic field. Pegmatites cross cut the amphibolites belonging to the Chiavenna Unit. b) Detailed image showing the sampled area, characterized by the contact zone between a pegmatitic dyke and the amphibolitic wall rock.

thinner ones crosscut the ones above, implying an intersection relationship between these two different sets. The thicker dykes have a strike of 265-250° N with a dip angle of 15-20° either toward N or S, while the thinners have a similar strike, but, due to their steeper attitude, they crosscut the thicker ones.

The rock-forming minerals in pegmatites are quartz, K-feldspar, plagioclase, muscovite and garnet whereas beryl, columbite, gahnite, uraninite and xenotime occur as main accessory phases.

Most of the dykes are affected by metasomatic and alteration processes due to late stage fluids circulation along rigid fractures that promoted kaolinization and zeolitization.

Furthermore, at the outcrop scale, the contacts between pegmatite and hosting amphibolite are not sharp (Fig. 2b) and the occurrence of a reaction rim is quite evident, as testified by centimetric aplitic veins that depart from the pegmatite dyke and inject the amphibolite wall rock.

A representative contact between a pegmatitic dike and the host amphibolites was sampled (sample volume 30x20x10 cm^3, Fig. 3) in order to study the melt-rock interactions that occurred during dikes intrusion.

ANALYTICAL METHODS

Major and trace elements whole rock analyses were obtained by inductively-coupled plasma mass spectrometry at Bureau Veritas Mineral Laboratories, Krakow (Poland). Analyzed samples close to the contact were obtained by microdrilling across the interface between pegmatite and amphibolite. Chemical compositions of mineral phases were obtained with a JEOL JXA-8200 WDS electron microprobe (EPMA) at the Dipartimento di Scienze della Terra "Ardito Desio", University of Milano. Analyses were acquired with an accelerated voltage of 15 kV and a beam current of 15 nA. Typical acquisition time was 30 s counting on peaks and 10 s counting on the background. The standards applied for the different elements are: omphacite (Na), sanbornite (Ba), rodonite (Mn, Zn), K-feldspar (K), olivine (Mg), grossular (Si, Ca, Al), ilmenite (Ti), fayalite (Fe), hornblende (F), graftonite (P), UO_2 (U), pure Cr, pure Nb and pure Ta. Several analyses presented in Supplementary Table 1S, mainly amphiboles and micas, are non-stoichiometric due to the occurrence of elements (e.g. Rb, Sr, U, and F) that were not always measured during the standard EPMA analytical routine or were intrinsically not accurate due to interference problems with other measured elements.

X-ray micro-computed tomography allowed the detailed study of the geometric relationship at the contact between dykes and wall rock. The scans were acquired with a MicroCT/DR BIR Actis 130/150 system, with a resolution of 14 μm at the Dipartimento di Scienze della Terra e

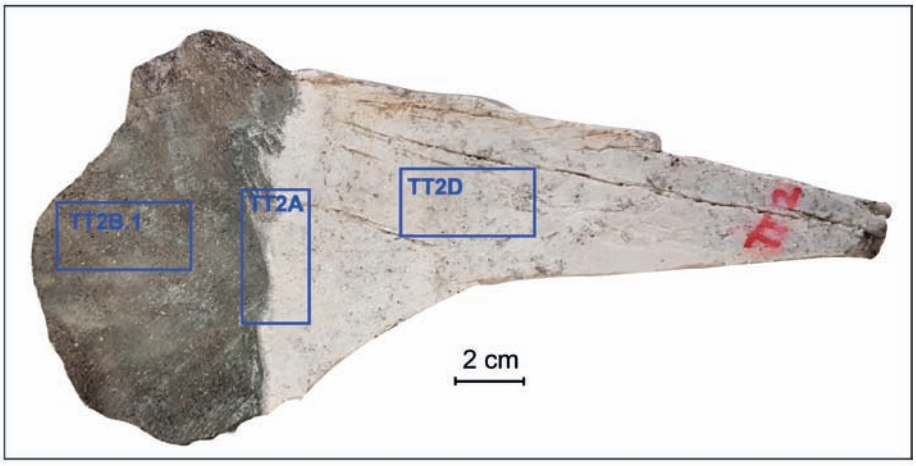

Fig. 3 - Sample TT2 showing the contact between amphibolites and granitic pegmatites from which thin sections TT2B.1 (inner amphibolite), TT2A (amphibolite-pegmatite contact) and TT2D (inner pegmatite) were obtained (indicated by the red rectangles). Other analyzsed samples were collected in the proximity of TT2 along the pegmatite-amphibolite contact.

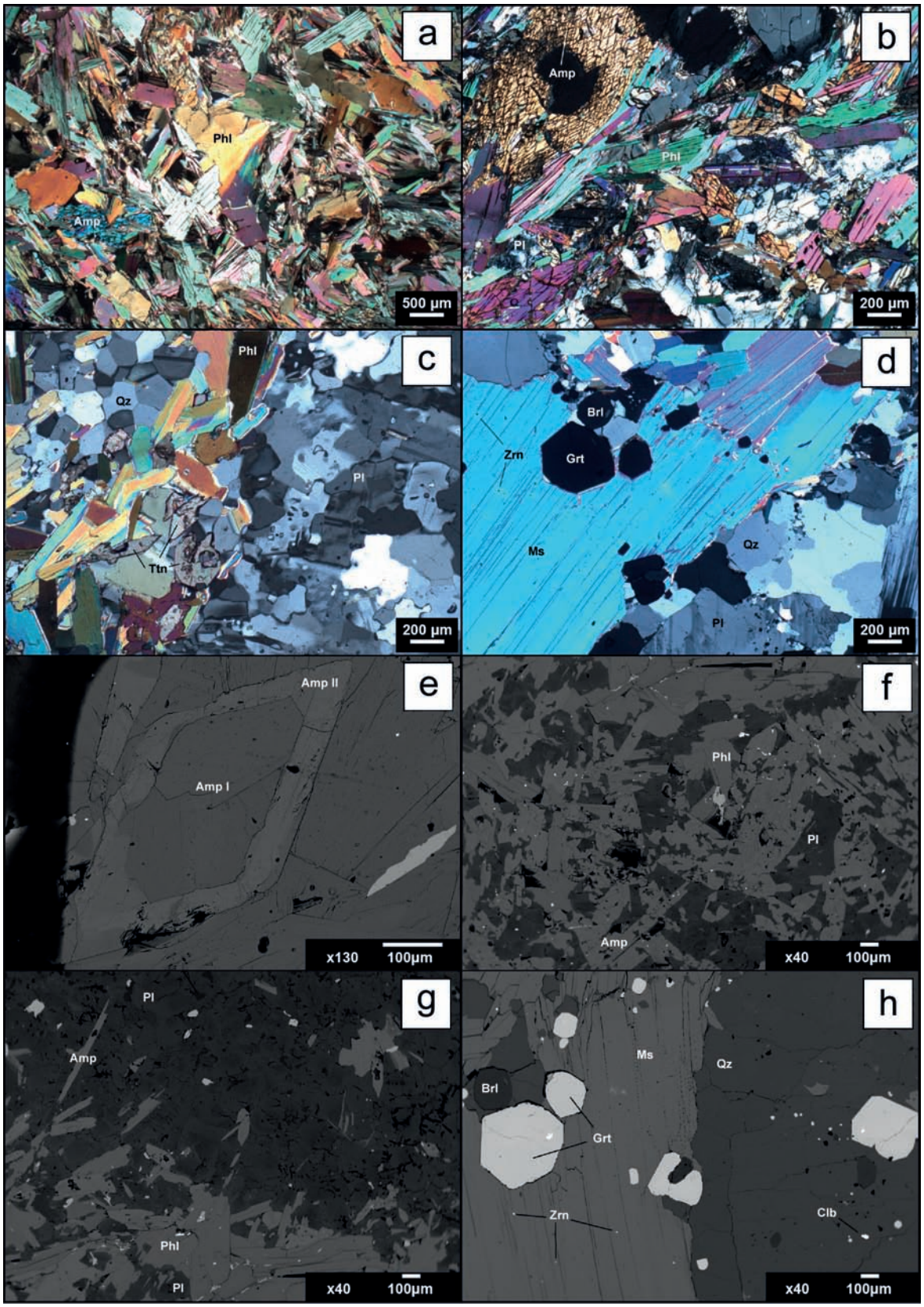

Fig. 4 - Photomicrographs and back-scattered electron images of representative amphibolites and pegmatite samples. a) Mineralogical association of the inner wall rock amphibolites, characterized by the occurrence of amphibole and phlogopite. b) Plagioclase appearance in the amphibolitic portion near the contact zone. c) Concentration of titanite crystals in the contact zone between amphibolite and pegmatite. d) Typical mineralogical association of the inner portion of the Tanno pegmatite, characterized by the occurrence of quartz, feldspar, plagioclase, muscovite, garnet, zircon, columbite and beryl. e) Typical amphibole zoning in the inner amphibolitic portion. f) Plagioclase appearance in the amphibolitic portion near the contact zone. g) Contact zone between amphibolite and pegmatite. h) Typical mineralogical association of the inner portion of the Tanno pegmatite.
Amp- amphibole; Phl- phlogopite; Pl- plagioclase; Qz- quartz; Ttn- titanite; Grt- garnet; Zrn- zircon; Brl- beryl; Ms- muscovite; Cl- columbite.

dell'Ambiente, University of Milano-Bicocca. MicroCT slices were then processed with the Avizo Fire (FEI-VSG™) software for 3D-reconstruction and rendering.

RESULTS

Textural analysis

Six samples were used for this study: TT2B.1, representative of the inner amphibolitic portions; TT2B, TT2C, TT2A, located at the contact zone between amphibolite and pegmatite; P3 and TT2D, located respectively in the intermediate and inner portion of the pegmatitic dyke. The inner amphibolite is medium-fine grained and displays disorganized texture, lacking any shape preferred orientation of mineral phases. The mineralogy consists of amphibole, phlogopite, ilmenite and minor fluorapatite, titanite, rutile, Nb-rich rutile and zircon (Fig. 4a). The amphibole has a patchy compositional zoning, as observed in the back-scattered electron images in (Fig. 4e), with the occurrence of two co-existing amphiboles. By means of EPMA analyses, we identified the occurrence of domains with a composition falling in the edenite-pargasite field (Leake et al., 1997), associated to darker domains (Fig. 4e) with a Mg-hornblende composition. Phlogopite occurs as a ubiquitous phase, with more pronounced modal abundance where allanite group minerals are present as well. The amphibolites have a peculiar mineralogy marked by the absence of plagioclase (Fig. 1S), a common phase at greenschist to amphibolite facies conditions in metamorphic mafic rocks. Plagioclase occurs only within a few centimetres from the contact with the pegmatite (Fig. 4b and f) together with titanite, which is commonly absent in the hosting amphibolite where the Ti-bearing phase is ilmenite. Also, fluorapatite appears in the amphibolite only close to the contact.

The pegmatite within 1-2 cm from the contact is fine-grained and presents an anisotropic texture. In this zone, the mineralogical association is composed of quartz, plagioclase, fluorapatite and, to a lesser extent, of K-feldspar, muscovite, pargasite, garnet and biotite (Fig. 4c and g). In the inner pegmatite the grain size become gradually larger reaching, in the core, a maximum of 3-4 cm, while the texture remains very poorly organized (Fig. 4d and h). Garnet is much more frequent and often concentrated in thin layers (Fig. 2S). Plagioclase develops a large grain-size, in particular in the intermediate zone, where centimeter-scale crystals are frequent. It also shows a shape preferred orientation with the elongated axis perpendicular to the contact, developing the typical comb texture of the pegmatite. The inner portions are also characterized by the occurrence of a great variability of REE-bearing accessory mineral phases, in addition to zircon, fluorapatite and columbite-(Fe), also monazite-(Ce), uraninite, xenotime-(Y), betafite and gahnite occur (Fig. 4d).

X-ray micro-computed tomography

The purpose of the X-ray micro-computed tomography (Micro-CT) is the creation of a set of slices that can be overlapped to provide a three-dimensional reconstruction of the sample. The using of the micro-CT reveals, at the millimetre scale, a gradual, diffused and discontinuous contact between the pegmatitic dike and the host amphibolite, characterized by a recurrent and extended interpenetration between the two components, revealing that the spatial interdigitation is very pronounced (Fig. 5). The amphibolites gradually give space to the pegmatitic dyke, developing an intermediate zone between the two components characterized by a visible loosing of the amphibolites shapes, here noticeable as isolated lobes of small dimensions, among which there is the developing of the pegmatitic portion.

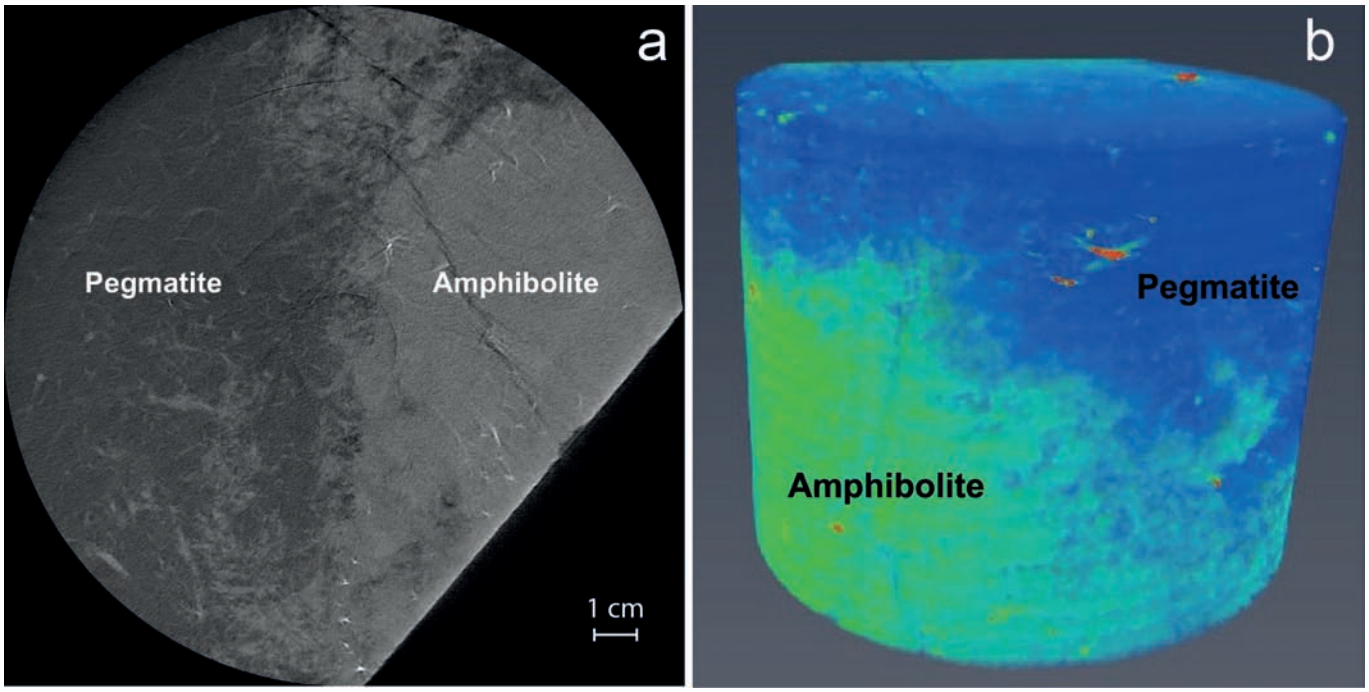

Fig. 5 - a) X-ray computed microtomography showing the contact between hosting amphibolite and the pegmatite dyke. Slice diameters measure 21.37 mm and 17.23 mm. b) 3D - reconstruction of the amphibolte-pegmatite contact. Green colors represent zones with higher density and greater atomic number, blue colors show lower density and smaller atomic number; red spots are denser minerals, such as oxides.

Mineral chemistry

Amphiboles

Amphiboles were normalized on the basis of 23 oxygen and considering Fe^{2+} as Fe total (Table 1S). The classification used for this study (Leake et al., 1997) allowed to distinguish three different amphibole types. Amphibole I and II are in the inner portion of the amphibolite, far from the contact aureole zone. In this area amphiboles have a patchy compositional zoning with variable Mg, Fe, Al and Na content (Fig. 6). Amphibole I is a Mg-hornblende, characterized by Na + K < 0.50 and Ca < 0.50; amphibole II is an edenite-pargasite, i.e. has a Na + K > 0.50 and Ti < 0.50 (Fig. 6a and b). BSE images corroborate two amphiboles generations (Fig. 4e). The brighter grey amphibole is overgrown on the darker grey one. These features are observed also in the TT2A and TT2B amphiboles in the inner amphibolite away from the pegmatite dyke.

Both amphibole I and amphibole II display no significant compositional changes approaching the contact (Fig. 7a and 7b). At the contact with the pegmatite dyke a compositionally homogeneous amphibole, chemically corresponding to a Mg-hornblende (Amphibole III in Fig. 6a), occurs. Amphibole III has an intermediate composition between amphibole I and II, in terms of Na+K content (Fig. 7b), with ($Mg/Mg+Fe^{2+}$) of amphibole II (Fig. 7a).

Micas

Micas belonging to the phlogopite-annite series were normalized on the basis of 11 oxygen atoms and considering Fe^{2+} as Fe total. The mineral chemistry data allow to identify the micas as phlogopites (Table 1S). Phlogopite into the amphibolitic wall rock shows no compositional variations as a function of the distance from the contact with pegmatite (X_{Mg}= $Mg/(Mg+Fe) \approx 0.72$).

The muscovite analyses were normalized on the basis of 11 oxygen atoms. The muscovite occurs only into the pegmatitic portions. Muscovite modal abundance increases approaching the dykes core, in which it often presents garnet, zircon, beryl, albite and columbite inclusions.

Plagioclase

The plagioclase analyses were normalized on the basis of 5 cations. Plagioclase occurs along the contact between amphibolite and pegmatite and in the pegmatite as a rock forming mineral. The albite component (Ab = Na/(Na +C a) x 100) of plagioclase in amphibolite increases towards the contact with pegmatite (Fig. 8), shifting from Ab_{45} to Ab_{60}, testifying for chemical exchange reaction between the amphibolite wall rock and the pegmatite dyke (Table 1S). Plagioclase in the pegmatite shows a nearly pure albitic composition at the core of the dyke, whereas Ca-content increases towards the contact reaching 0.6-0.7 (Na/Na+Ca) values (Fig. 8).

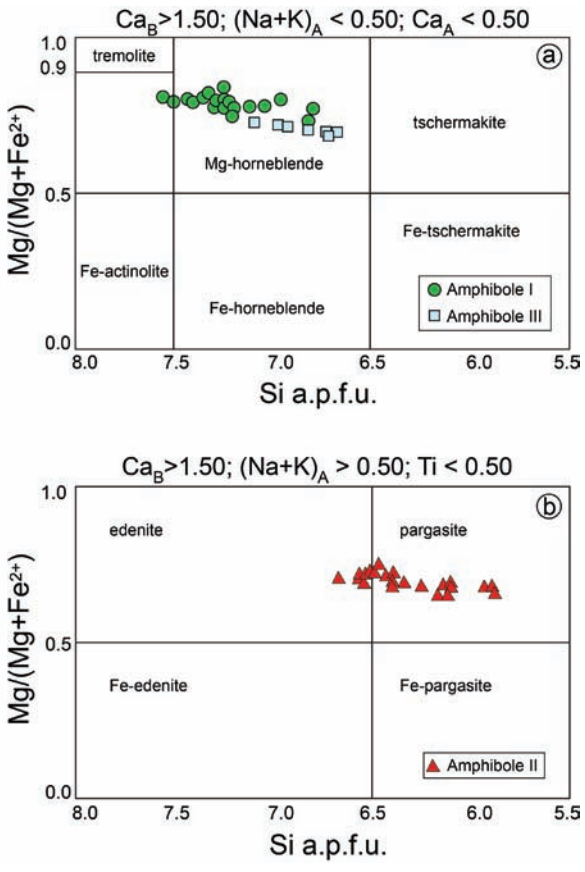

Fig. 6 - Mineralogical composition of amphiboles belonging to the TT2A and TT2B samples, after Leake et al. (1997). a) $Mg/(Mg + Fe^{2+})$ vs Si (a.p.f.u.) classification diagram for calcic amphibole group. b) $Mg/(Mg + Fe^{2+})$ vs Si (a.p.f.u.) classification diagram for sodic-calcic amphibole group.

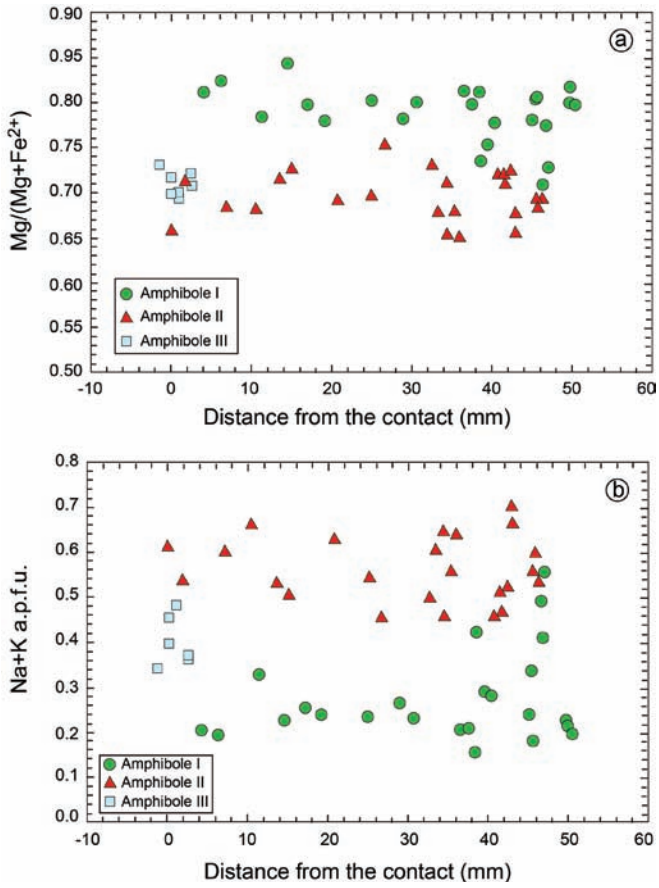

Fig. 7 - a) Variation of $Mg/(Mg + Fe^{2+})$ in the three amphibole generations as a function of distance from the contact. b) Variation of (Na + K) (a.p.f.u.) in amphiboles as a function of the distance from the contact.

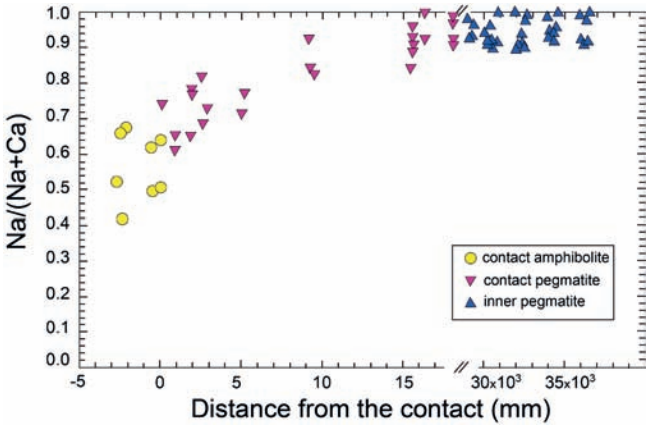

Fig. 8 - Na/(Na + Ca) in plagioclase as a function of the distance from the contact.

K-Feldspar

The K-feldspar analyses were normalized on the basis of 5 cations. The K-feldspar only occurs in the pegmatitic dykes and shows no compositional variations, neither as a function of the distance to the wall rock contact, nor intragranular, within the single feldspar. The medium feldspars composition indicates Or_{94} (Or = K/(Na + K +Ca) x 100) and Ab_6, while the Ca content is negligible (Table 1S).

Garnet

Garnet analyses have been normalized on the basis of 7 cations. They show no compositional variations linked to its position inside the pegmatitic dyke, but there are considerable compositional changes inside the crystals. Garnets are commonly zoned; significant are core to rim Mn variations from 22 wt% in the core down to 15.50 wt% at rim (Table 1S). As displayed by EPMA analyses the decrease of Mn toward the rim corresponds to a Fe^{2+} increase, suggesting that Mn is progressively substituted by Fe^{2+} during garnet growth.

Accessory minerals

The wall rock amphibolite shows a range of accessory minerals, with a prevalence of titaniferous phases as titanite, ilmenite and rutile. Some representative chemical analyses of accessory phases are shown in Table 1. There is also the occurrence, in the amphibolitic contact zone, of fluorapatite, which shows an increase of F percentage approaching the dyke contact. The titanite analyses were normalized on the basis of 5 oxygen atoms, the rutile ones on the basis of 4 oxygen atoms and ilmenite on 3 oxygen atoms.

Gahnite and Th-rich monazite-(Ce) were also analyzed and are characterized by sensible U, Ce, La and HREE contents. Each analyzed pegmatite contains zircon and columbite-(Fe), often zoned, with a Nb-enrichment towards the core of the crystals. The TT2A and TT2D samples have uraninite, xenotime-(Y) and monazite-(Ce) as well. TT2B sample's analysis permitted to recognize a Ti, Nb, Ta oxide belonging to the pyrochlore super-group (Atencio et al., 2010). The gahnite analyses were normalized on the basis 8 oxygen atoms, the columbite ones on the basis of 3 cations and 12 charges, while the betafite ones on the basis of 14 oxygen atoms.

Major, minor and trace elements whole rock analysis

The whole rock analyses (Table 2) show a compositional variability of major elements as a function of the distance from the contact between amphibolite and pegmatite. SiO_2 shows a significant increase towards the pegmatite, and continues to increase from the pegmatite rim to the pegmatite core. The Al_2O_3 content remains instead roughly constant.

Table 1 - Representative chemical compositions (in wt.%) of accessory phases in Tanno amphibolite and pegmatite.

	SiO_2	TiO_2	Al_2O_3	FeO	MnO	MgO	CaO	Na_2O	K_2O	P_2O_5	Nb_2O_5	Ta_2O_5	ZnO	UO_2	F	Total
Apatite																
TT2B	0.05			0.11	0.1		56.5			41.23					3.57	101.55
P5B	0.05			0.03	0.13		55.44			41.01					4.31	100.97
Titanite																
TT2B	30.89	36.67	2.08	0.67	0.06	0.01	28.69		0.02		0.26	0.27	0.02			99.63
P5B	31.17	35.7	2.63	0.59	0.12	0.01	28.73		0.01		0.11	0.06				99.11
TT2B.1	30.63	38.01	1.78	0.67			28.85									99.95
TT2A	30.88	37.47	1.98	0.63			28.7									99.66
Rutile																
TT2B		79.86	0.11	5.55			0.12				8.58	4.17				98.38
Betafite																
TT2B		15.61		0.44	0.19		15.31	1.21	0.12		9.96	31.25	0.06	24.47		98.57
Columbite																
P3		1.04		13.43	6.87	0.12					63.47	14.08	0.06	0.01		99.07
Ilmenite																
P5B		51.95		44.68	2.87	0.61	0.27					0.08				100.38
Gahnite																
P3	0.14		54,00	2.8	0.09	0.13							41.35			98.51

Table 2 - Whole rock major, minor and trace element compositions of Tanno amphibolite and pegmatite (standard deviations in brackets).

wt.%	Inner Pegmatite		Intermediate Pegmatite		Contact Pegmatite		Contact Amphibolite	
SiO_2	75.15	(0.01)	74.95	(0.01)	74.69	(0.01)	42.23	(0.01)
TiO_2	-	-	0.02	-	0.02	(0.01)	1.38	(0.01)
Al_2O_3	15.14	(0.01)	14.81	(0.01)	14.99	(0.01)	14.44	(0.01)
$Fe_2O_{3\,(t)}$	0.18	(0.04)	0.54	(0.04)	0.50	(0.04)	12.33	(0.04)
MnO	0.06	(0.01)	0.10	(0.01)	0.10	(0.01)	0.31	(0.01)
MgO	0.06	(0.01)	0.06	(0.01)	0.06	(0.01)	15.95	(0.01)
CaO	2.56	(0.01)	0.72	(0.01)	0.60	(0.01)	6.45	(0.01)
Na_2O	6.00	(0.01)	4.97	(0.01)	5.10	(0.01)	0.73	(0.01)
K_2O	0.33	(0.01)	3.17	(0.01)	3.49	(0.01)	4.89	(0.01)
P_2O_5	0.11	(0.01)	0.05	(0.01)	0.04	(0.01)	0.03	(0.01)
Cr_2O_3	-	-	-	-	-	-	0.04	(0.002)
L.O.I.	0.40		0.60		0.40		1.21	
Total	100.00		100.00		100.00		100.00	

ppm	Inner Pegmatite		Intermediate Pegmatite		Contact Pegmatite		Contact Amphibolite	
Ba	10.00	(1.00)	4.00	(1.00)	2.00	(1.00)	167.00	(1.00)
Ni	0.40	(0.10)	0.40	(0.10)	0.40	(0.10)	143.00	(0.10)
Sc	-	(1.00)	2.00	(1.00)	2.00	(1.00)	39.00	(1.00)
Be	30.00	(1.00)	11.00	(1.00)	7.00	(1.00)	31.00	(1.00)
Co	0.50	(0.20)	-		0.30	(0.20)	58.10	(0.20)
Cs	2.00	(0.10)	7.30	(0.10)	6.20	(0.10)	172.50	(0.10)
Ga	14.80	(0.50)	18.00	(0.50)	16.80	(0.50)	12.60	(0.50)
Hf	0.50	(0.10)	1.20	(0.10)	0.90	(0.10)	2.40	(0.10)
Nb	4.00	(0.10)	17.50	(0.10)	15.10	(0.10)	4.60	(0.10)
Rb	39.10	(0.10)	299.20	(0.10)	320.10	(0.10)	678.80	(0.10)
Sn	1.00	(1.00)	10.00	(1.00)	11.00	(1.00)	6.00	(1.00)
Sr	226.90	(0.50)	6.70	(0.50)	5.60	(0.50)	14.30	(0.50)
Ta	1.60	(0.10)	2.90	(0.10)	2.10	(0.10)	0.50	(0.10)
Th	1.50	(0.20)	2.20	(0.20)	1.20	(0.20)	0.80	(0.20)
U	18.70	(0.10)	14.60	(0.10)	8.10	(0.10)	1.40	(0.10)
V	-	-	-	-	-	-	201.00	(0.80)
W	-	-	1.30	(0.50)	0.90	(0.50)	2.00	(0.50)
Zr	7.20	(0.10)	23.70	(0.10)	16.90	(0.10)	94.90	(0.10)
Y	1.20	(0.10)	9.50	(0.10)	6.80	(0.10)	32.00	(0.10)
La	4.10	(0.10)	5.60	(0.10)	2.80	(0.10)	13.70	(0.10)

ppm	Inner Pegmatite		Intermediate Pegmatite		Contact Pegmatite		Contact Amphibolite	
Ce	8.20	(0.10)	11.00	(0.10)	5.20	(0.10)	38.30	(0.10)
Pr	0.86	(0.02)	1.30	(0.02)	0.58	(0.02)	5.52	(0.02)
Nd	3.00	(0.30)	4.80	(0.30)	2.00	(0.30)	25.40	(0.30)
Sm	0.86	(0.05)	1.43	(0.05)	0.83	(0.05)	5.60	(0.05)
Eu	0.10	(0.02)	0.09	(0.02)	0.03	(0.02)	1.41	(0.02)
Gd	0.46	(0.02)	1.44	(0.02)	0.80	(0.02)	4.73	(0.02)
Tb	0.06	(0.01)	0.28	(0.01)	0.17	(0.01)	0.73	(0.01)
Dy	0.31	(0.05)	1.77	(0.05)	1.18	(0.05)	5.04	(0.05)
Ho	0.04	(0.02)	0.32	(0.02)	0.20	(0.02)	1.21	(0.02)
Er	0.07	(0.03)	0.83	(0.03)	0.65	(0.03)	4.10	(0.03)
Tm	0.01	(0.01)	0.13	(0.01)	0.09	(0.01)	0.66	(0.01)
Yb	0.09	(0.05)	1.00	(0.05)	0.64	(0.05)	4.85	(0.05)
Lu	-	-	0.15	(0.05)	0.11	(0.05)	0.82	(0.05)
Cu	2.30	(0.10)	1.50	(0.10)	1.00	(0.10)	7.00	(0.10)
Pb	3.40	(0.10)	1.50	(0.10)	1.70	(0.10)	3.30	(0.10)
Zn	6.00	(1.00)	9.00	(1.00)	12.00	(1.00)	73.00	(1.00)
As	0.80	(0.50)	0.80	(0.50)	0.80	(0.50)	1.10	(0.50)
Bi	0.90	(0.10)	0.80	(0.10)	0.80	(0.10)	3.20	(0.10)
Au	0.60	(0.50)	0.80	(0.50)	1.70	(0.50)	2.30	(0.50)
Tl	0.20	(0.10)	-	-	-	-	3.70	(0.10)

FeO and MgO decrease towards the pegmatite, whilst Na_2O describes an opposite trend. K_2O evidences an elevated concentration along the pegmatite contact, while CaO is very abundant into the wall rock. TiO_2 exhibits a higher concentration in the amphibolite. The remaining elements do not show significant variations across the contact.

Trace elements concentration in the analyzed samples are reported in Table 2. The trace elements pattern of the pegmatite, normalized to chondrite (McDonough and Sun, 1995), shows enrichment in LILEs (large-ion lithophile elements) with respect to HFSEs (High Field Strength Elements). With respect to other HFSE, Zr, Nb and Ta, show higher concentrations, as they have been likely partitioned within Fe and Ti oxides (London, 2008), abundant in the pegmatite. REE pattern shows a slight enrichment in LREE with respect to HREE, even though their total tenor remains low (Fig. 9).

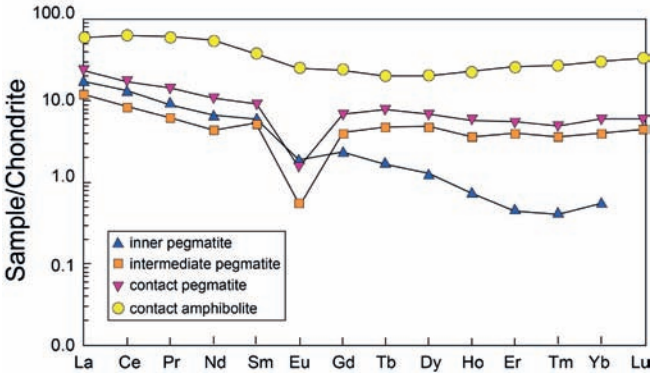

Fig. 9 - Chondrite normalized REE pattern of analyzed amphibolite and pegmatite (McDonough and Sun, 1995).

DISCUSSION AND CONCLUSIONS

Thermal regime

The macro-scale analyses of the Tanno pegmatitic body reveals a series of tabular, sub-planar and parallel dykes which crosscut the amphibolites of the Chiavenna Unit. The pegmatitic melt emplacement took place between 25±0.5 Ma (A. Guastoni, pers. comm). The thermal regime can be assumed to be ca. 550-600°C, the same temperature resulted from a study concerning the emplacement of the close Val Codera pegmatitic field. On the other hand, the amphibolite wall rock had, at the time of the emplacement, a similar temperature, as indicated by the isograds calculated for the Barrovian metamorphism of the Lepontine Dome (Todd and Engi, 1997). Following these data, the ambient temperature of the most amphibolites, at the time of the Tanno pegmatite intrusion, should had been approximately 550°C. A small temperature difference between the two systems had significant consequences on the geometry and metasomatism of the contact between dykes and wall rock, accordingly far to be sharp and with several interpenetrations. The X-ray micro-computed tomography of the contact portion showed, more in detail, what was observed at the outcrop scale, which is a complex geometric interaction between the two bodies, due to their small temperature difference.

Wall rock-dyke interactions

The contact between wall rock and pegmatitic melt caused a chemical disequilibrium in the system, enhanced by the elevate temperature, promoting chemical interactions between the two components, as highlighted by the peculiar distribution gradient for some elements. Whole rock analyses show the variation of some elements concentrations as a function of the distance from the contact, both in terms of major elements and trace elements. The study of the mineralogical phases and their mineral chemistry across the contact provide data in agreement with the X-ray fluorescence whole rock analysis.

One of the most striking features related to the melt-rock interaction is the disappearance of plagioclase in amphibolite far from the contact and its appearance, at about 5 mm from the contact towards the pegmatite.

The amphibolites of the Chiavenna Unit usually display a banded texture, characterized by a compositional layering with interleaved amphibole-rich and plagioclase-rich levels. The amphibolites hosting the Tanno pegmatites are somewhat different, as they are chiefly made of hornblende and accessory minerals and plagioclase is substantially lacking. Plagioclase appears only close, within 5 mm, to the contact and thus we suggest that his growth is strictly related to a melt-rock reaction. Furthermore, the plagioclase composition (Fig. 8) shows an increasing Na-content towards the contact, perfectly comparable to the albitic increase, towards the core, inside the pegmatite.

The plagioclase disappearance away from the contact correspond to other textural and compositional changes inside the amphibolite. Amphiboles away from the contact (Amphibole I and Amphibole II) are characterized by a patchy compositional zoning with compositions ranging from horneblenditic to edenitic terms (Fig. 6). Compositional zoning of amphiboles disappears moving towards the contact, together with the appearance of plagioclase. Within 5 mm from the contact amphiboles (Amphibole III) display an horneblenditic homogeneus composition (Fig. 6), suggesting that the original compositional zoning preserved away from the pegmatite, has been re-homogenized due to thermal effect and melt-rock reaction. Amphibole modal abundance also tends to decrease gradually towards the contact, in favour of a modal increase of phlogopite. Phlogopite shows no particular compositional variations, with the exception of a slight decrease in Ti-content towards the contact.

Concerning the accessory phases, they also show some variations in the contact amphibolite. Fluorapatite appears close to the contact; this is likely due to the elevate phosphorous supply of the pegmatitic melt, together with a greater Ca availability. For the same reason, i.e. Ca availability, titanite substitutes ilmenite as the Ti-bearing phase in the amphibolite.

Inside the pegmatitic dykes the consequences of the interactions between the two components result less evident. From the textural point of view there is a sharp decrease of the grain-size in proximity of the contact, likely due to faster cooling of the pegmatitic melt with respect to the core of the dyke. Concerning the compositional variations, Na content in plagioclase increases towards the core, with a stabilization, at about 2 cm from the contact, at values close to Ab_{95} (Fig. 8 and Table 1S).

Further information on the chemical gradients between amphibolite and pegmatite can be derived by trace element distribution. Sr exhibits a particular trend as a function of the distance from the contact, with higher concentration both in inner amphibolites and in inner pegmatite, as compared with the drastic decrease recorded in proximity of the contact. Also, Ba content varies significantly moving away from the contact, showing a higher concentration nearby the rim, where modal abundance of phlogopite and biotite, main Ba reservoirs, increases. While LREEs show little variations, HREEs vary substantially between the inner and the outer pegmatitic portions. In fact, the HREEs show an increase in proximity of the contact, likely due to the vicinity of amphibolite, where HREE contents are significantly higher with respect to pegmatite. The HREE enriched composition of the pegmatite close to the contact could be explained by the occurrence of numerous titanite crystal, that are lacking in the pegmatite core. Titanite could be a HREEs reservoir (Mulrooney and Rivers, 2005) and its concentration along the pegmatite external contact could explain the high HREE contents displayed by whole rock data (Fig. 9 and Table 2).

As regards to the remaining REEs, as previously mentioned, they do not show particular variations inside the pegmatite; nonetheless a significant increase in the contact area is observable. This can be attributed to the high concentration, inside the amphibolite, of allanite group minerals. The melt-rock interaction caused the destabilization of this accessory mineral, which, indeed, was not observed in proximity of the

contact. The mobilized REEs affected the pegmatitic contact portion, recorded by variations in the REEs ditribution.

The occurrence of gahnite, a Zn-bearing spinel, plays an important role for the understanding of the pegmatitic melt nature. Its presence indicates that this pegmatite belongs to the LCT (Lithium, Cesium, Tantalum) petrogenetic family (Černý and Ercit, 2005), characterized by the presence of significant amounts of Li, Ce and Ta. In addition, the distribution of Zn and Mn compared to Fe and Mg indicates relatively high degree of fractionation, which allows to classify this pegmatite as belonging to the rare-element class.

Profiting of mineralogical distribution across the contact, of mineral chemistry variations and of distribution of major and trace elements across the contact, we suggest the following reaction, responsible of all changes we observed at different scales:

Amphibole I + Amphibole II + Ilmenite + Pegmatitic melt → Amphibole III + Plagioclase + Phlogopite + Titanite + Apatite

This reaction describes the interaction between the melt and the wall rock. Melt-rock reaction caused the destabilization of two inner amphiboles (edenite and Mg-horneblende, Fig. 10), which gave space to a third amphibole, characterized by an intermediate horneblenditic composition. The great K supply from the melt allowed the concentration of a great phlogopite modal abundance, while plagioclase, during the crystallization, received a greater amount of Ca (obtained from the pegmatitic melt supply and from the primary Ca-amphibole destabilization) that modified the composition towards a greater anorthitic composition. This is in contrast with the plagioclase belonging to the pegmatite, which is strongly albitic in composition, reaching values close to Ab_{95}. The interaction also caused the break-down of ilmenite which, as observed in BSE images and petrographic observations, is absent in proximity of the contact, giving space to the titanite, which increases its modal abundance due to the Ca supply from the amphibolite.

Furthermore, the appearance, inside the amphibolite and in proximity of the contact, of fluorapatite, can be attributed to the high P supply from the pegmatitic melt combined with the increased Ca availability.

Despite the different interactions described, the amphibolitic reaction area in which the reaction occurs extends for 5 mm starting from the contact. This is simply noticeable considering that the pegmatitic melt was extremely depleted in fluids at the time of the emplacement into the wall rock.

Conclusions

In this study, we examined the interactions between the Tanno pegmatitic field and the hosting amphibolites of the Chiavenna ophiolitic unit. Textural, mineralogical and geochemical analyses allowed to individuate the occurrence of melt-rock interactions at the millimetre scale along intrusive contacts. On the basis of the whole rock geochemical data and mineral chemistry, it was possible to trace the petrogenetic features of the pegmatitic bodies. The mineralogical association of the pegmatites is made of quartz, Na-rich plagioclase, K-feldspar, garnet (almandine-spessartine), muscovite, biotite and a wide range of accessory minerals, that allow to obtain information on the pegmatite type and evolution. The presence of gahnite was fundamental in order to study the melt differentiation degree, which was proved to be evolved. The pegmatitic dykes intruded an amphibolitic wall rock, whose mineralogical association is made by amphibole, phlogopite, titanite, rutile, ilmenite, allanite group minerals and zircon.

Despite at the outcrop scale the intrusive contact between the pegmatitic dyke and the amphibolitic wall rock is sharp, a detailed sampling across the contact and related analyses allowed to identify both for amphibolite and pegmatite the occurrence of compositional variability dependent on the distance to the contact. SiO_2 and Na_2O increase from the amphibolites towards the pegmatite, while CaO, FeO and MgO show an opposite trend. This variability is clearly followed

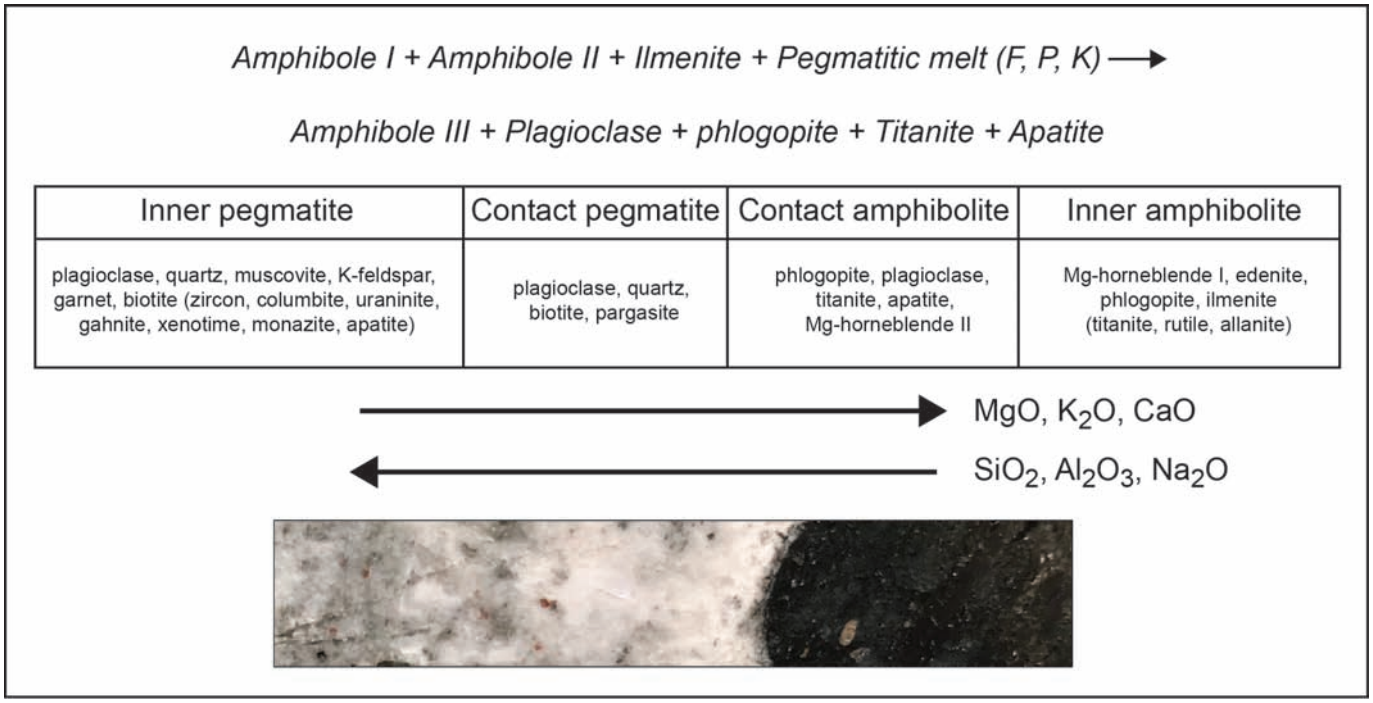

Fig. 10 - Variable mineralogical and whole rock composition, integrated with X-ray fluorescence data from an inner portion of the same amphibolite (Liati et al., 2003), as a function of the distance from the contact between amphibolite and pegmatite. A picture of the contact zone is shown as well.

by mineral chemistry variations, mainly observable in phases such as plagioclase and amphibole. The amphibolite equilibrium mineral assemblage does not contain plagioclase, which anyhow appears in proximity of the contact. From the plagioclase starting point inside the amphibolite towards the pegmatite core, it describes a gradual increase of the albitic content.

On the basis of these observations, it was possible to individuate, in proximity of the contact, the developing of a limited reaction area characterized by the appearance of plagioclase, titanite, phlogopite and fluorapatite. This mineralogical association is the result of the interaction between the pegmatitic melt and the amphibolite, as a result of a significant compositional gradient between the two portions. The developing of an extended chemical interaction between amphibolite and pegmatite was possible due to the small temperature difference at the time of the intrusion. This permitted the development of a marked micro-scale interdigitation in the contact zone, which enhanced the chemical relationships between the two portions.

This study opens new scenarios aimed at the comprehension of the mechanism and origin of the Tanno pegmatitic bodies and their relationships with the wall-rocks.

ACKNOWLEDGEMENTS

We greatly appreciated suggestions and comments by L. Secco and an anonymous reviewer who revised the first version of the manuscript: they helped us to significantly improve the paper quality. We wish to thank also A. Montanini for the editorial handling of the paper. Andrea Risplendente is greatly thanked for the careful electron-microprobe analyses. This research has been supported by the Italian Ministry of Education, University and Research (MIUR) through the grant [PRIN-2015C5LN35] "Melt–rock reaction and melt migration in the MORB mantle through combined natural and experimental studies".

Supplementary data to this article are available online at https://doi.org/10.4454/ofioliti.v45i1.530

REFERENCES

Atencio A., Andrade M.B., Christy A.G., Gieré R. and Kartashov P.M., 2010. The pyrochlore supergroup of minerals: nomenclature. Can. Miner., 48: 673-698.

Burri T., Berger A. and Engi M., 2005. Tertiary migmatites in the Central Alps: Regional distribution, field relations, conditions of formation and tectonic implications. Schweiz. Miner. Petrogr. Mitt., 83: 215-235.

Černý P. and Ercit T.S., 2005 The classification of granitic pegmatites revisited. Can. Miner., 43: 2005-2026.

Galli A., Le Bayon B., Schmidt M.W., Burg J.P., Reusser E., Sergeev S.A. and Larionov A., 2012. U-Pd zircon dating of the Gruf Complex: disclosing the late Varisican Granulitic lower crust of Europe stranded in the Central Alps. Contrib. Miner. Petrol., 163: 353-378.

Guastoni A., Pennacchioni G., Pozzi G., Fioretti A.M. and Walter J.M., 2014. Tertiary pegmatites dikes of the Central Alps. Can. Miner., 52: 191-219.

Huber R.K. and Marquer D., 1998 The tectonometamorphic history of the peridotitic Chiavenna unit from Mesozoic to Tertiary tectonics: a restoration controlled by melt polarity indicators (Eastern Swiss Alps). Tectonophysics, 296: 205-223.

Leake B.E., Woolley A.R., Birch W.D., Gilbert M.C., Grice J.D., Hawthorne F.C., Kato A., Kisch H.J., Krivovichev V.G., Linthout K., Lird J. and Mandarino J., 1997. Nomenclature of amphiboles: report of the subcommittee on amphiboles of the International Association Commission on New Minerals and Mineral Names. Miner. Mag., 61: 295-321.

Liati A., Gebauer D. and Fanning M., 2000. U-Pb SHRIMP dating of zircon from the Novate granite (Bergell, Central Alps): evidence for Oligocene-Miocene magmatism, Jurassic/Cretaceous continental rifting and opening of the Valais trough. Schweiz. Miner. Petrogr. Mitt., 80: 305-316.

Liati A., Gebauer D. and Fanning M., 2003. The youngest basic oceanic magmatism in the Alps (Late Cretaceous; Chiavenna unit, Central Alps): geochronological constraints and geodynamic significance. Contrib. Miner. Petrol., 146: 144-158.

London D., 2008. Pegmatites. Can. Miner. Spec. Publ., 10, 347 pp.

McDonough W.F and Sun S., 1995 The composition of the Earth. Chem. Geol., 120: 223-253.

Mulrooney D. and Rivers T., 2005. Redistribution of the rare-earth elements among coexisting minerals in metamafic rocks across the epidote-out isograd: an example from the St. Anthony Complex, northern Newfoundland, Canada. Can. Miner., 43: 263-294.

Nicollet C., Bosse V., Spalla M.I. and Schiavi F., 2018. Eocene ultra-high temperature (UHT) metamorphism in the Gruf Complex (Central Alps): constraints by LA-ICPMS zircon and monazite dating in petrographic context. J. Geol. Soc. London, 175: 774-787.

Oschidari H. and Zieger U.R.F., 1992. Vergleichende Sm-Nd und Rb-Sr Unterschungen and Bergeller Gerollen aus der Gonfolite Lombarda ("Sudalpine Molasse") und an Bergeller und Novate Granitoiden des Ursprungsgebietes. Ecl. Geol. Helv., 85: 375-384.

Ring U., 1992 The Alpine geodynamic evolution of Penninic nappes in the eastern Central Alps: geothermobarometric and kinematic data. J. Metam. Geol., 10: 33-53.

Rosenberg C.L., Berger A. and Schmid S.M., 1995. Observations from the floor of a granitoid pluton: inferences on the driving force of final emplacement. Geology, 23 (5): 443-446.

Rubatto D., Hermann J., Berger A. and Engi M., 2009. Protracted fluid-induced melting during Barrovian metamorphism in the Central Alps. Contrib. Miner. Petrol., 158: 703-722.

Schmid S.M., Aebli H.R., Heller F. and Zing A., 1989. The role of the Periadriatic Line in the tectonic evolution of the Alps. In: M.P. Coward, D. Dietrich, R.G. Park (Eds.), Alpine tectonics. Geol. Soc. London, p. 153-171.

Schmid S.M., Rück P. and Schreurs G., 1990. The significance of the Schams nappes for the reconstruction of the paleotectonic and orogenic evolution of the Penninic zone along the NFP-20 East traverse (Grisons, eastern Switzerland). Mém. Soc. Géol. Fr., 156: 263-287.

Steinmann M. and Stille P., 1999. Geochemical evidence for the nature of the crust beneath the eastern North Penninic basin of the Mesozoic Tethys Ocean. Intern. J. Earth Sci., 87: 633-643.

Stucki A., Rubatto D. and Trommsdorff V., 2003. Mesozoic ophiolite relics in the Southern Steep Belt of the Central Alps. Schweiz. Miner. Petrogr. Mitt., 83: 285-299.

Talerico C., 2001. Petrological and chemical investigation of a metamorphosed oceanic crust-mantle section (Chiavenna, Bergell Alps). Tesi dott., ETH Zurich, 153 pp.

Todd C.S. and Engi M., 1997. Metamorphic field gradients in the Central Alps. J. Metam. Geol., 15: 513-530.

Trommsdorf V., 1966. Progressive metamorphose kieseliger karbonatgesteine in den zentralalpen zwischen Bernina und Simplon. Schweiz. Miner. Petrogr. Mitt., 46: 431-460.

von Blackenburg F., 1992. Combined high-precision chronometry and geochemical tracing using accessory minerals: applied to the Central-Alpine Bergell intrusion (central Europe). Chem. Geol., 100: 19-40.

von Blanckenburg F., Fruh-Green G., Diethelm K.H and Stille P., 1992. Nd-, Sr, O-isotopic and chemical evidence for a two stage contamination history of mantle magma in the Central Alpine Bergell intrusion. Contrib. Miner. Petrol., 110: 33-45.

Received, December 5, 2019
Accepted, Dcember 30, 2019
First published online, January 3, 2020

LARGE-SCALE STRUCTURE OF THE DOLDRUMS MULTI-FAULT TRANSFORM SYSTEM (7-8ºN EQUATORIAL ATLANTIC): PRELIMINARY RESULTS FROM THE 45th EXPEDITION OF THE *R/V A.N. STRAKHOV*

Sergey G. Skolotnev*, Alessio Sanfilippo,✉, Alexander Peyve A.*, Filippo Muccini***, Sergey Yu. Sokolov*, Camilla Sani**, Kseniia O. Dobroliubova*, Carlotta Ferrando°, Nikolai P. Chamov*, Camilla Palmiotto°°, Alexey N. Pertsev°°°, Enrico Bonatti°°, Marco Cuffaro•, Anastasiya C. Gryaznova••, Konstantin N. Sholukhov°°°, Artem S. Bich••• and Marco Ligi°°**

* *Geological Institute, Russian Academy of Sciences, Moscow, Russia.*
** *Dipartimento di Scienze della Terra e dell'Ambiente, Università di Pavia, Italy.*
*** *Istituto Nazionale di Geofisica e Vulcanologia, Roma, Italy.*
° *Centre de Recherche Petrographique et Geochimique, CNRS, Vandoeuvre - Les-Nancy, France.*
°° *Istituto di Scienze Marine, CNR, Bologna, Italy.*
°°° *Institute of Ore Deposits, Petrography, Mineralogy and Geochemistry, Russian Academy of Sciences, Moscow, Russia.*
• *Istituto di Geologia Ambientale e Geoingegneria, CNR, c/o Dipartimento Scienze della Terra, Sapienza Università Roma, Italy.*
•• *Vernadsky Institute of Geochemistry and Analytical Chemistry, Russian Academy of Sciences, Moscow, Russia.*
••• *Polar Marine Geological Prospecting Expedition, Lomonosov, Russia.*
✉ *Corresponding author, e-mail: alessio.sanfilippo@unipv.it*

Keywords: *oceanic transforms; peridotite; gabbro; basalt; mantle exhumation; Mid Atlantic ridge.*

ABSTRACT

The Equatorial portion of the Mid Atlantic Ridge is displaced by a series of large offset oceanic transforms, also called "megatransforms". These transform domains are characterized by a wide zone of deformation that may include different conjugated fault systems and intra-transform spreading centers (ITRs). Among these megatransforms, the Doldrums system (7-8ºN) is arguably the less studied, although it may be considered the most magmatically active. New geophysical data and rock samples were recently collected during the 45th expedition of the *R/V Akademik Nikolaj Strakhov*. Preliminary cruise results allow to reconstruct the large-scale structure and the tectonic evolution of this poorly-known feature of the Equatorial Atlantic. Swath bathymetry data, coupled with extensive dredging, were collected along the entire megatransform domain, covering an area of approximately 29,000 km^2. The new data clearly indicate that the Doldrums is an extremely complex transform system that includes 4 active ITRs bounded by 5 fracture zones. Although the axial depth decreases toward the central part of the system, recent volcanism is significantly more abundant in the central ITRs when compared to that of the peripheral ITRs. Our preliminary interpretation is that a region of intense mantle melting is located in the central part of the Doldrums system as consequence of either a general transtensive regime or the occurrence of a more fertile mantle domain. Large regions of basement exposure characterize the transform valleys and the ridge-transform intersections. We speculate that different mechanisms may be responsible for the exposure of basement rocks. These include the uplift of slivers of oceanic lithosphere by tectonic tilting (median and transverse ridges formation), the denudation of deformed gabbro and peridotite by detachment faulting at inner corner highs, and the exposure of deep-seated rocks at the footwall of high-angle normal faults at the intersection of mid-ocean ridges with transform valleys.

INTRODUCTION

Our knowledge of the geodynamic evolution of mid-ocean ridges (MOR) relies on the idea that different sectors of an ocean ridge are separated by discontinuities oriented parallel to the direction of seafloor spreading. These are tectonically active features corresponding to oceanic transform boundaries. In a classical idea, an oceanic transform consists of a single narrow (a few km) strike-slip zone offsetting two mid-ocean ridge segments (Wilson, 1965). However, some oceanic transform domains can be locally characterized by a broad (> 100 km) and complex multi-fault zone of deformation similar to that of some continental strike-slip systems. These domains have exceptionally long age offset (up to 50 Ma), and are regarded as "megatransforms" or megatransform system (MTS) (Ligi et al., 2002). Examples of these MTS are those displacing the equatorial portion of the Mid-Atlantic Ridge (MAR) such as Romanche and St. Paul, or Andrew Bain in the South West Indian Ridge. These long transform zones display particularly complex morphologies, reflecting their evolution through time. In particular, the relative motion along MTS involves the deformation of extraordinarily thick and cold lithosphere. Following this rationale, Ligi et al. (2002) proposed that the extreme thickness of the lithosphere determines the unusual width and complex geometry of MTS. They found that long age-offset (> 30 Ma) faults produce two major symmetrical faults joining the two ridge segments, with a lens-shaped, complex and wide deformed area in between. The composite plate boundary at these locations strongly affects the main processes building the oceanic lithosphere, such as fluid circulation, mantle exhumation, mantle melting and magmatism (see also Sclater et al., 2005).

An archetypical example of megatransform is the Romanche fracture zone (FZ), where the morpho-bathymetry shows that the entire transform domain is deeper than MOR average bathymetry and that the lens-shaped deformed region is clearly bounded by two major fault systems, likely active at alternate periods (Ligi et al., 2002). The eastern Romanche ridge-transform intersection (RTI) clearly shows the effects of the lateral cooling due to the thick and cold lithosphere facing the warmer ridge segment tip: the style of spreading changes from normal to oblique and magmatism is reduced, or even absent, when approaching the transform. As a consequence, the accretionary process changes from a symmetric

rift valley at the centre of the segment to oblique asymmetric smooth-seafloor-like structures (Cannat et al., 2006) associated to a discontinuous gabbroic layer next to the RTI. Detailed geological data on the variability of volcanism in the region agree with this idea showing a general decrease in the degree of partial melting approaching the RTI (Ligi et al., 2005). Modelling of the subridge thermal structure suggests that the reason for the constipated magma production is basically due to a decrease in the along-axis thermal gradient (Bonatti et al., 1996a; 2001). Such a strong change in thermal conditions may result in a dramatic reduction of the melting region, possibly reflected in the style of seafloor morphologies. For this reason, the MAR equatorial portion has been interpreted as a major "thermal minimum", partly due to the "cold edge" effect related to the large offset transforms segmenting the ridge system (White et al., 1984; Schilling et al., 1995; Bonatti, 1996a).

North of the Romanche, the St. Paul system consists of four transform faults separated by three ITRs, offsetting the MAR by ~ 580 km and displaying a total age contrast of 40 Ma (Hekinian et al., 2000). The occurrence of these ITRs is counterintuitive, due to the high lithospheric thickness expected in the central portion of a megatransform. Hence, either active mantle upwelling or changes in plate motions towards a transtensive regime can be the driving forces for the opening of ITRs (Bonatti, 1978; Maia et al., 2016). North of St. Paul, the Doldrums MTS offsets the MAR axis for about 630 km. Although this system is arguably the most complex, including 4 ITRs and 5 transform faults, detailed bathymetric and sample analyses are confined to the westernmost sector (Fig. 1). Yet, there are few data so far on the basalts and basement rocks from this region, making the origin of this long-offset transform domain poorly constrained.

Here we report new geophysical and lithological data on a recent survey conducted during cruise S45 of the *R/V Akademik Nikolaj Strakhov* (November 2019). Multibeam data acquisition was carried out along the entire megatransform domain, covering the four ITRs for an area of approximately 29,000 km^2. Along with a preliminary characterization of > 1300 kg of rocks from 12 dredges, the new data are here used to interpret the evolution of this poorly known MTS.

GEOLOGICAL SETTING OF THE DOLDRUMS MEGATRANSFORM SYSTEM

Located in the northern portion of the Equatorial Atlantic, between 7ºN to 8º N, the Doldrums MTS displaces the MAR for about 630 km towards the east from 39.5ºW to 34ºW. Similar to other megatransforms, the Doldrums MTS defines a lens-shaped, 110 km-wide region of intense deformation. The average full spreading rate is approximately 30 mm/a (Cande et al., 1988), orthogonal to the MAR axis. Satellite-derived bathymetry and free-air gravity anomalies (Sandwell and Smith, 1997) suggest the occurrence of 3 ITRs bounded by 4 trans-

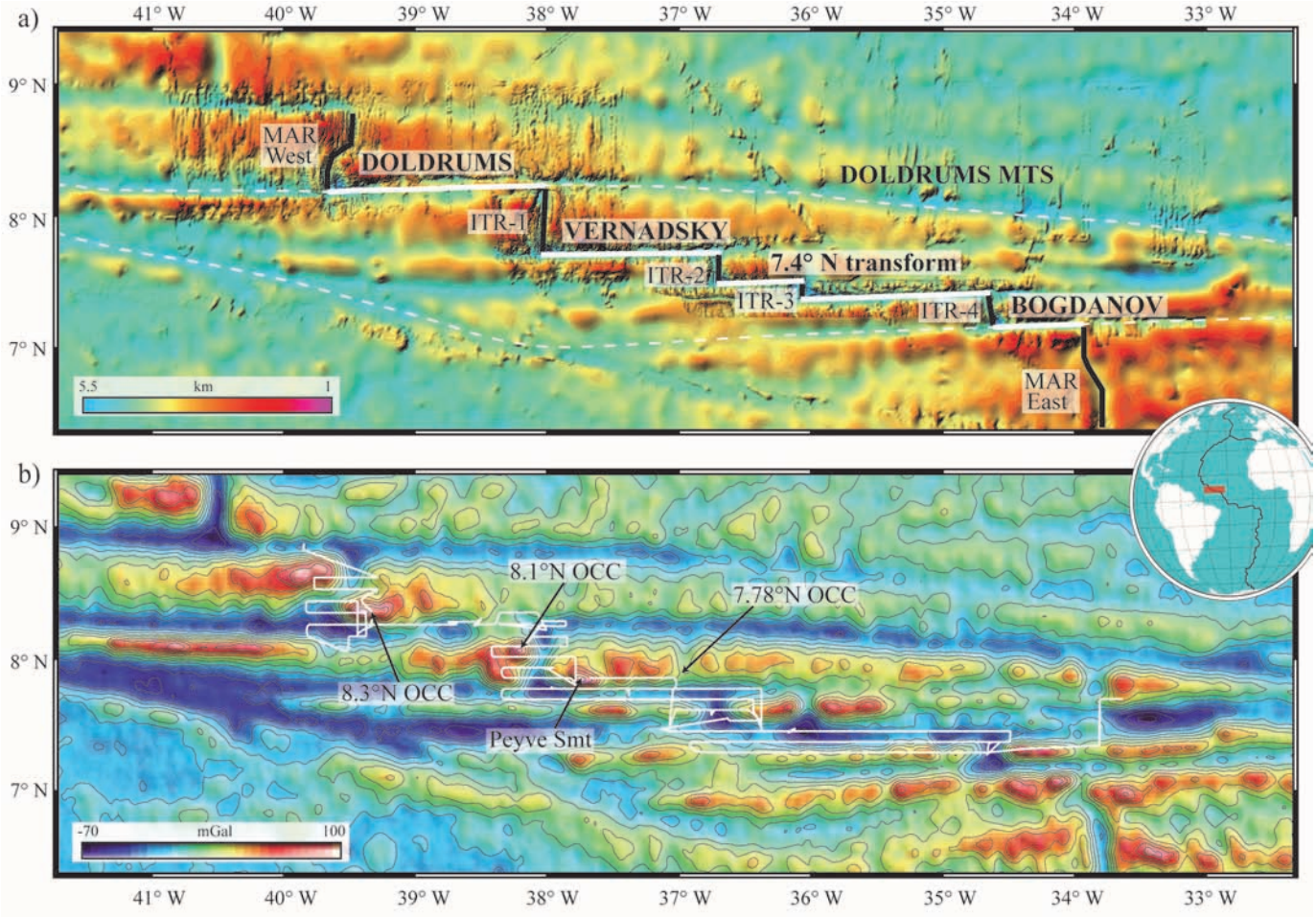

Fig. 1 - a) Doldrums MTS and associated intra-transform ridges and fracture zones offsetting the MAR superimposed upon the compilation of bathymetric data. b) Satellite-derived free air gravity field of the same area (Sandwell and Smith, 1997). Prominent structures described in the text are highlighted. Location of multibeam acquisition profiles is also indicated by white solid lines.

form valleys defined by the Doldrums, Vernadsky, 7.4ºN and Bogdanov transforms (Fig. 1). However, on closer inspection, the 7.4ºN transform may be divided in two strike-slip segments joined by a short ITR; this idea will be further confirmed by the bathymetric analyses of the present study. The length of transform offsets increases northward, reaching a maximum value of 177 km along the Doldrums transform. Considering a half spreading rate of 15 mm/a, the largest offset corresponds to an age offset of ~ 12 Ma. Previous multibeam surveys and dredge campaigns were conducted during cruises *R/V Strakhov* 6 and 9 (1987-88 and 1990) (Pushcharovsky et al., 1991; 1992). These cruises were mostly focused on the north-western portion of the Doldrums MTS and along the northern sector of the MAR, between the Doldrums and the Arkhangelsky FZs. Twenty-seven and thirteen dredges, respectively, were deployed in several locations during expeditions 6 and 9 (hereafter S06 and S09). Dredging stations span from the MAR sector north of the Doldrums FZ, to the transform valley and to the south towards the ITR-1 (Fig. 1a). More dredges were also collected along the Vernadsky transform valley and on the shallowest part of its northern transverse ridge named Peyve seamount (Fig. 1b). Fig. 2a shows the location of dredge hauls from S06 and S09 expeditions, distinguished from those collected during our new expedition on the basis of the size of the pie charts.

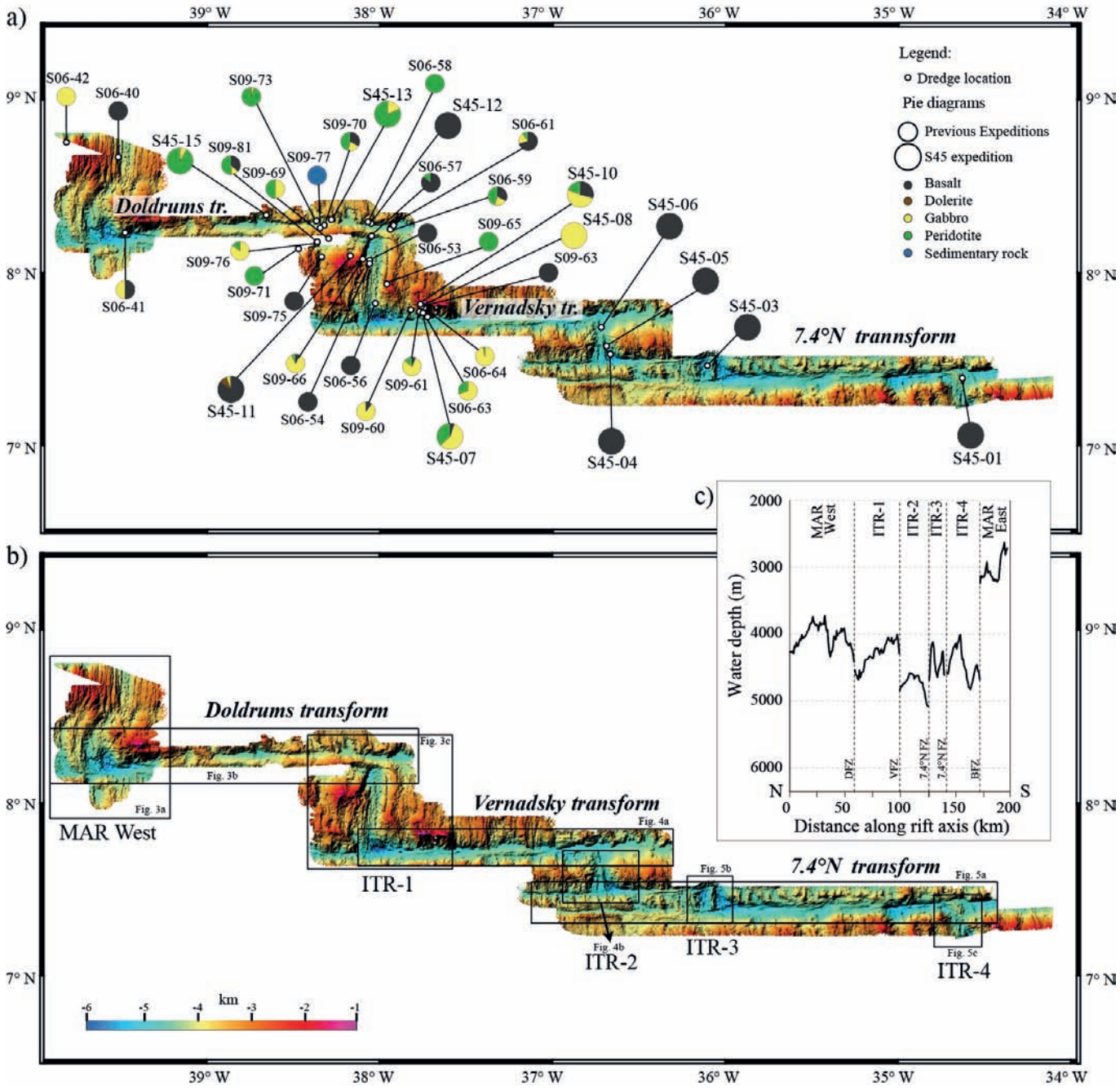

Fig. 2 - a) Shaded relief image of the Doldrums MTS obtained from swath bathymetry data acquired during the S45 expedition; grid resolution of 100 m; tr.- transform. Dredge locations from S06, S09 and S45 cruises are indicated by white dots. The pie diagrams refer to the compositional variability of lithologies (weight %) sampled in each dredge; large pie diagrams: S45 cruise; little pie diagrams: previous cruises. Locations of Figs. 3, 4 and 5 are indicated in (b). c) Axial depth profiles (direction N-S) along MAR-West, ITR-1, ITR-2, ITR-3, ITR-4 and MAR East; dotted vertical lines indicate the location of the transforms. DT- Doldrums transform; VT- Vernadsky transform; BT- Bogdanov transform.

The extensive dredging in the northern portion of the Doldrums MTS evidenced large regions of exposure of the oceanic basement along the Doldrums transform valley. This is typical of large fracture zone systems along the MAR, such as the 15°20'N (Kelemen et al., 2004), the Vema (Bonatti et al., 2005) and the Romanche FZs (Gasperini et al., 2001). One distinctive feature of the ITR-1 is, however, the occurrence of large portions of basement rocks including peridotites and deformed gabbros attributed to tectonic denudation through detachment faulting (Skolotnev et al., 2006). Here, rocks from the escarpment on the western wall of the rift valley, sampled during cruise 16 of *R/V Akademik Ioffe* in 2004, included fresh basalts and basalt breccia derived probably from the active axial volcanic ridge, along with gabbros ranging from highly deformed to severely altered. These hydrothermally altered rocks were considered as portions of the deepest zone of an active hydrothermal system located along a detachment surface.

45th EXPEDITION OF *R/V AKADEMIC NIKOLAJ STRAKHOV*

The S45 expedition was carried out by the *R/V A. N. Strakhov*, which is equipped with differential GPS and SEAPATH positioning system. Bathymetry data were acquired using the 12 kHz RESON SEABAT-8150 81P multibeam system, consisting of 234 (2° x 2°) beams with a total aperture of 150° and capable to acquire data at full ocean depth. PDS-2000 by RESON was used to acquire and process the raw data to build 100 m and 25 m cell size grids, highlighting new evidence of the large-scale tectonic fabric of this poorly known area. A sound velocity probe hull-mounted 1 m above the Sonar Head and interfaced directly to the multibeam provides the real-time water velocity at transducers required for beamforming. Sound velocity profile casts were taken twice per day to estimate the water column sound velocity and were integrated with the Levitus database. The multibeam data covered an area of about 29,000 km^2 and were collected along 18 E-W lines (total length is about 3,400 km) parallel to the five fracture zones forming the Doldrums MTS (Fig. 1). All the data presented in this work will be uploaded on a dedicated website or can be requested to the authors.

Seafloor sampling was achieved by using cylindrical dredges. Rocks collected were described on board, logged, sub-sampled and stored away; some rocks were cut and polished for thin section analyses. A total of 12 dredges out of 16 deployed in total recovered pillow basalts, dolerites, gabbroic rocks, peridotites, including tectonized varieties and sedimentary rocks. A detailed description of the dredge hauls is reported in the next sections and in Fig. 2a.

MORPHOLOGICAL CHARACTERISTICS OF THE DOLDRUMS MEGATRANSFORM SYSTEM

The morphological characteristics of the Doldrums MTS will be hereafter described from west to the east using the following terminology (see Fig. 2b). MAR West is the MAR segment approaching the Doldrums MTS from the north; ITR-1 represents the intratransform spreading centre between Doldrums and Vernadsky transforms; ITR-2 is located between Vernadsky and the northern valley of the 7.4ºN transform; ITR-3 joins the northern and southern valleys of the 7.4ºN transform; ITR-4 is located between the southern valley of the 7.4ºN and the Bogdanov transforms. We also defined other morphological features such as oceanic core complexes (OCCs) to indicate domed-shape structures related to exhumation of deep seated rocks by detachment faulting (after Cann et al., 1997).

MAR-West

The MAR segment approaching the Doldrums MTS consists of a 73 km-long rift valley subdivided by a nontransform offset into two ridge segments with different morphology (Fig. 3a). The northern segment displays a 30 km-long and 6 km-wide rift valley, with an average depth of ~ 4500 m. Its central part contains a narrow (500-800 m), 200 m-high neovolcanic ridge. Oceanic fabric typical of volcanic seafloor characterizes both sides of the rift valley, forming hills lineated perpendicular to the spreading direction. The northern and southern ends of this segment display for a length of 8-10 km a series of small (1-2 km-wide) depressions reaching a depth of 4350 m alternated to isometric highs with an average depth of 3860 m. The rift valley of the southern segment is not obvious. Its central part reaches a depth of 3950 m and then abruptly deepens to 5600 m in the nodal basin at the Doldrums ridge-transform intersection (RTI).

The eastern side of the rift valley is characterized by a dome-shaped structure hereafter called 8.3ºN OCC (Fig. 1b, 3a). This structure shows corrugations on the eastern flank defining a 30 x 35 km-wide corrugated surface. The summit reaches a depth of 1,300 m. The western side of the valley displays a prominent axial neovolcanic ridge parallel to the rift valley. This 6 km-wide volcanic ridge rises for 1,000 m above the base of the valley and extends to the south-east into the Doldrums transform (Fig. 3a).

Doldrums transform

The Doldrums transform consists of a right-lateral strike-slip fault with a length of 177 km and a width of 14-17 km. A ~ 130 km-long median ridge dissects the transform valley in its eastern sector. The median ridge is ~ 500 m high and is connected to the eastern shoulder of ITR-1. Rocks sampling during expedition S09 provided variably tectonized gabbros and predominantly peridotites (Fig. 3b, Pushcharovsky et al., 1991, 1992).

The northern wall of the Doldrums transform has a very rough topography. Its eastern sector consists of the southern terminations of abyssal hills penetrating into the transform valley with crests separated by depressions (4,500 m and 46,00 m), which likely represent old nodal basins. Dredges were deployed along the steep flanks of these structures at a distance of 185 (S45-12), 160 (S45-13) and 120 km (S45-15) from the MAR West axis. Most of these dredges recovered serpentinized and poorly deformed peridotites associated with minor Ox-bearing gabbros. Dredge S45-12 contained rounded rubbles of altered basalts with a thick Mn-coating, clearly derived from an ancient volcanic seafloor, and in agreement with the approximate age of ~ 12 Ma for the crust exposed in this sector of the fracture zone.

No bathymetric surveys were carried out along the valley to the south of median ridge in the current expedition, but its presence is confirmed by bathymetry data collected during previous cruises (S6).

Intratransform-1

The 55 km-long ITR-1 shows a symmetrical rift valley with a small (< 300 m high and 1 km wide) axial neovolcanic zone

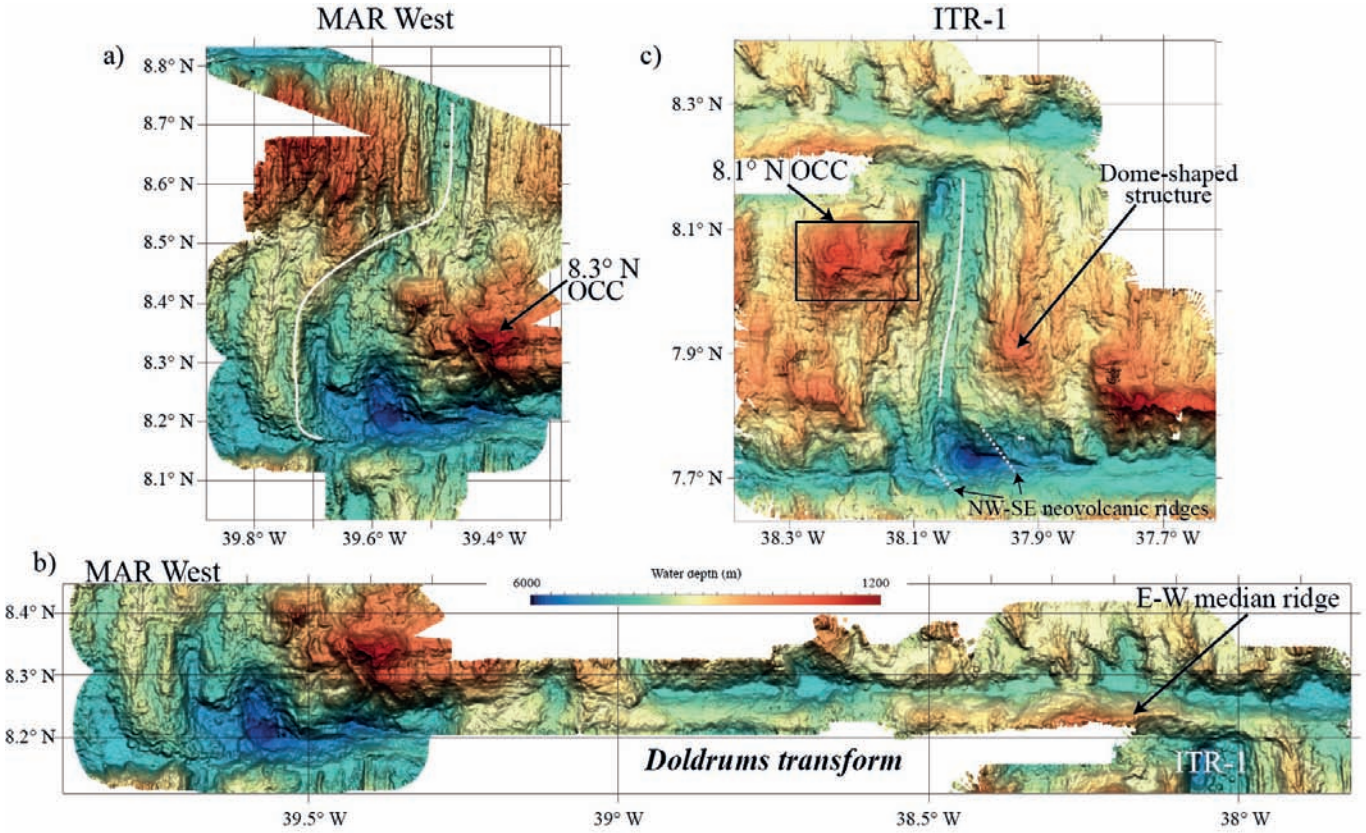

Fig. 3 - Details from the bathymetry of MAR-West (a); Doldrums transform (b) and ITR-1 (c). Structures described in the text are highlighted; white lines mark neovolcanic and axial ridges in MAR West and ITR-1, respectively.

elongated for the entire length of the ridge segment (Fig. 3c). To the north, the neovolcanic ridge is truncated by a well-developed median ridge that can be followed westwards along the Doldrums transform valley (see above). The volcanic activity appears mostly focused in the central portion of the rift valley. Here the axial valley is about 7 km-wide and 4,200-4,400 m-deep. Width and depth of the valley increase towards the south.

In the northern part of ITR-1, a dome-shaped structure, dominating the western flank of the rift valley, shows similarities with an oceanic core complex. The southern intersection with the Vernadsky transform has a large (7 × 15 km-wide) nodal basin, representing the deepest point of the entire Doldrums MTS (6,007 m). The nodal basin is flanked by prominent ridges up to 2 km wide and up to 400-600 m of relative height. The occurrence of fresh basalts dredged during S6 expedition (S06-56; Fig. 2) suggests a neovolcanic origin for these ridges. These ridges have NW-SE direction, different from the axial valley and from the N-S neovolcanic ridge in the northern part of the ridge segment. A small (diameter of 3-4 km) nodal basin, 5,100 m deep, is located at the northern RTI and on the western side of ITR-1. Dome-shaped morphologies are present also at the southern inner corner high that rises up to a depth of 2,450 m and evolves to the north into a ridge that is in continuity with the median ridge of the Doldrums transform.

8.1ºN Oceanic Core Complex

The dome-shaped structure located in the northern part of the ITR-1 in proximity of the Doldrums RTI, represents an inner corner high (Fig. 3c). This structure is elongated perpendicular to the rift valley for 25 km, has a width of 18 km and rises from the bottom of the central rift for almost 3,000 m (Fig. 3c), with a summit approaching a depth of 1,600 m. The eastern flank of the OCC is characterized by a series of listric normal faults (~ 15º) plunging to the East, whereas to the south deepens towards a linear volcanic fabric. One dredge (S45-11) recovered abundant dolerites, gabbros, serpentinite schists and few fresh basalts. According to Skolotnev et al., (2006), the occurrence of cataclastic basalts and schistose peridotites may reveal the possible occurrence of a detachment fault, although bathymetry data recently collected do not show clear evidence of a corrugated surface.

Vernadsky transform

The Vernadsky transform offsets the MAR by ~ 145 km. The transform valley has a width of 10-12 km, and depths ranging from 4,700 to 4,900 m (Fig. 4a). E-W elongated highs interpreted as median ridges are stretched parallel to the transform valley. Their width reaches 3 km and a relative height of 500 m. The northern wall of the fracture zone has a complex structure, with two local structural highs that sharply stand out from the adjacent volcanic fabric of this area: (i) Peyve Seamount (Peyve Smt) and (ii) 7.78ºN OCC. These structures will be described later. Similar to the northern wall of the Doldrums transform, abyssal hill terminations penetrate into the transform valley with crests separated by depressions, representing paleo nodal basins. Oceanic fabric on the southern wall of the Vernadsky fracture zone displays orientations varying from NW-SE to N-S. To the east, moving

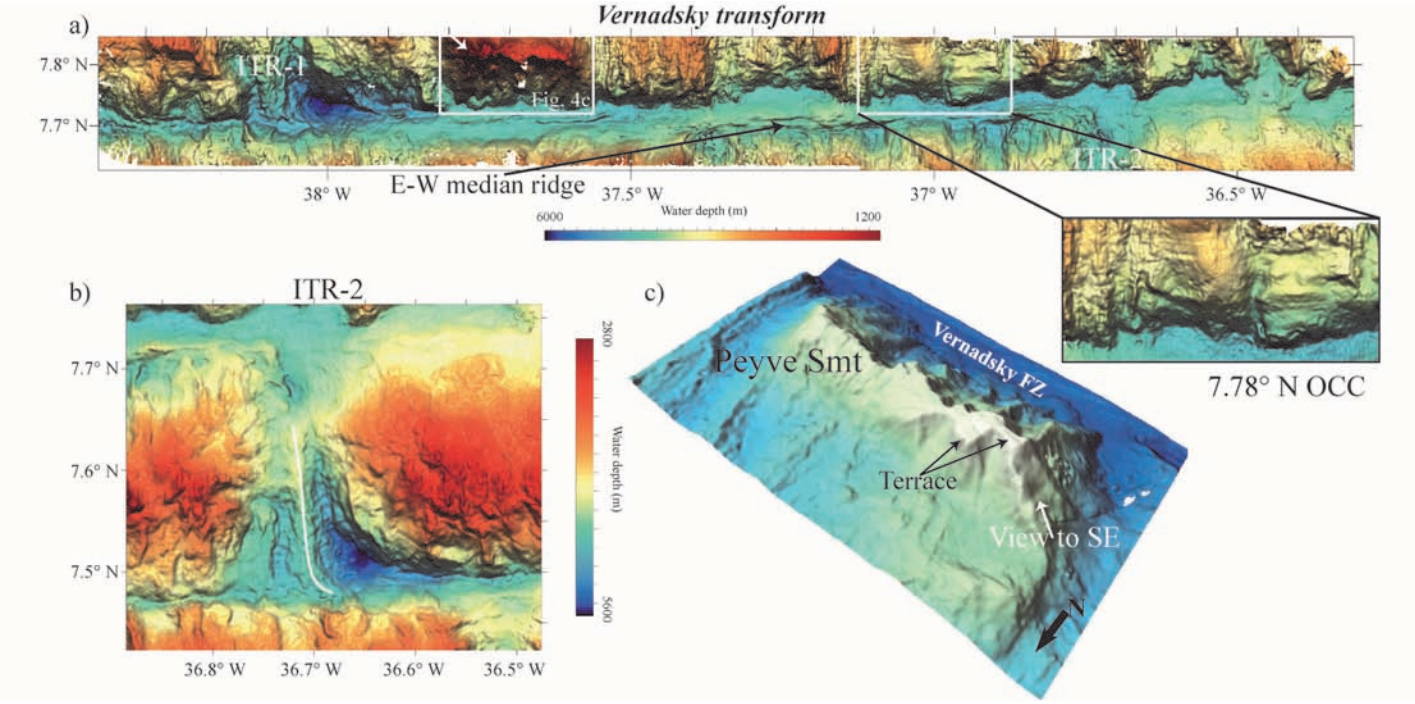

Fig. 4 - (a) Detailed bathymetry of the Vernadsky transform. The white boxes in the northern wall of the Vernadsky transform highlight the Peyve Smt and the 7.78ºN OCC. (b) Detailed bathymetry of the ITR-2; the white line marks the axial ridge. (c) Three-dimensional view from NW of the Peyve Smt. Color scale from blue (deep) to white (shallow). Note the flat top constituted by two terraces.

towards the northern ITR-2 RTI, the seafloor is composed of unusual tectonic structures probably resulting from the interaction between processes leading to abyssal hills and OCCs formation. Two of these structures are shown in Fig. 4a.

Peyve Seamount (7.8 ºN)

The Peyve Smt is a 37 km-long and 7 km-width structural high located 33 km to the east of the ITR-1 on the northern side of the Vernadsky transform (Fig. 4c). It is elongated parallel to the transform along the E-W direction with the western and eastern flanks shaped by high-angle normal faults plunging at ~ 25º. The top of the seamount is flat and it is the shallowest point of the entire Doldrums MTS (993 m) rising up to 2,700 m above the transform valley floor. The Peyve Smt does not have any corrugated surface and according to its structural position and morphology may be regarded as a part of the northern transverse ridge of the Vernadsky transform. The flat summit may result from erosion at sea level.

Three dredges, deployed on the southern slope and at the top of the seamount, recovered prevalently gabbros and minor peridotites. The south slope is characterized by variably deformed gabbros (from porphyroclastic to ultramylonitic) ranging from moderately primitive (Ol-bearing) to highly evolved Ti-Fe oxide-gabbros. Cataclastic peridotites and gabbros were recovered at the top of the structure. Massive basalts were also collected at station S45-07 and more copiously at S45-10. Recovered lithologies recall those of the samples collected during expeditions S06 and S09 (Fig. 2a).

7.78ºN Oceanic Core Complex

Along the northern wall of the Vernadsky transform, ~ 130 km to the east of ITR-1, an oceanic core complex exposes a ~ 20 km-long and 8-km wide corrugated surface (Fig. 4a). Corrugations are elongated parallel to the transform valley and are interrupted by deep scars as a result of subsequent high-angle normal faulting. The termination area deeps towards the west with an angle of ~ 6º below a zone of linear hills oriented perpendicular to the spreading direction and regarded as the original volcanic hanging wall. The size and the structure of the corrugated surface recall those of the Kane megamullion nearby the Kane ridge-transform intersection at 23º 30'N along the MAR (Dick et al., 2008).

Intratransform-2

The ITR-2 is a 27 km-long symmetrical ridge segment with a robust volcanic activity. A huge neo-volcanic ridge (~ 500 m high and 15 km long) is located in the central and in the southern parts of the rift valley, near its western side, extending southward into the valley of the 7.4º N transform (Fig. 4b) where the ITR-2 displays a deep nodal basin (width of 4 × 10 km) that reaches a depth of 5,720 m. Width and depth of the rift valley increase towards the south from 6 to 12 km and from 4,600 to 5,000 m, respectively. Western and eastern flanks (3,100-3,200 m) of the rift valley are uniform with no evidence of typical oceanic fabric or corrugated surfaces. Three dredges were deployed on the eastern rift shoulder where fresh basaltic glasses were recovered in the southern part (S45-04; S45-05), whereas partly altered basalts occurred in the northern sector (S45-06).

7.4º N transform

The 7.4º N transform fault consists of two active dextral strike-slip zones joined by a very short intratrasform spreading segment (ITR-3, Fig. 5a). The total length of the transform offset is 186 km. The northern transform valley is 5-6 km wide and 4,500-4,700 m deep, whereas the southern tranform valley is 7-8 km wide and 4,500-4,900 m deep. The northern wall of 7.4ºN transform, to the east of ITR-2, is characterized

by sigmoidal hills oriented NW-SE that turn WNW-ESE approaching the transform valley. Similar but more spectacular structures develop for nearly 60 km also to the east of ITR-3, where the seafloor is affected by several small sigmoidal hills (500-700 m-high) separated by parallel depressions oriented NW-SE that, close to the intersection with the transform valley, turn counter clockwise toward the WNW-ESE direction. Small sigmoidal ridges occur to the west of ITR-3 extending over a narrow band of ~ 20 km. Straight ridges with similar strike are distributed further to the west of ITR-3.

The southern wall of the 7.4ºN transform shows a distinct fabric. In particular, over a distance of ~ 25 km to the west of ITR-4, we identify three abyssal hill crests striking N-S (500-700 m-height and 5-6 km-wide) separated by narrow parallel depressions. Further to the west there is a region of 70 km where isometric structures can be regarded as OCC. Two en-echelon E-W oriented transverse ridges run more further to west between 36.25 W and 36.90 W. The largest of these ridges is 2-3 km wide and about 42 km long, and has a relative height of 700 m. Further to the west there is a region of ~ 70 km where isometric structures can be regarded as OCC (Fig. 5).

Intratransform-3

ITR-3 is located in the deepest part of the Doldrums MTS. It is a short (16 km-long) intra-transform ridge segment with a prominent (~ 1,200 m-high) neovolcanic ridge extending for the entire length of the ITR and into the transform valleys (Fig. 5b). The rift valley is very wide reaching 17 km in width. Depths range from 5,000 to 5,400 m. The rift flanks are characterized by small sigmoidal structures that generally are not shallower than 4,000 m. These sigmoidal structures are oriented NW-SE and are most prominent in the SE section of the ridge axis. At both ends of axial region, two depressions with a complex morphology represent the nodal basins with a depth of 5,590-5,660 m. The axial neovolcanic ridge strikes N-S, orthogonal to the transforms. The overall sigmoidal shape of ITR-3 recalls geometries of a pull-apart basin. One dredge, deployed on the western flank of the axial valley, recovered fresh basalts and volcanic glasses.

Intratransform-4

ITR-4 is 35 km-long and 15 km-wide spreading segment with bottom depth increasing southwards from 4,350 m to 5,050 m, and then abruptly decreasing towards the nodal basin (Fig. 5c). The axial valley is dominated by a ~ 1,000 m-high and ~ 20 km-long neovolcanic ridge located prevalently in the northern sector of the ridge segment. This neovolcanic ridge strikes along the NW-SE direction and extents northwards into the transform valley, where a nodal basin is absent. Dredging along the eastern flank of this volcanic ridge provided fresh pillow basalts with glass (S45-01). The rift valley is flanked to the east by a dome-shaped structure that reaches a water depth of 2,600 m and that most likely may represent an OCC. The western side of ITR-4 displays N-S oriented oceanic fabric. Finally, towards the south, the Bogdanov transform valley is dissected by an E-W elongated median ridge (previously mapped during expedition S22). This median ridge extends over the entire transform sector and intersects the prominent axial neovolcanic ridge of the MAR East.

GEOPHYSICS

Seismicity

In order to better define the present-day tectonic and magmatic activity over the entire Doldrums MTS, we carried out an analysis on seismicity based on instrumental recorded earthquakes occurred in the region. Earthquake parameters from January 1972 to December 2018 were obtained from the US Geological Survey Earthquake Catalogue (USGS). A total of 451 "reviewed" events with magnitude $M_w > 3$ were gathered after converting different magnitudes types to momentum magnitude M_w adopting strategies and magnitude conversion formulas suggested by Lolli et al. (2014). Seismicity within the Doldrums MTS generally follows the typical distribution of slow spreading ridges with earthquake epicenters clustered along mid-ocean ridge segments and transform faults (Fig. 6). However, the seismicity distribution along the five transform faults and the four ITRs of the Doldrums MTS presents unusual peculiarities.

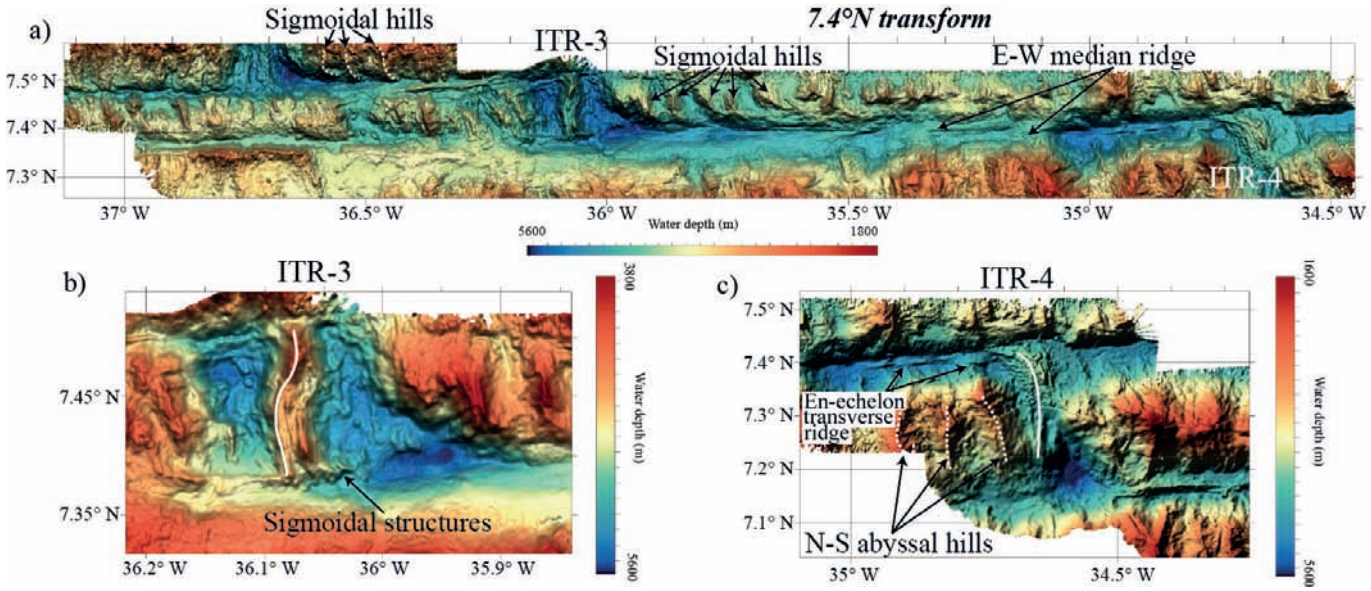

Fig. 5 - Detailed bathymetry of the 7.4ºN transform (a) ITR-3 (b) and ITR-4 (c). Structures described in the text are highlighted; the white lines mark the axial ridges in ITR-3 and ITR-4.

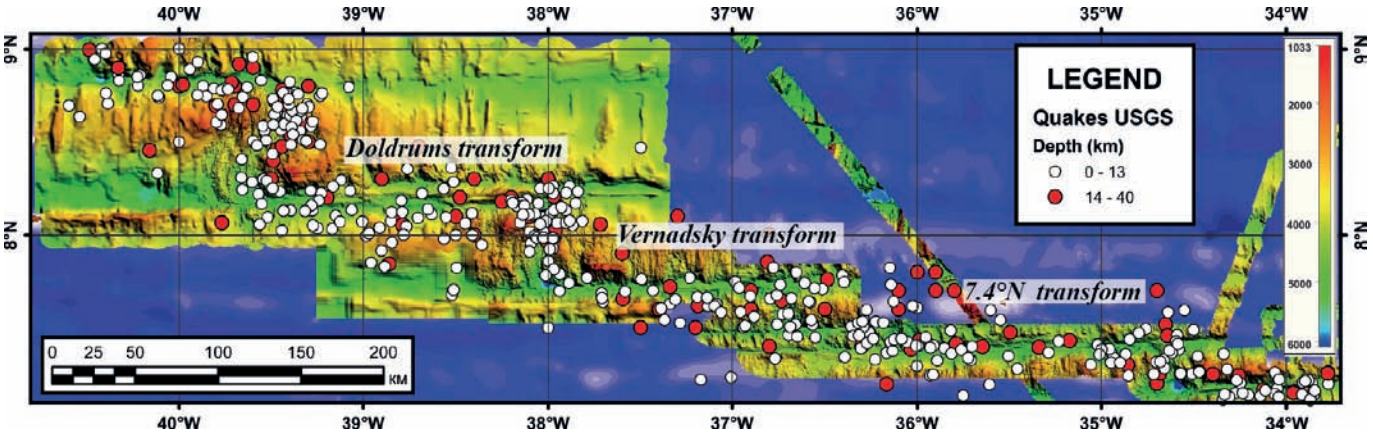

Fig. 6 - Seismicity of the Doldrums MTS region (from USGS earthquake catalogue) superimposed on multibeam bathymetry collected during S06, S09 and S45 expeditions of *R/V Akademik Nikolaj Strakhov* (1987-2019).

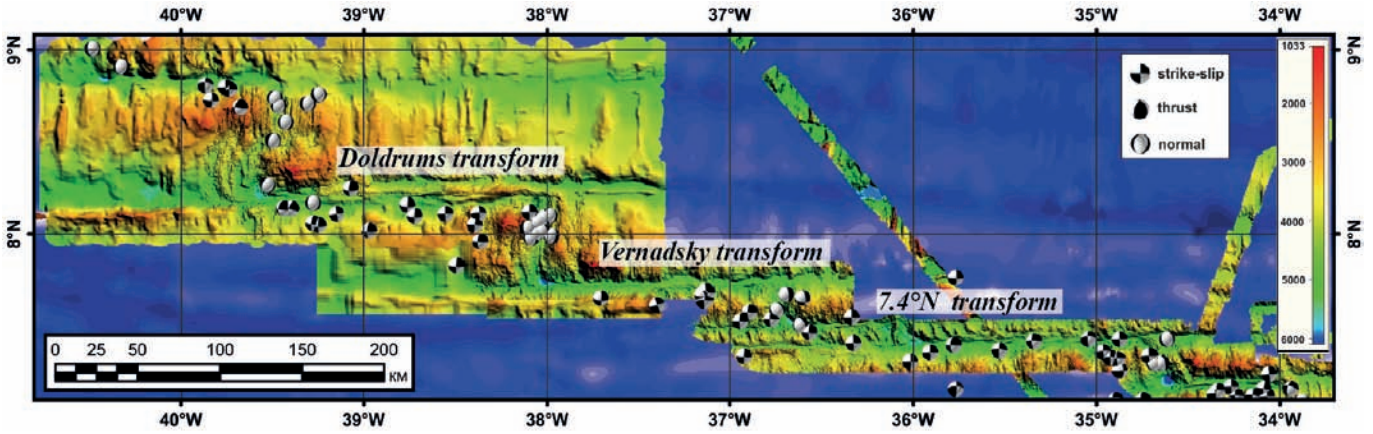

Fig. 7 - Harvard CMT focal mechanisms superimposed on multibeam bathymetry collected during S06, S09 and S45 expeditions of *R/V Akademik Nikolaj Strakhov* (1987-2019).

The USGS catalogue reports on only 10 events with magnitude $M_w \geq 6$ to have occurred in this region, mostly distributed along the transform faults. Focal mechanisms from the global Centroid Moment Tensor (CMT) catalogue show right-lateral strike-slip movements on near vertical E-W striking fault planes (Fig. 7). Seismicity along transform faults depends on the offset length and slip rate and the maximum magnitude of earthquakes scales with it (Boetcherr and Jordan, 2004). Although the Doldrums MTS transforms have similar slip rates and offset lengths, most of these large events occurred along the southern valley of the Doldrums transform where the largest event in the region with a magnitude M_w of 7.0 took place on November 1st, 1984. This suggests that the present day Doldrums principal displacement zone is within the southern valley and that the Doldrums transform is seismically the most active strike-slip fault in the region.

Along the axial valleys and flanks of ITRs lower magnitude seismic events ($M_w < 6$) occur with the exception of a large event with magnitude $M_w = 6.1$ that took place on the eastern flank of the dome-shaped northern inner corner high of ITR-1 (8.1°N OCC). Fault plane solutions from the CMT database suggests normal faulting trending perpendicular to the seafloor spreading (Fig. 7). Seismicity distribution along the axis of ITRs shows a strong asymmetry with the large number of events clustered at the northern ridge-transform intersections. The observed poor seismicity at the southern parts of intratransform spreading segments with the occurrence of corner highs and OCC along their eastern flanks, suggest that serpentinized upper mantle rocks may reduce the ability of stress accumulation, thus decreasing the number of detectable earthquakes.

Gravity Bouguer anomalies

Bouguer gravity anomalies from the WGM2012 grid (Balmino et al., 2012) are shown in Fig. 8 together with the 3,000 m contour line in order to highlight the main bathymetric features of the region. The WGM2012 Bouguer grid includes gravity corrections aimed at remove the effect of the water layer using a crustal and water density of 2,670 and 1,027 kg/m^3, respectively.

Negative Bouguer anomalies are centered along the major transform valleys, in particular, along the Arkhangelsky and the Vernadsky fracture zones suggesting relatively low-density rocks beneath transforms due to sedimentation and/or hydrothermal alteration of basement rocks including ultramafics serpentinization. Positive anomalies are centered mostly at inner corner highs, in particular at those where corrugated surfaces were observed suggesting exhumation of high-density deep-seated rocks at oceanic core complexes. However, gravity minima are also centered above some inner highs such as those located at the eastern RTI of the Arkhangelsky and

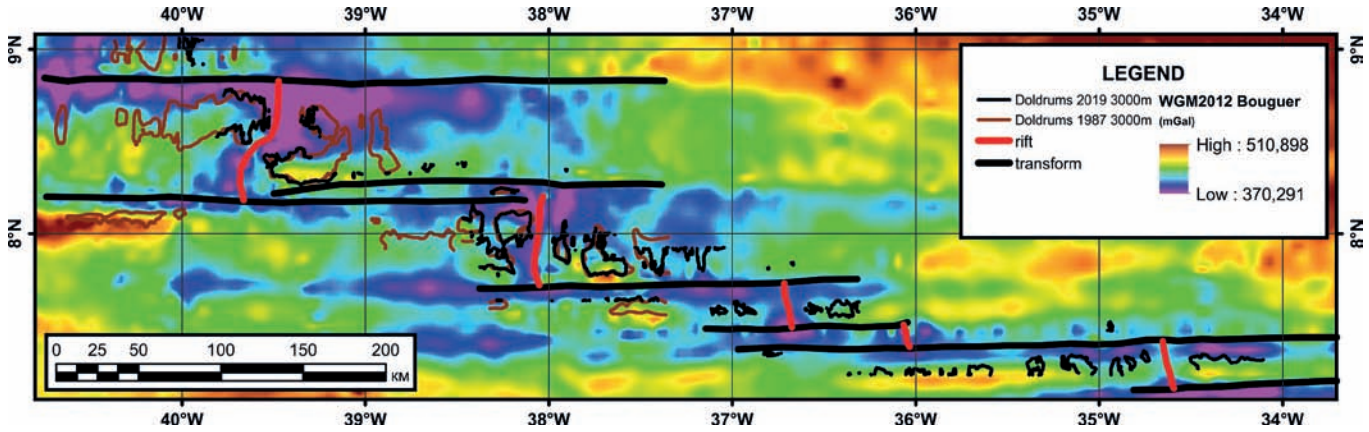

Fig. 8 - WGM2012 Bouguer anomalies and the 3000 m contour line (thick solid line) delineating the main structural features of the area.

the Doldrums transforms, probably related to a relative thick crust due to intense basaltic magmatism (Fig. 8). The western inactive part of the Doldrums fracture zone contains topo-gravity features similar to those observed in other transverse ridges such as that of Vema (Bonatti et al., 2003), although gravity anomalies are not very high on the southern flank of the transform valley.

LITHOLOGIES

During S45 we collected ~ 1,300 kg of rocks in 12 dredges deployed in different locations along the entire Doldrums MTS. Lithological proportions by weight are reported in Table 1 and in pie diagrams (Fig. 2a). Dredge hauls include basalt (~ 60 wt%), dolerite (~ 1 wt%), gabbro (~ 20 wt%) and peridotite (~ 19 wt%) (Fig. 9a). Few samples of sedimentary breccia and limestone were also recovered (< 0.5%). In the following sections we summarize rock descriptions divided per lithology.

We estimated mineral modal contents to define lithologies, and in basalts we defined vesicularity and phenocryst contents. Fresh glass and iron-manganese coating thicknesses were also measured. We used the semiquantitative scales from IODP Expedition 360 (MacLeod et al., 2017) to record the extent of alteration, and the crystal-plastic deformation and brittle intensities. Crystal-plastic deformation intensity was quantified based on the foliation, grain size, and relative proportions of neoblasts and graded from undeformed (grade 0) through clearly foliated (grade 2) to porphyroclastic (grade 3), mylonite and ultramylonite (grade 4 and 5, respectively). Brittle deformation was recorded from undeformed (grade 0), through fractured (grade 1), brecciated by numerous cracks without clast rotation (grade 2), densely fractured (grade 3), and well developed fault brecciation (grade 4) and cataclastic with grain size reduction > 70% (grade 5).

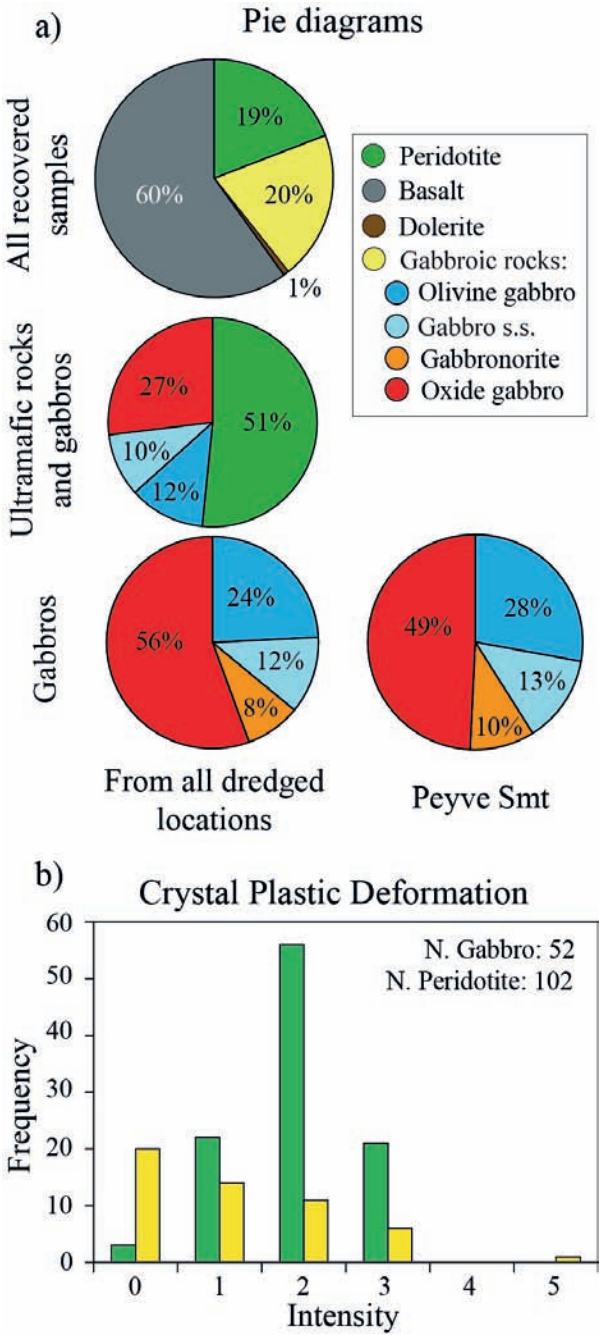

Fig. 9 - Lithology proportions and intensity of deformation for rocks recovered during the S45 cruise. a) Lithological proportion of S45 rocks (wt.%); from top to bottom we report the pie-chart diagrams of: all recovered samples, ultramafic rocks and gabbros, and all gabbros. The proportion of gabbros from the Peyve Smt is also shown separately. b) Semiquantitative evaluation of the crystal-plastic deformation intensity for S45 gabbros and peridotites based on ship-based observation.

Table 1 - Location and general description of dredges deployed during the S45 expedition.

Dredge	Location of dredging	On Bottom			Off Bottom				Contents (%)						Weight (kg)
		Latitude [°N] (dd.ddd)	Longitude [°W] (dd.ddd)	Water depth (m)	Latitude [°N] (dd.ddd)	Longitude [°W] (dd.ddd)	Water depth (m)	Full (V) Empty (X)	Peridotite	Gabbro	Dolerite	Basalt	Breccia	Limestone	
S45-01	East flank of ITR-4	7.355	34.653	4430	7.357	34.652	4400	V				100			250
S45-02	East shoulder of ITR-4	7.287	34.623	4800	7.29	34.593	3700	X							
S45-03	West flank of ITR-3	7.463	36.107	5500	7.475	36.077	4160	V				100			50
S45-04	East shoulder of ITR-2	7.53	36.668	5600	7.535	36.653	4950	V				100			100
S45-05	East shoulder of ITR-2	7.577	36.69	5125	7.578	36.683	4990	V				100			35
S45-06	East shoulder of ITR-2	7.685	36.72	4960	7.683	36.717	4900	V				100			40
S45-07	South flank of Peyve	7.768	37.752	3800	7.76	37.773	3400	V	37	58		4	1		350
S45-08	Top of Peyve	7.807	37.76	1950	7.803	37.762	1900	V		100					5
S45-09	East flank of ITR-1	7.962	38	4250	7.987	37.992	3700	X							
S45-10	Top of Peyve SM	7.818	37.767	1100	7.822	37.762	1040	V	19	52		29			80
S45-11	North flank of 8.1°N OCC	8.098	38.172	3000	8.092	38.177	2570	V	1	5	9	85			250
S45-12	North wall of Doldrums FZ; 185 km from active ridge	8.285	38.052	4100	8.3	38.052	3600	V				98	2		10
S45-13	North wall of Doldrums FZ; 160 km from active ridge	8.308	38.282	3850	8.307	38.285	3770	V	81	18		1			100
S45-14	North wall of Doldrums FZ; 135 km from active ridge	8.287	38.503	3700	8.31	38.482	3230	X							
S45-15	North wall of Doldrums FZ; 120 km from active ridge	8.333	38.658	3160	8.335	38.657	3150	V	91	8				1	70
S45-16	North wall of Doldrums FZ; 35 km from active ridge	8.24	39.403	4600	8.247	39.402	4200	X							

Basalt and dolerite

Based on preliminary evaluations dredged basalts were divided into three groups: (i) fresh, (ii) tectonized (mainly cataclastic) and (iii) basalts that went through substantial low temperature alteration.

Fresh basalt fragments are mainly angular and represent parts of pillow-lavas. Glass rims are fresh or slightly palagonitized and sometimes covered by thin Fe-Mn coating. Intact pillow basalts (Fig. 10a) and basaltic flows were recovered along the axial neovolcanic ridges of the intra-transform ridge segments, i.e, ITR-4 (dredge S45-01), ITR-3 (dredge S45-03) and ITR-2 (dredge S45-05 and S45-06). Fresh basalts were also collected on 8.1°N OCC (Dredge S45-11). Most basalts are aphyric to sparsely phyric (< 2% phenocrysts), and less than 20% are phyric (15-20% phenocrysts) with typically a microcrystalline matrix. Ol and plagioclase (pl) are present as phenocrysts in variable modal contents. Sparsely phyric basalts from dredge S45-11 are characterized by < 2% clinopyroxene (cpx) phenocrysts. Vesicularity is overall less than 5% by volume, with few samples showing up to 15% of vesicles. Fresh basalts display preserved glass from 2 to 20 mm in thickness.

The second group of basalts contains chlorite and generally displays evidence of incipient brittle deformation that locally develops to a cataclastic fabric with angular clasts of fractured basalts cemented by quartz (Fig. 11a). Tectonized basalts were collected at dredge S45-11 on the 8.1ºN OCC.

Basalts with low temperature mineralizations contain smectites, Fe-hydroxides and thick Fe-Mn crust (up to 30 mm). Altered basalts were mainly found at the northern wall of the Doldrums transform valley in dredge S45-12. This dredge was deployed at ~ 180 km from the MAR-West axis and at an approximate age of ~ 12 Ma. Thus, due to a long exposure time at seafloor, these basalts have been significantly modified by seawater interaction.

Dolerites were exclusively recovered at dredge S45-11 on the 8.1°N OCC. These rocks are identified based on the occurrence of a visible crystalline matrix, presenting a subophitic texture and locally including sporadic pl phenocrysts (Fig. 10b). All dolerite samples are altered as defined by the substitution of the original cpx by chlorite and pl by epidote and albite. Some samples are entirely replaced with hydrothermal minerals, also containing > 1 vol% of fine-grained disseminated pyrite (0.5-2.0 mm).

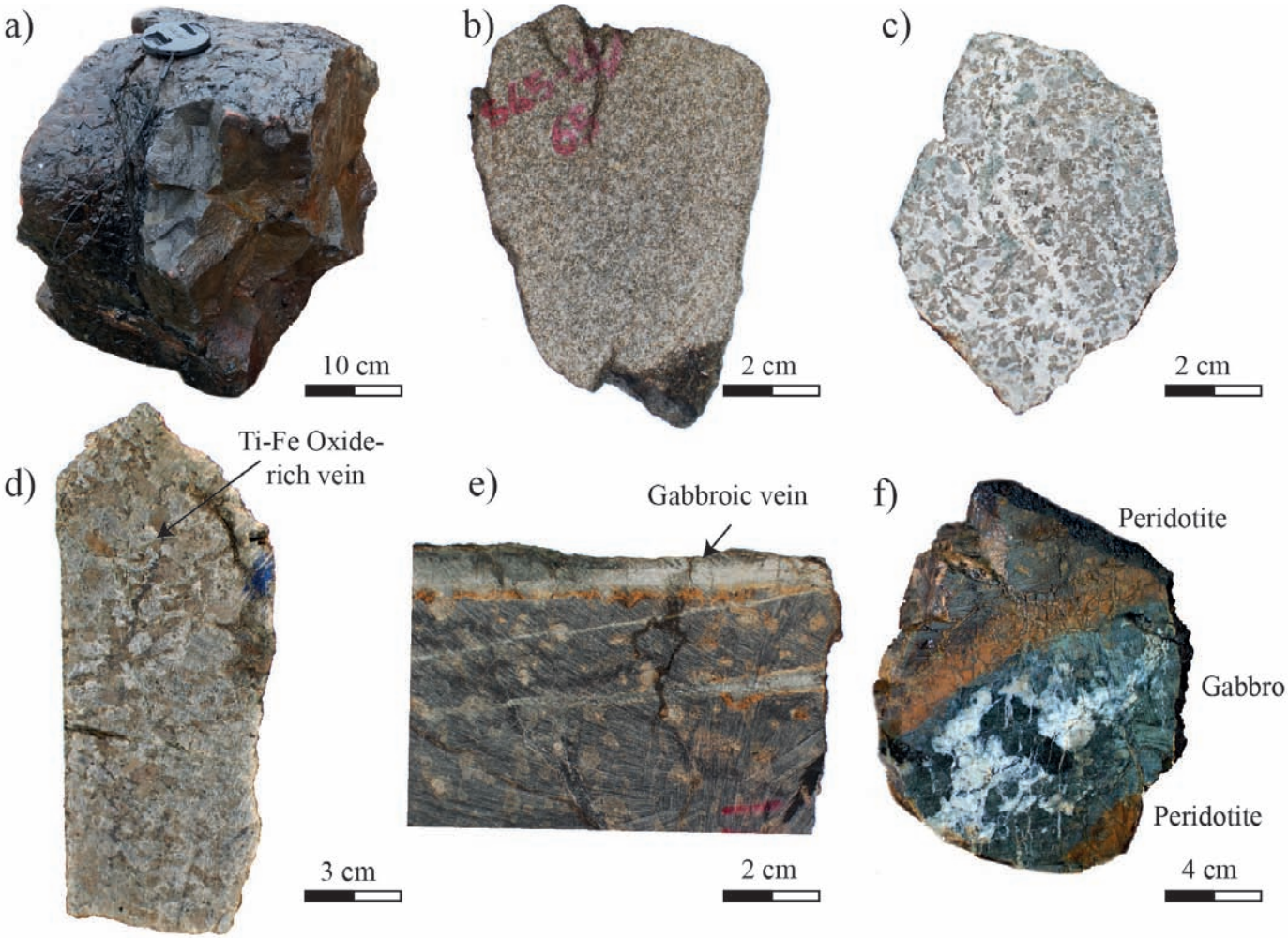

Fig. 10 - Photographs of S45 expedition samples showing the main lithologies. (a) sample S45-04/1 - fresh pillow lava from the east rift shoulder of the ITR-2. (b) sample S45-11/65- medium-grained dolerite from the 8.1°N OCC. (c) sample S45-7/18- medium-grained Ol-gabbro with sub-ophitic texture. (d) sample S45-15/15- oxide-gabbro exhibiting Fe-Ti-Ox rich patches organized in microveins from the Peyve Smt. (e) sample S45-13/1- coarse-grained partly serpentinized peridotite crosscut by two parallel gabbroic veins from the northern wall of the Doldrums transform. (f) sample S45-13/22- peridotite crosscut by a oxide-gabbro vein (~7 cm). Note that the contact between the vein and the peridotites is marked by a pyroxene-rich layer (~2 cm-thick).

Gabbro

Collected gabbros cover three principal varieties consisting of Olivine-gabbro (olivine, Ol > 5%), gabbro *sensu stricto* (Ol < 5%; Ti-Fe oxides, Ox < 2%), gabbronorite (orthopyroxene [opx] > 5%) and Fe-Ti-Ox gabbro (Ox > 2%) (Fig. 9). They have a bimodal distribution, with nearly 25% of relatively primitive Ol-gabbro and > 50% of evolved oxides-gabbro. Ol-gabbros and gabbro *s.s.* have granular to subophitic textures, and are mostly medium-grained (Fig. 10c). Large cpx and, more rarely, Ol oikocrysts containing pl chadacrysts locally occur within the subophitic gabbro. Ol ranges from partly serpentinized showing the typical mesh texture, to largely preserved and altered by clay minerals. Opx in gabbronorite has granular habit and is often replaced by a fine-grained assemblage of clay minerals. Fe-Ti oxides in oxide-gabbros occur as veins or discrete patches (Fig. 10d) locally forming cm-scale Ox-rich streams. Felsic veins are common within the samples, mostly limited to mm-scale veins with sharp straight boundaries. In few cases felsic intrusions reach 2 cm in thickness and reveal the occurrence of interstitial amphibole and minor quartz. Fig. 11d shows a felsic vein intruding a slightly deformed Ol-gabbro. At the contact between the two rock-types, the Ol-gabbro is pervaded and partly disrupted by the felsic material and amphibole coronas develop around the pre-existing pyroxene, evidence of chemical interactions at high temperature. This reaction front can reach a thickness of 4 cm.

Most gabbros are tectonized to different extent. Deformation ranges from crystal plastic deformation (Fig. 9b) to low-temperature cataclasites (< 5%). Plastically deformed gabbros range from weakly deformed (Fig. 11b) to ultramylonitic (Fig. 11c). They are defined by mm-scale porphyroclastic pyroxene and pl mantled by neoblastic assemblages most likely made up of the same minerals. Amphibole veins are widely observed in deformed gabbros. These features suggest a high-temperature deformation event likely occurred under the granulite-facies conditions. One sample (S45-07/16) shows

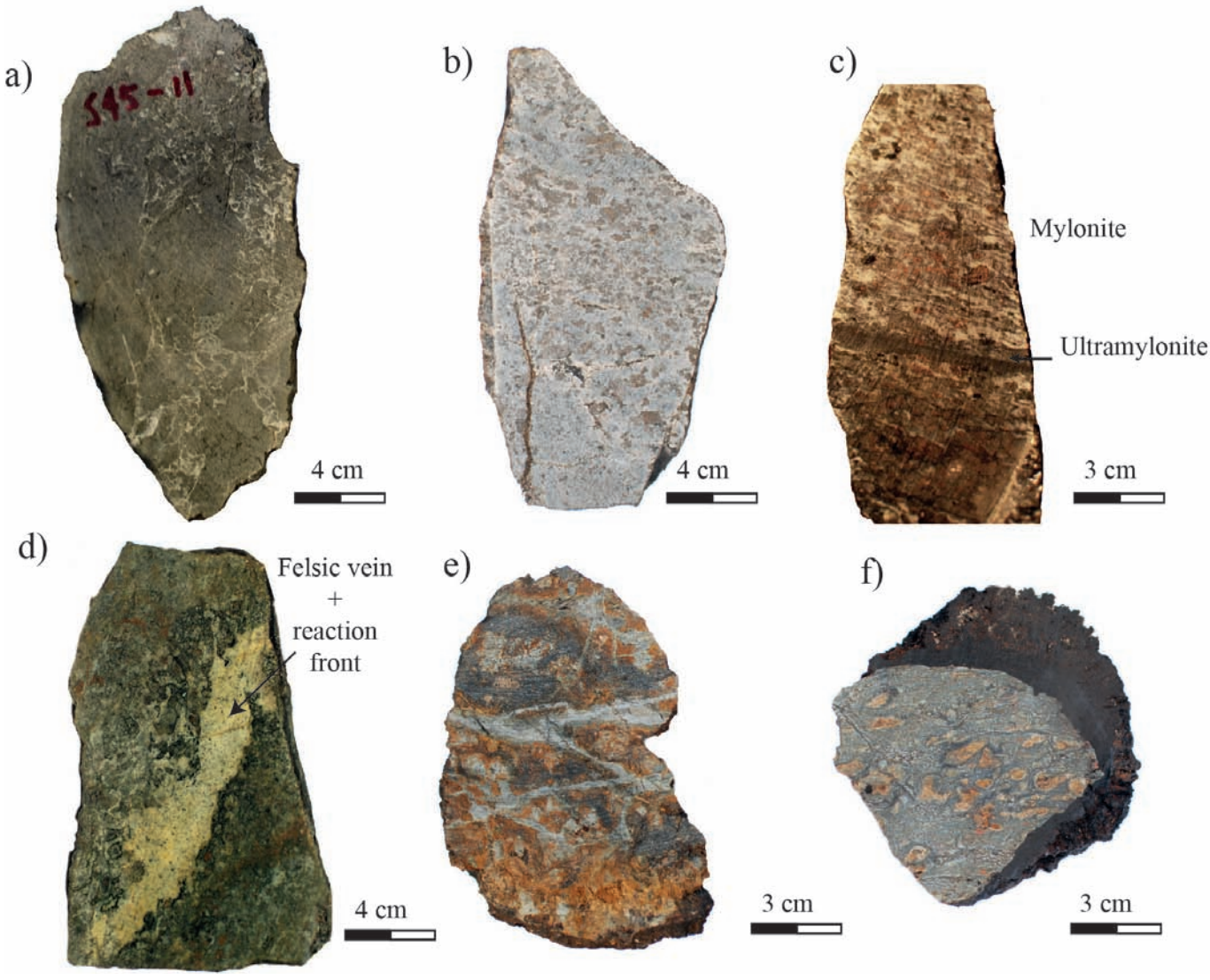

Fig. 11 - Photographs of variably tectonized S45 samples. (a) sample S45-11/82- basalt cataclasite cemented by quartz veins from the top of 8.1°N OCC (b) sample S45-07/22- coarse-to medium-grained gabbro weakly deformed under high temperature conditions. (c) sample S45-7/16- High temperature deformation gradient in gabbro showing a localization of the deformation from mylonitic to ultramylonite band; Peyve Smt. (d) sample S45-10/2- deformed Ol-gabbro intruded by plagiogranite vein (~ 3cm) (Peyve Smt.). (e) sample S45-15/8- deformed peridotite with a dense network of fractures filled by basaltic material with microcrystalline texture. (f) sample S45-13/27- foliated peridotite mainly serpentine and covered by a thick Mn-coat from northern wall of the Doldrums transform.

a characteristic deformation gradient from porphyroclastic to mylonitic with a sharp contact with an ultramylonitic level (5 mm) (Fig. 11c), evidence for the localization of deformation at high temperature conditions. Deformed gabbros are mainly found in association with peridotites at the 8.1°N OCC (Dredge S45-11) and at the Peyve Smt (Dredges S45-07, 10). These rocks were also found in some dredges along the northern wall of the Doldrums transform (S45-13 and S45-15).

The most representative collection of gabbros was dredged on Peyve seamount. Fe-Ti oxide gabbro varieties (35%) in association with plagiogranite veins of different size and shape along with isotropic Ol- to Ol-free gabbro (5% and 17%, respectively) were found on this seamount. Such associations are typical of lower crust exposed at ridge-transform intersections along slow-spreading ridges (e.g., Dick et al., 2019), as well as at the dike-gabbro transition at fast spreading ridges such as the ODP Hole IODP 1256D (Pacific Ocean; Teagle et al., 2006).

Peridotite

Harzburgites are the most common lithology among peridotites, but minor dunites are also present. Peridotite minerals are widely replaced by serpentine as effect of seawater interactions likely occurred at temperature < 500ºC, and depths that close to the RTI can reach 15 km (Boschi et al., 2013). A minor amount of samples shows replacement of the original phases by clay minerals, classically attributed to superficial weathering. Collected peridotites record crystal plastic deformation with mainly porphyroclastic texture (Figs. 9b, 11f). Pyroxenite and gabbroic veins (ranging from gabbro to leucocratic in composition) are found in some peridotites. Gabbroic veins locally reach 10 cm in thickness and contain abundant Fe-Ti Ox (Fig. 11f). The occurrence of mafic veins indicates different events of melt migration and interaction with the lithospheric mantle. Peridotites are mainly found on the Peyve seamount, on 8.1°N OCC (Dredge S45-11, serpentine schists) and along the northern slope of Doldrums transform. These peridotites are always associated with gabbros, including deformed gabbros. Along the northern wall of the Doldrums transform we sampled peridotites at different distance eastward from the MAR west. Further studies will allow us to investigate mantle composition variations with time revealing differences in melt production.

Sedimentary rocks

Few sedimentary rocks were collected at OCC 8.1°N (S45-11) and along the northern wall of the Doldrums transform (S45-15). They represent the tectono-sedimentary products of erosion and tectonic disruption of seafloor. Sedimentary rocks consist of polymictic breccia containing clasts of basalts, gabbros and serpentinized peridotites cemented by pelagic carbonates or by a silty matrix. Poorly sorted sandstones were also collected.

DISCUSSION

General architecture of the Doldrums megatransform system

The combination of data from previous expeditions S06 and S09 with those obtained during S45 allows us to present for the first time the large-scale structure of the Doldrums MTS. The bathymetric analysis confirms a complex architecture with five dextral transform faults subdivided by four active ITRs. All the transform faults are characterized by median ridges with variable width and length, subdividing the transform valleys. Strike-slip earthquake epicenters concentrate along the transform faults and their distribution suggests southward migration of the principal displacement zone of the Doldrums transform (Figs. 6 and 7). The location of ITRs is confirmed by the occurrence of seismic clusters with normal focal mechanisms along the rift shoulders and by the occurrence of neovolcanic axial ridges. We are confident that the so-far unknown large-scale structure of the Doldrums MTS is now better defined.

One fundamental observation is that each ITR is characterized by different morphological features, suggesting a large variability in the tectonic conditions within this megatransform domain. The peripheral rift segments (i.e., ITR-1 and ITR-4) represent the shallower portions of the Doldrums MTS, whereas those located in the central part are substantially deeper (Fig. 2c). Considering that the axial depth of MOR is assumed to be dependent on the thermal conditions of the subridge mantle (Klein and Langmuir, 1987), this would imply a lower mantle temperature for the internal portion of the Doldrums MTS, or an overall transtensive regime in this megatransform system. We must note, however, that the neovolcanic ridges of ITR-2 and ITR-3 are characterized by large and high axial volcanic ridges, while ITR-1 and ITR-4 are characterized by large rift valleys and small axial volcanic ridges. The occurrence of prominent axial ridges formed by fresh pillow basalts is indicative of a strong magmatic production within ITR-2 and ITR-3. Indeed, the highest points of ITR-2 and ITR-3 locally reach the elevation of ITR-1 and ITR-4, as well as those of MAR segments outside the Doldrums region. In addition, the neovolcanic ridges of ITR-2 and ITR-4 prograde towards the south and north, respectively, into the adjacent transform valleys, in further agreement with a period strong magmatic production.

A sustained volcanic activity in the central ITRs contradicts expectations of reduced magmatism in short spreading centers due to the cold edge effect at ridge-transform intersections (e.g., Fox and Gallo, 1984; Bonatti et al., 1992). This is also at odd with numerical models that suggest that the innermost portions of a long-offset transform are characterized by a thick lithosphere (e.g., up to 45 km for a 900-km offset; Ligi et al., 2002). We must consider, however, that mantle composition plays a major role in the style and amount of mantle melting (e.g., Stracke and Bourdon, 2009); the more fertile is the mantle source, the highest melting degrees are expected. Hence, volcanism in the innermost portion of Doldrums MTS may have been triggered by the occurrence of an anomalous fertile component located in the asthenosphere, remobilized by the activation of a transtensive regime. Alternatively, the magmatic production in this region was highly discontinuous in time and the large volcanic ridges of ITR-2 and ITR-3 represent the expression of a recent period of strong magmatic activity. Although we prefer the first hypothesis, this idea needs to be tested with geochemical studies of the fresh basalt glasses collected in the ITRs.

In this framework, we can now speculate on the origin of ITR-3. The 7.4ºN transform is subdivided in two active transform segments by a ~ 10 km-wide strongly-tectonized stripe of ocean floor. The latter is in turn crosscut by a lenticular depression representing the ITR-3 (Fig. 5a, b). According to dredge results, the huge neovolcanic zone within this ITR represents the youngest structure, and has N-S direction perpendicular to spreading direction. On the other

hand, the adjacent seafloor displays discordant sigmoidal hills that turn counter clockwise parallel to the transform valley. These structures recall extensional duplexes (Woodcock and Fischer, 1986) formed in an extensional dextral strike-slip system. Accordingly, we infer that the rift valley of ITR-3 may represent a pull-apart basin opened by a dextral strike-slip fault overstep (Fig. 5a, b). This idea is consistent with the occurrence of a prominent neovolcanic axial ridge, which testifies an abundant melt production and, by consequence, that the main lithospheric thinning was centered in this portion of the Doldrums MTS. The origin of this structure requires further analyses, and this model needs to be sustained by a throughout characterization of the volcanism in this region.

Mechanisms of exposure of mantle and lower crustal rocks

In the previous sections we have shown that oceanic basement rocks are exposed in large regions at the Doldrums MTS. Basement exposures are typical of large fracture zones along the MAR, such as the 15° 20'N (Putscharovskiy et al., 1988; Kelemen et al., 2004), the Vema (Bonatti et al., 2005), Romanche (Ligi et al., 2002) and the St. Paul FZs (Hekinian et al., 2000). In this study we show four mechanisms responsible for the exhumation of deep-seated rocks on the seafloor.

(1) The most typical mechanism to expose basement rocks in a transform domain is the formation of transverse ridges (e.g., Bonatti et al., 2005). These features represent topographic anomalies oriented parallel to the transform valley and exposing continuous sections of oceanic lithosphere (e.g., Auzende et al., 1989). Geophysical and sampling investigations suggest that these slabs of oceanic lithosphere are uplifted during changes in transform-related tectonics (Kastens et al., 1998). A similar origin is suggested here for the transverse ridges exposed along the fracture zones of our study area. One possible example is the Peyve Smt (Fig. 4c). This structure forms the northern wall of the Vernadsky transform, elongated for ~ 30 km parallel to the transform valley. In many aspects it is similar to known transverse ridges formed on the northern side of the Romanche FZ (Ligi et al., 2002) and on the southern side of the Vema FZ (Bonatti et al., 2005), but differs by smaller dimensions. According to the dredging results of S09 and S45, this structure exposes a section made up by peridotites and gabbros. The top of the sequence is most likely formed by deformed gabbros, which show a continuum from granulite-facies conditions (> 800ºC) to low temperature brittle cataclastic deformation. We note that the gabbros exposed on the Peyve Smt are mainly evolved oxide-gabbros, whereas primitive terms are lacking (Fig. 9). This may be due to a sample bias or, more likely, may indicate that the oceanic lower crust is mostly constituted by evolved terms. The same characteristics were documented by Brunelli (personal communication) in the transverse ridge of the Vema FZ, and interpreted as a consequence of extreme fractionation and longitudinal flow of magma from the segment center towards the transform. The widespread exposure of oxide-gabbros is also characteristic of the intersection between the Atlantis Bank OCC and the Atlantis II transform wall, in the SWIR, where Dick et al. (2019) reported an overall higher amount of evolved lithologies compared to Holes 735B and 1473A, in turn located in the medial portion of the same OCC (see Dick et al., 2000; MacLeod et al., 2017). The flat top of the Peyve Smt (Fig. 4c) and the lack of a basaltic layer suggest that this seamount was eroded in a subareal or shallow marine environments. Further analyses are necessary to understand the origin of this seamount, however it lacks corrugations and its location along the transform valley lead us to speculate that this transverse ridge formed under transpressive conditions in contrast with a transtensive origin for the Vema transverse ridge. Longer, but smaller transverse ridges were also detected on the southern flank of the 7.4º transform, but not easily interpreted due to the lack of a complete survey.

(2) Another mechanism able to expose basement rocks is the formation of median ridges. These features were firstly recognized in the Romanche FZ by Bonatti et al. (1974) and later in the Vema FZ and in the Indian and Pacific oceans (e.g., Lagabrielle et al., 1990; Dick et al., 1991; Gallo et al., 1986). Initially, they were interpreted as resulting from the diapiric rise of serpentinized mantle peridotites within the transform valley (Macdonald et al., 1986; Dick et al., 1991). Another interpretation seems to indicate that these are portions of the oceanic mantle uplifted by isostatic rebound (Detrick et al., 1982) or tectonic extension during the formation of a nodal basin (Lagabrielle et al., 1992). Median ridges are found in all the transforms of the Doldrums MTS (Fig. 2b). They bisect the transform valleys in two transform segments, but show a great variability in size and morphology. The largest median ridge is exposed within the Doldrums transform, covering most of the active transform valley (Fig. 3b). Dredging during S09 reveals the occurrence of peridotites and minor deformed oxide-gabbros, similar to those collected in the transverse ridges (Fig. 2a). Since these rocks are relatively unserpentinized, an origin by diapiric rise seems unlikely. The continuity of most of these median ridges with abyssal hills along the ITRs leads us to prefer an origin through tectonic extension following the formation of nodal basins.

(3) The shallowest portions of the rift shoulders are represented by the summits of oceanic core complexes. They consist in dome-shaped bodies exhumed through detachment faulting. First recognized at 30ºN in the MAR (Cann et al., 1997), OCC have been mapped in several locations along the MAR and are now considered a fundamental style of seafloor spreading at slow and ultra-slow spreading ridges (e.g., Escartin et al., 2008; 2017; Smith et al., 2014), as well as in back-arc basins (Ohara et al., 2001). One fundamental feature of OCCs is the occurrence of corrugations representing the exposure of the detachment fault surface. In our study area, we found several OCCs located along the transform walls or in the inner corner highs. OCCs are commonly formed in association with nodal basins. Amongst the OCCs exposed in the area, the 8.1ºN OCC was extensively dredged (Fig. 3c). It consists of highly tectonized gabbros and chloritized basalts. The occurrence of serpentine schists with sliding surfaces led us to suggest an exhumation process through detachment faulting (Fig. 11). The textural features of the gabbros are consistent with this interpretation, revealing a retrograde tectono-metamorphic evolution typical of OCCs worldwide (e.g., Dick et al., 2000; Boschi et al., 2006; Blackmann et al., 2006; MacLeod et al., 2017; Sanfilippo et al., 2018). For instance, these rocks retain textural evidence for high temperature deformation developed at hyper-solidus conditions, followed by the formation of amphibole-rich veins and, finally, by low-grade metamorphism (Skolotnev et al., 2006). Another interesting OCC has been detected at 7.78ºN and 36.96ºW along the 7.4ºN transform (Fig. 4a). At a distance of 130 km from the ITR-1, we can infer an age of

approximately 8.5 Ma. The detachment surface has large-scale well-developed corrugations covering an area of 160 km^2 cut in its central sector by two conjugated normal faults. Although we could not deploy any dredge along this OCC during S45, we stress that this represents an optimum location to collect lower crustal and mantle lithologies formed in the early stage of evolution of the Doldrums MTS. The striking similarity with the well-known Kane Megamullion core complex at 23ºN along the MAR (see Dick et al., 2008) makes the 7.4ºN OCC an ideal location to substantiate our knowledge on detachment faulting as an important accretionary process at slow spreading ridges.

(4) A last fundamental location where mantle peridotites and gabbros were collected in the Doldrums MTS are the cliffs of abyssal hills facing the transform valleys. These structures often constitute the walls of the transform valleys where neither detachment faults nor transverse ridges are observed. The best examples are exposed at the northern wall of the Doldrums transform (Fig. 3b), where dredges S45-13 and S45-15 collected peridotites and gabbros (Fig. 2a). We speculate that these cliffs represent the southward continuation of abyssal hills into the transform valley and delineate high-angle normal faults resulting from the opening of the axial valley. In contrast to the formation of a heterogeneous oceanic lithosphere exposed by detachment faulting, high-angle normal faults at slow spreading ridge are typically related to the development of a "normal" oceanic lithosphere, or in the hanging wall of asymmetric rift system (see Wernicke, 1985; Lagabrielle et al., 1990). This idea is sustained by geochemical investigation of the magmatism developed during detachment faulting which, in line with numerical and thermodynamic modelling, suggests that the magma budget plays a major role in the style of accretion of the oceanic lithosphere at slow spreading ridges (e.g., Escartin et al., 2008; Tucholke et al., 2008; Smith et al., 2014; Sanfilippo et al., 2018). Accordingly, the exposure of basement rocks along these high-angle normal faults allows investigating the accretionary process of what can be regarded as the "normal" volcanic seafloor formed in period of sustained magmatic activity. Preliminary results from geochemistry of the peridotites dredged during S06 and S09 expeditions show highly depleted compositions and a residual character (Sanfilippo, person. comm.), further supporting the idea of high degree of mantle melting and high magma budget in the Doldrums region.

CONCLUSIONS

The enormous amount of the new data collected during cruise S45 allow us to define for the first time the large-scale structure of the Doldrums MTS. Coupled with data from previous expeditions we can now anticipate some fundamental inferences on the formation and evolution of this unknown megatranform domain. The main conclusions of this study are summarized below:

1. Four seismically active intra-transform spreading segments subdivide the Doldrums MTS into five transform segments, which are well delineated by seismicity distribution and dextral strike-slip seismic fault plane solutions.
2. Although the axial depth of ridge segments decreases from the peripheral portions of the megatransform towards the innermost sectors, the central ITRs contain large neovolcanic axial ridges locally protruding within the transform valleys. This is indicative of abundant magmatic activity and may suggest a zone of high degree of mantle melting and/or active mantle upwelling in the central part of the Doldrums MTS. We speculate that this may be a consequence of a transtensive regime possibly centered in a zone of anomalous fertile asthenosphere.
3. Structural highs and dome-shaped structures are mostly represented by oceanic core complexes (i.e., 8.3ºN OCC; 8.1ºN OCC; 7.78ºN OCC). Dredging results on some of these features provided deformed mantle and lower crustal rocks typical of OCC worldwide agreeing with exhumation through detachment faulting. This view is also supported by positive Bouguer gravity anomalies centered on these structures suggesting emplacement of rocks with higher density. Deformed gabbros and positive Bouguer gravity anomaly also characterize the Peyve Smt., which is in turn interpreted as a portion of transverse ridge uplifted during a transpressive regime.
4. Large regions of basement exposure characterize the transform valleys and the ridge transform intersections. Four different mechanisms may be responsible for the exposure of basement rocks. They are: (i) formation of transverse ridges along the transform valleys (i.e., Peyve Smt); (ii) uplift of median ridges within the transform valleys; (iii) denudation of basement rocks and formation of the OCCs by detachment faulting at inner corner highs and (iv) exposure of deep-seated rocks at the footwall of high-angle normal faults at the ridge-transform intersections.

ACKNOWLEDGMENTS

We would like to thank the captain, the officers and the crew of *R/V Akademik Nikolaj Strakhov*. The chief scientist Elena Ivanova is also kindly thanked. This study was supported by the Russian Foundation for the Basic Research (project no. 18-55-7806 Ital_t, 18-05-00001, 18-05-00691), Russian Basic Research Program (projects no. 0135-2019-0050, 0135-2016-0013, 0137-2019-0012, 0136-2018-0025), by Accordo Bilaterale CNR/RFBR 2018-2020 (CUP-B36C17000250005) and by the Italian Programma di Rilevante Interesse Nazionale (PRIN_2017KY5ZX8). The study beneficed of constructive reviews by P. Tartarotti and one anonymous reviewer.

REFERENCES

Auzende J.M., Bideau D., Bonatti E. et al., 1989. Direct observation of a section through slow-spreading oceanic crust. Nature, 337: 726-729.

Balmino G., Vales N., Bonvalot S. and Briais A., 2012. Spherical harmonic modeling to ultra-high degree of Bouguer and isostatic anomalies. J. Geod., 86: 499-520.

Blackman D. K., Ildefonse B., John B.E. et al. 2006. Oceanic core complex formation, Atlantis massif, Proceed. Integr. ODP, 304/305: 304-605, https://doi.org/10.2204/iodp.proc.304305.2006.

Boettcher M.S. and Jordan T.H., 2004. Earthquake scalingrelations for mid-ocean ridge transform faults. J. Geophys. Res., 109: B12302.

Bonatti E., 1978. Vertical tectonism in oceanic fracture zones. Earth Planet. Sci. Lett., 37 (3): 369-379.

Bonatti E., Brunelli D., Buck W.R. et al., 2005. Flexural uplift of a lithospheric slab near the Vema transform (Central Atlantic): Timing and mechanism. Earth Planet. Sci. Lett., 240: 642-655.

Bonatti E., Brunelli D., Fabretti P. et al., 2001. Steady-state creation of crust-free lithosphere at cold spots in mid-ocean ridges. Geology, 29: 979-982.

Bonatti E., Emiliani C., Ferrara G. et al., 1974. Ultramafic-carbonate breccias from the equatorial Mid Atlantic Ridge. Mar. Geol., 16 (2): 83-102.

Bonatti E., Ligi M., Borsetti M. et al., 1996a. Lower Cretaceous deposits trapped near the equatorial Mid-Atlantic Ridge. Nature, 380, 518-520.

Bonatti E., Ligi M., Brunelli D. et al., 2003. Mantle thermal pulses below the Mid-Atlantic Ridge and temporal variations in the formation of oceanic lithosphere. Nature, 423: 499-505.

Bonatti E., Ligi M., Carrara G. et al., 1996b. Diffuse impact of the Mid Atlantic Ridge with the Romanche transform: an Ultracold Ridge/Transform Intersection. J. Geophys. Res., 101: 8043-8054.

Bonatti E., Peyve A., Kepezhinskas N. et al., 1992. Upper mantle heterogeneity below the Mid-Atlantic Ridge, 0°-15°N. J. Geophys. Res., 97, B4: 4461-4476.

Boschi C., Bonatti E., Ligi M. et al., 2013. Serpentinization of mantle peridotites along an uplifted lithospheric section, Mid Atlantic Ridge at 11°N. Lithos, 178: 3-23.

Boschi C., Früh-Green G.L. and Escartín J., 2006. Occurrence and significance of serpentinite-hosted, talc-and amphibole-rich fault rocks in modern oceanic settings and ophiolite complexes: An overview. Ofioliti, 31 (2): 129-140.

Cande S.C., LaBreque J.L. and Haxby W.F., 1988. Plate kinematics of the south Atlantic, chron C34 to the present. J. Geophys. Res., 93: 13479-13492.

Cann J.R., Blackman D.K., Smith D.K. et al., 1997. Corrugated slip surfaces formed at ridge-transform intersections on the Mid-Atlantic Ridge. Nature, 385 (6614): 329-332, http://dx.doi.org/10.1038/385329a0.

Cannat M., Sauter D., Mendel V. et al., 2006. Modes of seafloor generation at a meltpoor ultraslowspreading ridge. Geology, 3 (7): 605-608, https://doi.org/10.1130/G22486.1.

Detrick R.S., Cormier M.H., Prince R.A. et al., 1982. Seismic constraints on the crustal structure within the Vema Fracture Zone. J. Geophys. Res., 87: B13, https://doi.org/10.1029/JB087iB13p10599.

Dick H.J.B, Macleod C.J., Blum P. et al., 2019. Dynamic accretion beneath a slow-spreading ridge segment: IODP Hole 1473A and the Atlantis Bank Oceanic Core Complex. J. Geophys. Res., Solid Earth. Am. Geophys. Union, ff10.1029/2018JB016858f.

Dick H.J.B., Natland J.H., Alt J.C. et al., 2000. A long in situ section of the lower ocean crust: results of ODP Leg 176 drilling at the Southwest Indian Ridge. Earth Planet. Sci. Lett., 179 (1): 31-51.

Dick H.J.B., Schouten H., Meyer P.S. et al., 1991. Tectonic evolution of the Atlantis II fracture zone. In R.P. Von Herzen, P.T. Robinson et al. (Eds.), Proceed. ODP Sci. Res., 118: 359-398, http://dx.doi.org/10.2973/odp.proc.sr.118.156.1991.

Dick H.J.B., Tivey M.A. and Tucholke B.E., 2008. Plutonic foundation of a slow-spreading ridge segment: oceanic core complex at Kane Megamullion, 23°30-N, 45°20-W. Geochem. Geophys. Geosyst., 9 (5): Q0501, http://dx.doi.org/10.1029/2007GC001645.

Escartín J., Mevel C., Petersen S. et al., 2017. Tectonic structure, evolution, and the nature of oceanic core complexes and their detachment fault zones (13°20-N and 13°30-N, Mid Atlantic Ridge). Geochem. Geophys. Geosyst., 18 (4): 1451-1482.

Escartın J., Smith D.K., Cann J. et al., 2008. Central role of detachment faults in accretion of slow-spread oceanic lithosphere. Nature, 455 (7214): 790-794.

Fox P.J. and Gallo D.G., 1984. A tectonic model for ridgetransform-ridge plate boundaries: Implications for the structure of oceanic lithosphere. Tectonophysics, 104 (3-4): 205-242.

Gallo D.G., Fox P.J., Macdonald K.C., 1986. A Sea Beam investigation of the Clipperton Transform Fault: the morphotectonic expression of a fast slipping transform boundary. J. Geophys. Res., 91 (B3): 3455-3467.

Gasperini L., Bernoulli D., Bonatti E. et al., 2001. Lower Cretaceous to Eocene sedimentary transverse ridge at the Romanche Fracture and the opening of the of the equatorial Atlantic. Mar. Geol., 176 (1-4): 101-119.

Hekinian R., Juteau T., Gràcia E. et al. 2000. Submersible observations of Equatorial Atlantic mantle: The St. Paul Fracture Zone region. Mar. Geophys. Res., 21: 529, https://doi.org/10.1023/A:1004819701870.

Kastens K., Bonatti E., Caress D., Carrara G., Dauteuil O., Frueh-Green G., Ligi M. and Tartarotti P., 1998. The Vema transverse ridge (Central Atlantic). Mar. Geophys. Res., 20: 533.

Kelemen P.B., Kikawa E., Miller D.J. et al., 2004. ODP Leg 209 drills into mantle peridotite along the Mid-Atlantic Ridge from 14ºN to 16ºN. JOIDES J. Proceed. ODP 209 Initial Rep., 30 (1): 14-19.

Klein E.M. and. Langmuir C.H., 1987. Global correlations of ocean ridge basalt chemistry with axial depth and crustal thickness. J. Geophys. Res., 92: 8089-8115.

Lagabrielle Y. and Cannat M., 1990. Alpine Jurassic ophiolites resemble the modern central Atlantic basement. Geology, 18: 319-322.

Lagabrielle Y., Mamaloukas-Frangoulis V., Cannat M. et al., 1992. Vema Fracture Zone (Central Atlantic): Tectonic and magmatic evolution of the median ridge and the eastern ridge-transform intersection domain. J. Geophys. Res. Solid Earth, 97 (B12): 17331-17351.

Ligi M., Bonatti E., Cipriani A. and Ottolini L., 2005. Water-rich basalts at mid-ocean-ridge cold spots. Nature, 434: 66-69.

Ligi M., Bonatti E., Gasperini L. and Poliakov A.N.B., 2002. Oceanic broad multifault transform plate boundaries. Geology, 30: 11-14.

Lolli B., Gasperini P. and Vannucci G., 2014. Empirical conversion between teleseismic magnitudes (M_b and M_s) and moment magnitude (M_w) at the Global, Euro-Mediterranean and Italian scale. Geophys. J. Int., 199: 805-828.

MacLeod C.J., Dick H.J.B., Blum P. et al., 2017. Expedition 360 summary. In: C.J. MacLeod, H.J.B Dick,. P. Blum and the Expedition 360 Scientists (Eds.), Southwest Indian Ridge lower crust and Moho. Proceed. Intern. ODP 360: 1-267, http://dx.doi.org/10.14379/iodp.proc.360.103.2017.

Maia M., Sichel S., Briais A. et al., 2016. Extreme mantle uplift and exhumation along a transpressive transform fault. Nature Geosci., 9: 619-624, ISSN: 1752-0894, doi: 10.1038/NGEO2759.

OharaY., Yoshida T., Kato Y. and Kasuga S., 2001. Giant megamullionin the Parece Vela backarc basin. Mar. Geophys. Res., 22: 47-61.

Pushcharovsky Yu.M., Peyve A.A., Raznitsin Yu.N., Skolotnev S.G., Lapunov S.M and Tyrko N.N., 1988. Cape Verde fracture zone: rock composition and structures (Central Atlantic). Geotectonika, 6: 18-31 (in Russian).

Pushcharovsky Yu.M., Raznitsin Yu.N., Mazarovich A.O., Skolotnev S.G., Kepezinskas P.K., Tyrko N.N., Peyve A.A. and Dmitriev D.A., 1992. Fracture zones Arkhangelsky, Doldrums and Vernadsky in the Central Atlantic: structure and rocks composition. Geotectonika, 6: 63-79 (in Russian).

Pushcharovsky Yu.M., Raznitsin Yu.N., Mazarovich A.O. et al., 1991. Structure of the Doldrums fracture zone Central Atlantic. M. Nauka, 224 pp. (in Russian).

Sandwell D.T. and Smith W.H.F., 1997. Marine gravity anomaly from Geosat and ERS 1 satellite altimetry. J. Geophys. Res., 102 (B5): 10039-10054.

Sanfilippo A., Dick H.J.B., Marschall H.R., Lissenberg, C.J. and Urann B., 2018. Emplacement and high-temperature evolution of gabbros of the 16.5°N oceanic core complexes (Mid-Atlantic Ridge): Insights into the compositional variability of the lower oceanic crust. Geochem. Geophys. Geosyst., 20, https://doi.org/10.1029/ 2018GC007512.

Sclater J.G., Grindlay N.R., Madsen J.A. and Rommevaux-Jestin C., 2005. Tectonic interpretation of the Andrew Bain transform fault: Southwest Indian Ocean. Geochem. Geophys. Geosyst., 6: Q09K10, doi:10.1029/2005GC000951.

Schilling JG. et al., 1995. Thermal structure of the mantle beneath the equatorial Mid-Atlantic Ridge-Inferences from the spatial variation of dredged basalt glass compositions. J. Geophys. Res., 100: 10057-10076.

Skolotnev S.G., Peyve A.A., Lavrushin V.Yu, Demidova T.A., Abramov S.S., Eskin A.E., Krinov D.I., Petrov V.V., Razdolina N.V., Turko N.N., Tsukanov N.V., Chaplygina N.L. and Sharkov E.V., 2006. Geological structure and indicators of hydrothermal ore-bearing activity at the junction of the southern rift segment and the Doldrums Transform Fracture Zone, Central Atlantic. Dokl. Akad. Nauk, 407 (3): 372-377.

Smith D.K., Schouten H., Dick H.JB. et al., 2014. Development and evolution of detachment faulting along 50 km of the Mid-Atlantic Ridge near 16.5°N. Geochem. Geophys. Geosyst., 15: 4692-4710, https://doi.org/10.1002/2014GC005563.

Stracke A. and Bourdon B., 2009. The importance of melt extraction for tracing mantle heterogeneity. Geochim. Cosmochim. Acta, 73 (1): 218-238, https://doi.org/10.1016/j.gca.2008.10.015.

Teagle D.A.H., Alt J.C., Umino S. et al., 2006. Proceed. IODP, 309/312, doi: 10.2204/iodp.proc.309312.101.2006.

Tucholke B.E., Behn M.D., Buck W.R. and Lin J. 2008. Role of melt supply in oceanic detachment faulting and formation of megamullions. Geology, 36 (6): 455-458, https://doi.org/10.1130/G24639A.1.

Wernicke B., 1985. Uniform sense normal simple shear of the continental lithosphère. Can. J. Earth Sci., 22: 108-125.

White R.S., 1984. Atlantic oceanic crust: seismic structure of a slow-spreading ridge. Geol. Soc. London Spec. Publ., 13: 101-111, https://doi.org/10.1144/GSL.SP.1984.013.01.09.

Wilson J.T., 1965. A new class of faults and their bearing on continental drift. Nature, 207: 343-347.

Woodcock N.H. and Fischer M. 1986. Strike-slip duplexes. J. Struct. Geol., 8: 725-735.

Received, December 13, 2019
Accepted, January 8, 2020

PETROLOGY, GEOCHEMISTRY AND ORIGIN OF THE SIERRA DE BAZA OPHIOLITES (BETIC CORDILLERA, SPAIN)

J.A Lozano Rodríguez*, Encarnacion Puga*, Claudio Natali,✉, Gianluca Bianchini***,✉** and **Luigi Beccaluva*****

* *Instituto Andaluz de Ciencias de la Tierra (CSIC-UGR), Armilla, Granada, Spain.*
** *Dipartimento di Scienze della Terra, Università di Firenze, Italy.*
*** *Dipartimento di Fisica e Scienze della Terra, Università di Ferrara, Italy.*
✉ *Corresponding authors, e-mail: claudio.natali@unifi.it; bncglc@unife.it*

Keywords: *Ophiolite; Betic Cordillera; Mesozoic Tethys.*

ABSTRACT

In this work we present for the first time a petrological-geochemical and genetic study of the Sierra de Baza ophiolites, which represent one of the ophiolitic occurrences of the Betic Cordillera (Southern Spain). They are composed of ultramafic, mafic and sedimentary rocks, largely affected both by ocean floor and polyphasic metamorphism during the Alpine orogeny. Ultramafic rocks are serpentinized lherzolites and harzburgites, whereas the metabasites are meta-gabbros and meta-basalts. On the whole, Sierra de Baza ophiolites show striking geochemical similarities with those from other Betic occurrences, as well as with other Tethyan ophiolites of the Western Mediterranean (Calabria, Internal and External Ligurides, Platta, Corsica and Western Alps). In particular, metabasites show petrological and geochemical features similar to the E-MORB magmatism of the Atlantic Ridge between 45 and 63ºN generated under ultra-slow spreading ridge conditions. This process originated a strip of few hundreds km of ocean floor at the western end of the Tethys, located SE of the Iberian-European margin during the Mesozoic. The inversion of the stress regime in the European-Iberian and African geodynamics, starting from the Late-Middle Cretaceous, caused subduction and metamorphism in the eclogite facies of oceanic slices that were partially exhumed on the continental margin, forming the Betic Ophiolites. These ophiolites were disarticulated and dismembered as a result of the shift towards SW of the Alboran continental block, progressively separated from the AlKaPeCa (Alboran, Kabilias, Peloritani, Calabria) microplate, finally occupying their current position in the Betic Internal Zones.

INTRODUCTION

The ophiolites of the peri-Mediterranean Alpine domain, reflect a complex geological history including oceanic spreading, subduction, collision and final obduction. These Alpine ophiolites plausibly represent remnants of several oceanic strands of Mesozoic age forming the Tethys Ocean and developed between the continental margins of the European and African plates, an area characterized by the presence of several microplates and/or continental blocks (Handy et al., 2010). These ancient oceanic domains are currently incorporated into the Alpine-Himalayan orogenic belts, as result of several subduction and continental collision events between the main Eurasian, African and Indian plates and a series of microplates (including the Iberian Plate) originated from Gondwana fragmentation throughout the Mesozoic (Zheng, 2012). In this framework, the ultramafic and mafic rocks included in the Betic Cordillera (SE Spain) have been interpreted as an ophiolite association, i.e., metamorphosed remnants of a Mesozoic oceanic lithosphere, since the 1970s (Puga, 1977; Puga and Díaz de Federico, 1978). This hypothesis relating the Betic Ophiolite Association (hereafter named as BOA following Puga,1990) to a Mesozoic oceanic basin, was criticized at the beginning, due to the paucity of outcrops conforming to the three layers defined for Ophiolites in the Penrose Conference (1972), i.e., sections including peridotites/serpentinites, gabbros/basalts and deep sea sediments, such cherts, hypothetically corresponding to the stratigraphy of the oceanic lithosphere. In spite of this criticism, the Betic Ophiolites were identified as Mid-Oceanic-Ridge (MOR)-type by Puga (1977;1990), Bodinier et al. (1988), Morten et al. (1987), Puga et al. (1989a;1989b), who investigating BOA mafic and ultramafic lithologies emphasizing geochemical analogies with the rocks formed along the Atlantic Ridge and those included within the Jurassic Alpine-Apennine ophiolites. Later palaeogeographic, petrologic and geochemical studies (Guerrera et al., 1993; Puga et al., 1995; 1999b; 2000) corroborated the ophiolitic origin of the BOA rocks. Nevertheless, Gómez-Pugnaire et al. (2000) highlighted apparent petrological incongruence, emphasizing that the geochemical composition of Betic basalts/gabbros do not conform to Normal Mid Oceanic Ridge Basalt (N-MORB) and that the Betic ultramafic rocks are less residual with respect to the abyssal peridotites having prevalent harzburgite composition. This criticism on the oceanic nature of the BOA has been largely bypassed by recent papers which coupled geochronological data with new petrological and geochemical studies (e.g., Ruiz Cruz et al., 1999; 2007; Puga et al., 2002a; 2002b; 2005; 2007; 2009; 2011; Alt et al., 2012; Aerden et al., 2013), certainly ascribing the provenance of some BOA outcrops to a MORB-type tectonic setting, or to an Ocean-Continent-Setting (OCT). This hypothesis conforms to the interpretations proposed for ophiolite sequences of the Alps and Apennines (Beccaluva et al., 1979; Rampone et al., 1995; 2005; 2008; 2009; 2014; Marroni et al., 1998; Rampone and Piccardo, 2000; Borghini et al., 2007; 2016; Montanini et al., 2008; Manatschal and Müntener, 2009; Piccardo and Guarnieri, 2010; Rampone and Hofmann, 2012; Lagabrielle et al., 2015; Saccani, 2015). Worth of note, recent oceanographic studies emphasize that the rock associations of modern oceanic floors are more heterogeneous than what assumed in the past (e.g., Dick et al., 2003; Gale et al., 2013; Herbrich et al., 2015; Regelous et al., 2016) and, hence, the "ophiolite concept" interpreted as "fossil oceanic lithosphere with a unique and complete lithologic sequence" has also to be revisited and updated (Lagabrielle, 2009).

In this work, 55 meta-mafic and 17 meta-ultramafic rock samples collected from Sierra de Baza have been analyzed for their major trace element composition, and Sr-Nd isotopes were analyzed on 8 selected samples, in order to highlight analogies and differences with the other BOA sequences, with the final aim of better understanding the BOA in the framework of the Mesozoic Tethys puzzle, within the paleogeographic and geodynamic evolution of the Central-Western Mediterranean area.

GEOGRAPHICAL AND GEOLOGICAL SETTING OF THE SIERRA DE BAZA OPHIOLITES

The Betic Ophiolites Association (BOA), crops out discontinuously along 250 km in the central and eastern sectors of the Betic Cordillera (SE Spain, Supplementary Fig. 1). The BOA rocks are represented by tectonic slices ranging in size from decametres to kilometres, made by metamorphosed ultramafic and mafic lithologies sometimes associated with sedimentary rocks. These ophiolites are exclusively located in the Mulhacén Complex (MC), in the central and

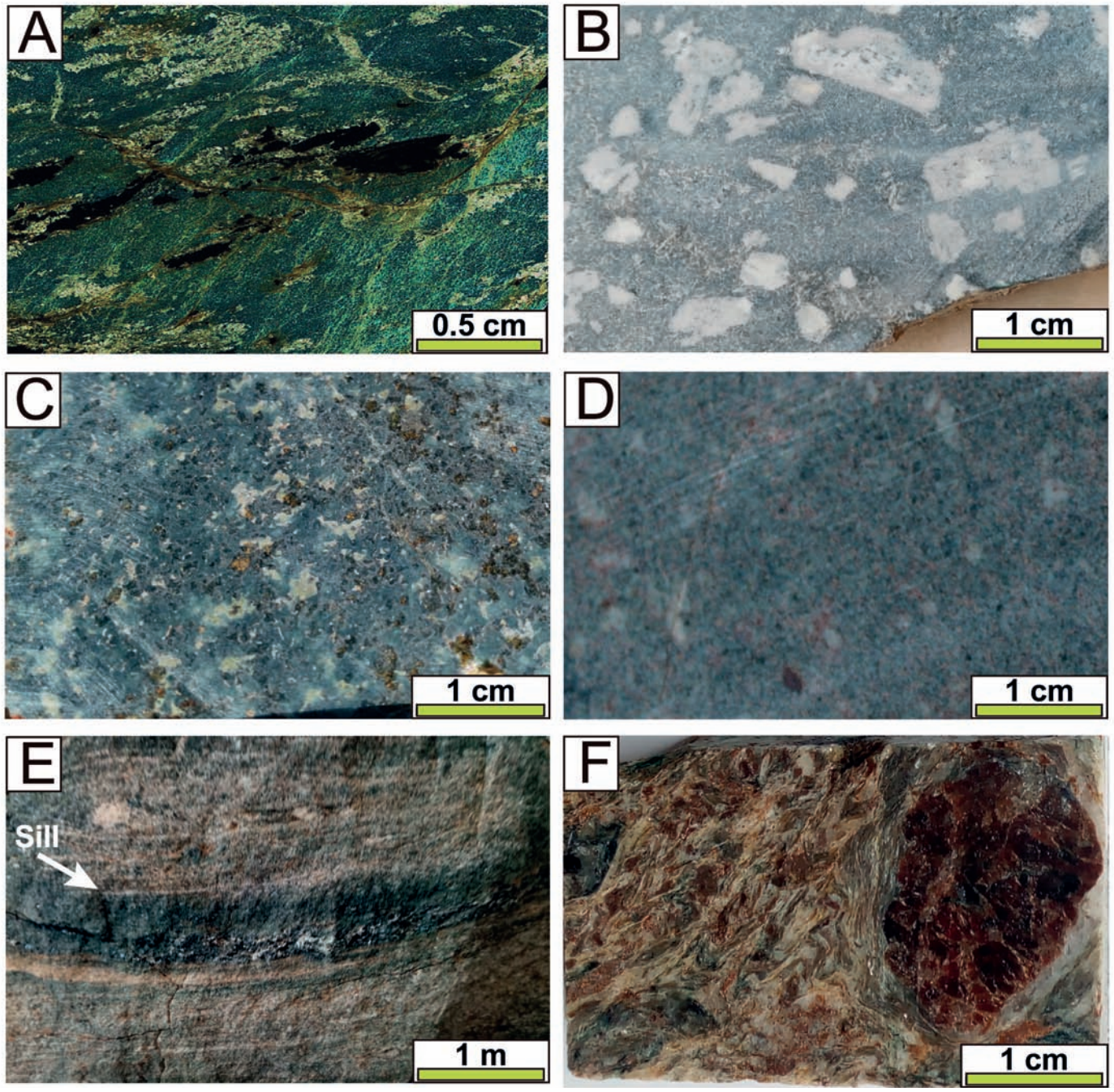

Fig. 1 - Macroscopic appearance of some BOA rocks in Sierra de Baza. A: serpentinite from a secondary harzburgite (Cani-277), showing large Magnetite crystals, surrounded by serpentinite (antigorite), along with minor chlorite and talc; B: Amphibolite from a porphyry textured gabbro, showing white phenocrysts of plagioclase in a doleritic matrix (Cani-83); C: Eclogite from pyroxene-rich gabbro (Cani-139B); D: Eclogite from basalt (CH-37); E: Epidote amphibolite from dolerite (sill) intruded into micaschists (Cani-285); F: Micaschists with large garnet porphyroblasts from a metapelite of the sedimentary sequence (Cani-252).

eastern area of the Betic Cordillera, and are never found in the underlying Veleta Complex (VC, Puga et al., 2002a; 2004a; 2004b; 2007; Aerden et al., 2013). This suggests that these two complexes pertained to different paleogeographic domains before and during the Jurassic-Cretaceous period, when the ophiolites originated from exhumation of an oceanic floor (Guerrera et al., 1993; Tendero et al., 1993; Puga et al., 1999a; 1999b; 2005; 2009; 2011). The VC rocks crop out through several tectonic windows below the (MC), forming the Nevado-Filábride Domain and representing the deepest rocks in the current tectonic pile of the Betic Cordilleras (Figs. 1A, 1B). The BOA outcrops, deriving from the Betic oceanic floor (Guerrera et al., 1993; Puga et al., 2002a; 2011), allow the reconstruction of the pristine oceanic lithostratigraphy represented in Supplementary Fig. 1. Parts of the oceanic floor were obducted on the crustal rocks (Caldera unit of the MC) of its adjoining western continental margin, and overthrust by those from its eastern continental margin (Sabinas crustal unit).

Each of these continental units consists of rocks deriving from a Paleozoic basement with abundant granitic and rhyolitic orthogneisses, covered by Triassic sediments (Nieto, 1996; Nieto et al., 2000; Puga et al., 2002a; 2004b; 2007). The main rock types forming the ophiolite unit in the lithostratigraphic reconstruction are, from bottom to top: serpentinites, intruded by rodingitized dolerite dykes, and eclogitized/amphibolitized gabbros, dolerite dykes and basalts. These rock types may be found covered by a metasedimentary sequence in which the intercalation of amphibolitized dolerite sills is common, probably deriving from thin basaltic levels. Among the BOA, those from Sierra de Baza are characterized by the largest number of outcrops and by a notable linear extension of about 23 km, from the town of Charches to the west, to the Los Olmos locality to the northeast. (Supplementary Fig. 1C). In particular, the size of the ultramafic bodies in Sierra de Baza ranges from 6-7 m in Las Canteras (2.5 km southeast of Los Olmos) to about 700 m in the outcrop known as La Canaleja.

SAMPLES AND ANALYTICAL METHODS

72 rock samples were collected from the Sierra the Baza complex. The Sierra de Baza mafic rocks (55 samples) consist of metamorphosed (olivine)-gabbros, dolerites and basalts. The meta-ultramafic rocks (17 samples) of the Sierra de Baza mainly consist of partially serpentinized lherzolites and harzburgites. Major element and Zr concentrations were determined on glass beads made of 0.6 g of powdered sample diluted in 6 g of $Li_2B_4O_7$ using a PHILIPS Magix Pro (PW-2440) X-ray fluorescence (XRF) spectrometer at the "Centro de Instrumentación Científica" of Granada University (40 samples). Precision was better than ±1.5% for a concentration of 10 wt%. Precision for Zr was better than ±4% at a concentration of 100 ppm. Trace elements other than Zr were determined at the University of Granada by ICP-mass spectrometry (ICP-MS) using a PERKIN ELMER Sciex-Elan 5000 spectrometer; sample solutions were prepared by digesting 0.1 g of sample powder with HNO_3 + HF in a Teflon-lined vessel at ~ 180°C and ~ 200 p.s.i. for 30 min, subsequently evaporated to dryness and dissolved in 100ml of 4 vol% HNO_3. The concentrations of the PM-S and WS-E international standards were not significantly different from the recommended values (Govindaraju, 1994). Precision was better than ±5% and ±2% for concentrations of 5 and 50 ppm, respectively. Sr-Nd isotope analyses were carried out at the University of Granada, where whole-rock samples were digested as described for the ICP-MS analysis, using ultra-clean reagents, and analyzed by thermal ionization mass spectrometry (TIMS) using a Finnigan Mat 262 spectrometer after chromatographic separation with ion exchange resins. Normalisation values were $^{86}Sr/^{88}Sr = 0.1194$ and $^{146}Nd/^{144}Nd = 0.7219$. Blanks were 0.6 and 0.09 ng for Sr and Nd respectively. External precision (2σ), estimated by analyzing 10 replicates of standard WS-E (Govindaraju, 1994), was better than 0.03% for $^{87}Sr/^{86}Sr$ and 0.015% for $^{143}Nd/^{144}Nd$. The measured $^{87}Sr/^{86}Sr$ of the NBS 987 international standard was 0.710250±0.000044, whereas measurements of the La Jolla Nd international standard yielded a $^{143}Nd/^{144}Nd$ ratio of 0.511844±0.000065.

PETROGRAPHY

Meta-ultramafic and meta-mafic rocks have been studied under polarized light optical microscope. The petrographic and mineralogical features, together with sample location, are reported in Tables 1 and 2. The lithologies forming the BOA in Sierra de Baza are the following: a) serpentinized lherzolites where relics of diopsidic clinopyroxene and spinel are preserved and serpentinized harzburgites in which acicular aggregates of olivine and orthopyroxene can be recognized (Fig. 1A); b) gabbros, crossed by dolerite dikes, mostly metamorphosed in eclogites and/or amphibolites, sometimes preserving plutonic or hypabyssal structures (Fig. 1B, C and D); c) basalts, which sometimes preserve flow structures and padded forms (pillow lavas, Fig. 1D); d) micaschists (Fig. 1E and F) and micaceous quartzites, with transition to calcschists with ankerite nodules, which are more abundant in the upper part. The gabbros, basalts and sedimentary lithologies in Sierra de Baza are similar to the lithologies from other outcrops of the BOA previously described by Puga et al. (2017). As mentioned above, meta-ultramafic rocks are mostly serpentinites sometimes preserving clinopyroxene relics characterized by chemical composition similar to that of fertile spinel lherzolites. The primary mineral association was constituted by olivine, clinopyroxene (diopside), orthopyroxene (enstatite), chromium-spinel, replaced by antigorite, chromium-magnetite and chlorite, talc and minor tremolite-actinolite. The antigorite matrix, which often surrounds the porphyroblasts of the other metamorphic minerals, is probably derived from olivine crystals. Chromium chlorite and chromium magnetite aggregates (Fig. 2A-1 and A-2), which probably replaced pre-existing chromium spinel, together with diopside and tremolite, were formed in successive, high and medium pressure metamorphic events. Clinohumite can also be observed (Lopez Sanchez-Vizcaıno et al., 2005). Serpentinized lherzolites generally contain antigorite, penninite, chromium and aluminium magnetite, diopsidic-clinopyroxene, titano-clinohumite and olivine (Fig. 2A-1). Serpentinized harzburgites generally contain antigorite, penninite, chromium magnetite and aluminum magnetite, talc, clinochlore and relics of olivine and orthopyroxene (Fig. 2A-2).

Meta-mafic rocks are abundant in Sierra de Baza, especially in the western sector, and are mainly eclogites and amphibolites derived from gabbros and dolerites. Samples preserved porphyric, gabbroid or doleritic igneous structures, mainly constituted by intergrowth of plagioclase and pyroxene crystals of different sizes, together with olivine

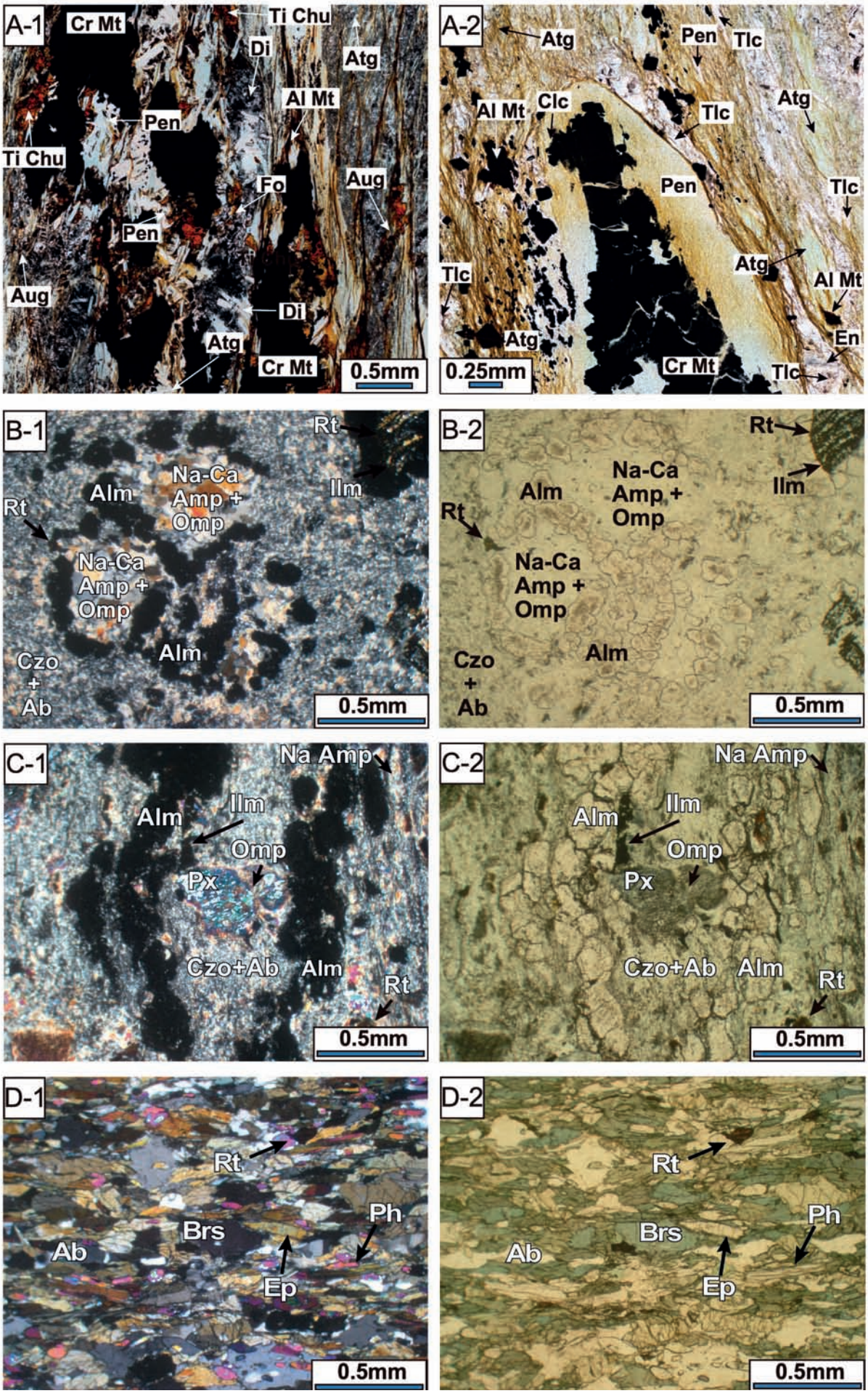
A-1
Cr Mt
Ti Chu
Di
Atg
Al Mt
Pen
Ti Chu
Fo
Aug
Pen
Aug
Di
Atg
Cr Mt
0.5mm
A-2
Atg
Pen
Tlc
Al Mt
Clc
Tlc
Atg
Pen
Tlc
Atg
Tlc
Al Mt
Atg
En
Cr Mt
Tlc
0.25mm
B-1
Rt
Alm
Na-Ca Amp + Omp
Ilm
Rt
Na-Ca Amp + Omp
Czo + Ab
Alm
0.5mm
B-2
Rt
Ilm
Alm
Na-Ca Amp + Omp
Rt
Na-Ca Amp + Omp
Czo + Ab
Alm
0.5mm
C-1
Na Amp
Alm
Ilm
Omp
Px
Czo+Ab
Alm
Rt
0.5mm
C-2
Na Amp
Alm
Ilm
Omp
Px
Czo+Ab
Alm
Rt
0.5mm
D-1
Rt
Ph
Brs
Ab
Ep
0.5mm
D-2
Rt
Ph
Brs
Ab
Ep
0.5mm

(Fig. 1B, C and D). The minerals that constitute igneous parageneses have been scarcely preserved in studied samples and can be identified only by microtextural analysis in some meta-basalts and meta-gabbros of the Cóbdar ophiolite, where relics of igneous parageneses formed by plagioclase, olivine ± clinopyroxene (augite) and ilmenite are recognized (Puga et al., 1999a; 2000; Puga 2005). Many of the meta-mafic rocks from Sierra de Baza show a great mineralogical complexity developed by the superposition of different post-magmatic processes throughout their evolution. The eclogites with porphyroblastic texture show aggregates of large, variously oriented omphacitic pyroxene and, to a lesser extent, garnet crystals, in a matrix formed by albite and epidote microcrystal intergrowth resulting from the metamorphic transformation of plagioclase. In the matrix of eclogites remnants of pristine ilmenite are found, together with more abundant rutile aggregates (Fig. 2B-1 and B-2). In many cases rutile crystals are present as small needles included in omphacite, indicating its formation during eclogitic metamorphism from preexisting ilmenite. A common feature is the formation of hydrated minerals at the edges of omphacite and garnet, typical of amphibolite and green schists facies parageneses, which partially superimposed the eoalpine eclogitic mineral assemblages during the subsequent mesoalpine and neoalpine episodes. These retrometamorphic minerals are fundamentally sodium-calcium amphibole and colorless mica (phengite). Crowns of almandine garnet that surrounds polymorphic aggregates mainly formed by omphacite and amphibole, are generally surrounded by aggregates of fine-grained albite and clinozoisite (Fig. 2B-1 and B-2), and amphibolitized eclogites also include symplectitic textures. Some of the meta-basalts derive from massive lavas mainly with columnar jointing and, to a lesser extent, pillow lavas and subvolcanic dikes. Meta-basalts usually preserve variolitic or porphyritic textures, although the primary igneous phenocrysts and the matrix have been completely replaced by metamorphic minerals during metamorphism in the eclogitic or amphibolitic facies (Fig. 2C-1 and C-2). In spite of the metamorphic recrystallization, the typical tholeiitic crystallization sequence, in which olivine is followed by a plagioclase and clinopyroxene can still be envisaged. Augitic clinopyroxene is generally replaced by omphacite and rutile, whereas plagioclase is mainly transformed into an aggregate of clinozoisite and paragonite, and, to a lesser extent, in glaucophane, during eclogitic metamorphism. The eclogitic mineral assemblage was affected by retrograde metamorphism in the Ab-Ep amphibolitic facies, forming albite, pistacite and various types of amphiboles, such as pargasite, edenite and tremolite, which formed at the expenses of the omphacite. The almandine shows edges characterized by symplectitic texture made of aggregates of Na-Ca amphibole crystals and phengite. Plagioclase is replaced by intergrowth of clinozoisite and albite (Fig. 2C-1 and C-2) or paragonite. Figs. 2D-1 and D-2 show an Ab-Ep amphibolite (Cani-26A) that presents an equilibrium mineral association of amphibole, epidote, albite, mica, chlorite and quartz. The mineral preferential orientation of metabasites, including the Na-Ca amphibole porphyroblasts forming a nematoblastic texture, follow the main foliage of the micashist, suggesting a common metamorphic process.

RESULTS

Whole rock geochemistry

The Sierra de Baza meta-mafic rocks

The major and trace element, as well as Sr-Nd isotope composition of the meta-mafic rocks from the Sierra de Baza is reported in Tables 3, 4 and 5. The MgO content is quite variable for the different lithotypes, ranging from 4.53 to 10.14 (wt%) in the meta-(Fe)-gabbros, from 2.99 to 9.10 (wt%) in meta-(Fe)-dolerites and from 2.99 to 11.94 (wt%) in meta-basalts. The TiO_2 content ranges from 0.83 to 3.91 (wt%) in the meta-(Fe)-gabbros, from 0.99 to 3.24 (wt%) in meta-(Fe)-dolerites and from 1.13 to 2.49 (wt%) in meta-basalts. The LOI content is generally low, varying from 0 to 3.33 (wt%) in the meta-(Fe)-gabbros, from 0.77 to 3.77 (wt%) in meta-(Fe)-dolerites (with the exception one sample showing a maximum value of 5.07 wt%) and from 0.60 to 4.69 (wt%) in meta-basalts.

In the TAS (Total Alkali-Silica) classification diagram, meta-mafic rocks show subalkaline (basalt and andesitic basalt) to transitional and alkaline (basanite, basalt and trachybasalt) affinities (Fig. 3A). However, in the Nb/Y *vs* Ti/Zr binary diagram (Pearce, 1996), which is based on the ratios of less mobile element, more appropriate for the classification of meta-mafic rocks, Sierra de Baza samples show a subalkaline affinity (Fig. 3B). This is also confirmed by the tholeiitic differentiation trend defined by these rocks on the ternary diagram of Irvine and Baragar (1971; Fig. 3C). In the Ti/1000 *vs* V tectonomagmatic diagram (Fig. 4A; Pearce, 2003) Sierra de Baza meta-mafic rocks show a typical MORB affinity, similar to other Alpine ophiolites such as the Ligurides, those from Corsica, Gets, Platta (Bill et al., 2000; Desmurs et al., 2002; Saccani et al., 2008; Montanini et al., 2008), and to other BOA occurrences (Puga et al., 2017). The amphibolitized sample Cani-300 shows comparatively higher Ti and V content probably deriving from a higher differentiation of the basaltic magma following the tholeiitic trend. On the other hand, samples Cani-288A and CH-12 plot outside of the MORB field in the Ti/1000 *vs* V diagram, showing a comparatively higher Ti/V ratio. The Sierra de Baza meta-mafic rocks have been also plotted in the Nb/Yb *vs* Th/Yb tectonomagmatic discrimination diagram of Pearce (1982), in which they mostly plot in the MORB-OIB mantle array, conforming to E-MORB-type

Fig. 2 - Plane polarized (right) and crossed-polarized (left) light photomicrographs of Sierra de Baza meta-mafic and meta-ultramafic rocks. A-1: Serpentinite (Cani-284) after lherzolite formed by diopside (Di) and forsteritic olivine (Fo) in a serpentine (Srp) matrix. It also shows aggregates of chromium magnetite (Cr Mt) altered to penninite (Pen) and Ti-clinohumite (Ti-Chu) coexisting with Fo, compatible with high P Eoalpine conditions; A-2: Serpentinite (Cani-277) after secondary harzburgite, with large Mt crystals, surrounded by Atp-type Srp, and minor chlorite (Chl) and talc (Tlc). Transformation of Cr Mt to Penninite (Pen) at the edge is observed. Enstatitic orthopyroxene (En) in a matrix formed by antigorite (Atg) and Tlc; B-1 and B-2: Eclogite after pyroxene-olivine gabbro, partially amphibolitized (CH-43) with coronitic texture where olivine has been replaced by omphacite (Omp) + almandine (Alm), the former subsequently transformed into sodium-calcium amphibole (Na-Ca Amp); C-1 and C-2: Eclogite with fluidal texture, replaced by an aggregate of very fine-grained clinozoisite (Czo) and albite (Ab) after igneous plagioclase, alternated with Alm and Omp beds originated in the eclogitic facies (RA-33B); D-1 and D-2: Amphibole epidotite with transition to amphibolite (Cani-26A), originated at the contact between doleritic dike and intruded carbonate sediments. This amphibolite is composed of Brs, Ab, Ep, phengite (Ph) and rutile (Rt). Abbreviations according to Kretz (1983).

Table 1 - Petrographic characterization and geographic location of the meta-mafic rocks from the Sierra de Baza.

Sample	Protolith	Metamorphic assemblage	Metamorphic texture	Metamorphic rock	Longitude	Latitude	Elevation
Cani-5B	Gabbro	Amp Na-Ca, Ab, Ep, Rt, Ttn, Mt	Porphyroblastic	Ab-Ep Amphibolite	520700	4131833	1527
Cani-5C	Gabbro	Amp Na, Ab, Ep, Rt, Ttn, Mt	Porphyroblastic	Ab-Ep Amphibolite	520700	4131833	1527
Cani-22	Dolerite	Brs, Hbl, Czo, Ab, Bt, Rt, Mt, Carb Fe	Porphyro-nematoblastic	Ab-Ep Amphibolite, Amphib. Calcschists	521062	4131764	1519
Cani-23	Dolerite	Brs, Ab, Ep, Mt, Rt, Chl	Grano-porphyroblastic	Ab-Ep Amphibolite	521146	4131765	1504
Cani-31	Basalt (sill)	Brs, Ab, Ep, Chl, Rt	Nematoporphyroblastic	Ab-Ep Amphibolite	518003	4131227	1483
Cani-35A	Dolerite	Amp Ca, Zo-Czo, Ab, Rt	Porphyro-nematoblastic	Ep Amphibolite	520764	4131851	1530
Cani-42	Basalt (sill)	Brs, Zo-Czo, tg, th, Ab, Ep, Chl, Rt	Nematoblastic	Ab-Ep Amphibolite	521276	4131720	1484
Cani-43	Basalt (sill)	Prg, Mg-Ktp, Ab, Czo, Rt, Ed, Carb, Sd	Grano-porphyroblastic	Ab-Ep Amphibolite	521276	4131720	1484
Cani-48	Dolerite	Amp Ca, Ab, Zo-Czo, Alm, Chl, Ph	Porphyroblastic	Garnet-epidote amphibolite	520592	4131594	1532
Cani-83	Px-Ol gabbro	Gln, Ab, Czo, Prg, Alm, Brown amp, Bt, Ilm, Rt, Ttn, Zrn	Granoblastic	Ab-Ep Amphibolite	520831	4133235	1238
Cani-136B	Basalt	Amp Ca, Ab, Ep, Rt, Mt, Qtz	Granonematoblastic	Ab-Ep Amphibolite	505157	4127561	1462
Cani-136C	Basalt	Omp, Alm, Amp Na-Ca, Czo, Ilm, Rt, Ab, Ph	Porphyro-nematoblastic	Eclogite	505157	4127561	1462
Cani-137A	Ferrogabbro-ferrodolerite	Gln, Omp, Rt, Alm, Ab, Ep, Qtz	Porphyroblastic	Garnet-epidote amphibolite	505046	4127410	1471
Cani-137B	Ferrogabbro-ferrodolerite	Gln, Omp, Rt, Alm, Ab, Ep, Qtz	Porphyroblastic	Garnet-epidote amphibolite	505046	4127410	1471
Cani-138	Basalt	Gln, Omp, Rt, Alm, Ttn	Porphyroblastic	Partially amphibolitized eclogite	506648	4127121	1602
Cani-139A	Px gabbro	Omp, Gln, Ab, Alm, Czo, Rt, Ilm, Carb, Colorless Mica	Porphyroblastic, Coronitic	Coronitic eclogite	506648	4127121	1602
Cani-139B	Px gabbro	Omp, Alm, Ab, Zo-Czo, Rt, Ilm	Coronitic	Coronitic eclogite	506648	4127121	1602
Cani-139C	Px gabbro	Omp, Amp Na-Ca, Ab, Alm, Rt, Czo, Bt, Ep	Porphyroblastic	Eclogite	506648	4127121	1602
Cani-250B	Dolerite	Gln, Alm, Rt, Amp Na-Ca, Ep, Colorless Mica	Porphyroblastic	Partially amphibolitized eclogite	508220	4127843	1597
Cani-253	Basalt (Pillow lava)	Amp Ca, Ab, Cpx, Ep, Carb	Porphyroblastic	Ab-Ep Amphibolite	509408	4128745	1662
Cani-281	Basalt	Amp Ca, Ep, Colorless Mica, Rt, Chl,, Ttn	Nematoblastic	Epidote amphibolite	521058	4131511	1515
Cani-282	Basalt	Zo-Czo, Ab, Chl, Carb	Nematoblastic	Epidotite	521058	4131511	1515
Cani-285	Dolerite	Amp Ca, Ep, Colorless Mica, Chl	Nematoblastic	Epidote amphibolite	513801	4128228	1749
Cani-288A	Dolerite (sill)	Amp Ca, Ep, Ab, Rt, Czo, Chl, Ttn, Zrn	Nematoblastic	Epidote amphibolite	513801	4128228	1749
Cani-298	Px gabbro	Omp, Alm, Amp Na-Ca, Czo, Llm, Rt, Ep	Porphyroblastic	Eclogite	508064	4127586	1557
Cani-300	Ferrodolerite	Gln, Brs, Ktp, Ab, Rt, Ep, Chl, Ilm, Qtz	Porphyroblastic	Ab-Ep Amphibolite	507928	4127809	1519
Cani-303	Basalt (sill)	Ep, Ab, Brs, Amp Na-Ca, Alm, Chl, Rt, Ilm, Bt, Qtz	Porphyro-nematoblastic	Epidote amphibolite	505109	4127255	1462
CH-10A	Gabbro	Omp, Amp Na, Rt, Ep, Ab	Porphyroblastic	Amphibolitized eclogite	506648	4127131	1598
CH-12	Px basalt	Gln, Alm, Rt, Ky, Gln, Ab, Ep	Porphyroblastic	Partially amphibolitized eclogite	506648	4127131	1598
CH-12B	Px basalt	Gln, Czo, Brown amp, Rt, Ab, Chl	Porphyroblastic	Ab-Ep Amphibolite	506648	4127131	1598
CH-21	Dolerite	Amp, Ab, Ep, Rt, Mt, Chl, Ap	Nematoblastic	Ab-Ep Amphibolite	513783	4128225	1741
CH-30	Basalt	Omp, Alm, Czo, Trm, Ab, Pg, Rt, Ilm	Porphyroblastic	Eclogite	507498	4126095	1462
CH-40	Basalt	Amp Ca, Ab, Ep, Omp, Rt, Px, Amp Na, Ilm	Porphyroblastic	Ab-Ep Amphibolite	507498	4126095	1462
CH-43	Ol gabbro	Omp, Brs, Trm, Alm, Ilm, Ab, Czo, Rt	Coronitic	Partially amphibolitized coronitic eclogite	507638	4126457	1482
CH-44	Ol-Px gabbro	Alm, Omp, Prg, Ktp, Trm, Ab, Zo-Czo, Rt, Brs, Ky, Act, Pg, Ph	Coronitic	Partially amphibolitized coronitic eclogite	507638	4126457	1482
CH-58	Dolerite	Amp Na-Ca, Alm, Czo, Ab, Ilm, Rt, Colorless Mica	Coronitic	Coronitic eclogite	507690	4126511	1462
CH-62	Px dolerite	Omp, Alm, Amp Na-Ca, Czo, Ilm, Rt, Ep	Coronitic	Coronitic eclogite	507761	4126185	1429
RA-33A	Basalt (Pillow lava)	Gln, Alm, Omp, Ab, Czo, Brown amp, Ilm, Rt	Porphyroblastic	Eclogite	507724	4126356	1452
RA-33B	Basalt (Pillow lava)	Amp Na, Alm, Omp, Rt, Ilm, Czo, Ab	Porphidoblastic	Eclogite	507724	4126356	1452

Mineral Abbreviations according to Kretz (1983): Ab- albite; Act- actinolite; Alm- almandine; Amp- amphibole; Brs- barroisite; Bt- biotite; Carb- carbonate; Chl- chlorite; Cpx- clinopyroxene; Czo- clinozoisite; Ed- edenite; Ep- epidote; Gln- glaucophane; Hbl- hornblende; Ilm- ilmenite; Ktp- katophorite; Ky- dysthene; Col. Mic- colorless mica; Mt- Magnetite; Omp- omphacite; Ph- phengite; Pg- paragonite; Prg- pargasite; Qtz- quartz; Rt- rutile; Sd- siderite; Trm- tremolite; Ttn- titanite; Zo- zoisite; Zrn- zircon.

Table 2 - Petrographic characterization and location of the meta-ultramafic rocks from Sierra de Baza.

Sample	Protolith	Metamorphic assemblage	Metamorphic texture	Metamorphic rock	Longitude	Latitude	Elevation
Cani-4A	lherzolite	Atg, Tr, Chr Mt, Chl, Carb	Porphyroblastic, veined	Serpentinite	521407	4131896	1520
Cani-4C	harzburgite	Atg, Chr, Mt, Tr	Porphyroblastic, veined	Serpentinite	521407	4131896	1520
Cani-4D	harzburgite	Atg, Tlc, Chr Mt, Tr	Porphyroblastic	Serpentinite	521407	4131896	1520
Cani-4E	harzburgite	Atg, Chr Mt, Tur, Pist, Di, Rt, Chl Mg	Granoblastic	Serpentinite, chlorite schist	521407	4131896	1520
Cani-52	harzburgite	Atg, Mt	Porphyroblastic	Serpentinite	519771	4131410	1615
Cani-53	harzburgite	Atg, Tlc, Mt, Chl	Porphyroblastic, veined	Serpentinite	519898	4131438	1589
Cani-119	lherzolite	Atg, Di, Mt,, Tr	Porphyroblastic	Serpentinite	514465	4128214	1754
Cani-277	harzburgite	Atg, Chr, Mt, Tlc, Pen, Clc, Ilm, En	Porphyroblastic, veined	Serpentinite	521261	4131697	1526
Cani-284	lherzolite	Atg, Chr, Mt, Ilm, Ti-Chu, Pen, Di, Aug, Ol	Porphyroblastic	Serpentinite	513801	4128228	1749
Cani-295	harzburgite	Atg, Chr, Mt, Tlc, Ilm, Tr	Porphyroblastic	Serpentinite	508223	4127622	1582
Cani-305	harzburgite	Atg, Chr, Mt, Chl, Tlc, Ilm	Porphyroblastic	Serpentinite	505139	4127188	1476
CH-25	harzburgite	Atg, Ilm, Tr, Rt	Porphyroblastic	Serpentinite	513801	4128228	1749
CH-27	lherzolite	Atg, Chr, Mt, Tur, Tlc, Chl	Porphyroblastic	Serpentinite	513801	4128228	1749
CH-80	harzburgite	Atg, Mt, Tr, Tlc, Chl, Act	Porphyroblastic, veined	Serpentinite	503737	4127681	1424
CH-84	lherzolite	Atg, Chr, Mt, Di, Rt, Chl	Porphyroblastic, veined	Serpentinite	511850	4127175	1678
CH-84B	lherzolite	Atg, Tr, Ilm	Porphyroblastic	Serpentinite	511850	4127175	1678

Mineral Abbreviations according to Kretz (1983): Act: actinolite; Atg- antigorite; Aug- augite; Carb- carbonate; Chl- chlorite; Chr Mt- chromium magnetite; Clc- clinochlore; Di- diopside; En- enstatite; Ol- olivine; Pen- penninite; Pist- pistacite; Rt- rutile; Tcl- talc; Trm- tremolite; Tur- tourmaline.

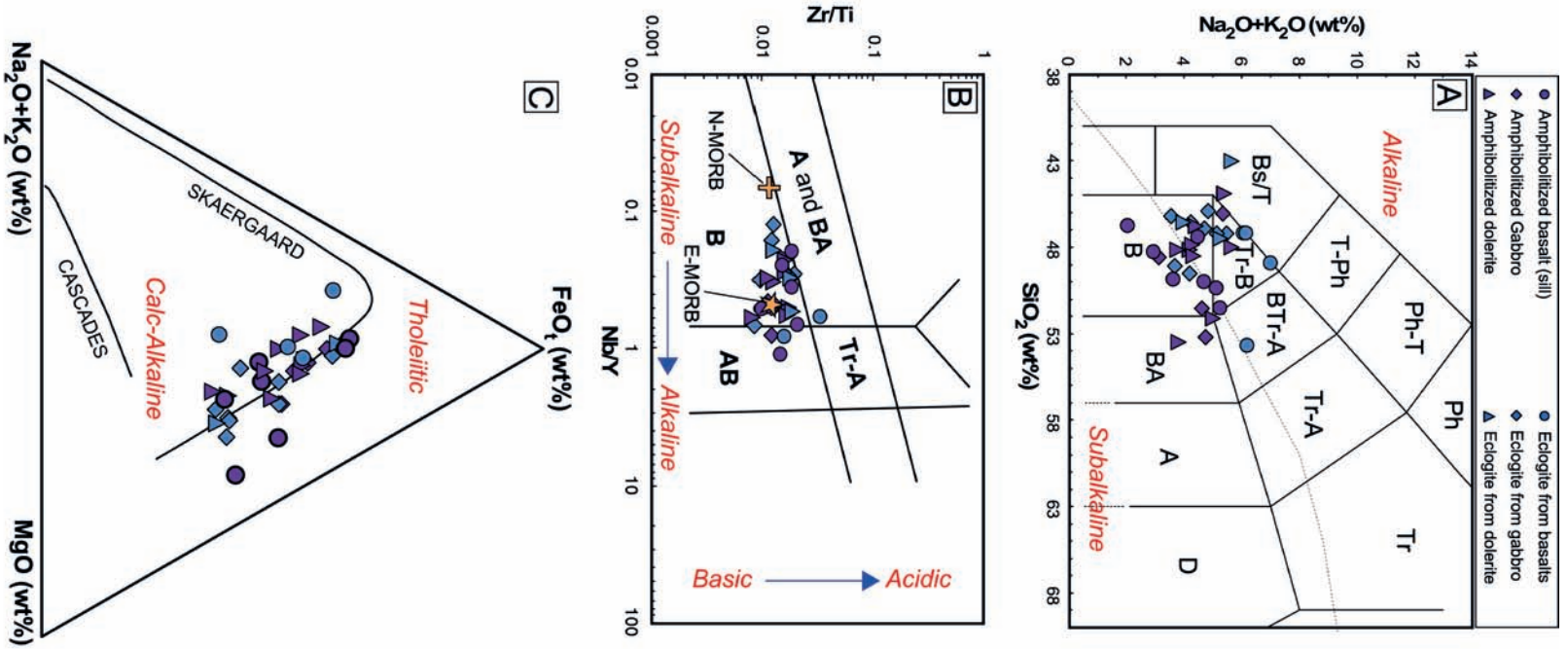

Fig. 3 - Geochemical affinity of the Sierra de Baza meta-mafic rocks, based on: A) Total Alkali-Silica (TAS) binary diagram (Le Bas and Streckeisen, 1991). B) Nb/Y *vs* Zr/Ti binary diagram (Pearce, 1996, modified from Floyd and Winchester, 1975) and C) FeOt-(NaO+K$_2$O)-MgO ternary diagram (Irvine and Baragar, 1971). B- basalt; BA- basaltic andesite; A- andesite; D- dacite; Tr-B- trachybasalt; BTr-A- basaltic trachyandesite; Tr-A- trachyandesite; Tr- trachyte; Bs/T- basanite/tephrite; T-Ph- tephritic phonolite; Ph-T- phonolitic tephrite; Ph- phonolite; AB- alkaline basalt.

Table 3 - Major and trace element composition of the Sierra de Baza meta-gabbros and meta-ferrogabbros.

	Meta-gabbros										Meta-ferrogabbros	
Metamorphic Rock	Ab+Ep amphibolite	Ab+Ep amphibolite	Ab+Ep amphibolite	Eclogite	Cor. Eclogite	Eclogite	Amph. Eclogite	Cor. Eclogite	Cor. Eclogite	Eclogite	Amphibolite	Cor. Eclogite
Protolith	Gabbro	Gabbro	Px-Ol gabbro	Px gabbro	Px gabbro	Px gabbro	Gabbro	Gabbro	Px-Ol gabbro	Px gabbro	Ferrogabbro	Ferrogabbro
#	18	19	20	21	22	23	24	25	26	27	28	29
Sample	Cani-5B	Cani-5C	Cani-83	Cani-139A	Cani-139B	Cani-139C	CH-10A	CH-43	CH-44	Cani-298	Cani-137A	Cani-137B
SiO_2 (wt%)	53.33	49.90	47.49	45.93	45.78	46.67	48.92	46.20	48.65	44.84	45.56	46.78
TiO_2	1.85	2.08	1.33	1.11	0.93	1.69	1.46	1.59	1.41	0.83	3.91	3.90
Al_2O_3	13.65	13.90	16.37	16.82	18.16	17.31	16.75	16.59	15.66	19.40	12.66	11.46
$Fe_2O_{3(tot)}$	12.63	13.20	9.93	11.63	8.82	8.95	8.71	9.29	11.53	8.19	14.77	16.49
MnO	0.06	0.07	0.10	0.21	0.14	0.17	0.05	0.16	0.24	0.08	0.15	0.29
MgO	6.54	4.53	6.68	7.17	10.14	6.84	9.19	9.75	7.90	9.24	6.49	5.69
CaO	7.08	8.32	12.53	10.25	11.28	11.24	9.25	10.94	9.90	10.22	9.55	8.57
Na_2O	4.09	4.11	2.88	4.28	3.17	4.18	3.71	3.68	3.29	4.41	4.95	4.88
K_2O	0.63	0.35	0.16	0.29	0.31	1.22	0.39	0.50	0.34	0.30	0.31	0.18
P_2O_5	0.14	0.21	0.16	0.14	0.26	0.49	0.16	0.35	0.10	0.08	0.45	0.77
LOI	0.00	3.32	2.23	1.42	0.41	0.82	1.41	0.38	0.97	1.97	0.83	0.65
Sum	100.00	99.99	99.86	99.25	99.40	99.57	100.00	99.43	99.99	99.55	99.63	99.63
Rb (ppm)	4.42	1.71	0.82	2.98	1.39	15.5	2.16	3.16	4.06	4.12	2.05	1.51
Sr	217	217	781	58.1	345	bdl	180	151	135	214	bdl	74.0
Ba	158	89.9	58.1	1691	62.5	bdl	44.5	22.4	205	9.52	bdl	135
Sc	47.8	51.7	33.0	28.6	18.9	bdl	26.3	32.4	34.1	20.9	bdl	62.7
V	263	307	187	177	132	228	168	187	201	116	870	815
Cr	289	337	377	397	631	317	300	461	294	387	150	150
Co	51.1	71.6	45.4	33.9	34.5	bdl	60.6	76.5	123	52	bdl	61.2
Ni	34.1	22.3	83.2	111	238	115	138	226	114	282	87.0	33.0
Cu	11.6	17.1	8.70	7.20	32.1	bdl	3.60	6.54	5.10	7.18	0.00	6.00
Zn	10.8	20.7	1.50	36.0	53.6	bdl	13.7	45.5	16.2	27.6	102	100
Y	12.6	35.0	17.4	20.2	13.7	18.0	13.9	22.2	18.6	15.7	33.5	57.0
Nb	10.0	17.0	8.00	3.24	3.88	bdl	9.40	6.50	5.80	1.94	bdl	28.9
Ta	0.38	0.99	0.25	0.28	0.36	0.43	0.26	0.65	0.30	0.22	0.49	0.54
Zr	131	162	89	79	106	153	72	165	79	62	206	282
U	0.22	0.44	0.21	0.10	0.06	0.44	0.23	0.13	0.21	0.22	0.37	0.41
Th	2.24	2.05	0.27	0.27	0.22	0.91	0.35	0.35	0.27	0.13	0.89	1.31
Pb	4.00	4.70	4.70	0.58	0.98	bdl	0.80	0.38	1.00	1.08	bdl	1.80
La	2.76	10.29	5.43	1.79	4.46	15.3	5.16	7.72	4.18	3.11	11.4	14.6
Ce	6.55	22.6	13.3	4.30	11.0	27.4	11.4	19.3	10.3	8.33	28.3	35.4
Pr	0.93	2.97	1.88	0.63	1.53	4.07	1.57	2.70	1.55	1.29	4.16	5.11
Nd	4.53	13.52	9.26	3.18	7.02	15.71	7.63	12.4	8.06	6.50	21.3	25.8
Sm	1.34	3.62	2.63	1.16	1.82	4.55	2.16	3.29	2.69	1.98	6.30	7.37
Eu	0.45	1.13	1.06	0.27	0.77	1.44	0.90	1.35	1.18	0.86	1.95	2.16
Gd	1.54	4.24	2.93	1.84	2.03	4.28	2.35	3.60	3.21	2.32	6.66	8.00
Tb	0.33	0.92	0.59	0.38	0.34	0.77	0.46	0.58	0.65	0.40	1.25	1.63
Dy	1.99	5.57	3.21	3.09	2.07	3.88	2.46	3.67	3.50	2.70	6.39	9.14
Ho	0.46	1.28	0.67	0.72	0.47	0.77	0.52	0.78	0.72	0.58	1.32	2.00
Er	1.41	3.72	1.80	1.90	1.26	1.97	1.37	2.11	1.93	1.56	3.50	5.57
Tm	0.25	0.63	0.28	0.30	0.21	0.31	0.21	0.33	0.30	0.23	0.56	0.91
Yb	1.54	3.73	1.60	1.80	1.21	1.77	1.15	1.94	1.80	1.37	3.20	5.42
Lu	0.21	0.51	0.22	0.26	0.17	0.24	0.16	0.29	0.25	0.20	0.47	0.80

Table 4 - Major, trace element composition of the Sierra de Baza meta-dolerites and meta-ferrodolerites.

	Meta-dolerites											Meta-ferrodolerites
Metamorphic Rock	Ab+Ep amphibolite	Ab+Ep amphibolite	Ab+Ep amphibolite	Ab+Ep amphibolite	Ep amphibolite	Amph. Eclogite	Ep amphibolite	Ep amphibolite	Ab+Ep amphibolite	Eclogite	Eclogite	Ab+Ep amphibolite
Protolith	Dolerite	Dolerite	Dolerite	Dolerite	Dolerite	Dolerite	Dolerite	Dolerite	Dolerite	Dolerite	Dolerite	Ferrodolerite
#	30	31	32	34	35	36	37	38	39	40	31	42
Sample	Cani-22	Cani-23	Cani-35A	Cani-48	Cani-95	Cani-250B	Cani-285	Cani-288A	CH-21	CH-58	CH-62	Cani-300
SiO_2 (wt%)	44.90	47.00	52.27	47.25	46.67	42.65	46.10	47.67	50.87	46.67	45.81	44.28
TiO_2	1.68	1.29	1.16	2.01	0.99	1.33	1.88	2.30	2.18	1.51	1.33	3.24
Al_2O_3	19.69	19.75	12.08	15.99	19.89	15.68	17.91	16.81	16.79	15.83	18.23	13.93
$Fe_2O_{3(tot)}$	9.99	8.45	10.01	11.14	6.17	17.26	11.42	10.12	10.58	9.13	7.79	15.32
MnO	0.21	0.08	0.18	0.17	0.10	0.40	0.11	0.16	0.14	0.20	0.12	0.10
MgO	2.99	5.38	4.43	5.60	6.61	5.19	7.97	4.76	4.05	8.81	9.10	7.67
CaO	11.92	11.34	13.61	10.25	12.66	9.30	5.13	12.99	7.74	10.54	11.67	8.37
Na_2O	3.08	2.92	3.67	5.30	4.09	5.15	3.55	3.53	4.70	4.13	3.54	4.87
K_2O	1.11	1.14	0.04	0.24	0.05	0.44	0.55	0.17	0.16	1.03	0.38	0.41
P_2O_5	0.36	0.17	0.02	0.35	0.16	1.58	0.30	0.38	0.26	0.31	0.32	0.32
LOI	3.77	2.48	2.54	1.39	2.39	0.77	5.07	0.89	2.54	1.19	0.98	0.69
Sum	99.69	100.00	100.01	99.70	99.77	99.73	99.99	99.78	100.01	99.34	99.25	99.20
Rb (ppm)	20.7	19.7	0.24	2.38	0.45	2.43	5.17	1.54	3.66	9.42	1.47	3.55
Sr	573	934	312	185	412	60.2	209	393	282	176	468	132
Ba	201	125	35.5	15.1	10.8	bdl	89.5	10.3	123	97.2	132	54.6
Sc	31.9	21.0	32.9	39.2	18.8	bdl	29.4	35.1	36.4	28.4	24.2	50.0
V	206	165	186	265	129	174	255	242	316	174	149	378
Cr	253	238	324	297	446	331	230	183	94.7	499	293	26.7
Co	58.9	48.9	86.2	44.1	50.9	bdl	54.2	55.0	53.6	86.7	85.7	79.5
Ni	90.1	76.4	138	129	172	0.00	311	117	184	195	207	233
Cu	162	3.60	5.10	8.53	43.9	0.00	66.0	29.5	114	6.71	26.4	28.0
Zn	51.7	0.70	113	68.6	43.7	0.0	94.3	102	171	47.8	56.4	81.5
Y	24.3	24.6	16.3	39.5	16.2	116	32.5	35.2	35.7	23.7	19.0	28.6
Nb	12.1	8.00	9.60	8.80	3.63	22.1	16.2	9.87	20.5	12.9	5.84	8.81
Ta	0.94	0.16	0.36	0.71	0.36	0.33	0.25	0.81	1.04	1.12	0.60	0.62
Zr	124	95	56	200	92	100	194	218	218	170	140	212
U	0.27	0.32	0.29	0.25	0.13	0.04	0.55	0.34	0.54	0.22	0.12	2.06
Th	0.74	0.51	0.84	0.64	0.47	0.05	0.97	0.60	1.13	0.68	0.33	0.46
Pb	3.21	3.30	10.5	2.27	1.63	bdl	3.60	7.96	37.0	0.61	0.99	3.10
La	9.26	8.73	7.62	8.18	4.70	0.32	11.3	9.22	12.7	9.63	6.89	18.7
Ce	20.1	20.4	17.2	21.3	11.9	0.63	27.8	24.1	27.3	21.8	17.4	38.5
Pr	2.67	2.84	2.07	3.18	1.77	0.09	3.89	3.62	4.19	2.85	2.43	4.48
Nd	12.3	13.5	9.45	15.7	8.62	0.46	18.5	17.0	20.2	12.7	11.1	18.5
Sm	3.55	3.47	2.40	4.71	2.43	0.18	4.93	4.89	5.46	3.21	2.91	4.20
Eu	1.52	1.40	0.79	1.66	0.97	0.11	1.62	1.61	1.75	1.20	1.18	1.48
Gd	3.99	3.77	2.58	5.49	2.74	0.81	5.35	5.61	5.81	3.49	3.17	4.37
Tb	0.66	0.73	0.51	0.92	0.44	0.66	1.06	0.92	1.15	0.57	0.52	0.73
Dy	4.10	3.99	2.75	6.26	2.65	10.20	5.79	6.16	6.36	3.76	3.13	4.85
Ho	0.88	0.86	0.59	1.48	0.56	4.05	1.22	1.34	1.36	0.84	0.68	1.08
Er	2.34	2.34	1.60	4.53	1.45	15.1	3.30	3.58	3.79	2.30	1.78	2.90
Tm	0.36	0.36	0.25	0.66	0.24	2.70	0.52	0.54	0.62	0.36	0.29	0.46
Yb	2.17	1.98	1.43	4.59	1.38	16.01	2.94	3.26	3.67	2.12	1.68	2.66
Lu	0.32	0.26	0.20	0.78	0.19	2.27	0.40	0.48	0.51	0.31	0.25	0.38

Table 5 - Major and trace element composition of the Sierra de Baza meta-mafic rocks.

	Meta-basalts										Meta-basalts (sills)		
Metamorphic Rock	Ab+Ep amphibolite	Amph. Eclogite	Amphibolite	Ep amphibolite	Eclogite	Ep amphibolite	Ab+Ep amphibolite	Eclogite	Eclogite	Eclogite	Eclogite	Ab+Ep amphibolite	Ab+Ep amphibolite
Protolith	Basalt	Basalt	Pillow lava	Basalt	Basalt	Basalt	Basalt	Pillow lava	Pillow lava	Basalt	Basalt	Basalt	Basalt
#	43	44	45	46	47	48	49	50	51	52	53	54	55
Sample	Cani-136B	Cani-138	Cani-253	Cani-281	CH-12	CH-12B	CH-40	RA-33A	RA-33B	ELUG-28	AUL-15	Cani-42	Cani-43
SiO_2 (wt%)	49.43	46.70	50.50	46.26	48.38	49.31	49.46			46.10	53.04	47.41	45.26
TiO_2	2.29	2.18	1.13	1.82	2.30	2.30	1.82			2.12	2.15	1.36	2.49
Al_2O_3	15.46	15.09	14.27	12.49	16.50	15.01	14.26			15.90	15.34	13.88	12.71
$Fe_2O_{3(tot)}$	11.49	12.49	9.43	9.79	7.77	10.01	8.81			15.44	12.60	13.43	14.43
MnO	0.18	0.20	0.10	0.18	0.07	0.05	0.05			0.08	0.11	0.13	0.09
MgO	2.99	5.87	5.99	11.94	6.02	6.91	8.88			6.88	2.19	10.76	4.21
CaO	12.85	9.82	11.10	14.09	10.28	9.90	9.28			4.78	6.25	8.07	11.71
Na_2O	3.42	5.17	4.68	1.84	6.58	4.18	4.64			5.51	5.69	2.45	3.98
K_2O	0.14	0.77	0.41	0.15	0.29	0.40	0.35			0.43	0.36	0.38	0.24
P_2O_5	0.64	0.43	0.22	0.14	0.57	0.36	0.42			0.28	0.85	0.16	0.19
LOI	0.87	0.71	1.82	1.04	0.60	1.57	2.04			1.52	1.19	1.98	4.69
Total	99.75	99.42	99.66	99.73	99.35	100.00	100.01			99.04	99.78	100.01	100.00
Rb (ppm)	1.44	0.10	6.69	6.92	1.64	2.92	1.22			3.33	7.68	3.26	1.66
Sr	190	bdl	553	153	61.6	170	255	132	84.2	150	275	177	195
Ba	39.2	15.0	93.0	3.09	15.0	75.9	59.8	443	634	14.0	26.4	55.0	79.2
Sc	36.4	bdl	39.0	33.8	31.7	36.6	32.0	24.3	26.1	36.8	bdl	33.0	62.3
V	313	284	327	203	246	270	290	145	155	281	188	190	440
Cr	153	355	356	407	108	163	661	218	265	224	91.0	527	113
Co	62.1	bdl	31.9	63.1	77.5	54.8	56.2	96.3	125	179	131	66.5	66.0
Ni	49.4	98.0	85.0	128	110	60.4	120	159	127	77.6	27.0	289	42.7
Cu	46.7	38.0	12.0	50.1	8.60	3.30	4.00	8.34	7.99	10.9	63.0	6.60	3.00
Zn	91.3	35.0	8.00	79.8	48.1	12.2	4.40	33.9	37.1	22.3	79.0	112	9.20
Y	48.4	21.6	22.3	26.6	23.8	20.0	35.9	18.3	18.0	25.4	49.0	20.2	21.3
Nb	9.64	bdl	8.10	6.67	20.1	22.5	24.4	3.74	3.96	10.8	28.8	10.3	11.1
Ta	0.86	0.74	0.36	0.57	1.58	0.75	0.62	0.58	0.64	1.18	2.15	0.14	0.24
Zr	249	182	120	157	207	195	222	20	25	24	417	87	141
U	0.29	0.46	0.51	0.45	1.90	0.93	0.82	0.16	0.04	0.61	1.07	0.61	0.19
Th	0.69	0.81	1.94	0.44	3.57	0.86	1.13	0.74	0.29	0.67	2.71	0.90	0.50
Pb	3.13	bdl	3.30	1.03	1.11	4.00	1.00	1.47	1.04	0.67	12.0	3.50	1.10
La	11.3	9.37	12.33	6.01	29.2	13.5	21.1	6.91	3.32	8.20	29.0	7.15	7.87
Ce	28.5	22.7	26.4	16.0	64.3	29.7	47.0	17.2	8.46	14.8	61.1	15.5	19.0
Pr	4.25	3.09	3.38	2.45	8.19	3.92	6.04	2.55	1.26	2.02	7.83	2.05	2.62
Nd	20.7	14.6	15.0	11.9	34.9	18.0	27.0	12.3	5.48	8.71	33.5	9.76	12.6
Sm	6.18	3.82	3.71	3.63	8.33	4.55	6.43	3.83	1.76	2.39	8.41	2.80	3.34
Eu	2.09	1.25	1.18	1.28	2.37	1.49	2.13	1.34	0.63	1.00	2.96	1.11	1.10
Gd	7.20	3.89	3.96	4.22	7.52	4.60	6.56	4.52	2.42	3.01	8.85	3.28	3.59
Tb	1.18	0.76	0.76	0.71	1.06	0.84	1.24	0.77	0.43	0.54	1.46	0.66	0.72
Dy	8.37	4.08	4.17	4.64	5.13	4.07	6.51	3.88	2.83	3.84	9.60	3.62	3.89
Ho	1.86	0.86	0.88	1.01	0.87	0.76	1.34	0.68	0.66	0.95	1.93	0.76	0.82
Er	5.53	2.31	2.40	2.55	2.08	1.83	3.52	1.97	1.90	2.75	4.89	2.07	2.24
Tm	0.75	0.36	0.37	0.40	0.32	0.26	0.52	0.30	0.29	0.43	0.72	0.33	0.36
Yb	5.22	1.99	2.10	2.29	2.01	1.38	2.80	1.76	1.71	2.70	4.18	1.89	2.07
Lu	0.89	0.26	0.27	0.31	0.28	0.17	0.35	0.27	0.25	0.37	0.60	0.27	0.30

and N-MORB-type mantle sources, irrespective to the superimposed type of metamorphism (Fig. 4B). However, some samples (Cani-5B, Cani-5C y CH-12) show a variable Th enrichment and plot above the MORB-OIB array. In our view, these anomalous samples reflect assimilation of sedimentary components similar in composition to the micaschists from the Sierra de Baza sedimentary sequence (Cani-286) and of the average Global Oceanic Subducting Sediments (GLOSS, Plank and Langmuir, 1998). In Fig. 4C, the Sierra the Baza meta-mafic rocks are plotted in the N-MORB normalized La_N/Sm_N *vs* La_N/Yb_N binary diagram (normalization values from Pearce, 2008). Most of the samples are characterized by a $(La/Sm)_N$ between 1.0 and 1.8, delineating a compositional trend between LREE-depleted compositions typical of ophiolitic basalts of the Alpine-Apennine domain (e.g., Corsica, Calabria and Platta) and the average of enriched mid Atlantic ridge (E-MAR) basalts from the 63°N (Wood et al., 1979). Only a minor sample subset (CH-12, CH-12B and CH-40) shows distinctive LREE enrichment being characterized by a $(La/Sm)_N$ between 1.8 and 2.1 and by $(La/Yb)_N$ over 5, thus plotting outside from the enrichment trend defined by E-MAR 63°-45°N (Wood et al., 1979). This could result either from the assimilation of sedimentary components, as proposed for the Gets ophiolites (Fig. 4C), by source enrichment, or by a comparatively low melting degree (Bill et al., 2000). In Supplementary Fig. 2A, the Sierra de Baza meta-mafic rocks are plotted in the N-MORB normalized Nb_N *vs* Th_N tectonomagmatic discrimination diagram for ophiolitic basalts and meta-basalts (Saccani, 2015). In this diagram, the studied rocks mainly plot across the E-MORB field, with few samples displaced toward the field of N- and G-MORB, the latter indicating garnet-bearing mantle source. Coherently, the Sierra de Baza rocks plotted in the chondrite-normalized $(Dy/Yb)_N$ vs $(Ce/Yb)_N$ diagram of Supplementary Fig. 2B (Saccani, 2015) mainly show an enriched E-MORB affinity, with subordinate samples showing N-MORB and G-MORB geochemical features, respectively.

To have a more general view of the whole trace element distribution, the Primitive Mantle (PM)-normalized distribution of incompatible elements of the meta-mafic rocks of Sierra de Baza is displayed in Fig. 5. The eclogitized (Fig. 5A) and amphibolitized (Fig. 5B) rocks generally show comparable element concentrations. However, a more careful view reveal that significant and distinct LILE distributions characterize the two meta-mafic lithotypes, with the eclogitized samples showing spikes in Ba, and to a lesser extent in Th, and the amphibolitized samples particularly enriched in Pb, and to a lesser extent in Sr. This results in a bimodal distribution in the Ba/Th vs Pb/Th diagram (not shown), with eclogitized samples characterized by very high Ba/Th (up to 6,300, median of 127) and low Pb/Th (median of 2), and amphibolitized samples characterized by relatively low Ba/Th (median of 61) and very high Pb/Th (up to 33, median of 4). These differences may be related to the effect of fluid metasomatism derived from the associated sediments during the different P-T-t paths suffered by these rocks (Breeding et al., 2004).

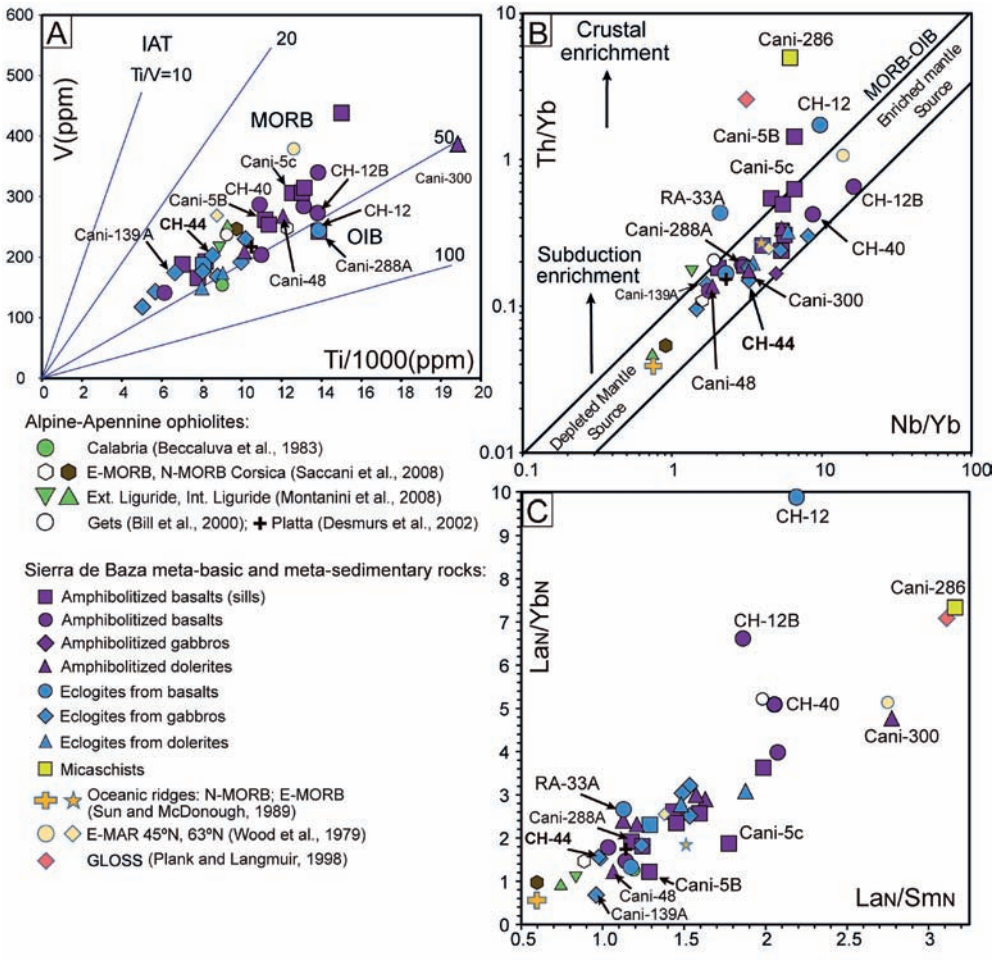

Fig. 4 -Tectonomagmatic discrimination diagrams A) Ti/1000 vs V (Pearce, 2003, modified after Shervais, 1982); B) Nb/Yb vs Th/Yb (Pearce, 1982); C) La_N/Sm_N vs La_N/Yb_N. N-MORB normalizing values are from Sun and McDonough (1989). Larger symbols refer to Sierra de Baza samples.

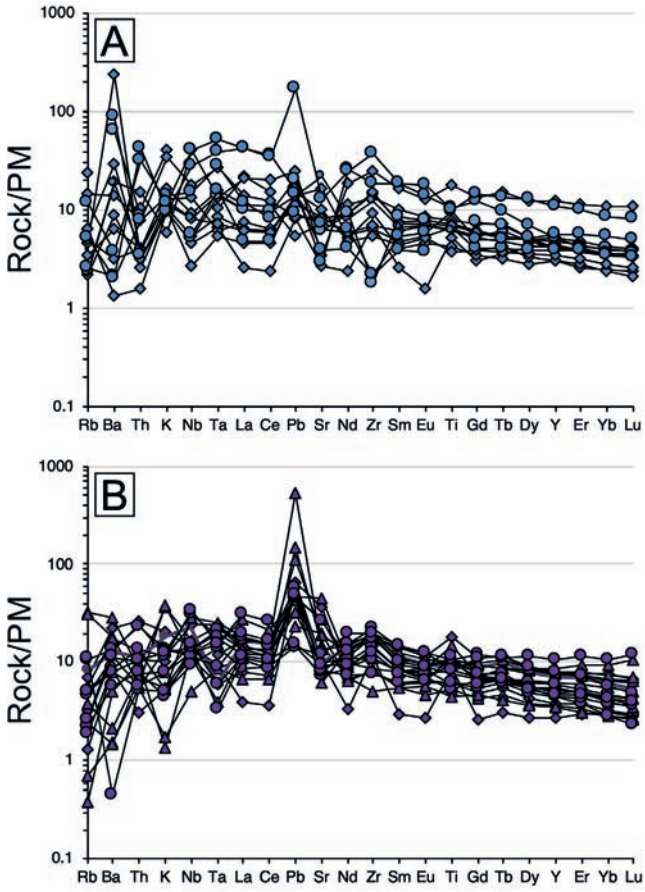

Fig. 5 - PM-normalized incompatible element distribution the of Sierra de Baza meta-mafic a) eclogitized; b) amphibolitized rocks. Normalization values and N-MORB composition are from Sun and McDonough (1989). Symbols as in Fig. 3.

The Sierra de Baza meta-ultramafic rocks

The major and trace elements composition of the meta-ultramafic rocks of the Sierra de Baza is reported in Table 6. CaO vs Al_2O_3 data are compared with other peridotites and serpentinites from the Betic Cordillera and Western Mediterranean ophiolites (Fig. 6). Serpentinized lherzolites are characterized by a limited Al_2O_3 content (3.63-4.31 wt%) coupled with a wider CaO variation (0.80-2.89 wt%), showing a scattered distribution between the trends depicted by Ronda peridotites, the Internal and External Ligurides, clinopyroxene-bearing serpentinites and serpentinized harzburgites from other BOA occurrences (Cerro de Almirez in Sierra Nevada, Puga et al., 1999b). This distribution suggests that cpx-bearing serpentinites derive from lherzolitic lithologies that locally suffered oceanic metasomatism followed by Alpine metamorphism with CaO depletion trending toward the values typical of serpentinized harzburgites. This is supported by the Al_2O_3/TiO_2 ratio (23.4 and 53.3) the average TiO_2 (0.13 wt%) and Cr (2650 ppm) contents (Table 6, see also Beccaluva et al., 1983; Pearce et al., 1984; Puga et al., 1999b; Puga, 2005). Serpentinized harzburgites from Sierra de Baza show an inverse distribution being characterized by very low CaO content (0.02-0.70 wt%) coupled with a wider Al_2O_3 variation (2.31-4.82 wt%) partially overlapping the compositional field of serpentinized harzburgites from Cerro de Almirez (Fig. 6). Noteworthy, serpentinites derive from mantle peridotite rocks that experienced variable fluid/rock interactions, which usually affect FeO and MgO contents (Deschamps et al., 2013). The composition of the Sierra de Baza serpentinites varies between 6.5 and 9.0 wt% and between 35 and 42 wt% for FeO (wt%) and MgO (wt%), respectively (Table 6), overlapping the compositional field of the abyssal peridotites of Niu (2004; Fig. 7A). In particular, the serpentinized harzburgites show a notable dispersion in

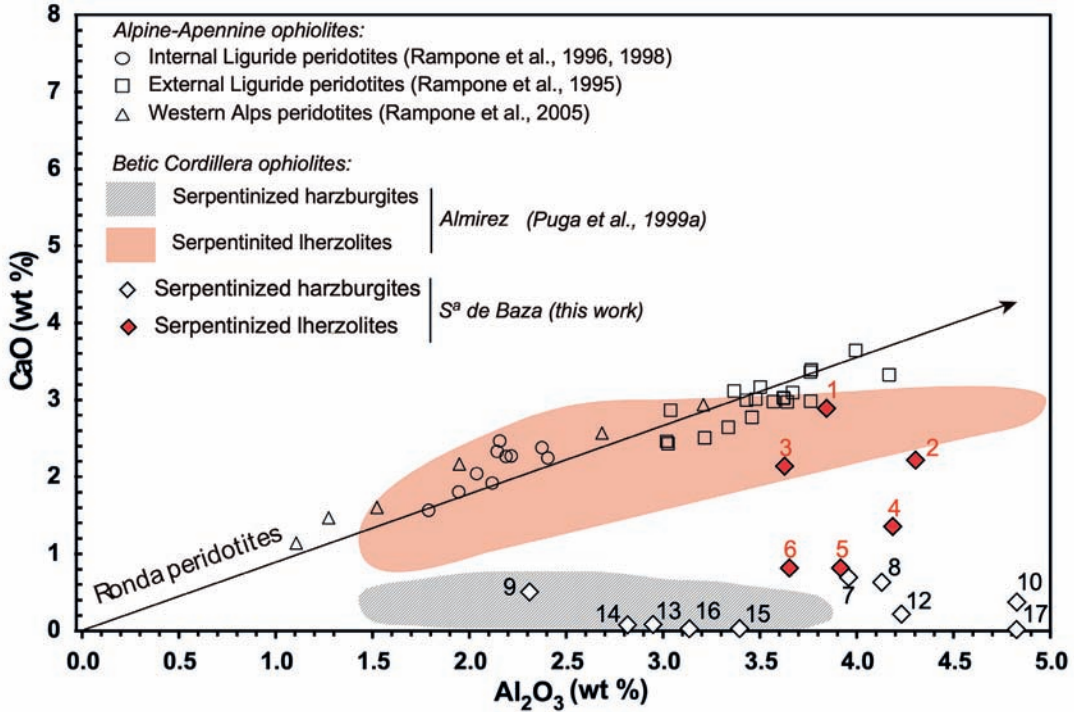

Fig. 6 - CaO vs Al_2O_3 (wt%) binary diagram reporting the compositional variation of Sierra de Baza meta-ultramafic rocks, in comparison with others from BOA (Cerro del Almirez), from Western Mediterranean ophiolitic occurrences (External and Internal Ligúrides, Western Alps), as well as from Ronda peridotite (modified from Puga et al., 1999b).

Table 6 - Major and trace element composition of the Sierra de Baza meta-ultramafic rocks.

Rock type	Meta-ultramafic															
Protolith	Lherzolite						Harzburgite									
#	1	2	3	4	5	6	7	8	9	10	12	13	14	15	16	17
Sample	CH-84B	Cani-04A	Cani-284	CH-27	Cani-119	CH-84	CH-25	Cani-04C	CH-80	Cani-04E	Cani-295	Cani-305	Cani-52	Cani-4D	Cani-53	Cani-277
SiO_2 (wt%)	39.79	42.36	41.23	40.17	41.39	41.20	41.94	41.89	41.16	41.36	41.62	41.19	41.08	46.20	42.23	44.71
TiO_2	0.15	0.13	0.11	0.12	0.07	0.08	0.06	0.09	0.04	0.10	0.08	0.09	0.039	0.15	0.03	0.12
Al_2O_3	3.49	3.88	3.23	3.68	3.47	3.23	3.48	3.65	2.03	4.23	3.75	2.60	2.48	3.04	2.75	4.39
$Fe_2O_{3(tot)}$	12.58	7.37	7.43	8.03	7.19	8.08	6.92	7.15	7.66	7.28	9.03	6.64	7.79	7.74	7.14	8.90
MnO	0.13	0.09	0.11	0.11	0.12	0.18	0.10	0.08	0.05	0.10	0.05	0.12	0.09	0.09	0.05	0.08
MgO	32.16	34.21	35.08	34.61	35.34	35.00	34.84	34.96	36.36	34.44	34.59	37.43	36.56	32.54	35.62	32.78
CaO	2.63	2.00	1.91	1.20	0.71	0.73	0.62	0.62	0.44	0.41	0.19	0.07	0.06	0.03	0.03	0.02
Na_2O	0.02	0.00	0.00	0.00	0.01	0.01	0.00	0.00	0.02	0.00	0.00	0.00	0.00	0.03	0.02	0.01
K_2O	0.01	0.00	0.01	0.00	0.01	0.01	0.00	0.01	0.00	0.03	0.00	0.00	0.00	0.01	0.00	0.00
P_2O_5	0.01	0.00	0.01	0.01	0.02	0.01	0.00	0.01	0.01	0.01	0.01	0.02	0.01	0.01	0.00	0.01
LOI	8.28	10.04	10.20	11.10	11.20	10.80	11.40	10.90	11.50	11.40	9.90	11.20	11.00	9.41	11.40	8.21
Total	99.24	100.04	99.32	99.02	100.21	99.34	99.36	99.35	99.27	99.36	99.22	99.34	99.12	99.23	99.25	99.23
Cs (ppm)	0.01	bdl	0.12	0.05	0.02	0.04	0.16	0.04	0.03	0.14	0.11	0.10	0.04	0.04	0.10	0.13
Rb	0.05	0.08	0.34	0.01	0.07	0.17	0.14	0.17	0.01	1.60	0.28	0.10	0.01	0.01	0.08	1.40
Sr	1.95	4.64	2.10	2.26	1.94	0.89	1.91	1.30	4.24	2.27	1.44	1.04	0.86	4.38	0.77	1.36
Ba	2.76	bdl	4.52	35.0	0.00	60.0	39.0	5.43	1.38	6.90	5.57	1.85	1.87	bdl	1.54	0.86
Sc	bdl	22.3	9.06	bdl	0.00	bdl	bdl	11.5	11.4	16.2	12.6	14.4	bdl	bdl	bdl	15.4
V	117	78.9	66.8	74.0	70.0	66.4	59.3	62.4	70.8	65.8	86.4	56.3	73.2	72.6	76.1	104
Cr	3233	2841	1874	2732	1675	2753	2007	1732	3402	1748	2833	2139	3216	2647	2664	2666
Co	79.0	100	93.1	174	86.0	bdl	128	69.7	97.0	54.8	110	45.7	81.0	98.0	105	62.7
Ni	1599	2097	1894	4229	1492	2019	2200	2054	2199	1169	1891	1631	2676	2161	2126	1421
Cu	62.0	41.4	27.2	64.0	37.0	54.0	105	23.8	5.03	17.0	3.48	30.1	79.0	84.0	81.0	26.2
Zn	97.0	56.7	36.1	69.0	79.0	70.0	84.0	48.0	69.9	69.2	79.4	99.5	77.0	76.0	70.0	87.1
Y	3.19	2.91	2.45	3.25	2.32	3.73	1.06	1.73	0.82	1.85	0.73	1.13	0.57	1.48	1.14	1.67
Nb	0.19	0.20	0.11	0.18	0.13	0.12	0.08	0.10	0.51	0.45	0.26	0.60	0.52	0.38	0.63	0.63
Ta	0.14	0.13	0.05	0.12	0.12	0.13	0.11	0.07	0.18	0.10	0.07	0.08	0.16	0.12	0.13	0.11
Zr	0.58	4.00	1.06	1.02	0.56	0.75	0.80	0.44	0.04	2.42	3.00	4.00	0.01	0.07	0.20	0.55
Hf	0.01	0.03	bdl	bdl	bdl	0.01	bdl	bdl	0.00	0.11	bdl	bdl	bdl	0.01	bdl	bdl
U	0.23	0.09	0.04	0.33	0.11	0.11	0.24	0.09	0.17	0.11	0.08	0.35	0.20	0.18	0.17	0.17
Th	0.11	0.01	0.02	0.03	0.25	0.09	0.03	0.04	2.71	0.41	0.07	0.12	0.09	0.05	0.09	0.31
Pb	0.34	1.50	0.63	0.56	2.00	0.41	1.47	0.33	0.90	1.93	0.37	12.45	0.42	1.33	0.83	0.66
La	0.49	0.18	0.25	0.21	0.91	0.67	0.41	0.18	0.32	0.89	0.13	0.38	0.33	0.09	0.80	0.55
Ce	0.97	0.19	0.48	0.39	2.10	0.56	0.37	0.16	0.76	1.67	0.26	0.69	0.38	0.25	0.31	0.80
Pr	0.19	0.09	0.08	0.09	0.24	0.17	0.11	0.06	0.09	0.21	0.04	0.09	0.08	0.04	0.25	0.12
Nd	0.92	0.54	0.52	0.58	1.02	0.83	0.47	0.35	0.39	0.83	0.17	0.41	0.35	0.21	0.99	0.49
Sm	0.34	0.25	0.17	0.29	0.31	0.30	0.14	0.13	0.09	0.22	0.05	0.11	0.09	0.11	0.21	0.13
Eu	0.09	0.09	0.07	0.10	0.10	0.09	0.05	0.05	0.02	0.05	0.01	0.03	0.02	0.02	0.05	0.03
Gd	0.43	0.34	0.26	0.43	0.36	0.42	0.17	0.20	0.10	0.25	0.09	0.14	0.09	0.15	0.19	0.16
Tb	0.08	0.08	0.05	0.08	0.06	0.07	0.03	0.04	0.02	0.04	0.02	0.02	0.02	0.03	0.03	0.03
Dy	0.54	0.50	0.35	0.55	0.40	0.52	0.18	0.24	0.11	0.26	0.13	0.18	0.09	0.21	0.19	0.21
Ho	0.12	0.11	0.09	0.13	0.09	0.13	0.04	0.06	0.03	0.06	0.03	0.04	0.02	0.05	0.04	0.05
Er	0.34	0.31	0.26	0.38	0.26	0.34	0.12	0.15	0.09	0.17	0.08	0.14	0.06	0.15	0.11	0.15
Tm	0.06	0.05	0.04	0.06	0.04	0.06	0.02	0.03	0.02	0.03	0.01	0.02	0.01	0.03	0.02	0.03
Yb	0.35	0.28	0.23	0.35	0.26	0.36	0.14	0.17	0.11	0.19	0.07	0.16	0.09	0.19	0.14	0.19
Lu	0.05	0.04	0.04	0.05	0.04	0.05	0.03	0.02	0.02	0.03	0.01	0.03	0.01	0.03	0.03	0.03

MgO vs FeO. The observed TiO_2 variation is in the upper range of the abyssal peridotites (Niu, 2004), and partially overlap the field abyssal serpentinites of Deschamps et al., (2013). Serpentinized lherzolites generally have a higher TiO_2 content than serpentinized harzburgites at comparable MgO (Fig. 7B approaching the value of the DM (Salters and Stracke, 2004). The MgO *vs* CaO variation of the Sierra de Baza serpentinites, reported in Fig. 7C, shows two different trends: a) the serpentinized lherzolites characterized by a decrease of MgO in parallel with an increase of CaO, plotting in the field of the abyssal peridotites and serpentinites (according to Niu, 2004 and Deschamps et al., 2013, respectively), and b) serpentinized harzburgites showing an opposite trend characterized by a marked decrease in CaO coupled to a slight decrease in MgO, possibly caused by intense ocean floor metasomatism, partially overlapping the field of abyssal peridotites (Niu, 2004). Likewise, serpentinized lherzolites from Sierra de Baza have a distinctly higher CaO (> 0.85 wt%) content, with respect to their harzburgitic counterparts (CaO < 0.85 wt%). These latter

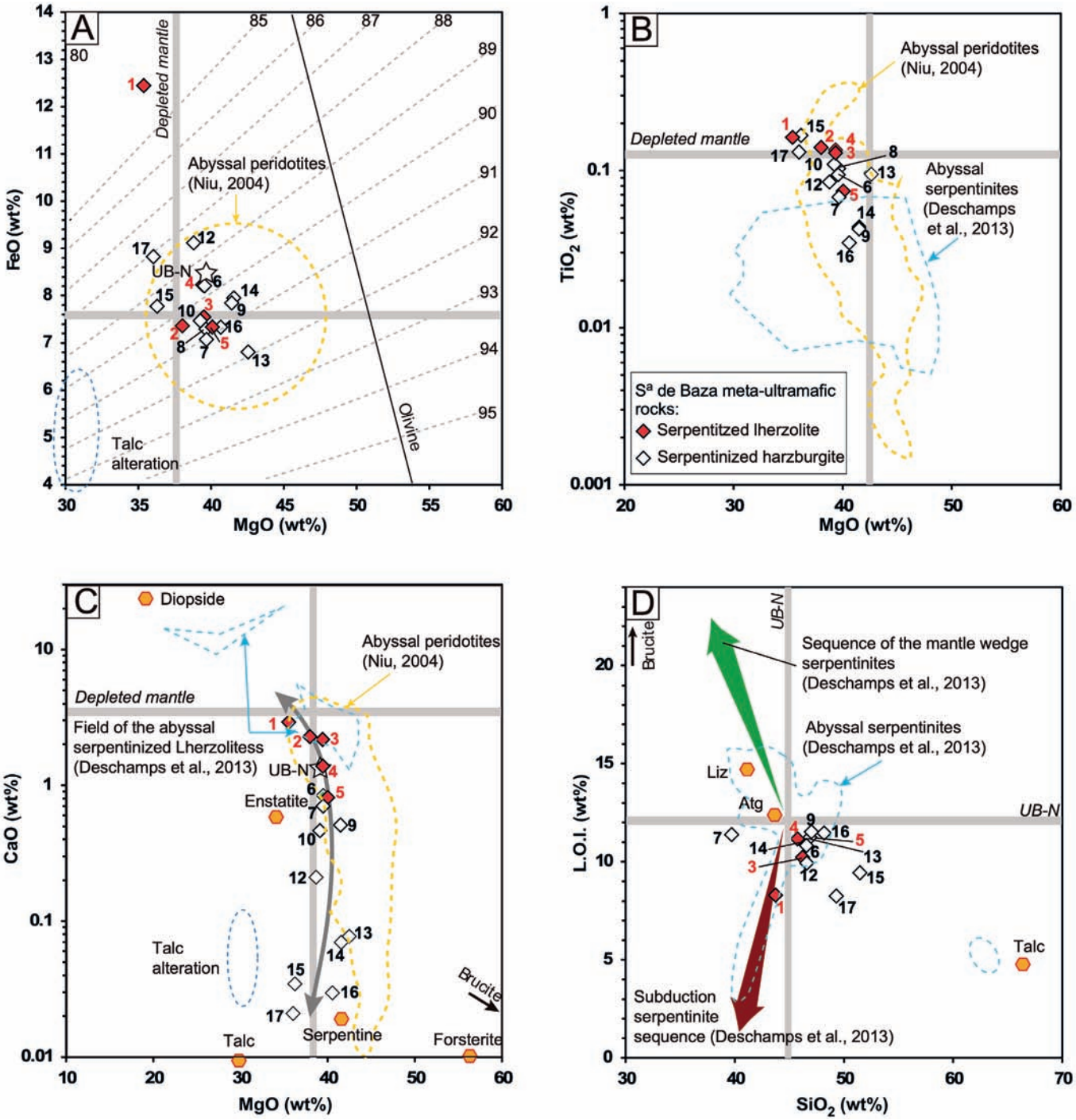

Fig. 7 - Binary diagrams of bulk rock composition (wt%) for Sierra de Baza serpentinites. A: MgO *vs*. FeO; B: MgO *vs*. TiO_2; C: MgO *vs*. CaO; D: SiO_2 against L.O.I. (loss on ignition). Estimated composition of the depleted mantle from Salters and Stracke (2004); compositions of abyssal peridotites from Niu (2004); UB-N international standard composition (star) from Georem (http://georem.mpch-mainz.gwdg.de). Modified from Deschamps et al. (2013).

depict a compositional trend toward low CaO and MgO (wt%) values, compatible with an increasing talc content (sample Cani-4D and Cani-277, Table 6). These features were also observed in the chlorite-bearing serpentinized harzburgites of Cerro del Almirez (Marchesi et al., 2013). The mineralogical variation of the Sierra de Baza serpentinites could be inherited by the pristine composition of the peridotite protoliths (lherzolites and harzburgites) as well as by ocean floor processes leading to tremolite and talc formation, as already observed in the MAR serpentinites (Allen and Seyfried, 2003; Bach et al., 2004; Paulick et al., 2006). The observed CaO depletion is a common feature of serpentinization processes (Coleman, 1977; Janecky and Seyfried, 1986; Miyashiro et al., 1969; Palandri and Reed, 2004), with the exception of local carbonate precipitation, which can increase the CaO content in the rock (e.g., Seifert and Brunotte, 1996). In Fig. 7D the Sierra de Baza samples partially overlap the composition of abyssal serpentinites (Deschamps et al., 2013), showing L.O.I. comparable or lower than the theoretical serpentine minerals (average of 12±3 wt%). The relatively low L.O.I. of the Sierra de Baza samples is incompatible with the presence of secondary brucite (low SiO_2 and very high L.O.I.), a common mineralogical feature of mantle wedge serpentinites (Deschamps et al., 2013). On the other hand, serpentinized harzburgites (in particular samples Cani-4D and Cani-277) show a trend characterized by SiO_2 increase coupled with L.O.I. decrease, typical of talc-bearing abyssal serpentinites. Most of the Sierra de Baza serpentinites are characterized by high bulk rock Al_2O_3/SiO_2 (> 0.05) and low MgO/SiO_2 (< 0.86), similar to the composition of Primitive and Depleted mantle (Supplementary Fig. 3). Serpentinized harzburgites are generally characterized by lower Al_2O_3 contents (samples CH-80, Cani-305, Cani-52, Cani-4D and Cani-53), with respect to serpentinized lherzolites depicting a trend parallel to the oceanic array (Snow and Dick, 1995; Bodinier and Godard, 2003; Niu, 2004). The presence of two samples (Cani-4D and Cani-277) showing comparatively lower MgO/SiO_2 is attributable to their enrichment in talc, a mineral that is commonly produced by the ocean floor metasomatic stage. The serpentinized lherzolites of Sierra de Baza are well clustered in a tight Al_2O_3/SiO_2 range (between 0.078 and 0.09), generally higher than that of serpentinized harzburgites, reflecting their mineralogy that include comparatively higher amounts of chlorite, epidote and the presence in one sample of tourmaline.

The primordial mantle (PM)-normalized incompatible element distribution of the Sierra de Baza serpentinites, shows particular enrichments in Pb and U together with a depletion in HFSE such as Zr and Hf, as well as in Sr (Fig. 8A). Similar elemental enrichments have been observed by other authors in subducted serpentinites (Deschamps et al., 2013). Noteworthy, the serpentinized harzburgites are characterized by lower Sr, Zr and Hf concentrations, and by higher content of U and Pb, with respect to serpentinized lherzolites.

The Chondrite (Ch)-normalized Rare Earth Elements (REE) patterns of the Sierra de Baza serpentinites are showed in Fig. 8B. Both serpentinites derived by lherzolites and from harzburgites show variable negative anomalies in Ce and Eu, the first more pronounced in serpentinized lherzolites and the second in serpentinized harzburgites. In general, the serpentinized lherzolites are richer in HREE with respect to the serpentinized harzburgites, consistent with the different amount of clinopyroxene of the former with respect to the latter.

The serpentinized lherzolites show lower LREE enrichment (La_N/Sm_N = 0.5-1.8) than the serpentinized harzburgites (La_N/Sm_N = 0.5-2.6).

Sr-Nd isotope systematics

The Sr and Nd isotopic composition of the metabasite from Sierra de Baza is reported in Tables 7 and Fig. 9. The $^{87}Sr/^{86}Sr$ varies in the range 0.70384-0.70838, whereas $^{143}Nd/^{144}Nd$ varies between 0.51247 and 0.51306. The meta-mafic rocks are characterized by a significant variation of the Sr (0.70384-0.70600) with respect to Nd (0.51306-0.51278) isotope ratios, whereas the meta-ultramafic sample (Cani-284) show the most radiogenic Sr (0.70838) and the least radiogenic Nd (0.51247) isotope composition. The distribution of Sierra de Baza meta-mafic rocks overlap with the wide range defined by other mafic and ultramafic rocks from alpine ophiolitic occurrences (internal Ligurides: Rampone et al., 1998; Alps: Stille et al., 1989; Platta: Schaltegger et al., 2002), the Mid Atlantic Ridge (Cipriani et al., 2004) and those from other ophiolitic occurrences of the Betic Cordillera (Lugros, Cóbdar, Algarrobo, Cerro del Almirez: Puga et al., 2011; 2017). The Sr isotopic values clearly reflect that the pristine geochemical budget of mantle rocks and mantle derived magmas has been modified, mainly by interaction with sea water during the ocean floor metasomatism, as invariably observed in serpentinites worldwide (Scambelluri et al., 2019).

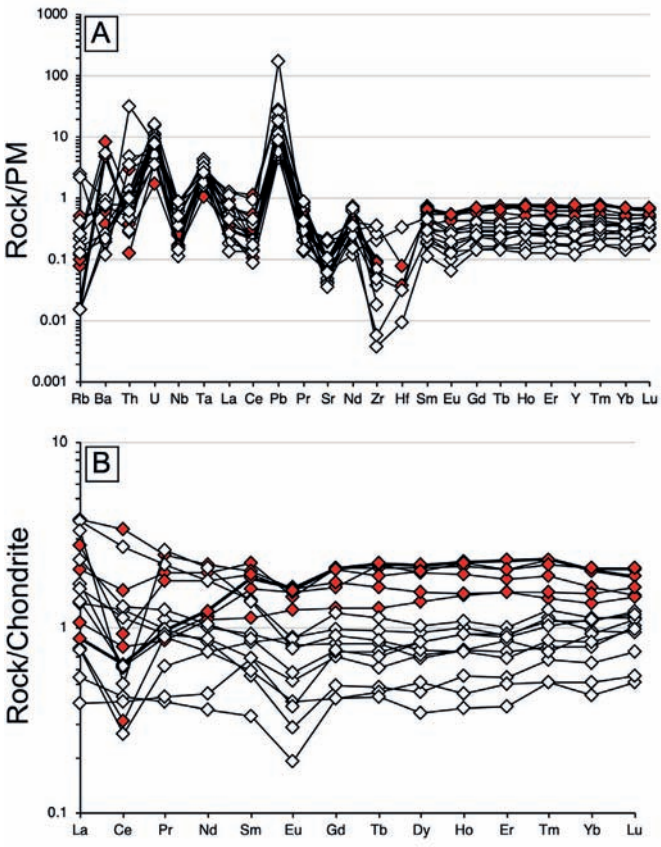

Fig. 8 - (A) Primitive Mantle (PM)-normalized incompatible element and (B) Chondrite (Ch)-normalized REE distribution the of Sierra de Baza serpentinites. Symbols as in Fig. 6. Normalization values are from Sun and McDonough (1989).

Table 7 - Sr-Nd isotope composition of the Sierra de Baza ophiolites.

Meta-mafic rock	Metamorphic Rock	Protolith	#	Sample	$^{87}Sr/^{86}Sr$	$^{143}Nd/^{144}Nd$
	Cor. Eclogite	Px-Ol gabbro	26	CH-44	0.70466	0.51305
	Eclogite	Px gabbro	27	Cani-298	0.70542	0.51302
	Ab+Ep amphibolite	Dolerite	32	Cani-35A	0.70627	0.51278
	Ab+Ep amphibolite	Dolerite	39	CH-21	0.70766	0.51298
	Ep amphibolite	Basalt	46	Cani-281	0.70384	0.51306
	Ab+Ep amphibolite	Basalt	49	CH-40	0.70545	0.51301
	Ab+Ep amphibolite	Basalt	54	Cani-42	0.70608	0.51285
Meta-ultramafic rock						
	Serpentinite	Lherzolite	3	Cani-284	0.70838	0.51247

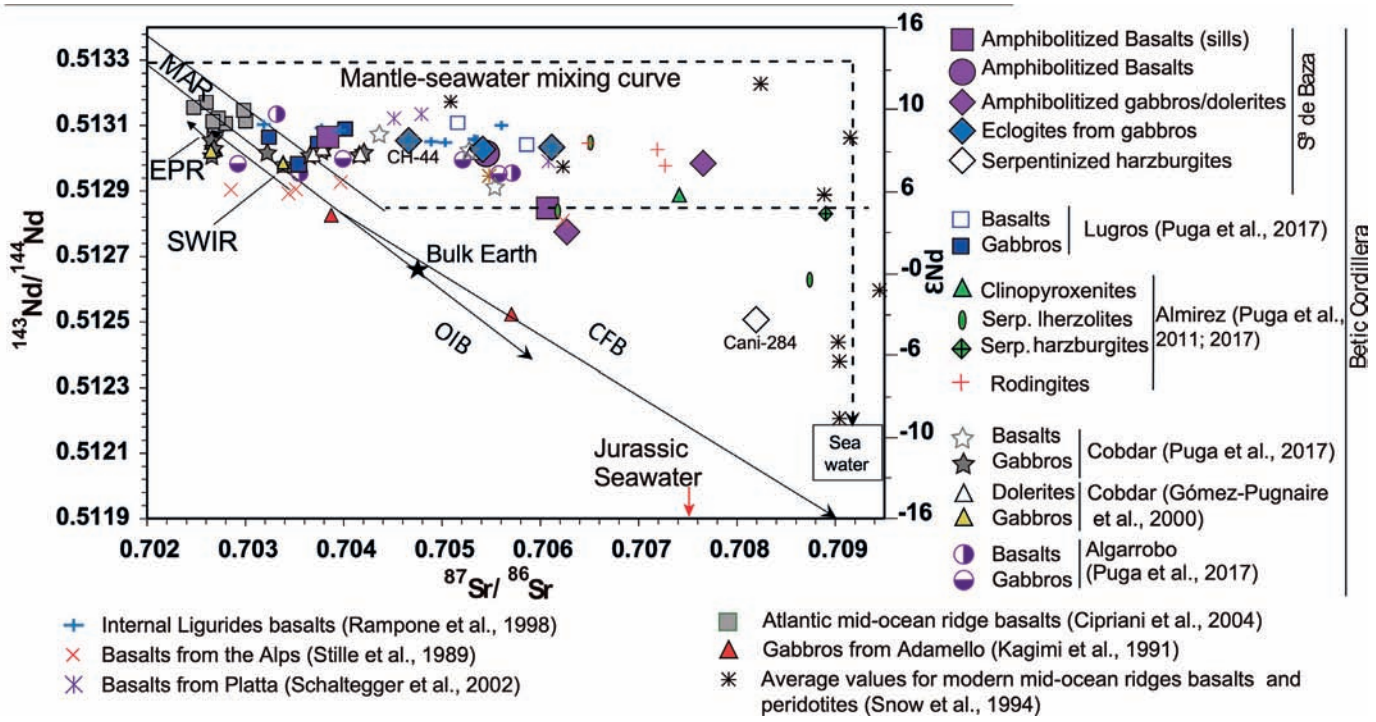

Fig. 9 - Present day $^{87}Sr/^{86}Sr$ and $^{143}Nd/^{144}Nd$ isotope composition of metabasite rocks from Sierra de Baza compared with metabasites and meta-ultramafic rocks from other Betic and Alpine ophiolite occurrences and abyssal peridotites (data from Snow et al., 1994). Dotted line represents the mantle-modern seawater mixing curve for abyssal peridotites. Sr-Nd isotopic values of EPR (Eastern Pacific Rise), MAR (Mid-Atlantic Ridge), SWIR (South Western Indian Ridge) and OIB (Oceanic Island basalts) are from Hoffman (1997), whereas CFV (Continental flood basalts) are from Marzoli et al. (1999). Jurassic Seawater composition is from Burke et al. (1992) and Jones et al. (1994), whereas modern seawater is from Snow et al. (1994).

DISCUSSION

Geochemical features of the Sierra de Baza Ophiolites

The meta-ultramafic rocks of Sierra de Baza ophiolitic association show geochemical features typical of seafloor metasomatism, that were mostly preserved during the subsequent metamorphic stages. The variable CaO depletion of serpentinized harzburgites plausibly resulted either by cpx paucity in the pristine peridotite protoliths by high degree partial melting and/or by the breakdown of clinopyroxene during serpentinization in oceanic environment (Bodinier et al., 1993; Puga et al., 1997; 1999b). However, their variable Al_2O_3 content, sometimes higher than that recorded in the associated serpentinized lherzolites, does not support their genesis by high melting degree of a fertile lherzolite (Fig. 6; Bodinier and Godard, 2003). This is also confirmed by the relatively high Al_2O_3/SiO_2 ratio of the Sierra de Baza serpentinites (Supplementary Fig. 3), which implies their protoliths experienced low partial melting before serpentinization (e.g., Snow and Dick, 1995; Paulick et al., 2006). Similar information derives from the Y *vs* Ti binary diagram of Pearce and Peate (1995), where Sierra de Baza serpentinites show analogies with peridotites from ridge segments originated by relatively low melting degree (Supplementary Fig. 4). According to Deschamps et al. (2013), in order to highlight the origin and the evolution of the meta-ultramafic rocks from the Sierra de Baza, the ratios of relatively mobile and immobile trace element have been investigated (Fig. 10). The serpentinized

harzburgites invariably show lower values of Yb with respect to serpentinized lherzolites, in agreement with the relative amount of clinopyroxene of the two lithotypes. Their U/Pb distribution is mainly along the magmatic array between the PM and E-MORB mantle domains, well displaced from the field of Tonga forearc harzburgites (Fig. 10A; Deschamps et al., 2013). Among the trace elements, Ti seems to be a useful tracer in the identification of the protolith of the serpentinites, since it is characterized by a limited mobility during serpentinization processes. Mantle wedge peridotite, which experienced extensive partial melting, are characterized by low bulk rock Ti content (Arai and Ishimaru, 2008). Therefore, when plotting the serpentinites on Yb *vs* Ti diagram, a common positive trend reflects processes of refertilization or depletion by melt extraction, defining distinct fields for the different ultramafic protoliths (Deschamps et al. 2013). In the Ti *vs* Yb diagram, all the investigated samples plot between the abyssal peridotites, abyssal and subducted serpentinites, showing a decidedly more fertile (or refertilized) composition with respect to mantle wedge serpentinites (Fig. 10B). The Sierra de Baza serpentinites also show lower Sr, Ba, and higher Pb at comparable Yb, concentrations, with respect to mantle wedge serpentinites confirming their geochemical affinity with abyssal peridotites, abyssal and subducted serpentinites (Fig. 10C, D and E). The Pb concentration of the studied serpentinites is always above the PM, in the range of abyssal peridotites and serpentinites, as well as in that of subducted serpentinites (Fig. 10F). Similar information on the origin of the Sierra de Baza serpentinites can be retrieved by the distribution of REE and other incompatible elements. Relevant and discriminant are the normalized ratios between light (L; i.e., La, Ce, Pr, Nd), medium (M; i.e., Sm, Eu, Gd, Tb) and heavy (H; i.e., Tm, Yb, Lu) REE. Serpentinized lherzolite REE patterns do not show peculiar enrichments in LREE ($LREE_N/HREE_N$ 0.4-1.9) and nearly flat $MREE_N/HREE_N$ (0.9-1.1), whereas serpentinized harzburgites are characterized by a general MREE depletion with respect to LREE and HREE ($MREE_N/LREE_N$ 0.4-1.7 and $MREE_N/HREE_N$ 0.7-1.1), which has been ascribed to loss of clinopyroxene and plagioclase during pre-orogenic oceanic serpentinization (Puga et al., 1997; 1999b). Noteworthy, the serpentinized lherzolites and harzburgites show REE patterns similar to abyssal and subducted serpentinites, respectively (Fig. 11; Deschamps et al., 2013). In particular, serpentinized harzburgites from Sierra de Baza show LREE enrichment consistent with subducted serpentinized harzburgites (LREE up to ~ 2 Ch). On the other hand, the studied serpentinites differ from mantle wedge serpentinites which show a more depleted composition for both serpentinized lherzolites (LREE up to ~ 1 Ch) and harzburgites (LREE up to ~ 0.2 and HREE up to 0.5 Ch). In other words, Sierra de Baza meta-ultramafic rocks do not share geochemical characteristics with mantle wedge settings, the archetype of which is represented by New Caledonian ophiolites (Secchiari et al., 2016; 2019).

Most of Sierra de Baza serpentinites, show variable Ce and Eu negative anomalies (Fig. 11A, B), that are clearly inherited by seawater (Bau et al., 1995). These geochemical features suggest for a genesis of serpentinites by high seawater/peridotite ratio at relatively low T (< 200°C). On the other hand, the observed REE distribution is inconsistent either with high-T hydrothermalism (Menzies et al., 1993; Allen and Seyfried, 2005) or even with melt-rock interaction (Niu et al., 1997; Rampone et al., 2018) that should produce LREE enrichment coupled with Eu positive anomaly, generally induced by plagioclase crystallization.

The serpentinites of abyssal origin are generated by hydration of the oceanic peridotites by the ocean floor hydrothermal activity, mainly concentrated in the neighboring of the oceanic ridges. After ocean floor metasomatic transformations, some Sierra de Baza serpentinites were affected by metamorphic changes during the subduction process, thus inheriting features typical of "subducted serpentinites" that were recognized in some of the analyzed samples. Subducted serpentinites are formed during convergence as they are associated with other metamorphic rocks of high P-low T (i.e. eclogites) that are also involved in the subduction processes. These genetic hypotheses are corroborated by the distribution of major elements, and of the fluid mobile elements (FME). They are inherited by the composition of the pristine mantle peridotite rocks, by ocean floor metasomatism and also by elemental re-distribution that occur during the complex P-T-t path that interested such rocks during the convergence that preceded the ophiolite obduction. The PM-normalized incompatible element distribution of the Sierra de Baza serpentinites is characterized by enrichments in FME such as Ba, U and Pb and negative anomalies in HFSE (Nb, Zr, Hf) and, to a lesser extent in Sr, which are geochemical features of abyssal and subducted serpentinites (Fig. 11A). On the other hand, mantle wedge serpentinites are characterized by a strong Sr enrichment and LREE depletion, geochemical features not observed in the Sierra de Baza serpentinites.

The enrichment in some FME (e.g., Ba, U, Pb) and depletion in HFSE result from the seawater/rock interactions that take place at mid-ocean ridges, as well as during subduction, by percolation of fluids released from different lithologies of the slab that also include sediments (Deschamps et al., 2013). The subducted serpentinites may be derived either from abyssal or OCT peridotites/serpentinites that, once incorporated into the accretion prism before exhumation, experienced a complex geological history (Deschamps et al., 2011). Chemical interactions occur with various lithologies, in particular with (meta)-sediments, and aqueous fluids, along the entire prograde path. These processes can play an important role in the FME enrichment (Deschamps et al., 2011; Lafay et al., 2013). The interaction of the Sierra de Baza ultramafic rocks with fluids (also containing halogens) is a process also recorded in various serpentinite occurrences world=wide (Bau, 1991; Bau and Dulski, 1995; Haas et al., 1995; Douville et al., 1999; Scambelluri et al., 2004; 2019; John et al., 2011; Kendrick et al., 2011; Marchesi et al., 2013), and is consistent with the presence of F-rich titanium clinohumite in=serpentinized harzburgites from the Cerro del Almirez (López Sánchez-Vizcaíno et al., 2005). The origin of U enrichment (Fig. 10E) observed for subducted serpentinites by Deschamps et al. (2013) can be ascribed to several processes. In the Sierra the Baza case-study, we speculate that U content could be controlled by percolation of fluids derived from sediments that are associated to serpentinites during the formation of orogenic mélanges, as proposed by Cannaò et al. (2015). In other words, part of the serpentinites formed on the ocean floor also suffered further element remobilization and metasomatism, being involved in a complex subduction P-T-t path (Olivier and Boyet, 2006; Deschamps et al., 2010; 2013; Kodolányi et al., 2012).

The meta-mafic rocks of Sierra de Baza ophiolitic association suffered amphibolitization and albitization processes, ultimately leading to Na_2O and SiO_2 increase with respect to CaO and immobile elements. Therefore, in order

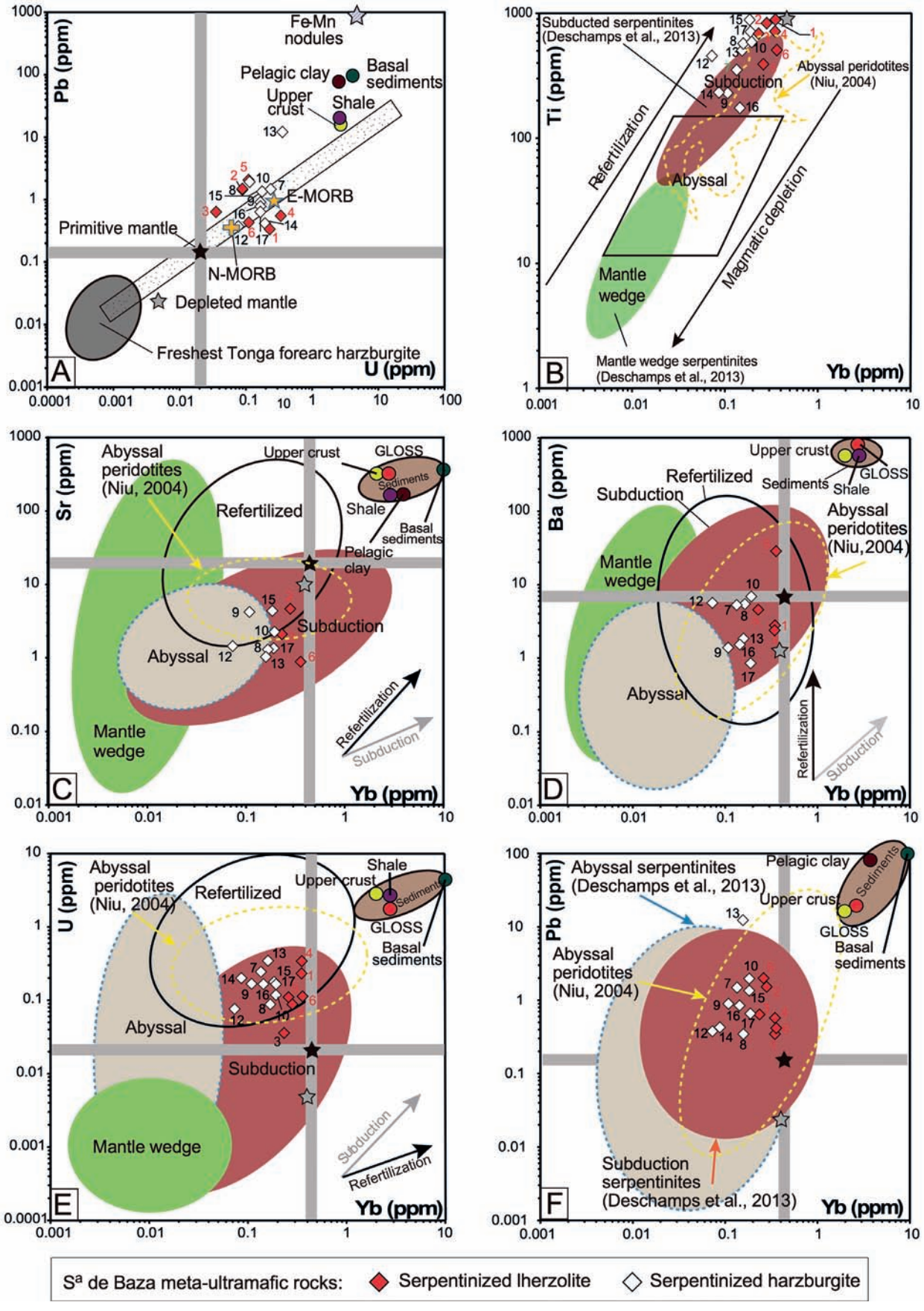

Fig. 10 - Whole rock a) U vs Pb, b) Yb vs Ti, c) Yb vs Sr, d) Yb vs Ba, e) Yb vs U, and f) Yb vs Pb variation diagrams reporting the compositional features of serpentinized peridotites of Sierra de Baza. Estimated composition of the depleted mantle from Salters and Stracke (2004); composition of the primitive mantle from McDonough and Sun (1995); compositions of the sedimentary end-members from Li and Schoonmaker (2003); Estimated composition of global subducted sediments (GLOSS) from Plank and Langmuir (1998), modified by Deschamps et al. (2013). Larger symbols refer to Sierra de Baza samples.

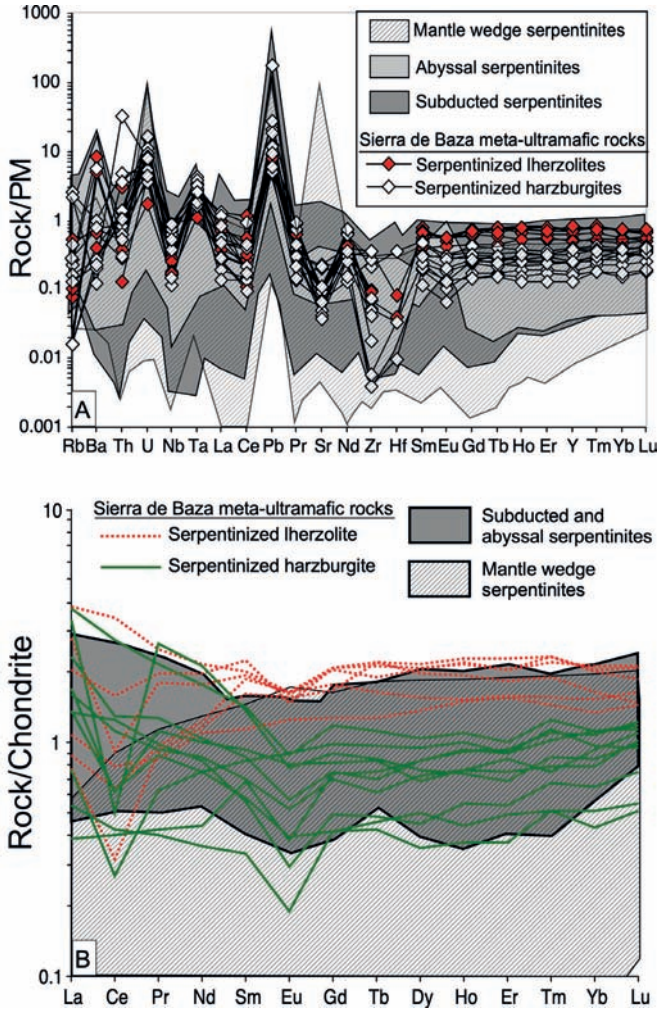

Fig. 11 - (A) PM-normalized incompatible element distribution the of Sierra de Baza meta-ultramafic rocks compared with mantle wedge (Mariana forearc: Parkinson and Pearce, 1998; Kodolányi et al., 2012; Cuba: Marchesi et al., 2006; New Caledonia: Marchesi et al., 2009; Ulrich et al., 2010; South Sandwich arc: Pearce et al., 2000; Savov et al., 2005), abyssal (MAR: Paulick et al., 2006; Jöns et al., 2010; Augustin et al., 2012) and subduction-related (Anatolia: Aldanmaz and Koprubasi, 2006; Betic Cordillera: Garrido et al., 2005; Zagros suture zone: Anselmi et al., 2000; Western Alps: Chalot-Prat et al., 2003; Dominican Republic: Deschamps et al., 2012; Newfoundland: Kodolányi et al., 2012) harzburgitic serpentinites . Normalization values are from Sun and McDonough (1989). (B) Chondrite-normalized REE patterns of meta-ultramafic rocks from Sierra de Baza compared to mantle wedge (Mariana forearc: Parkinson and Pearce, 1998; Kodolányi et al., 2012; Cuba: Marchesi et al., 2006; New Caledonia: Marchesi et al., 2009; Ulrich et l., 2010; South Sandwich arc: Pearce et al., 2000; Savov et al., 2005), abyssal (MAR: Paulick et al., 2006; Jöns et al., 2010; Augustin et al., 2012) and subduction-related (Anatolia: Aldanmaz and Koprubasi, 2006; Betic Cordillera: Garrido et al., 2005) harzburgitic serpentinites. Normalization values are from Sun and McDonough (1989).

to reconstruct their original magmatic affinity, appropriate classification diagrams based on the least mobile elements have been used. On this basis, Sierra de Baza mafic rocks mainly show tholeiitic affinity, with a differentiation trend mainly controlled by olivine/plagioclase fractionation, with a Nb/Y vs Zr/Ti variation mainly between the compositions of N- and E-MORB (Fig. 3B and C). This geochemical affinity is also confirmed by the V vs Ti/1000 diagram (Fig. 4A), which highlights the presence of a few samples (Cani-300, Cani-288, CH-12) plotting outside the MORB trend. Sample Cani-300 could be interpreted as a more differentiated product along with the tholeiitic trend, which results in the variable enrichment of FeO, TiO_2, Zr, Y and V (Miyashiro, 1975; Beccaluva et al., 1983). This is confirmed by petrographic observation which reports a higher content of rutile aggregates in these rocks, which formed after ilmenite during prograde metamorphism in the eclogite facies, prior to transformation into Ab-Ep amphibolite. Plotted in the Th/Yb vs Nb/Yb (Fig. 4B) and in the $(La/Yb)_N$ vs $(La/Sm)_N$ (Fig. 4C) sample Cani-288 is in the compositional range of N- and E-MORB, likewise most of Sierra de Baza meta-mafic rocks. On the other hand, the Th and La of some samples (including CH-12) highlight a possible contribution of pelitic sediments to a basalt of N-MORB composition (Fig. 4B and C). As proposed above, the Th enrichment, that often occurs together with other lithophile elements, could derive from the assimilation of sedimentary components by MORB-type basaltic magmas during their rise or emplacement in hypabyssal conditions (sills). This is confirmed by the similarity in composition of micaschists from the Sierra de Baza sedimentary sequence (Cani-286) and of the average Global Oceanic Subducting Sediments (GLOSS, Plank and Langmuir, 1998) that can be considered as potential contaminants. The LREE enrichment of a minor sample subset (samples CH-12, CH-12B and CH-40) could result either from the assimilation of pelitic sediment component, as proposed for the Gets ophiolites (Fig. 4C), or also by enrichment, or comparatively low melting degree of the mantle source (Bill et al., 2000). In the N-MORB normalized Nb_N vs Th_N tectonomagmatic discrimination diagram (Supplementary Fig. 2A) proposed by Saccani (2015), most of the Sierra de Baza meta-mafic rocks show E-MORB with minor N- and G-MORB geochemical affinities. This latter sample subset (samples RA-33B, Cani-281, Cani-282, Cani-303, CH-44) display an incompatible element composition similar to N-MORB with TiO_2 (1.08-2.16 wt%), P_2O_5 (0.10-0.22 wt), Zr (76-161 ppm),Y (18.58-48.45 ppm) and by Nb/Y (0.19-0.32) and Ti/V (40.97-53.68) ratios. These rocks have been however interpreted as transitional MORB (T-MORB) due to the comparatively higher Th content and by the LREE/HREE ratio and are plausibly generated by a mantle source slightly enriched during the pristine phases of oceanic opening (e.g., Venturelli et al., 1979). More recently Montanini et al. (2008) and Saccani et al. (2008), observed that similar rocks are also characterized by a comparatively high MREE/HREE ratio ($(Dy/Yb)_N$ from 1.15 to 1.59) with respect to N-MORB ($(Dy/Yb)_N = 1$, Sun and McDonough, 1989), thus ascribing the relative LREE/HREE enrichment mainly to the HREE depletion as a result of the presence of the residual garnet in their mantle sources (Saccani, 2015). In order to better discriminate between normal (N)- and garnet-influenced (G)-MORB source, the Sierra de Baza rocks have been also plotted in the chondrite-normalized $(Dy/Yb)_N$ vs $(Ce/Yb)_N$ classification diagram proposed by Saccani (2015), which confirms that most of the samples have a E-MORB affinity, whereas a sample subset shows garnet-bearing G-MORB geochemical features (Supplementary Fig. 2B).

Chondrite-normalized REE patterns of the Sierra de Baza meta-mafic rocks are shown in Fig. 12, which also reports for comparison the REE distribution of N- and E-MORB (Sun and McDonough, 1989). From this diagram it is evident that the most LREE depleted sample Cani-139A

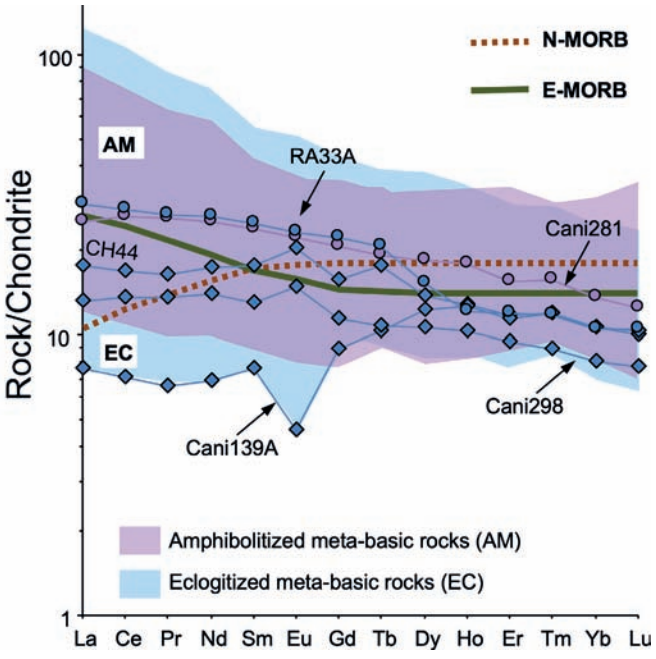

Fig. 12 - Chondrite-normalized REE diagram of the Sierra de Baza metabasites with composition approaching N-MORB and G-MORB fields in Supplementary Fig. 2. Normalization values are from Sun and McDonough (1989).

conforms to the REE distribution of N-MORB, whereas, according to their higher LREE/HREE ratio, samples Cani-281 and RA-33A can be assimilated to that of enriched E-MORB. Samples CH44 and Cani298 show intermediate REE features between E-MORB and N-MORB, plausibly recalling the geochemical features of G-MORB sources, due to their high MREE/HREE which is a feature of residual garnet in the mantle source.

The Sr-Nd isotopic composition of the investigated ophiolite association indicate that meta-mafic and meta-ultramafic rocks variably suffered seawater-rock interaction, with the least altered magmatic rocks showing a MORB-type source and the most altered mantle rocks decidedly trending to the composition of the Tethyan seawater. This trend, which is shared by Alpine ophiolites (Internal Ligurides- Rampone et al., 1998; Alps- Stille et al., 1989; Platta- Schaltegger et al., 2002) and other BOA rocks (Lugros- Puga et al., 2017; Cobdar- Puga et al., 2017 and Gómez-Pugnaire et al., 2000; Algarrobo- Puga et al., 2017; Cerro de Almirez- Puga et al., 2011 and 2017) point to a seawater composition intermediate between the Jurassic ($^{87}Sr/^{86}Sr$ 0.7072-0.7075, Burke et al., 1992, Jones et al., 1994) and modern seawater ($^{87}Sr/^{86}Sr$ 0.7092, Snow et al., 1994). The observed $^{143}Nd/^{144}Nd$ and $^{87}Sr/^{86}Sr$ displacement from the MAR array should have been related to the oceanic metasomatism that affected the BOA rocks that was particularly effective on meta-ultramafic rocks and associated rodingite dikes (Puga et al., 2011; 2017).

Age, origin and evolution of the Sierra de Baza ophiolites

The geochemical and isotopic affinity of the different types of mafic rocks of the Sierra de Baza ophiolites, and more in general of the whole BOA mainly correspond to tholeiitic magmatism of T-MORB to E-MORB affinities. These magma types originated at ocean ridges, such as the Atlantic Ridge, during the incipient oceanization following the continental rifting phase.

In the case of serpentinites generated in abyssal areas, they are generated from oceanic lithospheres associated with slow- (1 to 5 cm / year) to ultra-slow (< 2 cm/year) spreading ridges, which represent approximately one third of the 55,000 km of existing oceanic ridges on a global scale (Dick et al., 2003). These geological settings are characterized by intermittent magmatic and tectonic activity, which cause exposure of the shallow lithospheric mantle during amagmatic periods (Cannat et al., 1995; Karson et al., 2006). The relatively thin oceanic crust (1 to 7 km) and the presence of numerous normal faults on the flanks of the ridge axis promote serpentinization by fluid circulation from the deep oceanic lithosphere (Epp and Suyenaga, 1978; Francis, 1981; Mével, 2003). These abyssal serpentinites represent between 5 and 25% of the Atlantic seafloor (Cannat et al., 1995, Carlson, 2001; Mével, 2003). The exposure of these serpentinites on the ocean seafloor takes place in relation to the following tectonic environments: i) through normal high-angle faults originated from thinning and extension of the oceanic crust along the ridge; ii) in areas of lithospheric denudation due to low-angle faults that expose the lower part of the oceanic lithosphere on the seafloor in the so-called "ocean core complexes" or OCCs (oceanic core complexes: Cannat, 1993; Escartin et al., 2003; Michael et al., 2003; MacLeod et al., 2009); and iii) along large escarpments and transform faults that affect the ridges (Bonatti, 1976; Epp and Suyenaga, 1978; Francis, 1981; Bideau et al., 1991; O'Hanley, 1991; Karson and Lawrence, 1997; Mével, 2003; Morishita et al., 2009; Boschi et al., 2013). In contrast, the fast spreading ridges (> 9 cm / year) have a higher magmatic activity, which results in the formation of a thicker oceanic crust (7-10 km thick). In this framework, the abyssal peridotites would not be exposed on the seafloor (Sinton and Detrick, 1992), thus escaping serpentinization. The serpentinites of Sierra de Baza were subjected to a metasomatic process that transformed lherzolites into serpentinites. These rocks generally still preserved clinopyroxene and other mantle minerals, and include chrysotile or lizardite serpentine, derived by ocean floor metasomatism. Many of them were transformed into secondary harzburgites in a more advanced process of oceanic metasomatism, by destabilization of clinopyroxene and other mantle minerals to cause serpentine, chlorite, talc and iron oxides before undergoing the Alpine subduction process, during which antigorite (high-pressure serpentine polymorph) is formed together with other minerals such as newly formed olivine and enstatite (normally intercropped), in addition to clinohumite, iron oxide and talc.

The rifting process ultimately led to the development of the Tethyan Jurassic ocean basin starting from the Pliensbachian, between 190 and 180 Ma: (Puga et al., 2005; 2011 and 2017). Over the last decades, the BOA metamorphic mafic rocks were dated by many (U/Pb, Rb/Sr, K/Ar and Ar/Ar) radiometric methods, which revealed they formed within a wide time span, mainly between the Early and the Late Jurassic (Puga et al., 2017, Table 1). The ocean floor metamorphic stage developed between the Middle and the Late Jurassic (160-150 Ma), close to the end of magmatic phase. The BOA upper age limit (Early Cretaceous) is determined by the extensive development of a sedimentary sequence, superimposed on the igneous materials of the ocean floor, which locally preserves relics of Cretaceous fossils

(Tendero et al., 1993), and is intruded by igneous sills having mineralogical and geochemical composition similar to those of the underlying ophiolitic metabasites (Puga et al., 2011; 2017). These ocean floor sediments mainly represented by siliceous, clayey and carbonated lithologies, which ubiquitously cover both mafic and ultramafic rocks, have been metamorphosed together with the other BOA rocks. Between the Late Cretaceous and the Paleocene (90 to 60 Ma), the approximate limits for the generation of high P (eoalpine) Alpine metamorphism, the igneous lithotypes were transformed into eclogites (Puga et al., 2005; 2011; 2017). However, radiometric datings of the metabasites, demonstrate the existence of at least two more recent stages of retrograde metamorphic recrystallization, 1) a first one of Eocene-Oligocene age (mesoalpine), during which the eclogites are partially transformed into amphibolites and 2) a second one of Middle-Later Miocene age (neoalpine), in the green schist facies (Puga et al., 2017).

Paleogeographic reconstruction of the Betic area

The petrological, geochemical and geochronological similarities between the BOA rocks (including those of Sierra de Baza) and the Alpine-Apennine ophiolites, as well as the paleogeographic reconstructions of the Western Tethys during the Mesozoic, suggest that: a) continental break-up and opening of the Betic Tethys initiated during the Pliensbachien (from 190 Ma), while the Alpine-Apennine Tethys began in the Bathonian (from 170-165 Ma) (Schettino and Turco, 2009, Puga et al., 2011), and b) from the Titonian, the ocean floor generating the Betic and Alpine-Apennine ophiolites formed an oceanic strip, affected by transform faults, that linked the western Tethys and the central Atlantic (Favre and Stampfli, 1992; Guerrera et al., 1993; Schettino and Turco, 2009; Puga et al., 2017). The accretion rate of the ocean floor was around 12 mm/year according to the calculations made by Schettino and Turco (2009; see Puga et al., 2011), typical of ultra-slow spreading ridges, in agreement to the range of radiometric ages of ca. 30 Ma obtained from the beginning to the end of magmatism (Puga et al., 2017). Therefore, the Betic Tethys ocean floor could have reached ca. 200 km of width in the Jurassic, a large part of which would have been subducted during the Cretaceous, without having been exhumed to the surface in the form of eclogites.

Noteworthy, the ultra-slow spreading ridges are characterized by a low melting degree and low volcanic activity (e.g., Basch et al., 2019 and references therein). This generates small and non-continuous volcanic ridges, which are rich in serpentinites, alternated to amagmatic areas along the spreading axis (Michael et al., 2003; Dick et al., 2003). This style of ocean floor propagation is also analogous to processes in ocean-continent transition (OCT) zones near the continental margins (e.g., Whitmarsh et al., 2001). In modern analogue ultra-slow spreading ocean floor, Michael et al. (2003) demonstrated the existence of a significant hydrothermal activity. These authors verified that in current Arctic Ocean (a modern analogous) the central amagmatic zone is 300 kilometres long and that the mantle peridotites are directly located on the ridge axis, similarly to what proposed for the Betic Tethys. The same authors found significant relationships between the magmatic style and rate, local tectonics and hydrothermal processes. Many Betic ophiolites outcrops appear to have suffered hydrothermal activity, testified by the occurrence of rodingitized dolerite dykes intruded in peridotites (Puga et al., 1997; 1999a; 1999b; 2002a; 2002b, 2005, 2011, 2017, Alt et al., 2012). As noted above, this indicates that ocean floor alteration/metasomatic processes scavenged CaO from ultramafic rocks and metasomatised dolerite dikes, ultimately leading to formation of rodingites (Puga et al., 1999b; 2011). The ultra-slow spreading ocean floors are also characterized by a thick cover of pelitic sediments, an issue that is also common in the Betic ophiolites, whose sedimentary sequence is exceptionally thick (around 2 km), and indistinctly covers different mantle, plutonic and volcanic sequences (Fig. 13).

According to Puga et al. (2017), the subduction of the Betic Tethys initiated in the Late Cretaceous, lasted around 30-40 Ma, and affected the whole ocean floor and part of the two continental margins located on both sides (the NW part including the Veleta Complex and the SE part including the Sabinas Unit, Figs. 14B and 14C). The eoalpine subduction of the Betic Tethys involved the mafic, ultramafic and sedimentary rocks of the ocean floor, although also part of the rocks from both margins reached metamorphic conditions in eclogite facies. The rocks of the Veleta units, far from the subduction zone, escaped the high-pressure metamorphism, and underwent the conditions of amphibolitic facies (Puga et al., 2000; 2007). The subducted Betic ophiolitic rocks reached depths between 50 km and more than 100 km (Puga et al., 1995; 1997; 1999b; 2000; 2009a; 2017; Trommsdorff et al., 1998; Ruiz-Cruz et al., 1999; Padrón-Navarta et al., 2013).

BOA geological evolution followed the eoalpine and mesoalpine re-organization of the AlKaPeCa (Alboran, Kabilias, Peloritani, Calabria) microplate (also known as Mesomediterranean microplate), which occurred in the Late Cretaceous and Paleogene, in the Early Oligocene and, especially, during Early Miocene within a compressive framework that implied plate margins deformation including the Nevado-Filábride Domain. The result of the pre-orogenic and orogenic processes in the Betic Internal Zones was the formation of a proto-chain that was rapidly dismembered into fragments dispersed in the different chains of the Western Mediterranean Alpine Orogen (Rosenbaum et al., 2002). This evolution was accompanied by the SW displacement of the Alborán block, from the Oligocene during mesoalpine metamorphic event, which ended when it reached its current position.

CONCLUSIONS

The BOA constitutes a vestige of a fragmented and metamorphosed old ocean basin opened during the Mesozoic in the Western Alpine Tethys-Mediterranean as a result of the Pangea break-up.–The rifting and subsequent drifting and ocean opening were possibly influenced by pre-existing tectonic structures inherited from the Variscan orogeny. The ancient Betic Tethys originated starting from the Pliensbachian (Early Jurassic) and connected to the east with other ocean basins, currently represented by the ophiolites of the Alpine and Apennine domains, and to the west with the incipient central Atlantic Ocean. The Bétic Tethys must have been relatively narrow, with a limited width of few hundred kilometers at most. It was surely dissected by many transform faults and by extensive take-offs by low-angle faults. This result in an ocean floor composed of magmatic sectors characterized by basalts with pillow-lavas and gabbros, alternated, with amagmatic sectors, characterized by direct exposure on the ocean floor of ultramafic rocks, locally intruded by doleritic

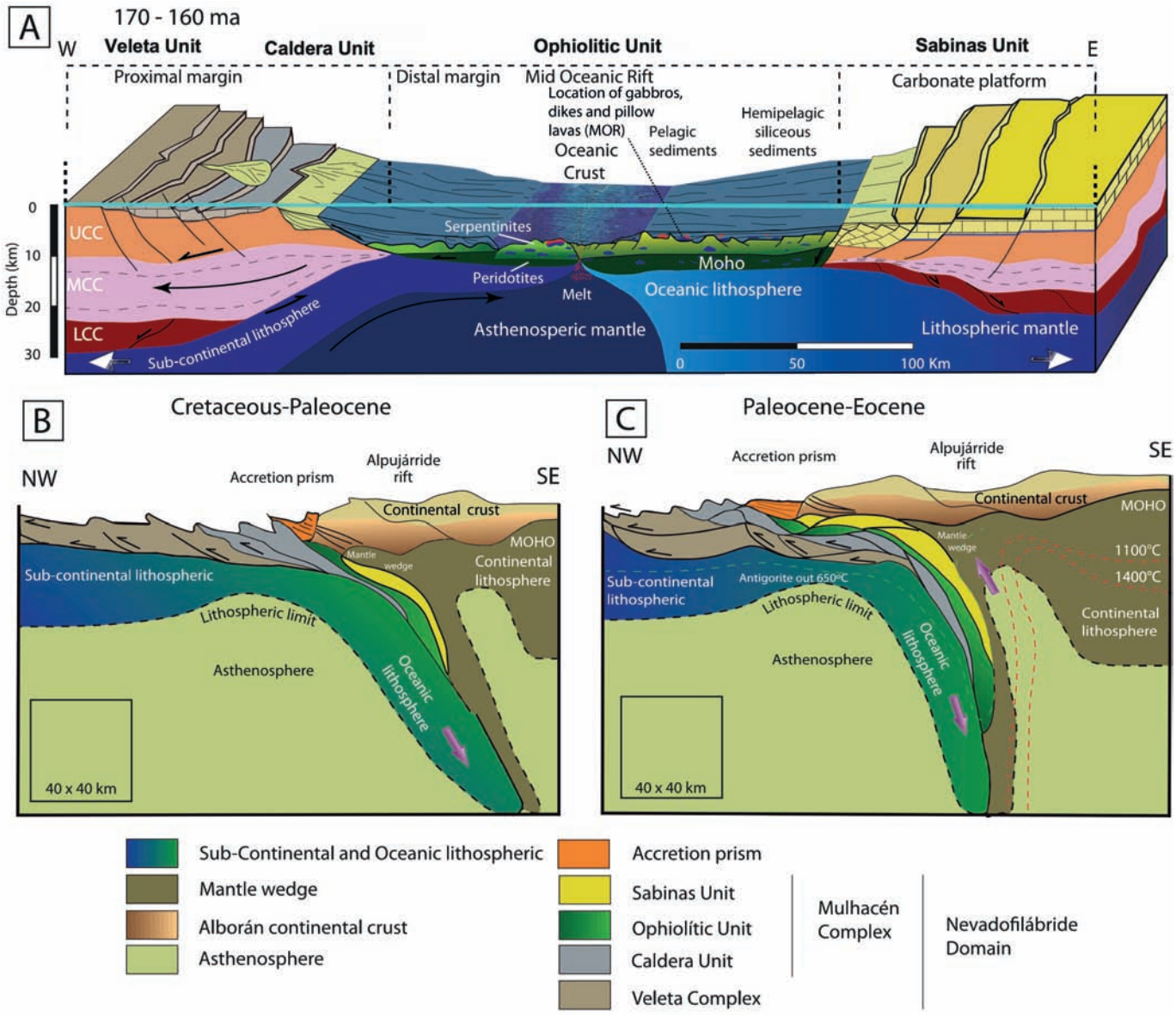

Fig. 13 - A: Paleogeographic reconstruction the Betic Tethys ocean floor during the Jurassic. Mid-oceanic accretion stage of an ultra-slow spreading ridge (< 20 mm / year), locally characterized by amagmatic sectors by high sedimentation rate. UCC: Upper Continental crust; MCC: Middle continental crust; LCC: Lower continental crust (modified from Hirth and Guillot, 2013 and Guillot et al., 2015); B and C: Geodynamic evolution of the Nevado-Filábride Domain during the Cretaceous-Paleogene convergent stage. B: Eoalpine subduction of the ocean floor and adjacent continental margins and metamorphism in eclogite facies; C: Partial exhumation of the subducted units and mesoalpine metamorphic evolution.

dikes. Similar to many Ligurian ophiolites, which are often associated with the remnants of the continental crust, BOA presents local indications of crustal assimilation, probably derived from rocks of the continental margins. This indicates a) proximity to the continental margin, at least during the early stages of ocean magmatism; and b) intermittent accretion, generally attributed to the ultra-slow spreading ridges (Puga et al., 2011). The convergence that began in the Late Cretaceous, after the reorganization of the main plates, interposed continental blocks (AlKaPeCa: Alboran, Kabilias, Peloritani, Calabria), determined the beginning of the subduction of the Betic ocean floor. This subduction was probably directed towards the S and SE, as it happened in other northern Alpine-Apennine domains and persisted until the Early Paleogene. The subducted BOA rocks were affected by an eoalpine metamorphism in the eclogite facies that ended with the exhumation of part of the studied ophiolite. This process was characterized by a pressure drop during partial exhumation of the BOA rocks and the initiation of retrograde metamorphism, which took place from the Late Paleogene, as indicated by the Ar/Ar datings on an amphibolite of Sierra de Baza (Puga et al., 2017).

ACKNOWLEDGMENTS

The authors gratefully acknowledge V. Basch and A. Secchiari (reviewers) and G. Borghini (editor) for their help in improving an earlier version of the manuscript.

Supplementary data to this article are available online at https://doi.org/10.4454/ofioliti.v45i1.532

REFERENCES

Aerden D.G.A.M., Bell T.H., Puga E., Sayab M., Lozano J.A. and Diaz de Federico A., 2013. Multi-stage mountain building vs. relative plate motions in the Betic Cordillera deduced from integrated microstructural and petrological analysis of porphyroblasts inclusion trails. Tectonophysics, 587: 188-206.

Aldanmaz E. and Koprubasi N., 2006. Platinum-group-element systematics of peridotites from ophiolite complexes of northwest Anatolia, Turkey: Implications for mantle metasomatism by melt percolation in a supra-subduction zone environment. Intern. Geol. Rev., 48: 420-442.

Allen D.E. and Seyfried W.E. Jr., 2003. Compositional controls on vent fluids from ultramafic-hosted hydrothermal systems at midocean ridges: An experimental study at 400°C, 500 bars. Geochim. Cosmochim. Acta, 67: 1531-1542.

Allen D.E. and Seyfried W.E., 2005. REE controls in ultramafic hosted MOR hydrothermal systems: an experimental study at elevated temperature and pressure. Geochim. Cosmochim. Acta, 69: 675-683.

Alt J.C., Garrido C.J., Shanks W.C., Turchyn A., Padròn-Navarta J.A., Lòpez-Sànchez-Vizcaino V., Gómez-Pugnaire M.T. and Marchesi C., 2012. Recycling of water, carbon, and sulfur during subduction of serpentinites: A stable isotope study of Cerro del Almirez, Spain, Earth Planet. Sci. Lett., 327/328: 50-60.

Anselmi B., Mellini M. and Viti C., 2000. Chlorine in the Elba, Monti Livornesi and Murlo serpentines: Evidence for sea-water interaction. Eur. J. Miner., 12: 137-146.

Arai S. and Ishimaru S., 2008. Insights into petrological characteristics of the lithosphere of mantle wedge beneath arcs through peridotite xenoliths: a review. J. Petrol., 49: 665-695.

Augustin N., Paulick H., Lackschewitz K.S., Eisenhauer A., Garbe-Schönberg D., Kuhn T., Botz R. and Schmidt M., 2012. Alteration at the ultramafic-hosted Logatchev hydrothermal field: Constraints from trace element and Sr-O isotope data. Geochem. Geophys. Geosyst., 13: Q0AE07. doi: 10.1029/2011GC003903.

Bach W., Garrido C.J., Paulick H., Harvey J. and Rosner M., 2004. Seawater-peridotite interactions: first insights from ODP Leg 209, MAR 15°N. Geochem., Geophys., Geosyst., 5. http://dx.doi.org/10.1029/2004GC000744.

Basch V., Rampone E., Crispini L., Ferrando C., Ildefonse B. and Godard M., 2019. Multi-stage reactive formation of troctolites in slow-spreading oceanic lithosphere (Erro-Tobbio, Italy): a combined field and petrochemical study. J. Petrol., 60: 873-906.

Bau M., 1991. Rare earth element mobility during hydrothermal and metamorphic fluid-rock interaction and the significance of the oxidation state of europium. Chem. Geol., 93: 219-230.

Bau M. and Dulski P., 1995. Comparative study of yttrium and rare-earth element behaviours in fluorine-rich hydrothermal fluids. Contrib. Miner. Petrol., 119: 213-223.

Bau, M. Dulski P. and Möller P., 1995). Yttrium and holmium in South Pacific seawater: Vertical distribution and possible fractionation mechanisms. Chem. Erde-Geochem., 55: 1-15.

Beccaluva L., Dostal J., Macciota G. and M. Zerbi., 1983. Trace element geochemistry of some ophiolites from Calabria (Southern ltaly). Ofioliti, 8: 325-332.

Beccaluva L., Ohnenstetter D. and Ohnenstetter M., 1979. Geochemical discrimination between ocean-floor and island-arc tholeiites. Appication to some ophiolites. Can. J. Earth Sci., 16: 1874-1882.

Bideau D., Hébert R., Hékinian R. and Cannat M., 1991. Metamorphism of deep-seated rocks from the Garrett Ultrafast Transform (East Pacific Rise near 13°25-S). J. Geophys. Res., 96: 10079-10099.

Bill M., Nägler Th.F. and Masson H., 2000. Major, minor, trace element, Sm-Nd and Sr isotope compositions of mafic rocks from the earliest oceanic crust of the Alpine Tethys. Schweiz. Miner. Petrogr. Mitt., 80: 131-145.

Bodinier J.L. and Godard M., 2003. Orogenic, ophiolitic, and abyssal peridotites. In: R.W. Carlson (Ed.), Treatise on Geochemistry, vol. 2., The Mantle and Core. Elsevier Sci. Ltd., p. 103-170.

Bodinier J.L., Dupuy C. and Dostal J., 1988. Geochemistry and petrogenesis of Eastern Pyrenean peridotites. Geochim. Cosmochim. Acta, 52: 2893-2907.

Bodinier J.L., Puga E., Diaz de Federico A., Leblanc M. and Morten L. 1993. Secondary harzburgites with spinifex-like textures in the Betic Ophiolitic Association (SE Spain). Terra Nova Abstr.t, 4,: 3.

Bonatti E., 1976. Serpentinite protrusions in the oceanic crust. Earth Planet. Sci. Lett., 32: 107-113.

Borghini G., Rampone E., Crispini L., De Ferrari R. and Godard M., 2007. Origin and emplacement of ultramafic-mafic intrusions in the Erro-Tobbio mantle peridotite (Ligurian Alps, Italy). Lithos, 94: 210-229.

Borghini G., Rampone E., Zanetti A., Class C., Cipriani A., Hofmann A.W. and Goldstein S., 2016. Pyroxenite layers in the Northern Apennines upper mantle (Italy) - generation by pyroxenite melting and melt infiltration. J. Petrol., 57: 625-653.

Boschi C., Bonatti E., Ligi M., Brunelli D., Cipriani A., Dallai L., D'Orazio M., Früh-Green G.L., Tonarini S., Barnes J.D. and Bedini R.M., 2013. Serpentinization of mantle peridotites along an uplifted lithospheric section, Mid Atlantic Ridge at 11° N. Lithos, 178: 3-23.

Breeding C.M., Ague J.J. and Bröcker M., 2004. Fluid-metasedimentary rock interactions and the chemical composition of arc magmas. Geology, 32: 1041-1044.

Burke W.H., Denison R.E., Hetherington E.A., Koepnick R.B., Nelson H.F. and Otto J.B., 1992. Variation of sea water 87Sr/86Sr throughout Phanerozoic time. Geology, 10: 516-519.

Cannaò E., Agostini S., Scambelluri M., Tonarini S. and Godard M., 2015. B, Sr and Pb isotope geochemistry of high-pressure Alpine metaperidotites monitors fluid-mediated element recycling during serpentinite dehydration in subduction melange (Cima di Gagnone, Swiss Central Alps). Geochim. Cosmochim. Acta, 163: 80-100.

Cannat M., 1993. Emplacement of mantle rocks in the seafloor at Mid-Atlantic Ridges. J. Geophys. Res., 98: 4163-4172.

Cannat M., Mével C., Maia M., Deplus C., Durand C., Gente P., Agrinier P., Belarouchi A., Dubuisson G., Hulmer E. and Reynolds J., 1995. Thin crust, ultramafic exposures, and rugged faulting patterns at the Mid-Atlantic Ridge (22°24°N). Geology, 23: 49-52.

Carlson R.L., 2001. The abundance of ultramafic rocks in Atlantic Ocean crust. Geophys. J. Intern., 144: 37-48.

Chalot-Prat F., Ganne J. and Lombard A., 2003. No significant element transfer from the oceanic plate to the mantle wedge during subduction and exhumation of the Tethys lithosphere (Western Alps). Lithos, 69: 69-103.

Cipriani A., Brueckner H.K., Bonatti E. and Brunelli D., 2004. Oceanic crust generated by elusive parents: Sr and Nd isotopes in basalt-peridotite pairs from the Mid-Atlantic Ridge. Geology, 32: 657-660.

Coleman R.G., 1977. Ophiolites. Springer-Verlag, New-York. 229 pp.

Deschamps F., Godard M., Guillot S., Chauvel C., Andreani M., Hattori K., Wunder B. and France L., 2012. Behavior of fluid-mobile elements in serpentines from abyssal to subduction environments: Examples from Cuba and Dominican Republic. Chem. Geol., 312/313: 93-117.

Deschamps F., Godard M., Guillot S. and Hattori K., 2013. Geochemistry of subduction zone serpentinites: A review. Lithos, 178: 96-127.

Deschamps F., Guillot S., Godard M., Andreani M. and Hattori K., 2011. Serpentinites act as sponges for fluid-mobile elements in abyssal and subduction zone environments. Terra Nova, 23: 171-178.

Deschamps F., Guillot S., Godard M., Chauvel C., Andreani M. and Hattori K., 2010. In situ characterization of serpentinites from forearc mantle wedges: timing of serpentinization and behavior of fluid-mobile elements in subduction zones. Chem. Geol., 269: 262-277.

Desmurs L., Müntener O. and Manatschal G., 2002. Onset of magmatic accretion within a magma-poor rifted margin: a case study from the Platta ocean-continent transition, eastern Switzerland. Contrib. Miner. Petrol., 144 (3): 365-382.

Dick H.J.B., Lin J. and Schouten H., 2003. An ultraslow-spreading class of ocean ridge. Nature, 426: 405-412.

Douville E., Bienvenu P., Charlou J.L., Donval J.P., Fouquet Y., Appriou P. and Gamo T., 1999. Yttrium and rare earth elements in fluids from various deep-sea hydrothermal systems. Geochim Cosmochim. Acta, 63: 627-643.

Epp D. and Suyenaga W., 1978. Thermal contraction and alteration of the oceanic crust. Geology, 6: 726-728.

Escartin J., Mével C., MacLeod C.J. and McCaig A.M., 2003. Constraints on deformation conditions and the origin of oceanic detachments: the mid-Atlantic ridge core complex at 15-45°N. Geochem. Geophys. Geosyst., 4: 1-37.

Favre P. and Stampfli G.M., 1992. From rifting to passive margin: the examples of the Red Sea, Central Atlantic and Alpine Tethys. Tectonophysics, 215: 69-97.

Floyd P.A. and Winchester J.A., 1975. Magma type and tectonic setting discrimination using immobile elements. Earth Planet. Sci. Lett., 27: 211-218.

Francis T.J.G., 1981. Serpentinization faults and their role in the tectonics of slow spreading ridges. J. Geophys. Res., 86: 11616-11622.

Gale A., Dalton C.A., Langmuir C.H., Su Y. and Schilling J.G., 2013. The mean composition of ocean ridge basalts. Geochem. Geophys. Geosyst., 14: 489-518.

Garrido C.J., López Sánchez-Vizcaíno V., Gómez-Pugnaire M.T., Trommsdorff V., Alard O., Bodinier J.L. and Godard M., 2005. Enrichment of HFSE in chlorite-harzburgite produced by high-pressure dehydration of antigorite-serpentinite: Implications for subduction magmatism. Geochem. Geophys. Geosyst., 6: Q01J15.

Gómez-Pugnaire M.T., Braga J.C., Martín J.M., Sassi F.P. and Moro A., 2000. Regional implications of a Palaeozoic age for the Nevado-Filabride cover of the Betic Cordillera, Spain. Schweiz. Miner. Petrogr. Mitt., 80: 45-52.

Govindaraju K., 1994. Compilation of working values and sample description for 383 geostandards. Geostand. Newsl., 18: 1-158.

Guerrera F., Martin-Algarra F. and Perrone V., 1993. Late Oligocene-Miocene syn-late orogenic successions in western and central Mediterranean chains from the Betic Cordillera to the Southern Apennines. Terra Nova, 5: 525-544.

Guillot S., Schwartz S., Reynard B., Agard P. and Prigent C., 2015. Tectonic significance of serpentinites. Tectonophysics, 646: 1-19.

Haas J.R., Shock E.L. and Sassani D.C., 1995. Rare earth elements in hydrothermal systems: Estimates of standard partial molal thermodynamic properties of aqueous complexes of the rare earth elements at high pressures and temperatures. Geochim. Cosmochim. Acta, 59 (21): 4329-4350.

Handy M.R., Schmid S.M., Bousquet R., Kissling E. and Bernoulli D., 2010. Reconciling plate-tectonic reconstructions of Alpine Tethys with the geological-geophysical record of spreading and subduction in the Alps. Earth Sci. Rev., 102: 121-158.

Hart S.R. and Zindler A., 1986. In search of a bulk-Earth composition. Chem. Geol., 57: 247-267.

Herbrich A., Hoernle K., Werner R., Hauff F., van den Bogaard P. and Garbe-Schönberg D., 2015. Cocos Plate Seamounts offshore NW Costa Rica and SW Nicaragua: Implications for large-scale distribution of Galápagos plume material in the upper mantle. Lithos, 212/215: 214-230.

Hirth G. and Guillot S., 2013. Rheology and tectonic significance of serpentinite. Elements, 9: 107-113.

Hoffman A.V., 1997. Mantle geochemistry: the message from oceanic volcanism. Nature, 385: 219-229.

Irvine T.N. and Baragar W.R.A., 1971. A guide to the chemical classification of the common volcanic rocks. Can. J. Earth Sci., 8: 523-548.

Jagoutz E., Palme H., Baddenhausen H., Blum K., Cendales M., Dreibus G., Spettel B., Lorenz V. and Vanke H., 1979. The abundance of major, minor and trace elements in the earth's mantle as derived from primitive ultramafic nodules. Geochim. Cosmochim. Acta, 11 (2): 2031-2050.

Janecky D.R. and Seyfried W.E. Jr., 1986. Hydrothermal serpentinization of peridotite within the oceanic crust: experimental investigations of mineralogy and major element chemistry. Geochim. Cosmochim. Acta, 50: 1357-1378.

John T., Scambelluri M., Frische M., Barnes J. and Bach W., 2011. Dehydration of subducting serpentinite: implications for halogen mobility in subduction zones and the deep halogen cycle. Earth Planet. Sci. Lett., 308: 65-76.

Jones C.E., Jenkyns H.C., Coe A.L. and Hesselbo S.P., 1994. Strontium isotopic variations in Jurassic and Cretaceous sea water. Geochim. Cosmochim. Acta, 58: 3061-3074.

Jöns N., Bach W. and Klein F., 2010. Magmatic influence on reaction paths and element transport during videnceization. Chem. Geol., 274: 196-211.

Karson J.A. and Lawrence R.M., 1997. Tectonic setting of serpentinite exposures on the western median valley wall of the MARK area in the vicinity of site 920. In: J.A Karson, M. Cannat, D.J. Miller and D. Elthon (Eds.), Proceed. O.D.P., Sci. Res., 153: 5-21.

Karson J.A., Kelley D.S., Williams E.A., Yoerger D.R. and Jakuba M., 2006. Detachment shear zone of the Atlantis Massif core complex, Mid-Atlantic Ridge, 30°N. Geochem. Geophys. Geosyst., 7: Q06016.

Kendrick M.A., Scambelluri M., Honda M. and Phillips D., 2011. High abundances of noble gas and chlorine delivered to the mantle by serpentinite subduction. Nature Geosci., 4: 807-812.

Kodolányi J., Pettke T., Spandler C., Kamber B.S. and Gméling K., 2012. Geochemistry of ocean floor and fore-arc serpentinites: constraints on the ultramafic input to subduction zones. J. Petrol., 53: 235-270.

Kretz R. 1983. Symbols of rock-forming minerals. Am. Miner., 68: 277-279.

Lafay R., Deschamps F., Schwartz S., Guillot S., Godard M., Debret B. and Nicollet C., 2013. High-pressure serpentinites, a trap-and-release system controlled by metamorphic conditions: example from the Piedmont zone of the western Alps. Chem. Geol., 343: 38-54.

Lagabrielle Y., 2009. Mantle exhumation and lithospheric spreading: An historical perspective from investigations in the oceans and in the Alps-Appennines ophiolites. It. J. Geosci., 12: 279-293.

Lagabrielle Y., Vitale Bovarone A. and Ildefonse B., 2015. Fossil oceanic core complexes recognized in the blueschist metaophiolites of Western Alps and Corsica. Earth-Sci. Rev., 141: 1-26.

Le Bas M.J. and Streckeisen A.L., 1991. The IUGS systematics of igneous rocks. J. Geol. Soc. London, 148: 825-833.

Li Y.H. and Schoonmaker J., 2003. Chemical composition and mineralogy of marine sediments. In: F.T. Mackenzie (Ed.), Sediments, diagenesis, and sedimentary rocks, Treatise on geochemistry. Elsevier Sci. Ltd., 7: 1-35.

López Sánchez-Vizcaíno V., Trommsdorff V., Gómez-Pugnaire M.T., Garrido C.J., Müntener O. and Connolly J.A.D., 2005. Petrology of titanian clinohumite and olivine at the high-pressure breakdown of antigorite serpentinite to chlorite harzburgite (Almirez Massif, S. Spain). Contrib. Miner. Petrol., 149: 627-646.

Lozano J.A., Puga E., Garcia-Casco A., Martínez-Sevilla F., Contreras Cortés F., Carrasco Rus J. and Martín-Algarra A., 2018. First evidence of prehistoric eclogite quarrying for polished tools and their circulation on the Iberian Peninsula. Geoarchaeol., 33: 364-385.

MacLeod C., Searle R.C., Murton B.J., Casey J.F., Mallows C., Uns worth S.C., Achenbach K.L. and Harris M., 2009. Life cycle of oceanic core complexes. Earth Planet. Sci. Lett., 287: 333-344.

Manatschal G. and Müntener O., 2009. A type sequence across an ancient magma- poor ocean-continent transition: the example of the western Alpine Tethys ophiolites. Tectonophysics, 473: 4-19.

Marchesi C., Garrido C.J., Godard M., Belley F. and Ferré E., 2009. Migration and accumulation of ultra-depleted subduction-related melts in the Massif du Sud ophiolite (New Caledonia). Chem. Geol., 266: 171-186.

Marchesi C., Garrido C.J., Godard M., Proenza J.A., Gervilla F. and Blanco-Moreno J., 2006. Petrogenesis of highly depleted peridotites and gabbroic rocks from the Mayari-Baracoa Ophiolitic Belt (eastern Cuba). Contrib. Miner. Petrol., 151: 717-736.

Marchesi C., Garrido C.J., Padrón-Navarta J.A., López Sánchez-Vizcaíno V. and Gómez-Pugnaire M.T., 2013. Element mobility from seafloor serpentinization to high-pressure dehydration of antigorite in subducted serpentinite: Insights from the Cerro del Almirez ultramafic massif (southern Spain). Lithos, 178: 128-142.

Marroni M., Molli G., Montanini A. and Tribuzio R., 1998. The association of continental crust rocks with ophiolites (Northern Apennines, Italy): Implications for the continent-ocean transition. Tectonophysics, 292: 43-66.

Marzoli A., Renne P.R., Piccirillo E.M., Ernesto M., Bellieni G. and De Min A., 1999. Extensive 200-Million-year-old continental flood basalts of the Central Atlantic Magmatic Province. Science, 284: 616-618.

McDonough W.F. and Sun S.-S. 1995. The composition of the Earth. Chem. Geol., 120: 223-253.

Menzies M.A., Long A., Ingram G., Tatnell M. and Janecky D., 1993. MORB peridotite-sea water interaction: experimental constraints on the vidence of trace elements, $^{87}Sr/^{86}Sr$ and $^{143}Nd/^{144}Nd$ ratios. In: H.M. Prichard, T. Alabaster, N.B.W. Harris and C.R. Neary (Eds.), Magmatic processes and plate tectonics. Geol. Soc. London Spec. Publ., 76: 309-322.

Mével C., 2003. Serpentinization of abyssal peridotites at mid-ocean ridges. C.R. Géosci., 335: 825-852.

Michael P.J., Langmuir C.H., Dick H.J.B., Snow J.E., Goldstein S.L., Graham D.W., Lehnert K., Kurras G., Jokat W., Mühe R. and Edmonds H.N., 2003. Magmatic and amagmatic seafloor generation at the ultraslow-spreading Gakkel ridge, Arctic Ocean. Nature, 423: 956-961.

Miyashiro A., 1975. Classification, characteristics and origin of ophiolites. J. Geol., 83: 249-281.

Miyashiro A., Shido F. and Ewing M., 1969. Composition and origin of serpentinites from the Mid-Atlantic Ridge near 24 and 30°N. Contrib. Miner. Petrol., 23: 117-127.

Montanini A., Tribuzio R. and Vernia L., 2008. Petrogenesis of basalts and gabbros from an ancient continent-ocean transition (External Liguride ophiolites, Northern Italy). Lithos, 101: 453-479.

Morishita T., Hara K., Nakamura K., SawaguchiT., Tamura A., Arai S., Okino K., Takai K. and Kumagai H., 2009. Igneous, alteration and exhumation processes recorded in abyssal peridotites and related fault rocks from an oceanic core complex along the Central Indian Ridge. J. Petrol., 50: 1299-1325.

Morten L., Bargossi G.M., Martınez-Martınez J.M., Puga E. and Dıaz de Federico A., 1987. Meta-gabbro and associated eclogites in the Lubrın area, Nevado-Filabride complex, Spain, J. Metam. Geol., 5: 155-174.

Nieto J.M., 1996. Petrología y geoquímica de los or togneises del Complejo del Mulhacén, Cordilleras Béticas. Ph. D. Thesis, Univ. Granada, 211 pp.

Nieto J.M., Puga E. and Díaz De Federico A., 2000. Late Variscan pyroclastic rocks from the Mulhacén Complex (Betic Cordillera, Spain). In: H. Leyrit and Ch. Montenat (Eds), Volcaniclastic rocks, from magmas to sediments. Gordon and Breach Sci. Publ., p. 217-224.

Niu Y., 2004. Bulk-rock major and trace element compositions of abyssal peridotites: implications for mantle melting, melt extraction and post-melting processes beneath mid-ocean ridges. J. Petrol., 45: 2423-2458.

Niu Y., Langmuir C.H. and Kinzler R.J., 1997. The origin of abyssal peridotites: a new perspective. Earth Planet. Sci. Lett., 152: 251-265.

O'Hanley D.S., 1991. Fault-related phenomena associated with hydration and serpentine recrystallization during serpentinization. Can. Miner., 29: 21-35.

Olivier N. and Boyet M., 2006. Rare earth and trace elements of microbialites in Upper Jurassic coral- and sponge-microbialite reefs. Chem. Geol., 230: 105-123.

Padrón-Navarta J.A., López Sanchez-Vizcaino V., Hermann J., Connolly J.A.D., Garrido C.J., Gómez-Pugnaire M.T. and Marchesi C., 2013. Tschermak's substitution in antigorite and consequences for phase relations and water liberation in high-grade serpentinites. Lithos, 178: 186-196.

Palandri J.L. and Reed M.H., 2004. Geochemical models of metasomatism in ultramafic systems: serpentinization, rodingitization, and sea floor carbonate chimney precipitation. Geochim. Cosmochim. Acta, 68: 1115-1133.

Parkinson I.J. and Pearce J.A., 1998. Peridotites from the Izu-Bonin-Mariana forearc (ODP Leg 125): Evidence for mantle melting and melt-mantle interaction in a supra-subduction zone setting. J. Petrol., 39: 1577-1618.

Paulick H., Bach W., Godard M., De Hoog J.C.M., Suhr G. and Harvey J., 2006. Geochemistry of abyssal peridotites (Mid-Atlantic Ridge, 15°20-N, ODP Leg 209): implications for fluid/rock interaction in slow spreading environments. Chem. Geol., 234: 179-210.

Pearce J.A., 1982. Trace element characteristics of lavas from destructive plate boundaries. In: R.S. Thorpe (Ed.), Orogenic andesites and related rocks. John Wiley and Sons, Chichester, England, p. 528-548.

Pearce J.A., 1996. A user's guide to basalt discrimination diagrams. In: D.A. Wyman (Ed.), Trace element geochemistry of volcanic rocks: Applications for massive sulphide exploration. Short Course Notes. Geol. Ass. Can., 12: 79-113.

Pearce, J.A., 2003. Supra-subduction zone ophiolites: The search for modern analogues. In: Y. Dilek and S. Newcomb (Eds.), Ophiolite concept and the evolution of geological trhought. Geol. Soc. Am. Spec. Pap., 373: 269-293.

Pearce J.A., 2008. Geochemical fingerprinting of oceanic basalts with applications to ophiolite classification and the search of the Archean oceanic crust. Lithos, 100: 14-48.

Pearce J.A. and Peate D.W.,1995. Tectonic implications of the composition of volcanic arc magmas. Ann. Rev. Earth Planet. Sci., 23: 251-285, doi: 10.1146/annurev.ea.23.050195.001343

Pearce J.A., Barker P.F., Edwards S.J., Parkinson I.J. and Leat P.T., 2000. Geochemistry and tectonic significance of peridotites from the South Sandwich arc-basin system, South Atlantic. Contrib. Miner. Petrol., 139: 36-53.

Pearce J.A., Harris N.B.W. and Tindle A.G., 1984. Trace element cliscrimination diagrams for the tectonic interpretation of granitic rocks. J. Petrol., 25: 956-983.

Piccardo G.B. and Guarnieri L., 2010. Alpine peridotites from the Ligurian Tethys: an updated critical review. International Geol. Rev., 52: 1138-1159.

Plank T. and Langmuir C.H., 1998. The chemical composition of subducting sediments and its consequences for the crust and mantle. Chem. Geol., 145: 325-394.

Puga E., 1977. Sur l'existence dans le complexe de la Sierra Nevada (Cordillère Bétique, Espagne du sud) d'éclogites et sur leur origine probable à partir d'une croûte océanique mésozoique. C.R. Acad. Sci., 285: 1379-1382. (In French)

Puga E., 1990. The Betic Ophiolitic Association (Southeastern Spain). Ofioliti, 15: 97-117.

Puga E., 2005. A reappraisal of the Betic Ophiolitic Association: The westernmost relic of the Alpine Tethys Ocean. In: I.R. Finetti (Ed.), Deep seismic exploration of the Central Mediterranean and Italy. CROP 1 Volume, Univ. Trieste, Italy, Elsevier, p. 665-704.

Puga E. and Díaz de Federico A., 1978. Metamorfismo polifásico y deformaciones alpinas en el Complejo de Sierra Nevada (Cordillera Bética). Implicaciones geodinámicas. In: Reunión sobre la geodinámica de las Cordilleras Béticas y el Mar de Alborán. Univ. Granada, Secret. Publ., Granada, Spain, p. 79-111 (In Spanish).

Puga E., Bodinier J.L., Díaz de Federico A., Morten L. and Nieto J.M., 1997. Pseudo-spinifex meta-ultramafic rocks containing eclogitized rodingite dykes in the Betic Ophiolitic Association (SE Spain): evidence of Alpine subduction following an ocean-floor metasomatic process. Quad. Geodin. Alp. Quatern., 4: 98-99.

Puga E., Díaz de Federico A., Bargossi G.M. and Morten L., 1989a. The Nevado-Filábride metaophiolitic association in the Cóbdar region (Betic Cordillera, SE Spain): preservation of pillow structures and development of coronitic eclogites. Geodin. Acta, 3: 17-36.

Puga E., Díaz De Federico A. and Demant A., 1995. The eclogitized pillows of the Betic Ophiolitic Association: Relics of the Tethys ocean floor incorporated to the Alpine Chain after subduction. Terra Nova, 7: 32-43.

Puga E., Díaz de Federico A., Fediukova E., Bondi M. and Morten L., 1989b. Petrology, geochemistry and metamorphic evolution of the ophiolitic eclogites and related rocks from the Sierra Nevada (Betic Cordilleras, southeastern Spain). Schweiz. Miner. Petrogr. Mitt., 69: 435-455.

Puga E., Díaz De Federico A., Manteca Martinez J.I., Rodríguez Martinez Conde J.A. and Díaz Puga M.A., 2004a. The Canteras-Galifa Neogene conglomerates: Evidence for an ophioli- tic association submerged in the Mediterranean Sea at the eastern end of the Betic Chain. Ofioliti, 29: 213-230.

Puga E., Díaz de Federico A., Fanning M., Nieto J.M., Rodríguez Martínez-Conde J.A., Díaz Puga M.A., Lozano J.A., Bianchini G., Natali C. and Beccaluva L. 2017. The Betic ophiolites and the evolution of the western Tethys. Geosciences, 7: 31.

Puga E., Díaz de Federico A. and Nieto J.M. 2002a. Tectonostratigraphic subdivision and petrological characterisation of the deepest complexes of the Betic zone: a review. Geodin. Acta, 15: 23-43.

Puga E., Díaz de Federico A., Nieto J.M. and Díaz Puga M.A., 2007. Petrología, evolución geodinámica y georrecursos del Espacio Natural de Sierra Nevada. Estud. Geol., 6: 19-40.

Puga E., Díaz de Federico A., Nieto J.M., Díaz Puga M.A. and Rodríguez Martínez-Conde J.A., 2009. The Betic Ophiolitic Association: A very significant geological heritage that needs to be preserved. Geoheritage, 1: 11-31.

Puga E., Díaz De Federico A., Nieto J.M., Díaz Puga M.A., Rodríguez Martinez Conde J.A. and Manteca Martinez J.I., 2004b. Argumentos petro- lógicos y geoquímicas para la subdivisión del Complejo Nevado-Filábride en los Complejos del Veleta y del Mulhacén. VI Congr. Geol. España, Zaragoza (España). Geo-Temas, 6: 101-104.

Puga E., Fanning C.M., Díaz de Federico A., Nieto J.M., Beccaluva L., Bianchini G. and Díaz Puga M.A., 2011. Petrology, geochemistry and U-Pb geochronology of the Betic Ophiolites: Inferences for Pangaea break-up and birth of the westernmost Tethys Ocean. Lithos, 124: 255-272.

Puga E., Fanning C.M., Nieto J.M. and Díaz de Federico A., 2005. New recrystallization textures in zircons generated by ocean-floor and eclogite facies metamorphism: a cathodoluminescence and U-Pb SHRIMP study with constraints from REE elements. Can. Miner., 42: 183-202.

Puga E., Nieto J.M. and Díaz de Federico A., 2000. Contrasting P-T paths in eclogites of the Betic Ophiolitic Association (Mulhacén Complex, SE Spain). Can. Miner., 38: 1137-1161.

Puga E., Nieto J.M., Díaz de Federico A., Bodinier J.L. and Morten L., 1999a. Petrology and metamorphic evolution of ultramafic rocks and dolerite dykes of the Betic Ophiolitic Association (Mulhacén Complex, SE Spain): evidence of Eo-Alpine subduction following an ocean-floor metasomatic process. Lithos, 49: 107-140.

Puga E., Ruiz Cruz M.D. and Díaz De Federico A., 1999b. Magnetite-silicate inclusions in olivine of ophiolitic meta-gabbros from the Mulhacén Complex (Betic Cordillera, SE Spain). Can. Miner., 37: 1191-1209.

Puga E., Ruiz Cruz M.D. and Díaz De Federico A., 2002b. Polymetamorphic amphibole veins in metabasalts from the Betic Ophiolitic Association (SE Spain): Relics of ocean-floor metamorphism preserved throughout the Alpine Orogeny. Can. Miner., 40: 67-83.

Rampone E. and Hofmann A.W., 2012. A global overview of isotopic heterogeneities in the oceanic mantle. Lithos, 148: 247-261.

Rampone E. and Piccardo G.B., 2000. The ophiolite-oceanic lithosphere analogue: new insights from the Northern Apennine (Italy). In: J. Dilek, E. Moores, D. Elthon and A. Nicolas (Eds.), Ophiolites and oceanic crust: New insights from field studies and Ocean Drilling Program. Geol. Soc. Am. Spec. Pap., 349: 21-34.

Rampone E., Borghini G. and Basch V., 2018. Melt migration and melt-rock reaction in the Alpine-Apennine peridotites: Insights on mantle dynamics in extending lithosphere. Geosci. Front., 11: 151-166.

Rampone E., Borghini G., Romairone A., Abouchami W., Class C., and Goldstein M.L., 2014. Sm-Nd geochronology of the Erro-Tobbio gabbros (Ligurian Alps, Italy): insights into the evolution of the Alpine Tethys. Lithos, 205: 236-246.

Rampone E., Hofmann A.W., Piccardo G.B., Vannucci R., Bottazzi P. and Ottolini L., 1995. Petrology, mineral and isotope geochemistry of the External Liguride peridotites (Northern Apennines, Italy). J. Petrol., 36: 81-105.

Rampone E., Hofmann A.W and Raczek I., 1998. Isotopic constraints within the Internal Liguride ophiolite (N. Italy): the lack of a genetic mantle-crust link. Earth Planet. Sci. Lett., 16: 175-189.

Rampone E., Hofmann A.W. and Raczek I., 2009. Isotopic equilibrium between mantle peridotite and melt: Evidence from the Corsica ophiolite. Earth Planet. Sci. Lett., 288: 601-610.

Rampone E., Piccardo G.B. and Hofmann A.W., 2008. E., Multistage melt-rock interaction in the Mt. Maggiore (Corsica, France) ophiolitic peridotites: microstructural and geochemical evidence. Contrib. Miner. Petrol., 156: 453-475.

Rampone E., Romairone A., Abouchami W., Piccardo G.B. and and Hofmann A.W., 2005. Chronology, petrology, and isotope geochemistry of the Erro-Tobbio peridotites (Ligurian Alps, Italy): Records of late Palaeozoic lithospheric extension. J. Petrol., 46, 799-827.

Regelous M., Weinzierl C.G. and Haase K.M., 2016. Controls on melting at spreading ridges from correlated abyssal peridotite-mid-ocean ridge basalt composition. Earth Planet, Sci. Lett., 449: 1-11.

Rosenbaum G., Lister G.S. and Duboz C., 2002. Relative motions of Africa, Iberia and Europe during Alpine orogeny. Tectonophysics, 359: 117-129.

Ruiz Cruz M.D., Puga E. and Díaz de Federico A., 2007. Exsolution microstructures in amphiboles from metabasalts of the Betic ophiolitic association (SE Spain). Eur. J. Miner., 19: 547-556.

Ruiz Cruz M.D., Puga E. and Nieto J.M., 1999. Silicate and oxide exsolution in pseudo-spinifex olivine from metaultramafic rocks of the Betic Ophiolitic Association: A TEM study. Am. Miner., 84: 1915-1924.

Saccani E., 2015. A new method of discriminating different types of post-Archean ophiolitic basalts and their tectonic significance using Th-Nb and Ce-Dy-Yb systematics. Geosci. Front., 6: 481-501.

Saccani E., Principi G., Garfagnoli F. and Menna F. 2008. Corsica ophiolites: Geochemistry and petrogenesis of basaltic and metabasaltic rocks. Ofioliti, 33: 187-207.

Salters V.J.M. and Stracke A. 2004. Composition of the depleted mantle. Geochem. Geophys. Geosyst., 5: Q05B07.

Savov I.P., Ryan J.G., D'Antonio M., Kelley K. and Mattie P., 2005. Geochemistry of serpentinized peridotites from the Mariana Forearc Conical Seamount, ODP Leg 125: Implications for the elemental recycling at subduction zones. Geochem. Geophys. Geosyst., 6: Q04J15. doi: 10.1029/2004GC000777.

Scambelluri M., Cannaò E., and Gilio M., 2019. The water and fluid-mobile element cycles during serpentinite subduction. A review. Eur. J. Miner., 31: 405-428.

Scambelluri M., Fiebig J., Malaspina N., Müntener O. and Pettke T., 2004. Serpentinite subduction: implications for fluid processes and trace-element recycling. Intern. Geol. Rev., 46: 595-613.

Schaltegger U., Desmurs L., Manatschal G., Müntener O., Meier M., Frank M. and Bernoulli D., 2002. The transition from rifting to sea-floor spreading within a magma-poor rifted margin: field and isotopic constraints. Terra Nova, 14: 156-162.

Schettino A. and Turco E., 2009. Breakup of Pangaea and plate kinematics of the Central Atlantic and Atlas regions. Geophys. J. Intern., 178: 1078-1097.

Secchiari A., Montanini A., Bosh D., Macera P. and Cluzel D., 2016. Melt extraction and enrichment processes in the New Caledonia lherzolites: evidence from geochemical and Sr-Nd isotope data. Lithos, 260: 28-43.

Secchiari A., Montanini A., Bosh D., Macera P. and and Cluzel D., 2019. Sr, Nd, Pb and trace element systematics of the New Caledonia harzburgites: Tracking source depletion and contamination processes in a SSZ setting. Geosci. Front., 11: 37-55.

Seifert K. and Brunotte D., 1996. Geochemistry of serpentinized mantle peridotite from site 897 in the Iberia Abyssal Plain. In: R.B. Whitmarsh, D.S. Sawyer, A. Klaus and D.G. Masson (Eds.), Proceed. ODP Sci. Rep., 149: 413-424.

Shervais J.N., 1982. Ti-Y plots and the petrogenesis of modern and ophiolitic lavas. Earth Planet. Sci. Lett., 59: 101-118.

Sinton J.M. and Detrick R.S., 1992. Mid-ocean ridge magma chambers. J. Geophys. Res., 97: 197-216.

Snow J.E. and Dick H.J.B., 1995. Pervasive magnesium loss by marine weathering of peridotite. Geochim. Cosmochim. Acta, 59: 4219-4235.

Snow J.E., Hart S.R. and Dick H.J.B., 1994. Nd and Sr isotope evidence linking mid-oceanridge basalts and abyssal peridotites. Nature, 371: 57-60.

Stille P., Clauer N. and Albrecht J., 1989. Nd isotope composition of the Jurassic Tethys seawater and the genesis of Alpine Mn-deposits. Evidences from Sr-Nd isotope data. Geochim. Cosmochim. Acta, 53: 1095-1099.

Sun S.S. and McDonough W.F., 1989. Chemical and isotopic systematic of oceanic basalts; implications for mantle composition and processes. In: A.D. Saunders and M.J. Norry (Eds.), Magmatism in the oceanic basins. Geol. Soc. London Spec. Publ., 4: 313-345.

Tendero J.A., Martín-Algarra A., Puga, E. and Díaz de Federico A., 1993. Lithostratigraphie des métasédiments de l'association ophiolitique Nevado-Filabride (SE Espagne) et mise en evidence d'objets ankeritiques evoquant des foraminifères planctoniques du Crétacé: consequences paléogéographiques. C.R. Acad. Sci. Paris, 316: 1115-1122.

Trommsdorff V., López Sánchez-Vizcaíno V., Gómez-Pugnaire M.T. and Müntener O., 1998. High pressure breakdown of antigorite to spinifex-textured olivine and orthopyroxene, SE Spain. Contrib. Miner. Petrol., 132: 139-148.

Ulrich M., Picard C., Guillot S., Chauvel C., Cluzel D. and Meffre S., 2010. Multiple melting stages and refertilization as indicators for ridge to subduction formation: The New Caledonia ophiolite. Lithos, 115: 223-236.

Venturelli G., Capedri S., Thorpe R.S. and Potts P.J., 1979. Rare-earth and other element distribution in some ophiolitic metabasalts of Corsica, Western Mediterranean. Chem. Geol., 24: 339-353.

Wood D.A., Tarney J., Varet J., Saunders A.D., Bougault H., Joron J.L., Treuil M. and Cann J.R., 1979. Geochemistry of basalts drilled in the North Atlantic by IPOD Leg 49: implications formantle heterogeneity. Earth Planet. Sci. Lett., 42: 77-97.

Whitmarsh R.B., Manatschal G. and Minshull T., 2001. Evolution of magma-poor continental margins from rifting to seafloor spreading. Nature, 413: 150-154.

Zheng Y.F. 2012. Metamorphic chemical geodynamics in continental subduction zones. Chem. Geol., 328: 5-48.

Received, December 2, 2019
Accepted, January 7, 2020

GUIDELINE FOR PAPER PUBLICATION

Language

The accepted language is English.

Manuscript submission

- The Journal consists of two main sections: **"Articles"** and **"Abstracts and Reviews"**. The latter concerns articles and books which have been published or submitted for publication elsewhere. A further section, "Letters", accepts comments, critical observations and replies regarding papers published in the Journal or any significant topic related to ophiolites or modern oceanic lithosphere.

ARTICLES

- To submit a manuscript you need to be registered as Author (please select this option at the end of the registration page: https://www.ofioliti.it/index.php/ofioliti/user/register). The manuscripts must be submitted online using the following web address: http://www.ofioliti.it/index.php/ofioliti/author/submit/
- A pdf version (max 12 Mb) of the manuscript (including text, figures and tables) must be uploaded.
- The corresponding author must indicate manuscript title, authors, and corresponding author data.
- Manuscripts to be published in the "Articles" need to be submitted in the following form:
  - Title.
  - First and last name of the authors.
  - Affiliation of each author.
  - Name and e-mail of the corresponding author.
  - Keywords (4-8) describing in order: i) main object of the paper, ii) attributes and specific aspects, iii) age, iv) locality
  - A brief and informative cover letter introducing the main target of the submitted manuscript.
  - Names and e-mail addresses of 3 potential reviewers.
  - Abstract: a complete but synthetic summary should precede the paper.
  - Text: a clear hierarchic order of the chapters is recommended. References in the text should be in brackets in the form: (Shakespeare et al., 1600), (Reagan and Gorbaciov, 1985). Paleontological names, in latin, should be displayed in italics. Foot page notes should be double-spaced and inserted at the end of the page they refer to, with a progressive number from the first to the last one.
  - The lines in the manuscript must be numbered continuously from beginning to end of the manuscript.
- Mathematics:
  - In-line equations should be typed as text.
  - Use of graphics programs and equation editors should be avoided, unless part of commonly available word-processing packages (Word, Pages, etc.).
  - Particularly complex equations or formulas can be send as a raster image (JPEG or TIFF).

References

The format of the references is shown in the following examples:

- Sclater J.G., Hawkins J.W., Mammerichx J. and Chace C.G., 1972. Crustal extension between the Tonga and Lau Ridges: petrologic and geophysical evidence. Geol. Soc. Am. Bull., 83 (2): 505-517.
- Holmes A., 1965. Principles of Physical Geology. Nelson, London, 1288 pp.
- Upton E.C.J., 1967. Alkaline pyroxenites. In: P.I.Willies (Ed.). Ultramafic and related rocks,Wiley, New York, p. 281-288.

Figures

- General:
  - At submission all line-drawings and photographs need to be included at the end of the pdf version of the manuscript.
  - For review purposes, the illustrations must be clearly legible and relatively easy to handle.
  - Authors will be asked to send original electronic versions to the Executive Editor only when manuscript is accepted.
  - All illustrations should be numbered.
  - All illustrations, whether line drawings or photographs, are termed figures.
  - Tables and photograph plates must have a separated numeration.
  - Captions must be typed on a separate sheet.
- About digital images:
  - We prefer TIFF, JPEG or native files for line drawings and TIFF or JPEG files (at least 300 dpi) for photographs and micro-photographs.
  - Pattern and screens: Avoid using dot screens and gray shades if possible, when dot screens are scanned dropouts or moiré patterns often occur.

  - If they are essential to the understanding of the figure try to make them coarse and use patterns instead of dot screens.
  - The pattern should look like dots and not appear as uniform gray at final publication scale.
  - If you use a dot screen it must be between 20% and 80% and a difference at least of 30% must be used between two adjacent dot screen fields.
  - Avoid fine lines and hairlines, preferably no finer than 1 pt.
- Figure size:
  - Digital images must be dimensioned using the figure final size, at least.
  - All illustrations should fit the width of a column (85 mm), two-thirds of a page (120 mm, with vertical aligned caption) or a full page (180mm).
- Other tips:
  - Subpanels of multipanel figures should be labelled with lower-case roman letters, (a), (b) etc.
  - Avoid mixing typefaces and style of figures within the same paper. Plan all type sizes large enough so that the smallest letters will beat least 1.5 mm tall after reduction.
  - Bar scales are preferred to numerical scales.
  - Calibrate graphic scales in metric units.
  - Indicate latitude and longitude on maps.
  - Where necessary, mark top.
  - All lettering on illustrations must be drafted, not typed or handwritten. Composite Photo plates must be mounted on a surface (max.180 x 250 mm).
  - Tables must be typed on separate sheets (as .xls excel files) and be as short as possible. They should be self explanatory and should supplement, not duplicate the text.
- Color images:
  Color illustrations will be accepted without additional fees for the online version. For color reproduction in print, extra costs are required. When you resubmit the final version please indicate your preference for color: in print or online only. In the latter case please check that the different grey patterns can be distinguished in the black and white printed version.

Supplementary material

Supplementary files can be uploaded separately during the submission process.

ABSTRACTS AND REVIEWS

- In the section "Abstracts and Reviews", the text should be in English.
- Tables and figures can be included.
- Both Abstracts and Reviews should be complete of title, author(s) and reference to the book or the journal where the paper is published. The title of the review can be different from that of the original work and can concern just specific aspects of it.

Print and reprints cost

- Together with your proof you will find an " Offprint Order form". Please return that completed and signed toghether with the corrected proof.
- The Authors must contribute to the Journal print with 100 €.
- The reprints cost is not included and it depends on the page numbers of the paper. If you would like to purchase reprints of your article please fill the "offprint order form" that will be send you by ETS with the proof of your article.
- Color illustrations and double (folded) figures will be accepted; however, the authors will be expected to make a contribution to extra costs.
- The print fee, reprints cost and the extra costs must be paid using the Authors Fees web section (right column of the Home Page).

Editorial process

- Authors are encouraged to submit the final text, figures and tables by email to the Executive Editor of Ofioliti (Alessandra Montanini, email: alessandra.montanini@unipr.it).
- It is recommended that Authors provide the final version of the text preferably in Microsoft WORD for DOS or MacOsX.
- Informations about file identification, operating system, version of WORD processing are also required.
- As with the requirements for the manuscript, the main text, list of references, table and figure captions should be stored in separate text files with clear file names.
- The Associate Editors have the right to introduce minor language corrections to the final version of the manuscript. A pdf proof version of your paper will be sent to the corresponding author, to be checked for the typesetting/editing.
- The Authors are not expected to make changes or correction that constitute departures from the paper in its accepted form.
- Proof must be returned within 3 days by e-mail to the address info@edizioniets.com.
- Ofioliti will do everything possible to get your paper corrected and published as quickly and accurately as possible. Therefore it is important to ensure that all of your correction are sent back to us in one communication.
- Subsequent correction will not be accepted.

We inform that we welcome abstracts of papers on ophiolites published elsewhere, to be sent according to the form below.

OFIOLITI

ABSTRACT CARD

Authors.....

Title .....

Institution(s) .....

.....

Published or in press on (journal) .....

(Vol.) (n°) (Year) (Pages)

Submitted to (journal) .....

TEXT

OFIOLITI SUBSCRIPTION ORDER FORM FOR 2019-2020

PAYMENT METHOD

BY WEB-PAGE

http://www.ofioliti.it

PayPal account or credit card

PAYMENT ENCLOSED:

1- **Bank draft:** Intesa San Paolo
IBAN IT 21 U 03069 14010 100000001781 BIC/SWIFT BCITITMM

2- **Postal cheque:** c.c.p. n° 14721567 Edizioni ETS

PLEASE SEND INVOICE

To the postal address.....

.....

PLEASE CHARGE MY CREDIT CARD

1- EuroCard 2- MasterCard 3- VISA

Card No ☐☐☐☐☐☐☐☐☐☐☐☐☐☐☐☐

CVV2 ☐☐☐ Exp. Date ___/_____

Holder name.....

Signature ..... Date

Edizioni ETS, Palazzo Roncioni - Lungarno Mediceo, 16, 56127 Pisa (ITALY)
Tel. +39.050.29544
Fax +39.050.20158
ofioliti@edizioniets.com
www.edizioniets.com

SUBSCRIPTION PRICE

Ofioliti is issued twice per year, with possible supernumerary special issues.

The subscription price for the EU countries is

EUR 150.00 for institutions and libraries;
EUR 35.00 for individuals.

The subscription price for the other countries is

EUR 200.00 for institutions and libraries;
EUR 50.00 for individuals.

The subscription price includes both the printed and the online journal versions.

Edizioni ETS
Palazzo Roncioni - Lungarno Mediceo, 16, I-56127 Pisa
info@edizioniets.com - www.edizioniets.com
Finito di stampare nel mese di gennaio 2020